

**Investigation of Mixture Formation and
Combustion in an Ethanol Direct Injection plus
Gasoline Port Injection (EDI+GPI) Engine**

By

Yuhan Huang

A thesis in fulfilment of the requirements for the degree of
Doctor of Philosophy

School of Electrical, Mechanical and Mechatronic Systems
Faculty of Engineering and Information Technology
University of Technology Sydney

December 2016

Certificate of Original Authorship

This thesis is the result of a research candidature conducted jointly with another university as part of a collaborative doctoral degree. I certify that the work in this thesis has not previously been submitted for a degree nor has it been submitted as part of requirements for a degree except as part of the collaborative doctoral degree and/or fully acknowledged within the text.

I also certify that the thesis has been written by me. Any help that I have received in my research work and the preparation of the thesis itself has been acknowledged. In addition, I certify that all information sources and literature used are indicated in the thesis.

Signature of Student:

Date:

Acknowledgements

To pursue a doctoral degree could be a long and challenging journey. Through this journey, I fortunately received help and support from the following wonderful people who made this journey enjoyable and fruitful.

First of all, I would like to thank my principle supervisor Associate Professor Guang Hong who provided huge support and guidance. She invested numerous efforts in supervising me and always cared about my progress and future career. The experience I have acquired and research training I have received from her will greatly benefit my research career. I would also like to thank my co-supervisor Professor Ronghua Huang who supported the spray experiments at the Huazhong University of Science and Technology (HUST). Furthermore, I appreciate the discussion and support received from Dr. Jack Wang, Professor Xiaobei Cheng and Dr. Zhaowen Wang.

I really appreciate Nizar Al-Muhsen and Yuan Zhuang for your time and assistance in the engine experiments. The ethanol fuel provided by the Manildra Group is greatly acknowledged. Many thanks to Peng Deng, Sheng Huang and Yinjie Ma for your suggestions and help in the spray experiments at HUST. I also appreciate Laurence Stonard, John Funnell, Peter Tawadros and Jack Liang for your excellent support in the maintenance of the engine. Thanks to Vahik Avakian and Matthew Gaston for your valuable support in the engine CFD modelling.

I gratefully thank my close friends Mahdi Hassan, Nizar Al-Muhsen, Sayed Royel, etc. for the wonderful time we spent together throughout my candidature at UTS. I wish you all health and success.

This study was sponsored by the dual doctoral degree program between UTS and HUST. The funding provided by the China Scholarship Council is gratefully appreciated.

Last but most importantly, I would like to thank my wife Jennifer Liu for her support and care. No matter how tired I was in the office, I always felt warm and relaxed once I got home. With you by my side, there is no difficulty I could not cope with and there is no dream I could not realise. Meanwhile, I would also like to thank my parents and parents-in-law for their love and support.

List of Publications

Journal articles

- [1] **Y. Huang**, G. Hong. Investigation of the effect of heated ethanol fuel on combustion and emissions of an ethanol direct injection plus gasoline port injection (EDI + GPI) engine. *Energy Conversion and Management* 2016; 123: 338-347.
- [2] **Y. Huang**, G. Hong, R. Huang. Effect of injection timing on mixture formation and combustion in an ethanol direct injection plus gasoline port injection (EDI+GPI) engine. *Energy* 2016; 111: 92-103.
- [3] **Y. Huang**, S. Huang, R. Huang, G. Hong. Spray and evaporation characteristics of ethanol and gasoline direct injection in non-evaporating, transition and flash-boiling conditions. *Energy Conversion and Management* 2016; 108: 68-77.
- [4] **Y. Huang**, G. Hong, R. Huang. Investigation to charge cooling effect and combustion characteristics of ethanol direct injection in a gasoline port injection engine. *Applied Energy* 2015; 160: 244-254.
- [5] **Y. Huang**, G. Hong, R. Huang. Numerical investigation to the dual-fuel spray combustion process in an ethanol direct injection plus gasoline port injection (EDI+GPI) engine. *Energy Conversion and Management* 2015; 92: 275-286.
- [6] **Y. Huang**, S. Huang, P. Deng, R. Huang, G. Hong. The Effect of Fuel Temperature on the Ethanol Direct Injection Spray Characteristics of a Multi-hole Injector. *SAE Int. J. Fuels Lubr.* 2014; 7: 792-802.

Conference proceedings

- [7] **Y. Huang**, G. Hong. An Investigation of the Performance of a Gasoline Spark Ignition Engine Fuelled with Hot Ethanol Direct Injection. *Australian Combustion Symposium*, the Combustion Institute, Melbourne Australia; 2015.
- [8] **Y. Huang**, G. Hong, R. Huang. The Effect of Volume Ratio of Ethanol Directly Injected in a Gasoline Port Injection Spark Ignition Engine. *10th Asia-Pacific Conference on Combustion*, the Combustion Institute, Beijing China; 2015.

- [9] **Y. Huang**, S. Huang, R. Huang, G. Hong. Macroscopic and Microscopic Characteristics of Ethanol and Gasoline Sprays. *19th Australasian Fluid Mechanics Conference*, Melbourne Australia; 2014.
- [10] **Y. Huang**, G. Hong. Development of a Numerical Model for Investigating the EDI+GPI Engine. *19th Australasian Fluid Mechanics Conference*, Melbourne Australia; 2014.
- [11] **Y. Huang**, G. Hong, R. Huang. Numerical Investigation to the Effect of Ethanol/Gasoline Ratio on Charge Cooling in an EDI+GPI Engine. *SAE paper 2014-01-2612*; 2014.
- [12] **Y. Huang**, G. Hong, X. Cheng, R. Huang. Investigation to Charge Cooling Effect of Evaporation of Ethanol Fuel Directly Injected in a Gasoline Port Injection Engine. *SAE paper 2013-01-2610*; 2013.

Abstract

Ethanol direct injection plus gasoline port injection (EDI+GPI) is a new technology to utilise ethanol fuel in spark-ignition engines more effectively and efficiently than E10 or E85 fuels in the current market. It takes the advantages of ethanol's high octane number and great enthalpy of vaporisation which allow higher compression ratio and consequently increase the thermal efficiency. Primary experimental investigation showed that the engine performance was improved by EDI+GPI. The thermal efficiency was increased, the NO emission was decreased and the spark timing could be advanced without engine knock. However, the CO and HC emissions were increased when EDI was applied. To understand the mechanisms behind the experimental results, the mixture formation and combustion processes of an EDI+GPI engine were investigated using CFD simulation, and constant volume chamber and engine experiments.

To investigate the spray and evaporation characteristics of ethanol fuel and provide experimental data for CFD simulation, spray experiments were conducted in a constant volume chamber using high speed shadowgraphy imaging technique. The results showed that ethanol fuel evaporated slowly when fuel temperature was in the range of 275-325 K. However, the evaporation rate increased quickly when fuel temperature was higher than 350 K. The low evaporation rate of ethanol fuel in low temperature environment implied that EDI should be only applied in high temperature engine environment. When the excess temperature was smaller than 4 K, the spray behaved the same as the subcooled spray did. The spray collapsed when the excess temperature was 9 K. Flash-boiling did not occur until the excess temperature reached 14 K.

Numerical simulation of the EDI+GPI engine showed that the overall cooling effect of EDI was enhanced with the increase of ethanol ratio from 0% to 58%, but not with further increase of ethanol ratio. When the ethanol ratio was greater than 58%, the fuel impingement became severe and a large number of liquid ethanol droplets were left in the combustion chamber during combustion, leading to local over-cooling in the near-wall region and over-lean mixture at the spark plug gap. As a consequence, the CO and HC emissions increased due to incomplete combustion. Compared with GPI only condition, the faster flame speed of ethanol fuel in EDI+GPI condition resulted in shorter combustion initiation duration and major combustion duration, leading to the increase of IMEP and thermal efficiency when the ethanol ratio was 0-58%. However, the

combustion performance was deteriorated by over-cooling and fuel impingement when ethanol ratio was greater than 58%. Experimental results showed consistently that the combustion and emission performance of this engine could be the best in the ethanol ratio of 40-60% at the investigated engine condition (medium load, 4000 rpm and early EDI timing of 300 CAD BTDC). Numerical results showed that the best engine performance was resulted from effective charge cooling and combustion efficiency improved by avoiding the wall wetting, over-lean and local over-cooling issues. Numerical simulations were also carried out to investigate the effect of direct injection timing on the EDI+GPI. The results showed that when the EDI timing was retarded from 300 to 100 CAD BTDC, the mixture around the spark plug became leaner and the distribution of equivalence ratio became more uneven. Moreover, late EDI timing at 100 CAD BTDC resulted in severe fuel impingement and caused local over-cooling effect and over-rich mixture. Consequently, the combustion speed and temperature were decreased by retarded EDI timing, leading to the decreased NO emission and the increased HC and CO emissions. The fuel impingement and incomplete combustion of late EDI timing at 100 CAD BTDC could be addressed by reducing the ethanol ratio to an appropriate point.

Experiments on the EDI+GPI engine were conducted to verify the idea of EDI heating on improving the engine performance, which was developed based on the understanding gained from the numerical investigation. Results showed that EDI heating effectively reduced the CO and HC emissions at the original engine's spark timing of 15 CAD BTDC. Meanwhile, the NO emission was slightly increased, but still much smaller than that in GPI only condition. However, the IMEP and combustion speed were slightly reduced by EDI heating. To enhance the effect of EDI heating, experiments were conducted at varied spark timing. The results at the MBT timing (19 CAD BTDC) showed that the reduction of IMEP by EDI heating was less significant whilst the CO and HC emissions were effectively reduced. Therefore EDI heating was effective to address ethanol's low evaporation rate and over-cooling effect issues in the development of EDI+GPI engine in terms of minimizing the emissions.

Contents

Certificate of Original Authorship.....	i
Acknowledgements	ii
List of Publications.....	iii
Abstract.....	v
Contents.....	vii
List of Tables	x
List of Figures.....	xi
Definitions and Abbreviations.....	xvi
1 Introduction.....	1
1.1 Research background and motivation	1
1.2 Research methodology and objectives	2
1.3 Thesis outline	3
2 Literature Review	5
2.1 Development of EDI+GPI.....	5
2.2 CFD engine modelling	8
2.2.1 Turbulence modelling	9
2.2.2 Spray modelling	10
2.2.3 Combustion modelling.....	17
2.3 Fuel properties and effect on spray combustion.....	26
2.3.1 Fuel properties.....	26
2.3.2 Spray characteristics of ethanol and gasoline fuels.....	30
2.3.3 Measuring the charge cooling effect	34
2.3.4 Combustion characteristics of ethanol fuel	36
2.3.5 Fuel heating to generate fine and fast evaporating sprays	40
3 Experimental Setup and CFD Model	43
3.1 Test rig for investigating EDI sprays	43
3.1.1 EDI injector	43
3.1.2 Constant volume chamber optical system.....	44
3.1.3 Test fuel.....	46

3.1.4	Experimental conditions.....	47
3.1.5	Image Processing	47
3.2	CFD model of EDI+GPI engine.....	50
3.2.1	Computational mesh	51
3.2.2	Spray sub-models.....	53
3.2.3	Combustion sub-models.....	55
3.2.4	Boundary and initial conditions	58
3.2.5	Model verification.....	59
3.3	Test rig for investigating EDI heating.....	64
3.3.1	Engine setup and ethanol heating.....	64
3.3.2	Instruments and measurements	66
3.3.3	Test fuels	67
3.3.4	Engine experiment conditions.....	67
3.3.5	In-cylinder pressure data processing.....	69
4	EDI Spray Characteristics.....	71
4.1	Characteristics of non-evaporating and evaporating sprays.....	71
4.2	Characteristics of flash-boiling sprays	75
4.3	Spray transition process.....	78
4.4	Implications for engine emissions.....	80
4.5	Summary	81
5	Mixture Formation and Cooling Effect of EDI+GPI.....	83
5.1	EDI+GPI sprays	83
5.2	Cooling effect of EDI.....	87
5.3	Effect of ethanol ratio on charge cooling	93
5.4	Summary	100
6	Combustion and Emission characteristics of EDI+GPI	102
6.1	Combustion and emissions of EDI+GPI	102
6.2	Effect of ethanol ratio on combustion	109
6.3	Effect of EDI timing on fuel evaporation, mixing and combustion	115
6.4	Effect of small ethanol ratio on reducing fuel impingement.....	123
6.5	Summary	125

7	Effect of EDI Heating on Engine Performance	128
7.1	Engine performance of EDI heating at original spark timing	128
7.2	Combustion characteristics of EDI heating at original spark timing	133
7.3	Engine performance of EDI heating at MBT timing.....	138
7.4	Summary	142
8	Conclusions and Future Work	144
8.1	Conclusions	144
8.2	Suggestions for future work	147
	References	149
	Appendix	164

List of Tables

Table 2.1: The cost of various simulation approaches [57]	10
Table 2.2: Physical and chemical properties of ethanol and gasoline fuels.....	26
Table 2.3: Experimental conditions in [45] and [117]	39
Table 3.1: Specifications of the EDI+GPI engine.....	65
Table 3.2: EDI heating experiment conditions	68
Table A.1: List of engine simulation conditions and related publications.....	164
Table A.2: List of spray experiment conditions and related publications.....	165
Table A.3: List of engine experiment conditions and related publications.....	166

List of Figures

Figure 2.1: The evolution processes of a liquid fuel spray [60].....	12
Figure 2.2: Different types of secondary breakup [75].....	14
Figure 2.3: Droplet distortion.....	15
Figure 2.4: Schematics of laminar (left) and turbulent (right) Bunsen premixed flames [85].....	18
Figure 2.5: Combustion regimes of turbulent premixed flames [86].....	20
Figure 2.6: Schematics of laminar (a) and turbulent (b) non-premixed flames[55]	21
Figure 2.7: Combustion regimes of turbulent non-premixed flames, (a) [55], (b) [85]..	21
Figure 2.8: Schematics of combustion styles with different overall equivalence ratios (ϕ_L is the lean flammability limit and ϕ_R is the rich flammability limit) [87]	22
Figure 2.9: Parameters for describing the premixed and non-premixed flames [55].....	24
Figure 2.10: Saturation vapour pressures of gasoline, ethanol and iso-octane fuels	27
Figure 2.11: Comparison between the ethanol vapour pressures calculated from the experimental data [101] and Yaws' handbook [100].....	28
Figure 2.12: Laminar flame speeds of ethanol and gasoline fuels [102]	29
Figure 2.13: Primary breakup structures of gasoline (a) and ethanol (b) sprays [111]...	32
Figure 3.1: Overall view of the EDI injector tip (left) and the magnified image of the nozzle holes (right).....	44
Figure 3.2: Lateral view of the spray plumes and their directions.....	44
Figure 3.3: Front view of the spray plumes and their footprints.....	44
Figure 3.4: Schematic of the EDI spray experiment apparatus.....	45
Figure 3.5: Ethanol fuel properties (data source: [100]).....	46
Figure 3.6: Shadowgraphy spray image processing method.....	48
Figure 3.7: Effect of the threshold vaule on the detected spray boundary.....	49
Figure 3.8: Cross-sectional view of the geometry of the cylinder head.....	51

Figure 3.9: Geometry decomposition.....	52
Figure 3.10: Computational mesh.....	52
Figure 3.11: Measured valve lifts of the intake and exhaust valves	52
Figure 3.12: Computational meshes with different grid densities	60
Figure 3.13: Grid size sensitivity	61
Figure 3.14: Comparison of the experimental and numerical results of EDI spray pattern at 1.5 ms ASOI in a constant volume chamber @ 6.0 MPa injection pressure, 0.1 MPa ambient pressure and 350 K ambient temperature.....	61
Figure 3.15: Comparison of the experimental and numerical results of EDI spray tip penetration in a constant volume chamber @ 6.0 MPa injection pressure, 0.1 MPa ambient pressure and 350 K ambient temperature.....	62
Figure 3.16: Comparison between the measured and simulated values of in-cylinder pressure and heat release rate at different ethanol ratios.....	63
Figure 3.17: Schematic of the EDI+GPI engine	64
Figure 3.18: Schematic of EDI fuel heating system	65
Figure 3.19: logarithmic pressure-volume diagram [184]	70
Figure 4.1: Spray images in non-evaporating and evaporating conditions.....	72
Figure 4.2: Averaged pixel intensity of the spray area at 8 ms ASOI for sprays in non-evaporating and evaporating conditions.....	73
Figure 4.3: Spray tip penetrations in non-evaporating and evaporating conditions	73
Figure 4.4: Spray projected areas in non-evaporating and evaporating conditions	74
Figure 4.5: Spray angles in non-evaporating and evaporating conditions.....	74
Figure 4.6: Spray images in flash-boiling conditions (Please refer to the electronic version of this figure for a clearer interpretation of the droplet explosion).....	76
Figure 4.7: Schematic of the droplet flash-boiling process	76
Figure 4.8: Averaged pixel intensity of the spray area at 8.0 ms ASOI for sprays in flash-boiling conditions.....	77
Figure 4.9: Spray tip penetrations in flash-boiling conditions.....	77

Figure 4.10: Spray projected areas in flash-boiling conditions.....	78
Figure 4.11: Spray angles in flash-boiling conditions	78
Figure 4.12: Spray images in the transition process (Please refer to the electronic version of this figure for a clearer interpretation of the spray cloud)	79
Figure 5.1: Spatial distributions of spray droplets and air flow velocity vectors on the engine symmetry plane of EDI+GPI E46 at: (a) the intake TDC, (b) the end of GPI injection, (c) 15 CAD after the start of EDI, and (d) at the spark timing	84
Figure 5.2: Structure of the EDI spray at: (a) 15 CAD after the start of EDI injection, (b) the end of EDI injection and (c) the BDC.....	85
Figure 5.3: Distributions of gasoline and ethanol fuel mass fractions and overall equivalence ratio by spark timing	86
Figure 5.4: Cooling effect enhancement of EDI: (a) comparison of in-cylinder mean temperature in E0, E46 and E100 conditions, (b) the temperature reduced by EDI.....	88
Figure 5.5: Mass of the injected and evaporated fuels (a) and the enthalpy for their evaporation (b) in E0, E46 and E100 conditions	90
Figure 5.6: Saturation vapour pressures of gasoline [101] and ethanol [100] fuels	91
Figure 5.7: In-cylinder temperature distribution on a vertical plane passing through the spark plug predicted for GPI only E0 (a), EDI+GPI E46 (b) and EDI only E100 (c) conditions at the spark timing	92
Figure 5.8: In-cylinder temperature distribution on a horizontal plane predicted for GPI only E0 (a), EDI+GPI E46 (b) and EDI only E100 (c) conditions at the spark timing ..	93
Figure 5.9: In-cylinder temperature distributions by spark timing	94
Figure 5.10: Ethanol droplet distributions of EDI+GPI E46 at the end of EDI (left) and spark timing (right)	95
Figure 5.11: Variation of mean in-cylinder temperature by spark timing with the ethanol ratio	95
Figure 5.12: Completeness of the ethanol and gasoline evaporation by spark timing....	96
Figure 5.13: Ideal cooling potential and charge cooling realized	97
Figure 5.14: Distribution of equivalence ratio around the spark plug by spark timing ..	98

Figure 5.15: Distributions of the ethanol spray droplets at the end of EDI injection	99
Figure 6.1: Flame propagation in GPI only E0 and EDI+GPI E46	103
Figure 6.2: In-cylinder temperature in GPI only E0 and EDI+GPI E46 conditions	104
Figure 6.3: The mass of unburnt vapour (a) and liquid (b) fuels	106
Figure 6.4: Formation of NO (a) and CO (b) emissions during the combustion	107
Figure 6.5: Spatial distributions of temperature, O, OH, and NO at 405 CAD	109
Figure 6.6: Distributions of O ₂ and CO at 405 CAD	109
Figure 6.7: In-cylinder pressure varying with the ethanol ratio	110
Figure 6.8: IMEP varying with the ethanol ratio	110
Figure 6.9: CA0-10% and CA10-90% varying with the ethanol ratio	111
Figure 6.10: Flame propagation and distributions of OH mass fraction at 375 CAD and 395 CAD varying with the ethanol ratio	112
Figure 6.11: The distributions of ethanol liquid droplets, equivalence ratio and cylinder temperature at 395 CAD varying with the ethanol ratio	113
Figure 6.12: Measured engine emissions varying with the ethanol ratio	114
Figure 6.13: Experimental results of IMEP, ISNO, ISCO and ISHC varying with EDI timing	115
Figure 6.14: Variations of mass of the vapour ethanol fuel with crank angle degrees at three injection timings	116
Figure 6.15: Air flow velocity vectors on the engine symmetry plane at the start and end of EDI injection with different EDI timings	117
Figure 6.16: Distributions of the vapour mass fractions of gasoline and ethanol fuels and the equivalence ratio on a vertical plane passing through the spark plug by spark timing	118
Figure 6.17: Variation of wall film mass with crank angle degrees	119
Figure 6.18: Evolution of flame-brush with different EDI timings	119
Figure 6.19: Spatial distributions of combustion temperature with different EDI timings	120

Figure 6.20: Distributions of flame brush, ethanol droplets, equivalence ratio and combustion temperature at EVO with different EDI timings	121
Figure 6.21: Distribution of NO mass fraction at EVO	122
Figure 6.22: Distribution of CO mass fraction at EVO	123
Figure 6.23: Distributions of the equivalence ratio and wall film of smaller amount of ethanol fuel at IT100 by spark timing	124
Figure 6.24: Distributions of flame brush, ethanol droplets and in-cylinder temperature of smaller amount of ethanol fuel at IT100 at the time of EVO.....	125
Figure 7.1: Effect of ethanol fuel temperature on the IMEP.....	129
Figure 7.2: Effect of ethanol fuel temperature on the indicated thermal efficiency	130
Figure 7.3: Variation of ISCO with ethanol fuel temperature	131
Figure 7.4: Variation of ISHC with ethanol fuel temperature	131
Figure 7.5: Variation of ISNO with ethanol fuel temperature	133
Figure 7.6: Effect of ethanol fuel temperature on the in-cylinder pressure and heat release rate.....	133
Figure 7.7: Variation of lambda with ethanol fuel temperature.....	135
Figure 7.8: Effect fuel temperature on the EDI spray structure.....	136
Figure 7.9: Variation of CA0-10% with ethanol fuel temperature	137
Figure 7.10: Variation of CA10-90% with ethanol fuel temperature	138
Figure 7.11: Effect of spark timing on IMEP (a) and NO emission (b) at ethanol ratios of 0%, 55% and 100%.....	139
Figure 7.12: Effect of EDI heating on IMEP at the MBT timing	140
Figure 7.13: Effect of EDI heating on ISCO at the MBT timing.....	141
Figure 7.14: Effect of EDI heating on ISHC at the MBT timing.....	141
Figure 7.15: Effect of EDI heating on ISNO at the MBT timing	142

Definitions and Abbreviations

Acronyms

ABDC	After bottom dead center
ASOI	After the start of injection
ATDC	After top dead center
BBDC	Before bottom dead center
BDC	Bottom dead center
BTDC	Before top dead center
CAD	Crank angle degrees
CFD	Computational fluid dynamics
DI	Direct injection
ECFM	Extended Coherent Flame Model
EDI	Ethanol direct injection
EDI+GPI	Ethanol direct injection plus gasoline port injection
EVC	Exhaust valve close
EVO	Exhaust valve open
GDI	Gasoline direct injection
GPI	Gasoline port injection
IC	Internal combustion
IMEP	Indicated mean effective pressure
ITNFS	Intermediate turbulent net flame stretch
IVC	Intake valve close
IVO	Intake valve open
MBT	Minimum spark advance for best torque
MFB	Mass fraction burnt
PDF	Probability Density Function
PI	Port injection
RANS	Reynolds Averaged Navier-Stokes
SI	Spark ignition
TDC	Top dead center

Symbols

A_p	Particle surface area
C_D	Drag coefficient
D_i	Diffusion coefficient in air
N_i	Molar flux of vapour
P	Pressure
D	Dissipation term of flame area
D_i	Diffusion coefficient in air
P_1	Source term due to turbulence interaction
P_2	Source term due to dilatation in the flame
P_3	Source term due to expansion of burned gas
P_4	Source term due to normal propagation
T	Temperature
U_L	Laminar flame speed
V	Volume
X_i	Mole fraction of species i
Y_i	Mass fraction of species i
Z	Mixture fraction
B_m	Spalding mass number
Da	Damköhler number
Ka	Karlovitz number
Re	Reynolds number
We	Weber number
ϕ	Fuel/air equivalence ratio
Σ	Flame area density
Γ_K	ITNFS term
c	Progress variable
c_p	Heat capacity
d	Diameter
h	Heat transfer coefficient
m	Mass

k	Turbulent kinetic energy
r	Radius
y	Distortion of the droplet
γ	Specific heat ratio
ε	Turbulent dissipation rate
σ	Surface tension
ρ	Density
μ	Dynamic viscosity
ν	Kinematic viscosity
t	Time
μ_t	Turbulent viscosity
u	Velocity
w	Turbulent velocity fluctuation
l_t	Integral turbulent length scale
l_d	Diffusion thickness
l_r	Reaction zone thickness
τ_t	Turbulent time scale
τ_c	Chemical time scale
τ_k	Kolmogorov time scale
k_c	Mass transfer coefficient
δ_l	Flame thickness
$\varphi_{realized}$	Percentage of charge cooling realized
$CA_{0-10\%}$	Combustion initiation duration
$CA_{10-90\%}$	Major combustion duration
Pa/Ps	Ambient-to-saturation pressure ratio
$E'X'$	X% ethanol by volume. e.g. E46 is 46% ethanol via direct injection plus 54% gasoline via port injection
$IT'XXX'$	Injection timing of XXX CAD BTDC
ΔT	Spray excess temperature
ΔT_{actual}	Actual cooling effect
ΔT_{ideal}	Ideal cooling potential

Subscripts

<i>d</i>	Droplet phase
<i>g</i>	Gas phase
<i>i</i>	Species <i>i</i>
<i>l</i>	Liquid phase
<i>p</i>	Particle
<i>rel</i>	Relative
<i>sat</i>	Saturation
∞	Ambient bulk gas

Chapter One

1 Introduction

1.1 Research background and motivation

The worldwide concern of fossil fuel depletion and greenhouse effect has driven our society to rely more and more on renewable energy resources and alternative fuels. Ethanol fuel is considered as one of the promising alternative fuels for internal combustion (IC) engines because it can be produced from bio-mass via established and new processes [1]. In the past decade, the global consumption of ethanol fuel has increased from 4.5 billion gallons in 2000 to 21.8 billion gallons in 2012 [2]. Compared with gasoline fuel, ethanol has many advantages such as greater enthalpy of vaporisation, larger octane number, faster laminar flame speed and smaller stoichiometric air/fuel ratio. Its advantages should be fully taken in the development of new engine technologies such as engine downsizing targeting to reduce the energy consumption and CO₂ emission [3].

At present, ethanol is mostly used via blending with gasoline fuel, such as E10 (gasoline containing 10% of ethanol by volume) for commercial passenger cars and E85 (gasoline containing 85% of ethanol by volume) for flexible fuel vehicles. However, ethanol fuel blended with gasoline fuel at a fixed ratio cannot fully exploit the ethanol's potentials in improving the engine performance. Experiments showed that different ethanol/gasoline blending ratios were required to optimize the engine performance in different operation conditions [4-7]. Therefore ethanol direct injection plus gasoline port injection (EDI+GPI) has been proposed and investigated to make the use of ethanol fuel more effectively and efficiently in spark ignition (SI) engines [8-11].

EDI+GPI is aimed to take the advantages of ethanol fuel including its thermal and chemical benefits to enhance the charge cooling effect and anti-knock ability, and

consequently to increase the compression ratio and thermal efficiency of SI engines. Preliminary experimental investigation showed engine performance improved by EDI+GPI in a single cylinder SI engine [8, 12]. EDI+GPI showed its leveraging effect on reducing the gasoline fuel consumption by increasing indicated mean effective pressure (IMEP), volumetric efficiency, thermal efficiency and allowing advanced spark timing without engine knock. Meanwhile, the NO emission was reduced. However, the CO and HC emissions were increased when EDI+GPI was applied. It was inferred that the direct injection of ethanol fuel played an important role, including the enhanced cooling effect due to ethanol's larger enthalpy of vaporisation, strong anti-knock ability due to its greater octane number and improved combustion efficiency due to its faster laminar flame speed.

Although experiments have demonstrated the advantages of EDI+GPI, the way how ethanol fuel affects the mixture formation and combustion processes remains a hard and costly task for experimental investigation. Nowadays, multidimensional computational fluid dynamics (CFD) modelling has been proven a useful tool to investigate the in-cylinder flows. Compared with experiment-based approach, CFD simulation can significantly reduce both time and cost in design and production in IC engine applications. Moreover, unlike experimental investigations which are mainly focus on the macroscopic parameters of engine performance, CFD results can provide detailed and visualized information about the complicated flows inside the combustion chamber which can only be acquired in very costly optical experiments. Therefore, this thesis is dedicated to understand the mixture formation and combustion processes of the EDI+GPI engine by numerical simulation using the CFD code ANSYS FLUENT. Method for improving the performance of the EDI+GPI engine was proposed based on the understanding gained from the CFD simulation and was investigated experimentally.

1.2 Research methodology and objectives

This project was aimed to understand the mixture formation and combustion processes in an EDI+GPI engine by CFD simulation, constant volume chamber and engine experiments. A thorough understanding of spray combustion characteristics of the EDI+GPI engine is of great importance to utilise ethanol fuel more effectively and efficiently in SI engines, thus facilitate the use of biofuel and protect the environment.

To realise this goal, a CFD engine model was developed using the ANSYS FLUENT. EDI spray experiments in a constant volume chamber were conducted to investigate the ethanol spray and evaporation characteristics and provide information for engine modelling. The engine model was verified against the experimental results of the constant volume chamber and EDI+GPI engine. The verified model was then applied to understand the mixture formation and combustion processes of the engine. A good understanding of the mechanisms behind the experimental results was gained. EDI heating was proposed to address the issues of ethanol's the low evaporation rate and over-cooling effect in the EDI+GPI engine. Experiments on the EDI+GPI engine fuelled with heated ethanol fuel were carried out to verify the proposed idea. Detailed aims of this project are described as follows.

- 1) To experimentally investigate the EDI spray and evaporation characteristics in a constant volume chamber using high speed shadowgraphy imaging technique.
- 2) To develop and verify a CFD model for the EDI+GPI engine using ANSYS FLUENT.
- 3) To numerically investigate the effects of EDI on the in-cylinder mixture formation and combustion characteristics of the EDI+GPI engine.
- 4) To numerically investigate the effects of different EDI injection strategies on the mixture formation and combustion processes.
- 5) To experimentally verify the ideas developed based on the understanding achieved through the CFD modelling on the EDI+GPI engine.

1.3 Thesis outline

The contents of the following chapters of this thesis are outlined as follows.

Chapter Two reviews the background information of EDI+GPI systems, ethanol spray characteristics and CFD engine modelling from published works.

Chapter Three introduces the developed CFD engine model and the experimental apparatuses including the constant volume chamber and the EDI+GPI engine test rig.

Chapter Four presents and discusses the experimental results of ethanol spray and evaporation characteristics in non-evaporating, evaporating and flash-boiling conditions and the implications for the application of EDI in IC engines.

Chapter Five presents and discusses the numerical results of mixture formation process of the EDI+GPI engine, including the in-cylinder flows, the sprays of dual-injection, and the charge cooling effect of EDI.

Chapter Six presents and discusses the numerical results of combustion process of the EDI+GPI engine, including the combustion and emission characteristics of EDI+GPI, and the effects of ethanol ratio and injection timing on the combustion characteristics.

Chapter Seven presents and discusses the experimental results of the performance of the EDI+GPI engine fuelled with heated ethanol fuel.

Chapter Eight concludes this thesis by summarizing the outcomes of each chapter and recommending future work.

Chapter Two

2 Literature Review

2.1 Development of EDI+GPI

Promoted by financial incentives and renewable energy policies, bio-ethanol fuel is becoming more and more popular globally in recent years. Ethanol fuel is usually used as a substitute or octane-enhancer for gasoline fuel in SI engines. It can be used as a neat fuel or blended fuel with gasoline in SI engines. Extensive research has been conducted to investigate the performance of renewable/alternative fuels in IC engines. The combustion processes of ethanol, gasoline and methane-hydrogen-blend were investigated in an optically accessible port fuel injection SI engine [13]. Balki et al. [14] experimentally investigated the effect of compression ratio on the combustion and emission performance of an SI engine fuelled with pure ethanol. The spray characteristics and flame propagation of bio-ethanol in an optical direct injection (DI) SI engine were investigated [15]. Almeida et al. [16] evaluated the catalytic converter aging process of a four-cylinder SI engine fuelled with hydrous ethanol.

The above studies showed the advantages in thermal efficiency and life of the catalytic convertor of using neat ethanol fuel in the tested conditions. However, as a neat fuel, ethanol may not be suitable to power SI engines in some conditions because of its low volatility, low heating value and high enthalpy of vaporisation, especially in cold conditions [17, 18]. It was reported that gasoline fuelled engines could be started at ambient temperature as low as -40 °C, whilst ethanol fuelled engines could not be started at temperature lower than 13 °C without an auxiliary system for cold starting [17]. The insufficient production of ethanol fuel also limits its usage as a neat fuel to replace gasoline fuel. At present, therefore, ethanol is mostly used via blending with gasoline fuel, such as E10 and E85. Blending ethanol with gasoline can improve the fuel properties and

consequently improve the engine combustion process, resulting in higher combustion efficiency and lower engine-out emissions. Many studies have been reported in this field. Karavalakis et al. [19] measured the gaseous and particulate emissions of spray-guided and wall-guided DI SI engines fuelled with ethanol/gasoline and iso-butanol/gasoline blends. Ozsezen et al. [20] investigated the performance of a vehicle fuelled with 5% and 10% alcohol/gasoline blends. Suarez-Bertoa et al. [21] measured the regulated and unregulated emissions from an Euro 5a flexible fuel vehicle fuelled with different gasoline/ethanol blends. Turner et al. [6] investigated the combustion performance of a DI SI engine with various ethanol/gasoline blending ratios. The results showed that blending ethanol with gasoline could reduce emissions and increase efficiency subject to the blending ratio.

One of the drawbacks of blending ethanol with gasoline at a fixed ratio is that it limits ethanol's potential role in improving the engine performance over the wide range of engine operation conditions. To make the use of ethanol fuel more flexibly and efficiently, EDI+GPI was proposed for SI engines [8]. The concept dual-injection is not new for compression ignition (CI) engines. It's applications to diesel engines have been intensively investigated. For example, to reduce the NO and soot emissions by reducing in-cylinder temperature, water was injected by a port injection (PI) system whilst diesel was supplied in a separate DI system [22-26]. Water PI was used to enhance the hydrogen energy share in a diesel CI engine [27]. Recently, a dual-injection strategy called Reactivity Controlled Compression Ignition (RCCI) was developed for CI engines, in which a lower reactivity fuel (e.g., gasoline) was injected via PI and a more reactive fuel (e.g., diesel) was injected via DI [28-35]. Although it has been applied to CI engines, the dual-injection applied to SI engines is still relatively new.

Cohn et al. firstly proposed to use ethanol DI in a downsized, turbocharged and high compression ratio gasoline PI SI engine [11, 36]. They proposed that a small amount of ethanol fuel was directly injected into the cylinder as an anti-knock agent, whilst gasoline fuel was port injected. By doing so, the engine knock propensity could be reduced due to the higher octane number of ethanol fuel, and supplemented by the cooling effect enhanced by direct injection and ethanol's greater enthalpy of vaporisation. The reduced knock propensity would make it possible to increase the compression ratio and use turbocharging for downsized SI engines, and consequently increase the thermal efficiency.

Toyota developed a D-4S (Direct injection 4-stroke gasoline engine system Superior version) engine equipped with a PI injector and a DI injector for gasoline fuel only [37]. The gasoline PI is applied in part load and the gasoline DI is applied in full load. By doing so, the compression ratio of the D-4S engine has been increased to 12.7 in production cars [38].

Ford introduced the 3.5L turbocharged “EcoBoost” engine in the 2010 Lincoln MKS [10]. The gasoline PI was used for starting and medium-load operations, while the E85 DI was used in high-load operation to avoid engine knock. The “EcoBoost” engine showed significant leveraging effect of E85 on reducing the gasoline fuel consumption and CO₂ emission. Similar to the “EcoBoost” engine which was mainly for passenger cars, Ford was developing another gasoline-E85 dual-injection twin-turbo 5.0L engine named “Bobcat” which was seen more as an alternative for truck diesel engines [39, 40]. E85 DI was only used to eliminate the knock in high load conditions and the engine was operated like a conventional gasoline PI engine in other conditions. A 10-gallon tank of E85 would last anywhere from 100 to 20000 miles depending on how much heavy-load conditions the truck is driven under. If no E85 is available, the engine can still run on just gasoline, albeit at reduced power. The “Bobcat” engine would be comparable to a Ford’s 6.4L Power Stroke diesel engine, but would cost only one third the price to make as no exhaust gas after-treatment systems would be necessary [39].

Zhu et al. [41] investigated the combustion characteristics of a single cylinder SI engine fuelled by three dual-injection strategies, including gasoline PI plus gasoline DI, gasoline PI plus E85 DI, and E85 PI plus gasoline DI. Recently, Wang et al. [42] compared the performance of a dual-fuel spark ignition (DFSI) engine fuelled with alcohols-gasoline (alcohols PI plus gasoline DI) and gasoline-alcohols (gasoline PI plus alcohols DI). The results in [41] and [42] showed that the engines fuelled by gasoline PI and alcohol DI demonstrated higher efficiency than other injection strategies because alcohol DI better utilized the high enthalpy of vaporisation of alcohol fuels. Wu et al. [9] tested the dual-injection concept as a flexible way to use bio-fuels, where the gasoline was used via PI and ethanol or DMF was used via DI. The leveraging effect of using ethanol fuel on reducing the consumption of gasoline fuel in an EDI+GPI engine was experimentally studied [8]. The anti-knock ability [12, 43, 44] of the ethanol DI plus gasoline PI were experimentally investigated. The combustion characteristics of gasoline PI plus ethanol

or DMF DI dual-injection were investigated in an optical engine [45]. The optical results showed that gasoline-ethanol dual-injection had faster combustion speed than that of gasoline PI.

The experimental investigations reviewed above confirmed the advantages in combustion efficiency and control of EDI+GPI over the conventional single injection fuel system. To understand the mechanisms behind the experimental results and further exploit ethanol's potentials, the in-cylinder flows, fuel evaporation and mixing, combustion and emission formation processes need to be investigated. However acquiring this information experimentally can be difficult and costly. CFD modelling has been proven a feasible and economic tool to get the visualised in-cylinder flows and thus shorten the research cycle [46]. So far, however, only a few papers have been published on the spray combustion modelling of dual-injection systems. Yang et al. [31] numerically studied the dual-injection combustion mode with gasoline PI plus diesel DI. The combustion process of in-cylinder fuel blending by gasoline PI plus early diesel DI was modelled [47]. The reactivity gradient of a dual fuelled engine with gasoline PI plus diesel DI was numerically investigated [48]. Lu et al. [49] simulated the combustion and emission processes of a dual-fuel sequential combustion (DFSC) engine with n-heptane PI plus iso-octane DI. The simulations in the above studies did not include the fuel port injection process. Instead the port injected gasoline was assumed to be homogenous in the combustion chamber before combustion or intake valve close (IVC). However, experimental and numerical results showed that the port injected gasoline fuel was not fully evaporated as expected or evenly distributed in the combustion chamber before combustion or IVC [50-52].

EDI+GPI has been in development due to its great potential in taking the advantages of ethanol fuel to increase the engine compression ratio and thermal efficiency. As reviewed above, following the preliminary experimental investigation of EDI+GPI, it is needed to understand the in-cylinder fuel and gas behaviours of EDI+GPI engines.

2.2 CFD engine modelling

As a reviewed above, CFD modelling is a valid approach. Modelling spray combustion of EDI+GPI is challenging because it is a typical example of partially premixed SI

combustion and the distributions of the two fuels at each computational grid vary. As a result, solving the spray combustion fields of two fuels simultaneously can be much more computationally expensive than that of a single injection system [51]. IC engine modelling includes the modelling of the turbulence fields, spray evaporation and mixing, combustion and emission formation. The following sub-sections review the approaches and latest progress in the modelling of turbulence, spray and combustion in IC engines.

2.2.1 Turbulence modelling

To numerically simulate the turbulence fields, a set of partial differential equations for continuity, momentum (Navier-Stokes equations), energy and state of thermodynamic variables need to be solved [53]. Unfortunately, analytical solutions for the Navier-Stokes equations are not available, except for a few very simple conditions. Therefore numerical method is usually used to solve the governing equations. Currently the most popular numerical method is the Reynolds Averaged Navier-Stokes (RANS) in which the local fluctuations and turbulence structures are integrated in the mean quantities. To close the Reynolds stress term, the most commonly used approach is the $k-\varepsilon$ two-equation turbulence model. To date, most of the research on engine modelling has used RANS based $k-\varepsilon$ turbulence model because of its reliable results and computational efficiency [54].

However, the modelling ability of RANS approach is only limited to the macroscopic flow fields. An improved approach is the large eddy simulation (LES) where the large structures (typically the structures larger than computational grid size) of the flow are explicitly computed, whilst only the effect of sub-grid-scale (SGS) motions is modelled [55, 56]. LES offers the ability to see more details of the flow structures and is strongly dependent on the computational grid size [57]. When the grid size is larger than the largest turbulence scale, then LES approach deteriorates to RANS approach. Actually, due to the limitation of computational source, LES is more applicable for flow fields with a moderate Reynolds number and a moderate geometry size [58]. Although LES provides more details for the turbulence fields, it may be not necessary or suitable for some IC engine applications such as turbulent combustion. This is because the rate-controlling processes of molecular mixing and chemical reaction occur at the smallest scales. The scales of these processes can be much smaller than the solved structures in LES and they

have to be modelled as in RANS [59]. Besides, LES is often referred to as a model for the turbulence only. When it comes to engine applications, the various sub-models, including spray and combustion sub-models, should also be modified to adapt the LES simulation appropriately [58]. In fact, LES is still at the early stage of engine modelling [55].

In another extreme case, when the LES filtering scale reduces to be smaller than the smallest turbulence size, then all the turbulence fluctuations and structures are directly solved without averaging or using turbulence models. This approach is called direct numerical simulation (DNS). DNS provides the most accurate numerical solution to the turbulence flows. However, DNS simulation is only limited to fundamental research applications with low Reynolds numbers and small geometric domains due to its tremendous requirement for the computer speed and memory [60]. Table 2.1 compares the cost and ready year of different turbulence modelling approaches [57]. The cost (grid and steps) was estimated based on that the target flow was for a car or airliner. The ready year was estimated based on the hypothesis that computer power increased by a factor of five every five years. Table 2.1 illustrates that even the LES approach is not available for industrial use in the next three decades. In fact, it was concluded that DNS for real engine simulation was not possible in the foreseeable future [61, 62].

Table 2.1: The cost of various simulation approaches [57]

Approach	Re-dependence	3/2D	Empiricism	Grids	steps	Ready year
2D URANS	Weak	No	Strong	10^5	$10^{3.5}$	1980
3D URANS	Weak	No	Strong	10^7	$10^{3.5}$	1995
LES	Weak	Yes	Weak	$10^{11.5}$	$10^{6.7}$	2045
Quasi-DNS	Strong	Yes	Weak	10^{15}	$10^{7.3}$	2070
DNS	Strong	Yes	None	10^{16}	$10^{7.7}$	2080

2.2.2 Spray modelling

2.2.2.1 Spray modelling approaches

Currently, two approaches are being used to treat the liquid fuel sprays in CFD simulations, namely the Eulerian-Eulerian approach and the Eulerian-Lagrangian

approach. The continuous gas phase is treated using the Eulerian method in both approaches. The major difference of these two approaches is the different ways in which they treat the dispersed spray droplets. In Eulerian-Eulerian approach, the spray droplets are treated as continuous phase so that each droplet in the spray field has different diameters, velocities, temperatures and positions. This approach is also referred to as Continuous Droplet Model (CDM). Theoretically the spray field could be solved by following the behaviours of each droplet. However there are millions of droplets in a single spray. As a result, the Eulerian-Eulerian approach is prohibitive for practical computations [63].

Alternatively, a more affordable method to deal with the spray droplets is the Eulerian-Lagrangian approach. This approach is based on the Monte-Carlo statistical method and often called as the Discrete Droplet Model (DDM). The spray is represented by a number of discrete parcels. Each parcel contains a group of identical non-interacting droplets. By solving the ordinary differential equations for the trajectory, momentum, heat and mass transfer of a single droplet, it solves the equations for all the droplets in the whole parcel. The interactions between the gas and liquid phases are taken into account by the source terms in the partial differential equations of the gas phase. Obviously, the larger the number of the parcels is, the more accurate of the representation for the spray behaviours [63, 64]. The main advantage of the Eulerian-Lagrangian approach is that it can achieve an accurate representation of the spray droplets distribution at a much lower cost than the Eulerian-Eulerian approach. As a result, the Eulerian-Lagrangian approach is the dominant method for liquid fuel sprays in RANS and LES simulations [63].

2.2.2.2 Droplet breakup

A liquid fuel spray involves a variety of complex phenomena. As shown in Figure 2.1, a spray experiences turbulence and cavitation within the nozzle, primary and secondary breakup, droplet-gas momentum exchange, turbulent dispersion, evaporation, drag and distortion, collision and coalescence, and spray-wall interaction processes when it is injected from an injector.

A liquid jet emanating from a nozzle into an ambient gas is inherently unstable. It may break up into droplets of diameters comparable to the jet diameter or into droplets of diameters several orders of magnitude smaller [65]. The breakup of a liquid jet has been

quantitatively studied for more than a century. However the atomisation (or primary breakup: the breakup from continuous liquid jet into discrete blobs, ligaments or droplets) process is still the least understood among all the spray evolution processes [54, 63, 66, 67]. Many atomisation mechanisms have been proposed, such as aerodynamic interaction, liquid turbulence and cavitation within the nozzle, velocity profile rearrangement, abrupt change of boundary conditions at the nozzle exit, and pressure oscillations of liquid supply [60, 66]. However, none of these mechanisms could explain the liquid atomisation phenomenon sufficiently because they did not taken into account the influences of nozzle geometry, physical and thermodynamic properties of the injected liquid and ambient gas simultaneously [66]. Therefore, researchers realized that the liquid atomisation process was controlled by a number of factors, rather than a single mechanism. A consistent view for the past decades has been that the liquid atomisation process was controlled by three main factors, namely the aerodynamics, nozzle cavitation and turbulence [68].

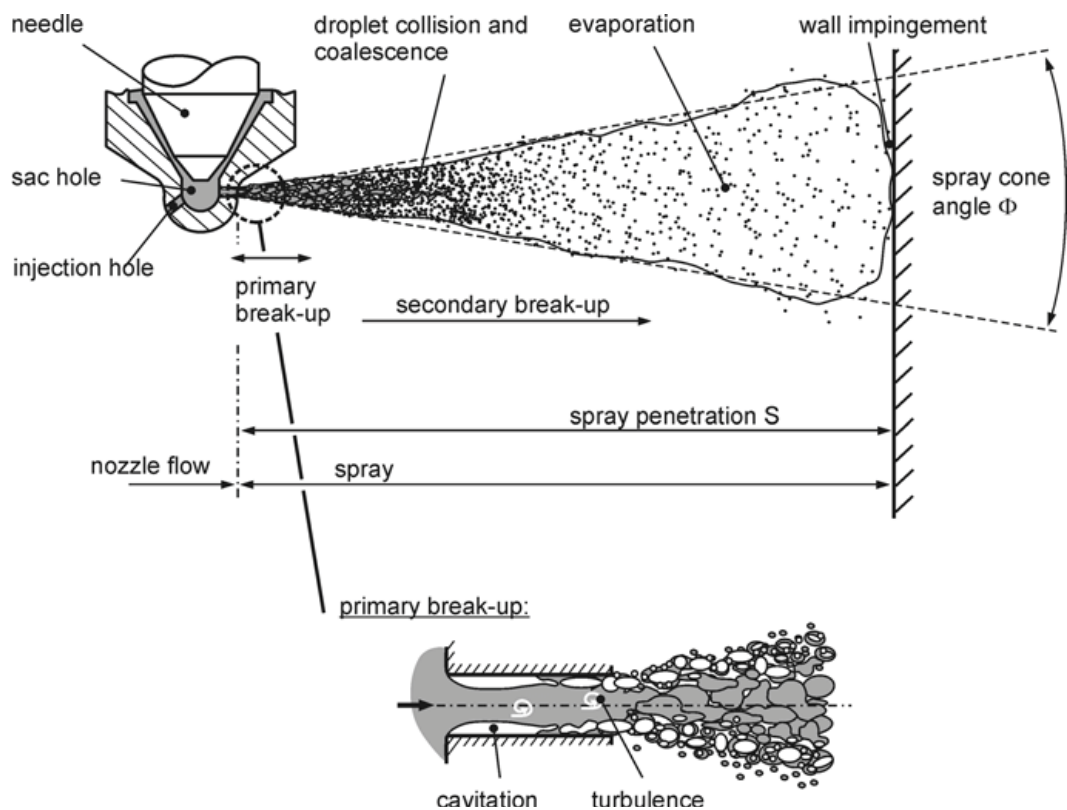


Figure 2.1: The evolution processes of a liquid fuel spray [60]

Modelling the primary breakup process is a difficult task since the inner structure and fundamental mechanisms of liquid atomisation are still largely uncertain [63, 66]. Sophisticated primary breakup model should take into account the nozzle internal flow

conditions, such as nozzle geometry details, turbulence and cavitation. This approach needs to model the nozzle internal flow and couple it with the primary breakup process [69-71]. An approximate method to represent the complexity of initial atomisation is to specify larger droplets or blobs similar to the injector hole diameter at the nozzle exit and model the secondary breakup process using various breakup models [50, 72, 73]. This method is often referred to as blob injection concept [50, 63, 64, 72, 74].

Secondary breakup is the process that blobs, ligaments or bigger droplets generated from the primary breakup process breakup into smaller droplets. Primary and secondary breakup processes do not act on the droplets at the same time, but subsequently. Although the secondary breakup has many similarities with the primary breakup, their fundamental mechanisms are quite different. Unlike the complex primary breakup, the secondary breakup process is much simpler, which is mainly controlled by the aerodynamic instabilities caused by the relative inter-phase velocity [60, 68]. The droplet presents different breakup types with the increase of relative velocity between the droplet and the ambient gas. Based on the breakup mechanism, which depends on the Weber number and the deformation (breakup) time, secondary breakup can be classified into bag breakup, stripping breakup and catastrophic breakup. The Weber (We) number is defined as,

$$We = \frac{\rho_g u_{rel}^2 d_d}{\sigma} \quad \text{Equation 2.1}$$

where ρ_g is the density of the gas, u_{rel} is the relative velocity of the droplet, d_d is the undisturbed droplet diameter, σ is surface tension of the liquid.

Figure 2.2 demonstrates different types of secondary breakup [75]. Secondary breakup starts with a droplet stretched towards a flat disk. Bag breakup occurs when the Weber number is in the range from 12 to 80. In the bag breakup, the flat disk is under an outward force and deforms into a thin bag-like membrane, which finally breaks into many smaller droplets. The stripping breakup regime is in Weber number of 80-350. The force turns to inwards and the membrane is stripped at the edges. The catastrophic breakup occurs when the relative velocity is extremely high and the Weber number becomes larger than 350. Extremely high shear rates at the gas liquid interfaces result in droplet elongation and finally breakup due to Rayleigh instabilities [76].

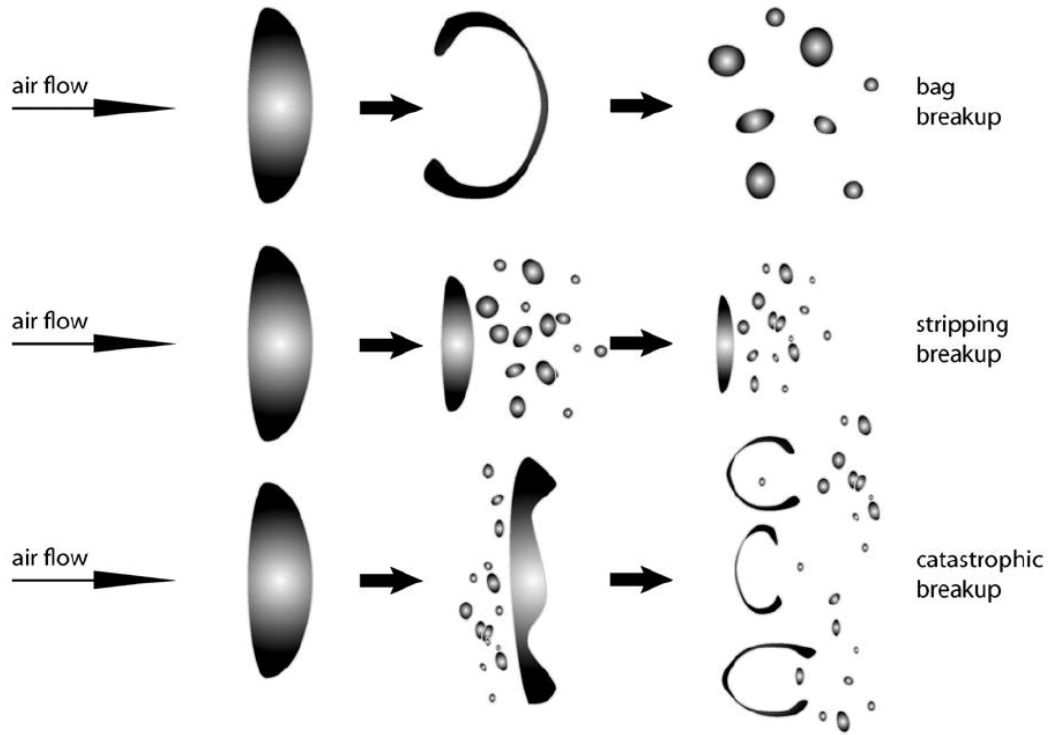


Figure 2.2: Different types of secondary breakup [75]

A number of breakup models have been developed based on different breakup mechanisms. Using the appropriate sub-model is of crucial importance in CFD simulation [63]. The spray Weber number is a reliable indicator for choosing the spray breakup models [77]. So far the most widely used numerical models for droplet breakup simulation are the Taylor Analogy Breakup (TAB) and Kelvin–Helmholtz instability breakup models because of their robustness [76]. TAB model is based on Taylor’s analogy between an oscillating and distorting droplet and a spring-mass system. The restoring force of the spring is analogous to the surface tension. The external force is analogous to the gas aerodynamic force. The damping forces due to the liquid viscosity are taken into account. The main limitation of the TAB model is that it only keeps track of one oscillation mode corresponding to the lowest order spherical zonal harmonic whose axis is aligned with the relative velocity vector between the droplet and the gas. This oscillation mode is the most important for the bag and the stripping breakup regimes. Other oscillation modes become important in large Weber number sprays. Therefore TAB breakup model is suitable for low Weber number sprays [78]. Specifically, TAB model is recommended for $We < 100$ sprays [76, 77, 79].

An alternative to the TAB model for high Weber number ($We > 100$) sprays is the WAVE breakup model in which the Kelvin-Helmholtz instability dominates the droplet breakup [79]. It considers the breakup of the droplets to be induced by the relative velocity between the gas and liquid phases. The model assumes that the breakup time and the child droplet size are related to the fastest-growing Kelvin-Helmholtz instability. The wavelength and growth rate of this instability are used to predict the details of the newly-formed droplets.

2.2.2.3 Droplet distortion and drag

To predict the penetration of the sprays in the ambient gas, it is critical to take into account the distortion and the drag of the moving droplets. For a rigid spherical droplet, the definition of the drag coefficient can be described by Equations 2.2 and 2.3 [80].

$$C_{D,s} = \frac{24}{Re_d} \left(1 + \frac{1}{6} Re_d^{2/3}\right) \quad Re_d \leq 1000 \quad \text{Equation 2.2}$$

$$C_{D,s} = 0.424 \quad Re_d > 1000 \quad \text{Equation 2.3}$$

The definition of the droplet Reynolds number is given by Equation 2.4 [80].

$$Re_d = \frac{\rho_g u_{rel} d_d}{\mu_g} \quad \text{Equation 2.4}$$

where μ_g is the dynamic viscosity of the gas phase.

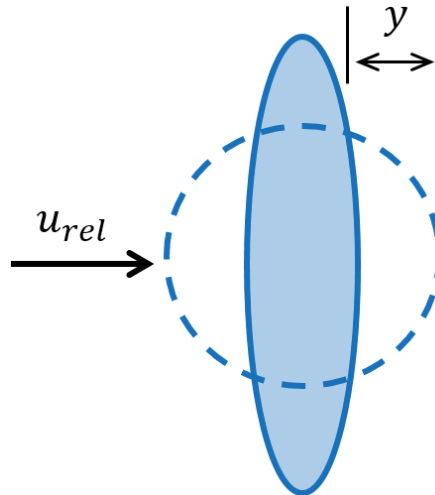


Figure 2.3: Droplet distortion

However, a major difference between the liquid and solid droplets is that the liquid droplets would deform when moving in gas phase while the solid droplets would not. When an initially spherical droplet moves fast in the air, its spherical shape distorts to a disk, as illustrated in Figure 2.3. Consequently the windward area and drag coefficient increase greatly. A dynamic drag model proposed by Liu et al. assumed that the droplet drag coefficient was related to the magnitude of the drop distortion as defined by Equation 2.5 [80].

$$C_D = C_{D,s}(1 + 2.632y) \quad \text{Equation 2.5}$$

where y is the distortion of the droplet and is derived from the TAB model, as defined by Equation 2.6 [80].

$$\frac{d^2y}{dt^2} = \frac{C_F \rho_g u_{rel}^2}{C_b \rho_l r^2} - \frac{C_k \sigma}{\rho_l r^3} y - \frac{C_d \mu_l}{\rho_l r^3} \frac{dy}{dt} \quad \text{Equation 2.6}$$

where r is the undisturbed droplet radius, ρ_l is the density of the liquid phase, $y = 0$ means no distortion, $y = 1$ means that a droplet deforms into a disk and $y > 1$ assumes the droplet breaks up. To match the experiments and theory, the constants C_F , C_k and C_d were chosen to be 1/3, 8 and 5 respectively [79].

2.2.2.4 Droplet heat and mass transfer

The quality of modelling the evaporation of practical fuels is important to the overall accuracy of the prediction of spray combustion [63]. This is because the droplets have to evaporate so that the fuel can mix with the oxygen in molecular level before the chemical reaction occurs [81]. Normally the presence of a flame zone located several droplet diameters away from the droplet centre [75]. The numerical models for the droplet heating and evaporation processes can be categorised into six groups with increasing complexity as follows [82].

- 1) Models with an assumption that the droplet temperature is uniform and constant.
- 2) Models with an assumption that the droplets have infinite thermal conductivity so that there is no temperature gradient inside the droplets.
- 3) Models with an assumption that the droplets have finite thermal conductivity, but there is no re-circulation inside the droplets.

- 4) Models with an assumption that the droplets have both finite liquid thermal conductivity and the re-circulation inside the droplets is modelled via the introduction of a correction factor to the liquid thermal conductivity.
- 5) Models with the re-circulation inside the droplets taken into account via vortex dynamics.
- 6) Models to solve the full Navier-Stokes equations.

The first group is too simplistic and is only used for analytical studies. The last two groups are too complex to be used in CFD codes in the foreseeable future. Currently the groups 2-4 are actually incorporated in CFD codes. Although different codes have different structures, the basic approaches of spray modelling used in them are rather similar [83]. The commonly used assumptions in evaporation models are spherical droplets, quasi stationary conditions at the droplet surface, and homogeneous droplet temperature [60, 83, 84]. Correction functions are used to overcome the simplifications for transient heating, drop deformation or internal circulation [84].

The energy for the evaporation process of spray droplets is transferred from the ambient gas to the droplets via conduction, convection and radiation. The absorbed thermal heat results in diffusive and convective mass transfer of fuel vapour from droplet surface into the gas. Normally the radiative heat transfer is neglected because it is small compared to the convective effect [60]. There are two evaporation models in the ANSYS FLUENT code, namely the Diffusion Controlled Model and the Convection/Diffusion Controlled Model [79]. The first model assumes that the evaporation rate is governed by the gradient diffusion and it is suitable for low evaporation rate conditions. The second model takes into account both the effects of diffusion and convection. It is more suitable for high evaporation rate sprays. The heat transfer between the droplet and the ambient gas is taken into account according to a heat balance that relates the sensible heat change in the droplet to the convective and latent heat transfer. The governing equations of the two evaporation models will be described in details in Section 3.2.2.

2.2.3 Combustion modelling

Generally flames can be categorised into premixed combustion, non-premixed combustion and partially premixed combustion. Each type of combustion can be further classified by laminar and turbulent flames. Different modelling methods are used to

simulate different combustion types. In the present study, the ECFM partially premixed combustion model is used to simulate the stratified spray combustion process in the EDI+GPI engine. The partially premixed combustion model is usually a combination of premixed and non-premixed combustion models. Therefore, the premixed and non-premixed combustion are discussed before introducing the partially premixed combustion and its modelling.

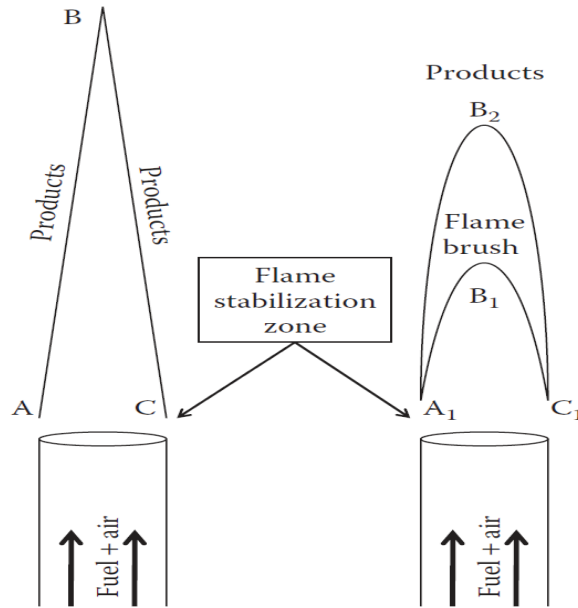


Figure 2.4: Schematics of laminar (left) and turbulent (right) Bunsen premixed flames [85]

2.2.3.1 Premixed combustion

In premixed combustion, fuel and oxidizer are mixed at the molecular level prior to ignition. The fresh mixture and the burnt gases are separated by a thin reaction zone. Homogeneous charge SI engine is a typical example of this combustion type. Figure 2.4 demonstrates the effect of the turbulence on the premixed flames. The most important and well-documented quantitative difference between laminar and turbulent premixed combustion is that turbulent flame is much thicker than a laminar one [85]. For laminar premixed flames, there is an interesting relation between the thermal flame thickness δ_l , the laminar flame speed U_L , and the kinematic viscosity of the fresh gas ν :

$$Re_f = \frac{\delta_l U_L}{\nu} \approx 4 \quad \text{Equation 2.7}$$

When the thermal flame thickness is defined as the distance of 98% temperature jump between the fresh air and the burnt gas, the flame Reynolds number becomes a constant of 4. This relation is often implicitly used for the development of turbulent premixed combustion model [55].

Turbulent combustion involves various length, velocity and time scales to describe the turbulent flow field and chemical reactions [55]. To analyse turbulent combustion, a few dimensionless parameters were introduced. Reynolds (Re) number is used to describe the turbulent flow,

$$Re = \frac{u' l_t}{\nu} \quad \text{Equation 2.8}$$

where u' is the velocity rms (related to the square root of the turbulent kinetic energy k), l_t is the integral turbulence length scale.

Damköhler number (Da) is used to describe the combustion speed,

$$Da = \frac{\tau_t}{\tau_c} \quad \text{Equation 2.9}$$

where τ_t is the turbulent time scale and τ_c is the chemical time scale. $Da \geq 1$ means fast chemical reaction where the internal structure of the flame is not strongly affected by turbulence. This type of flame is also called ‘flamelet’. $Da \leq 1$ stands for low reaction rate where the reactants and products are mixed by turbulent structures before reaction.

Karlovitz number (Ka) is the ratio of chemical time scale τ_c to Kolmogorov time scale τ_k ,

$$Ka = \frac{\tau_c}{\tau_k} \quad \text{Equation 2.10}$$

The relationships between the above three dimensionless parameters can be used to categorise the combustion regimes. Figure 2.5 shows the typical combustion conditions in three main categories of practical engines, namely the IC engines, the Aero Gas Turbines and the Power Gas Turbines. The arrows indicate the likely direction of change due to lean-burn technologies [86]. The line of $Ka = 1$ is called Klimov–Williams line. $Ka < 1$ is the flamelet regime or thin wrinkled flame regime, $1 < Ka \leq 100$ is the thickened wrinkled flame regime or thin reaction zone, and $Ka > 100$ is the thickened flame regime or well-stirred reactor [55]. Specifically the flamelet regime can be further classified into

wrinkled and corrugated flames depending on the ratio of u'/U_L [55, 86]. Typical IC engines operate in the wrinkled flamelet range.

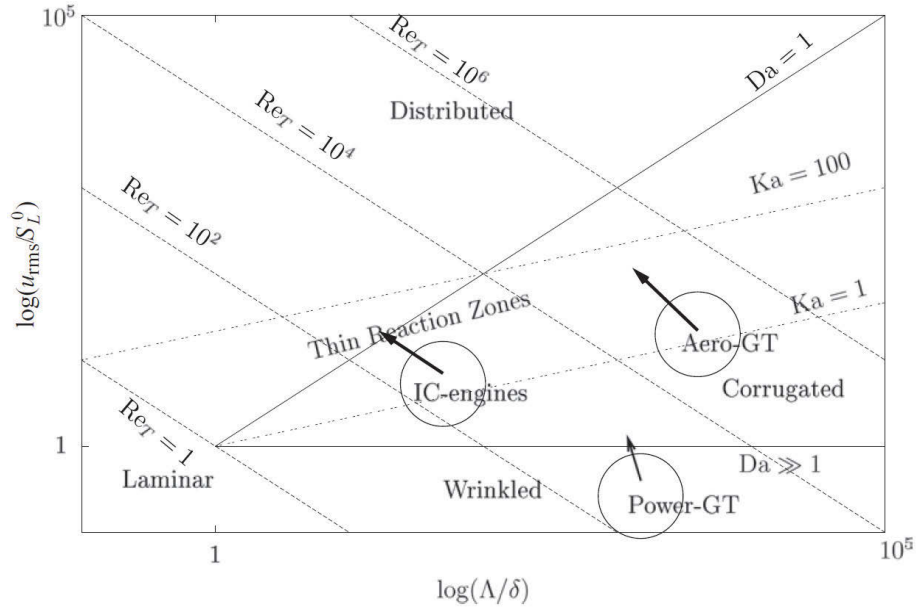


Figure 2.5: Combustion regimes of turbulent premixed flames [86]

2.2.3.2 Non-premixed combustion

In non-premixed combustion flames, the fuel and oxidizer enter the reaction zone in two separate flows. They must be mixed for their molecules to collide and react. As a result, the burning speed cannot be faster than the mixing rate. Therefore, non-premixed flames are often called as diffusion flames because the diffusion process controls the rate of non-premixed combustion [85]. Consequently non-premixed combustion modelling problem can be simplified to a mixing problem. Direct injection compression ignition engine is a typical example of non-premixed combustion.

Figure 2.6(a) is a schematic of the structure of a laminar non-premixed flame. The fuel and the oxidizer are on two sides of a reaction zone. The burning rate is controlled by the molecular diffusion rate of the reactants toward the reaction zone [55]. Figure 2.6(b) demonstrates the structure of a turbulent non-premixed flame. Z is the mixture fraction, l_t is the turbulence integral length scale, l_d and l_r are the diffusion thickness and reaction zone thickness respectively. Similar to premixed flames, the two major effects of turbulence on a non-premixed flame are increasing the area of the stoichiometric surface and changing the structure of the reaction zone attached to the surface [85]. In premixed

combustion, Re , Da and Ka are used to classify the combustion regimes. In non-premixed turbulent combustion, however, the diffusion flame does not propagate and thus has no flame speed. Besides the thickness of the flame depends on the aerodynamics which control the thickness of the local mixing layers between the fuel and the gas. Therefore it is hard to find a fixed reference length scale for non-premixed flames. These two factors make it difficult to define a uniform classification for non-premixed turbulent combustion. Different researchers have different classifications for non-premixed flames. Figure 2.7 gives two examples of non-premixed combustion regime classification based on different criteria [55, 85].

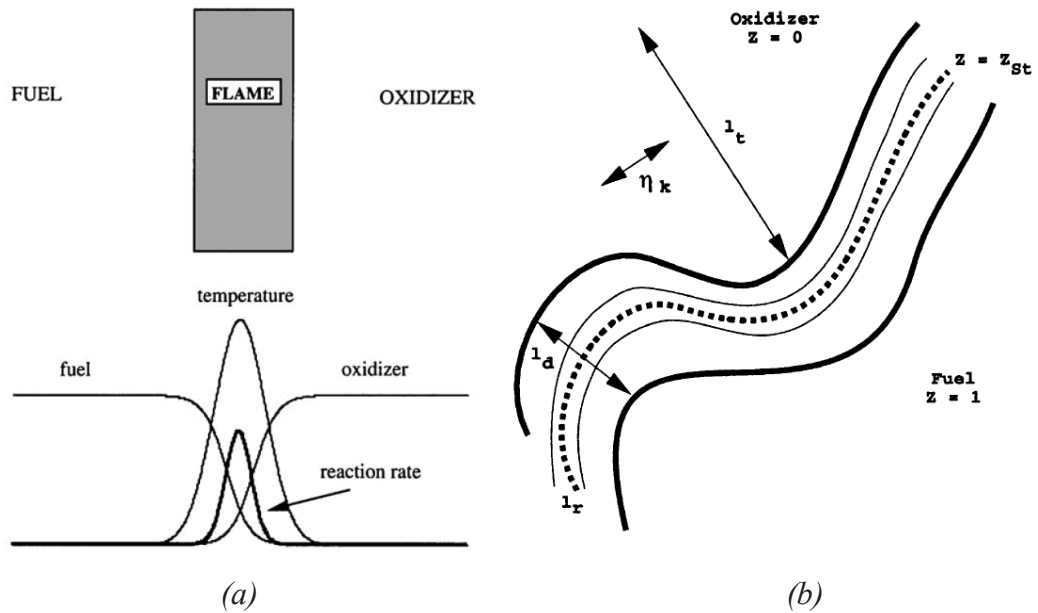


Figure 2.6: Schematics of laminar (a) and turbulent (b) non-premixed flames [55]

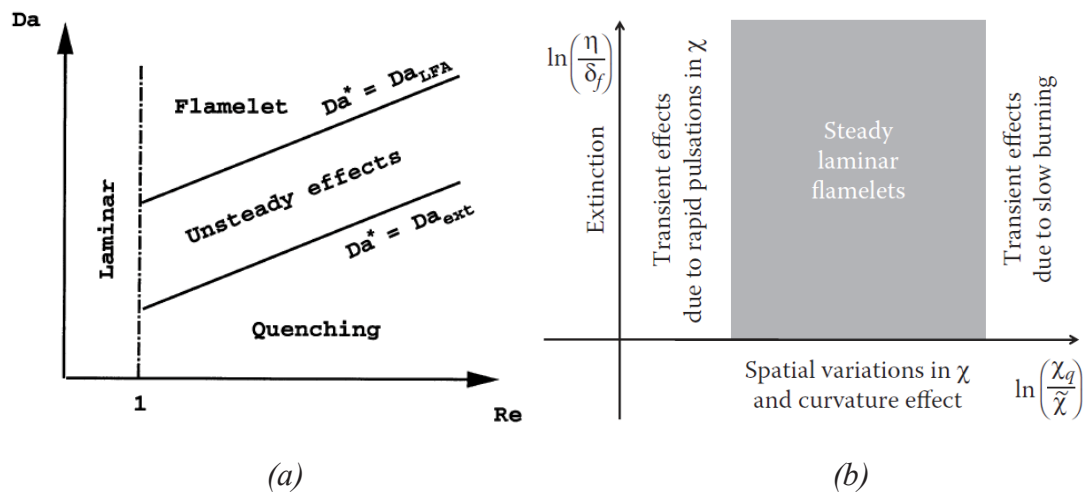


Figure 2.7: Combustion regimes of turbulent non-premixed flames, (a) [55], (b) [85]

2.2.3.3 Partially premixed combustion

An essential characteristic of spray combustion is that the fuel is injected into the combustion zone in liquid form. The evaporation and diffusion processes occur prior to the combustion. By the time of combustion, part of the fuel has mixed with the oxidizer in molecular level but in-homogeneously, and evaporating and mixing processes are still occurring. As a result, spray combustion shows features of both non-premixed and premixed combustion. This combustion type is called partially premixed combustion. Direct injection stratified charge SI engine is a typical example of this combustion type.

Compared with premixed combustion, partially premixed turbulent combustion involves at least the following five specific characteristics [85].

- 1) The burning rate depends on the inhomogeneity of the mean mixture composition.
- 2) The burning rate depends on the turbulent pulsations in the local mixture composition.
- 3) Mixture-controlled afterburning of lean and rich combustion products.
- 4) An increase in the flame surface area due to mixture inhomogeneity.
- 5) Variations in the local burning rate due to the heat and reactant fluxes from/to neighbouring leaner or richer combustion products.

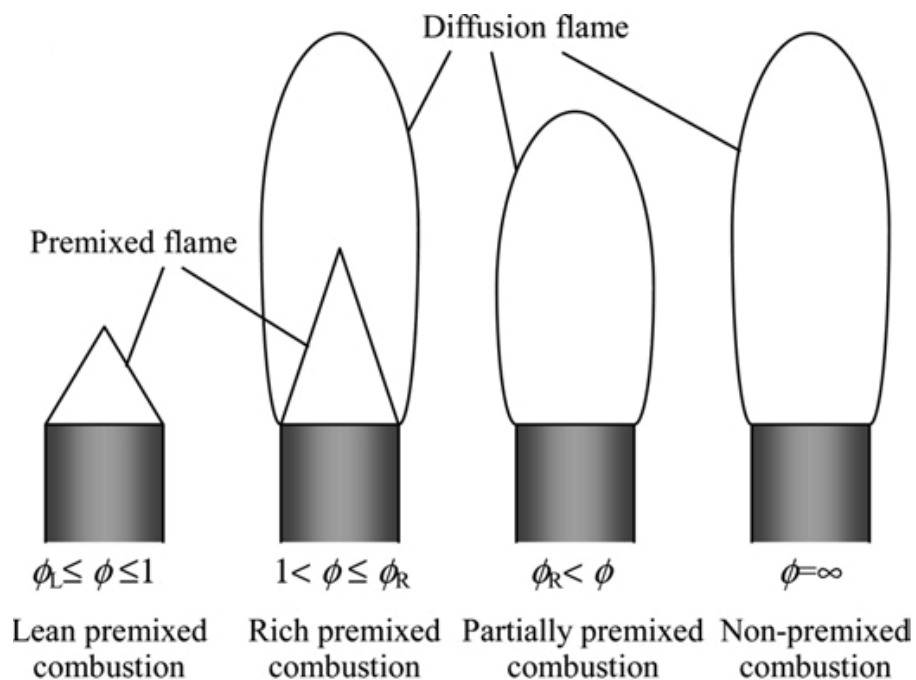


Figure 2.8: Schematics of combustion styles with different overall equivalence ratios (ϕ_L is the lean flammability limit and ϕ_R is the rich flammability limit) [87]

Figure 2.8 shows how a gaseous Bunsen flame changes from premixed combustion to partially premixed combustion and then non-premixed combustion by increasing the overall equivalence ratio Φ . For lean or stoichiometric premixed combustion ($\phi_L < \phi \leq 1$), the flame has a cone shape. A richer mixture ($1 < \phi < \phi_R$) changes the cone flame into a double-flame which has an internal premixed flame and an external diffusion flame. If the mixture equivalence ratio exceeds the rich flammability limit ($\phi > \phi_R$), the internal premixed flame disappears and only the external diffusion flame remains. Such a flame is called a partially premixed flame. If the mixture only contains pure fuel ($\phi = \infty$), then the flame becomes the non-premixed (diffusion) flame.

Although spray combustion is of great important in practical applications, partially premixed flames have not been studied systematically [85, 87]. Contemporary understanding of the physics of partially premixed turbulent combustion is mainly based on the knowledge of premixed and non-premixed flames.

2.2.3.4 Combustion modelling

To model the combustion process, two parameters are introduced for different types of flames, as shown in Figure 2.9. Since the burning rate of a non-premixed combustion flame is controlled by the molecular diffusion of the reactants toward the reaction zone, therefore, its modelling can be greatly simplified to a mixing problem. By solving the balance equations for mixture fraction Z , it is able to identify the flame properties (flame location, burning speed, temperature etc.). The mixture fraction Z is defined as [79],

$$Z = \frac{Z_i - Z_{i,ox}}{Z_{i,fuel} - Z_{i,ox}} \quad \text{Equation 2.11}$$

where Z_i is the elemental mass fraction for species i . The subscripts *ox* and *fuel* denote the values at the oxidizer and fuel stream inlets respectively.

To model the premixed combustion flame, the progress variable c is introduced where $c=0$ represents the fresh mixture and $c=1$ stands for the burnt one. The progress variable c is defined as a normalized sum of the product species mass fractions [79],

$$c = \frac{\sum_i \alpha_i (Y_i - Y_i^u)}{\sum_i \alpha_i Y_i^{eq}} \quad \text{Equation 2.12}$$

where Y_i is the mass fraction of species i , α_i is the constant which is typically zero for reactants and unity for a few product species, superscript u denotes the unburnt reactant and superscript eq denotes chemical equilibrium.

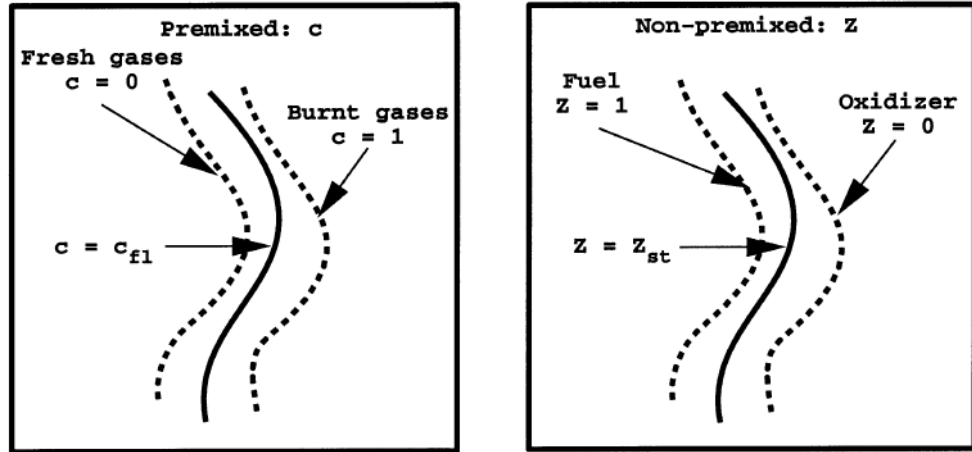


Figure 2.9: Parameters for describing the premixed and non-premixed flames [55]

As mentioned above, non-premixed flames do not propagate and cannot be characterized using length scales as that in premixed flames, such as laminar flame speed and laminar flame thickness. This is why most non-premixed combustion models use the flamelet approach. The main advantage of the flamelet concept is that it decouples the complex chemical structure of the flame from the flow dynamics by solving the equations for the mixture fraction Z . Therefore, the flame structure and flow dynamics can be modelled independently. The flamelet structure is either described with a simplified analytical formulation or with a flamelet library involving the detailed chemical structure of the flame [88].

Premixed turbulent flames are often found to contain thin reaction surfaces that are highly stretched and wrinkled by the turbulence [79, 88]. Premixed combustion is much more difficult to model than non-premixed combustion because of the occurrence of counter-gradient transport in the presence of strong heat release [88]. To capture the laminar flame speed, the internal flame structure needs to be resolved, as well as the detailed chemical kinetics and molecular diffusion processes [79]. In premixed turbulent combustion, the progress variable c is commonly used to describe the complete thermochemical state of the combustion system. The various quantities of interest, such as the species mass fractions and temperature, can be obtained by choosing a suitable definition for the reaction progress variable [88]. In the past decades, the focus of theoretical studies of

premixed turbulent combustion was on obtaining an analytical expression for the burning velocity of an unperturbed fully developed flame [85]. However this problem has not been solved yet and new solutions are still been proposed in recent years. The two main limitations of these models are, 1) turbulence is assumed to be known, and 2) the development of premixed turbulent flames is not addressed with a single exception [85].

The partially premixed combustion model is usually a combination of premixed and non-premixed combustion models. The progress variable c determines the position of the flame front. Behind the flame front ($c=1$), the mixture is burnt and the mixture fraction Z solution is used. Ahead of the flame front ($c=0$), the species mass fractions, temperature, and density are calculated from the mixed but unburnt mixture fraction. Within the flame ($0 < c < 1$), a linear combination of the unburnt and burnt mixtures is used [79]. The predictive capabilities of such a combined approach will be limited by the predictive capabilities of the less accurate approach, that is, a model of turbulent premixed combustion [85].

To model the spray combustion process in an IC engine, either detailed chemistry mechanisms or combustion models are used. CFD models coupled with detailed chemical reaction mechanisms were applied to simulate the multi-component fuel spray combustion [89, 90]. However, coupling the chemistry with the CFD solver is very time consuming and incompatible for complex industrial configurations [91, 92]. Instead, Extended Coherent Flame Model (ECFM) was adopted to simulate the combustion process of SI engines [91, 93, 94]. To accommodate the increasingly complex chemical kinetics, realistic turbulence/chemistry interaction and multiple combustion regimes in three-dimensional time-dependent device-scale CFD modelling is a difficult task in turbulent combustion [95]. A hybrid approach of Probability Density Function (PDF) method and laminar flamelet model was applied to address the issue [95]. To reduce the computational cost, the complex reaction mechanisms can be pre-computed and stored in look-up tables [92, 96]. The ECFM combined with PDF look-up tables were used to model the turbulent diesel spray flames [97, 98]. A presumed PDF model was applied to predict the turbulent flow behaviour and temperature distribution of a diesel spray combustion flame [99]. A tabulated chemistry method was developed to investigate turbulence-chemistry interactions of premixed, non-premixed and partially premixed flames [92].

2.3 Fuel properties and effect on spray combustion

2.3.1 Fuel properties

Ethanol fuel has been widely used as petroleum surrogate or octane enhancer in IC engines and its properties are very different to that of gasoline fuel. The fuel properties, such as surface tension, viscosity, enthalpy of vaporisation, saturation vapour pressure and heating value, can significantly affect the spray breakup, evaporation and combustion processes. Therefore it is critical to define the fuel properties correctly in the CFD codes so that it is possible to gain an accurate prediction for the fuel spray and the consequent combustion processes. For pure ethanol fuel (ethyl-alcohol), the physical and chemical properties can be found from the engineering handbooks, such as the Yaws' handbook [100]. Gasoline fuel consists mostly of organic compounds ranging from C₂ to C₁₄. The physical and chemical properties of iso-octane (2, 2, 4 - trimethylpentane) are similar to gasoline's and they are commonly used to represent gasoline fuel in experimental and numerical investigations. Table 2.2 lists the main physical and chemical properties of gasoline and ethanol fuels at 300 K.

Table 2.2: Physical and chemical properties of ethanol and gasoline fuels

Properties ②	Fuel	Ethanol	Gasoline
Chemical formula (-)		C ₂ H ₆ O	C ₈ H ₁₈ ①
Density (kg/m ³)		785.5 [100]	714.9 [100]
Specific heat (J/kg•K)		2339 [100]	2041 [100]
Viscosity (kg/m•s)		0.001007 [100]	0.0004549 [100]
Research octane number (-)		106 [8]	91~98
Stoichiometric air/fuel ratio (-)		9.0:1 [8]	14.8:1 [8]
Boiling point (K)		351.44 [100]	372.39 [100]
Diffusion coefficient in air (m ² /s)		1.196 × 10 ⁻⁵ [100]	6.410 × 10 ⁻⁶ [100]
Lower heat value (MJ/kg)		26.9 [8]	42.9 [8]
Enthalpy of vaporisation (kJ/kg)		948 [101]	298 [101]
Saturation vapour pressure (kPa)		8.773 [100]	28.828 [101]
Surface tension (N/m)		0.02314 [100]	0.01816 [100]
Laminar burning velocity @ stoichiometric equivalent ratio, 100 kPa, 100 °C (m/s)		~0.62 [102]	~0.49 [102]

① Iso-octane is used to represent gasoline fuel; ② Properties at temperature of 300 K.

Saturation vapour pressure is an important factor indicating the liquid’s volatility. The vapour pressure of the fuel is the driving force for the droplet evaporation process. Therefore it is of great importance to provide accurate vapour pressure values over the entire range of possible droplet temperature in the calculation. The vapour pressure varying with temperature for ethanol fuel is taken from the Yaws’ handbook [100]. Although most of the physical and chemical properties of liquid and gaseous iso-octane are similar to that of gasoline, the vapour pressure of gasoline is much larger than iso-octane’s because of the light components in gasoline fuel, as shown in Figure 2.10. For instance, the measured vapour pressure of gasoline is 32.0 kPa at 30 °C [101], whilst the vapour pressure of iso-octane is only 8.3 kPa at the same temperature [100]. Therefore the saturation vapour pressure for gasoline is calculated from the experimental data [101] using the Clausius-Clapeyron equation [103],

$$\log P_{sat} = -1374.46/T + 6.04135 \quad \text{Equation 2.13}$$

where T is the temperature in Kelvin, P_{sat} is the vapour pressure in kPa.

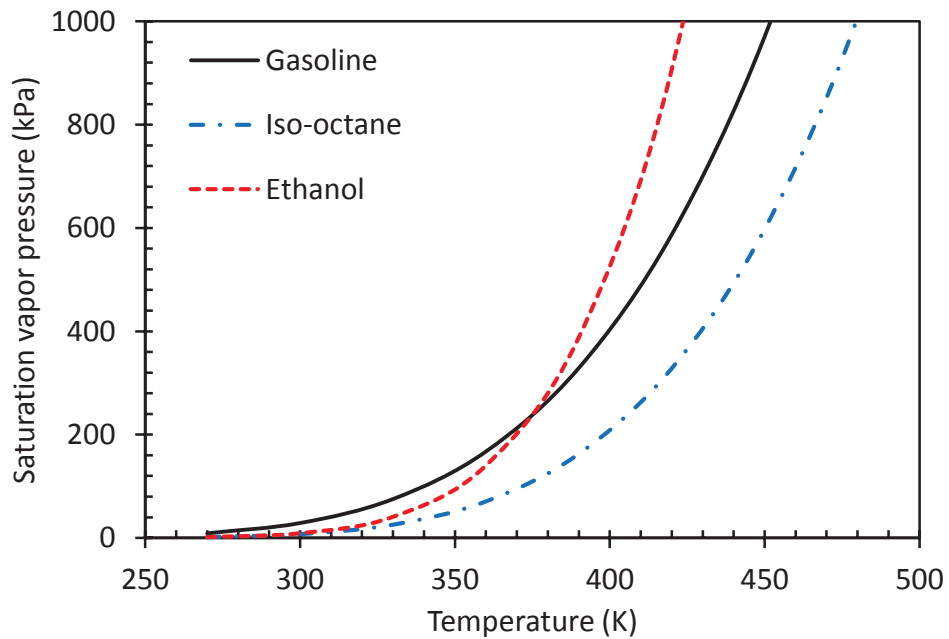


Figure 2.10: Saturation vapour pressures of gasoline, ethanol and iso-octane fuels

An equation for ethanol vapour pressure has also been derived as well using the experimental data reported in [101],

$$\log P_{sat} = -2116.68/T + 7.95847 \quad \text{Equation 2.14}$$

The correlation of vapour pressure-temperature with a higher accuracy provided in the Yaws' handbook is,

$$\log P_{sat} = 22.969 - \frac{2864.2}{T} - 5.0474 \log T + 3.7448 e^{-11T} + 2.7361 e^{-7T^2}$$

Equation 2.15

Figure 2.11 compares the calculated vapour pressure values from the Equations 2.14 and 2.15. As shown in Figure 2.11, the calculated vapour pressure from the experimental data agrees well with that from the Yaws' handbook. Therefore, the correlations of vapour pressure-temperature of gasoline and ethanol fuels are considered accurate.

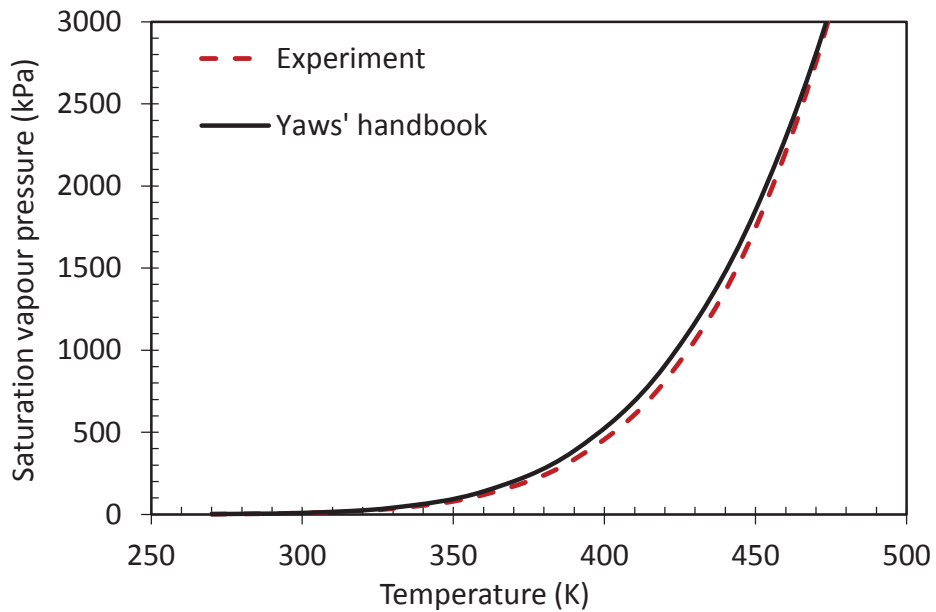


Figure 2.11: Comparison between the ethanol vapour pressures calculated from the experimental data [101] and Yaws' handbook [100]

Laminar flame speed is another important property in the modelling of IC engines. It is a key factor for the turbulent flame propagation of the mixture [104]. In premixed combustion modelling, the mixture is homogeneous and laminar flame speed is constant throughout the domain. In partially premixed combustion modelling, however, the mixture is not uniform in the computational domain. As a result, the laminar flame speed is not constant. The laminar flame speed depends strongly on the composition, temperature and pressure of the unburnt mixture. Currently accurate analytical expression

for the laminar flame speeds is unavailable [79, 85]. Instead, it is usually measured from experiments or computed from 1-D simulations.

As laminar flame speed is a key parameter in the turbulent combustion flames, many experimental investigations were carried out to measure the laminar flame speeds for gasoline and ethanol fuels under various initial conditions [102, 104-106]. In the present study, the experimentally measured laminar flame speeds in [102] were used for the simulations. As shown in Figure 2.12, the laminar flame speeds reach the peak when the equivalence ratio is in the range of 1.0-1.2 and ethanol fuel has a higher flame speed than gasoline does over a wide range of equivalence ratio.

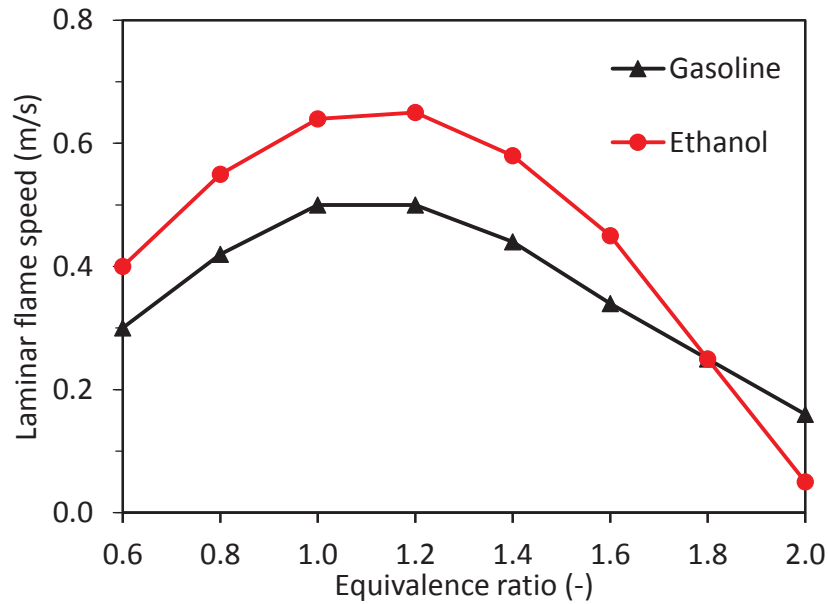


Figure 2.12: Laminar flame speeds of ethanol and gasoline fuels [102]

Other important thermo-chemistry properties of gasoline and ethanol fuels are calculated using the correlations from the Yaws' handbooks as follows.

The correlation of viscosity of ethanol (unit: kg/m-s) is,

$$\mu = 10^{-9.4406 + \frac{1.1176e^3}{T} + 0.0137 \cdot T - 1.5465e^{-5} \cdot T^2} \quad \text{Equation 2.16}$$

The correlation of viscosity of gasoline (unit: kg/m-s) is,

$$\mu = 10^{-18.042 + \frac{2.0021e^3}{T} + 0.0371 \cdot T - 3.4486e^{-5} \cdot T^2} \quad \text{Equation 2.17}$$

The correlation of surface tension of ethanol (unit: N-m) is,

$$\sigma = 67.036e^{-4} \cdot \left(1 - \frac{T}{516.25}\right)^{1.2222} \quad \text{Equation 2.18}$$

The correlation of surface tension of gasoline (unit: N-m) is,

$$\sigma = 47.434e^{-4} \cdot \left(1 - \frac{T}{543.96}\right)^{1.1975} \quad \text{Equation 2.19}$$

The correlation of diffusion coefficient in air of ethanol (unit: m²/s) is,

$$Di = -0.05889e^{-4} + 3.6615e^{-8} \cdot T + 7.6299e^{-11} \cdot T^2 \quad \text{Equation 2.20}$$

The correlation of diffusion coefficient in air of gasoline (unit: m²/s) is,

$$Di = -0.03648e^{-4} + 2.0520e^{-8} \cdot T + 4.3354e^{-11} \cdot T^2 \quad \text{Equation 2.21}$$

2.3.2 Spray characteristics of ethanol and gasoline fuels

Gasoline direct injection (GDI) has several advantages over port fuel injection, including improved fuel economy and transient response, more precise air-fuel ratio control, extended EGR tolerance limit, selective emissions advantages and enhanced potential for system optimization [107]. On the other hand, direct injection of ethanol (EDI) can bring the engines further advantages, such as enhanced charge cooling effect and anti-knock ability. The increasingly stringent regulations and worldwide concern for fossil fuel depletion have driven the GDI technology and alternative fuels like ethanol come into practical use on road. Since it is diesel engine that firstly adopted fuel injection technology, most of the early experimental and numerical works were on diesel sprays. However these conclusions for diesel sprays might be not applicable for sprays of gasoline, ethanol or their blends.

To exploit the potentials of EDI, the spray and mixture formation characteristics should be investigated as they are the key factors that influence the combustion and emissions of the engine. Experimental results showed that the NO emission decreased, and CO and HC emissions increased with EDI injection in a gasoline port injection engine [8]. The NO emission was decreased due to the cooling effect enhanced by EDI and CO and HC emissions were increased due to poor mixing, local over-cooling and fuel impingement at high ethanol ratio conditions [51, 108]. However opposite experimental results were

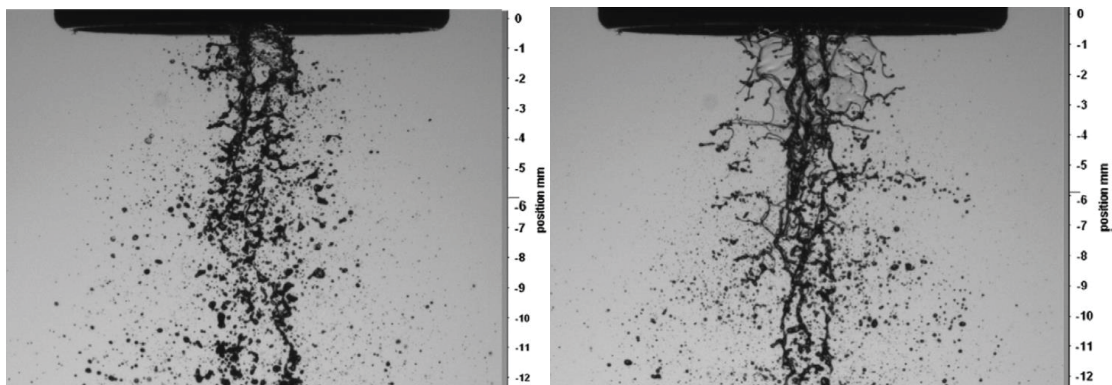
reported in [43]. NO emission increased and CO and HC emissions decreased when EDI was applied. Furthermore, both HC and NO emissions were reduced by EDI as reported in [9]. The above different results might be caused by the evaporation process of EDI spray in different engine conditions in different investigations.

The adequate performance of direct injection systems is the key factor to achieve the benefits of GDI and EDI. Since ethanol fuel has lower stoichiometric air/fuel ratio and heating value, more mass of ethanol fuel should be injected into the cylinder in order to maintain the same output power and equivalence ratio. More injected fuel results in larger spray momentum and longer spray tip penetration, which may lead to fuel impingement on cylinder and piston walls. Besides, gasoline and ethanol sprays would show different breakup regimes (Bag Breakup, Stripping Breakup, or Catastrophic Breakup) or vaporisation patterns (flash or non-flash boiling sprays) due to their different physical properties [66, 109]. The spray flash-boiling may occur in engine conditions which would destroy the designed spray direction and mixture distribution in the combustion chamber [109, 110]. Therefore, investigating the spray and evaporation characteristics is of great importance for extending the use of ethanol fuel.

Compared with gasoline, ethanol has larger surface tension, viscosity, density, specific heat and enthalpy of vaporisation, but lower vapour pressure at low temperature conditions, as shown in Figure 2.10. Theoretically, the breakup and evaporation rates of ethanol spray should be lower than that of gasoline spray, thus resulting in longer spray tip penetration and bigger droplet size [65]. However, experimental results have not reached a consensus. Regarding the spray tip penetration, despite of the differences in the experiments, gasoline and ethanol showed very similar behaviours [110-113]. On the other hand, some researchers observed that the spray tip penetration decreased with the increase of ethanol fraction [114, 115]. It was reported that gasoline spray penetrated faster than ethanol did with low injection pressures, whilst ethanol spray had higher penetration rate than gasoline did in high injection pressure conditions. The ethanol spray penetrated further than gasoline did under all injection pressures when the sprays were fully developed [116]. For the spray cone angle, it showed almost the same cone angle for ethanol and gasoline sprays with a high-pressure swirl injector [113]. However experiments in [111, 112, 114] measured larger spray cone angles of ethanol than gasoline's. Regarding the spray droplet size, most studies observed that ethanol (or E85)

sprays had larger Sauter Mean Diameter (SMD) than gasoline did [112, 113, 117]. However the SMDs of ethanol and gasoline sprays measured in [111] were very similar in spite of the large differences in viscosity and surface tension. The different results in experiments and theoretical analysis may be caused by various factors. Theoretical analysis does not take into consideration of the injector type, nozzle internal fuel flow, injection pressure, ambient temperature and pressure simultaneously. One effective way to take these factors into account would be introducing the dimensionless parameters, such as Weber number, Reynolds number and air-to-fuel density ratio. Sprays with similar dimensionless parameters showed similar characteristics and structures [118].

Although the fuel properties of ethanol are different to that of gasoline, the different spray behaviours in theoretical analysis were not been observed in the experiments. As in the intensive experimental studies reviewed above, they all focused on the macroscopic characteristics of ethanol and gasoline sprays, such as the spray tip penetration, spray angle and droplet size. However the real effect of fuel properties may be on the microscopic spray behaviours, such as the breakup and evaporation processes. Figure 2.13 demonstrates the primary breakup process of ethanol and gasoline sprays from a low-pressure multi-hole port fuel injector [111]. As shown in Figure 2.13, ethanol spray has larger and thinner, sheet-like ligaments near the nozzle exit than gasoline does due to ethanol's larger viscosity and surface tension.



(a)

(b)

Figure 2.13: Primary breakup structures of gasoline (a) and ethanol (b) sprays [111]

The fuel evaporation process strongly affects the consequent mixture formation, combustion and emission processes. This is because the droplets must vaporise before

they can burn [75, 81]. However, little work has been done in this field. A better vaporisation of ethanol fuel was used to explain the experimental results of decreased spray tip penetration and increased spray angle with the increase of ethanol/gasoline fraction [114]. Some reported a slower vaporisation of ethanol spray than gasoline's because of the light components in gasoline fuel [119]. It was found that ethanol had a faster vaporisation rate due to its higher vapour pressure in high temperature conditions in experiments [120]. Numerical studies showed that the evaporation rate of ethanol direct injection was lower than that of gasoline in naturally aspirated SI engines [121, 122]. However the simulated evaporation rate of ethanol was as high as that of gasoline in a turbocharged engine [123]. It was found that the fuel temperature played an important role in the evaporation process of ethanol spray. Ethanol evaporated more slowly than gasoline did in low temperature conditions, but faster when the temperature was higher than 375 K [121].

The fuel temperature can change in a wide range from non-evaporating (cold start in winter) to flash-boiling sprays in real engine conditions. The effect of fuel temperature on gasoline spray injected by swirl-type injectors was investigated [124-127]. It was found that the spray collapsed with faster evaporation rate, longer penetration length and smaller droplet size when the temperature was above the saturation temperature. Recently, the multi-hole injectors have attracted more attention for DI SI engines because of their advantages in stability of spray pattern and flexibility of spray plume targeting [128]. However the majority of work published to date on multi-hole injectors concerns diesel nozzles [110]. Aleiferis et al. [110, 117, 129-131] conducted extensive experiments on the multi-hole injector spray behaviours of various fuels and ambient conditions. The studies were focused on the spray shape transformation of flash-boiling sprays (or spray collapse: transition from a multi-jet spray to a single-jet spray) either by increasing the fuel temperature or decreasing the ambient pressure. Zeng et al. [109] investigated the transition process from non-flash boiling to flare flash boiling sprays using alcohol fuels. It was reported that the spray flash boiling occurred at $P_a/P_s=1$ (ambient-to-saturation pressure ratio) and spray collapsed at $P_a/P_s=0.3$. However, recent study for ethanol spray from a multi-hole injector found that the spray flash boiling did not occur as soon as the liquid temperature was higher than the boiling point ($P_a/P_s=1$) [132].

The spray data in the constant volume chamber can also be very useful for engine modelling. The measured values can be used to define the initial settings for the spray simulations. This is believed to be an effective and accurate method [50]. To verify the spray models in IC engines, the most commonly used method is to compare the simulated and measured spray structures in constant conditions [50, 94, 133-140]. In Chapter 4, the effects of fuel temperature on the ethanol spray and evaporation characteristics from a multi-hole injector are studied in a constant volume chamber as part of investigation to the novel fuel system EDI+GPI [8].

2.3.3 Measuring the charge cooling effect

The fuel DI technology has been developed to cater the more and more stringent local and global emission regulations over the past few years. The high direct injection pressure (5 to 10 MPa) makes it possible for the liquid fuel droplets to evaporate in tens of crank angle degrees and thus absorb the thermal energy from the in-cylinder air [141]. Compared with fuel PI, DI is more effective for charge cooling due to fuel evaporation inside the combustion chamber. Moreover, the cooling effect of DI can be further enhanced by the fuels with greater enthalpy of vaporisation, such as ethanol fuel.

Cooling effect of DI has been measured in different ways. The most effective way may be to measure the in-cylinder temperature directly. Kar et al. [101] and Price et al. [142] used a cold wire resistance thermometer to measure the in-cylinder temperature in PI and DI engines. However this method requires fast response of the temperature sensor and protection for the fragile sensor. So the measurements were only performed in non-firing conditions [101, 142]. The Planar Laser Induced Fluorescence (PLIF) thermometry technique was used to measure the cylinder temperature of DI engines [143]. Up to date, the experimental methods to quantify the charge cooling used the parameters linked to the charge cooling directly or indirectly, such as in-cylinder pressure, volumetric efficiency, anti-knock ability, etc. Ahn et al. [144] used in-cylinder pressure to evaluate the cooling effect of ethanol fuel. Wyszynski et al. [145] measured the volumetric efficiency of different fuels on a DI SI engine fitted with both port and direct fuel injection systems. However, using intake air flow rate to quantify the amount of charge cooling only captured part of the cooling effect that took place during the intake stroke. Fuel evaporation process may continue after the intake valves are closed, and even in the

combustion process [146]. To evaluate the cooling effect on a special aim, knock onset was used to measure the charge cooling effect in a turbocharged SI engine equipped with both PI and DI of blended ethanol/gasoline fuels [146, 147]. Similar investigation was carried out in an attempt to identify the thermal and chemical benefits of DI and PI [148]. They reached the same conclusion that the ethanol's cooling effect enhancement to the engine performance was comparable to that of its higher Octane number [147, 148]. To quantify the thermal and chemical benefits of ethanol fuel, it is reported that a 2-8 kJ/kg increase of "cooling power" of the mixture has the same impact as one-point increase of research octane number [149]. Or 10% of ethanol addition to gasoline results in five-point increase of research octane number [20].

Meanwhile, numerical simulations have also been applied to investigate the cooling effect. 0-D simulations (involving no engine geometry) were performed to calculate the theoretical improvement in volumetric efficiency of DI over PI [145]. 1-D gas dynamics and thermodynamics engine simulations were carried out to investigate the anti-knock effect of direct injection with ethanol/gasoline blends [147]. As the 0-D and 1-D simulations were developed for special purposes, the information obtained in the results was limited. Kasseris et al. [146] used 3-D numerical modelling to investigate the effect of intake air temperature on the amount of realized charge cooling. The simulation results showed that almost all the theoretical charge cooling was realized when the intake air temperature was increased to 120 °C. However the simulated evaporation rate of ethanol fuel in low temperature conditions (naturally aspirated engines) was much lower than gasoline's [121, 122]. This limited the cooling effect of ethanol fuel.

Although quantitative measurement of the cooling effect has not been defined, it is certain that qualitatively the cooling effect of DI is stronger than that of PI and cooling effect of DI can be further enhanced by the fuels with greater enthalpy of vaporisation, such as ethanol fuel. Experimental investigation showed improvement in the performance of a single cylinder SI engine equipped with EDI+GPI [8]. It was inferred that the charge cooling enhanced by EDI played an important role. In Chapter 5, the charge cooling effect of EDI was investigated using three-dimensional CFD modelling.

2.3.4 Combustion characteristics of ethanol fuel

Compared with gasoline fuel, ethanol has several advantages in improving the engine combustion due to its properties which can be divided into two categories:

- 1) Direct benefits (or chemical benefits), which can improve the engine efficiency and emissions by improving the combustion process directly. These properties include higher octane number, faster laminar flame speed and lower stoichiometric air/fuel ratio etc.
- 2) Indirect benefits (or thermal benefits), which can improve the mixture formation process, and thus improve the consequent combustion and emission processes. These properties include larger enthalpy of vaporisation, higher vapour pressure at high temperature conditions and higher vapour pressure of ethanol/gasoline blends etc.

Among these properties, ethanol's enthalpy of vaporisation and octane number have attracted the most attention in the recent research on alternative fuels for IC engines. Engine downsizing is a trend in automotive engineering to deal with the increasingly stringent regulations, especially the regulations for CO₂ emission. They require the SI engines not only to reduce the pollutant emissions but also to improve the thermal efficiency [3, 149-151]. However one major issue associated with the downsized engines is the increased knock propensity [3, 149]. Ethanol's anti-knock ability strengthened by its strong charge cooling effect and high octane rating offers the possibility to address the issue of engine knock [149].

Stronger cooling effect can reduce the intake air temperature and consequently increase the volumetric efficiency. The reduced intake temperature can help reduce the knock propensity of the engine. The cooling ability relies greatly on the spray and mixture formation processes. In order to explore the most out of its maximum charge cooling potential, the spray process needs to be carefully arranged. Especially when it comes to downsized engines, wall wetting is more easily to occur which could significantly reduce the actual cooling effect [134, 152]. Poor mixing process also increases the knock propensity [134]. High enthalpy of vaporisation may bring some disadvantages as well. Numerical study found that the heat flux remained almost constant with the increase of enthalpy of vaporisation and consequently led to a lower evaporation rate [153].

So far most ethanol fuel has been used via blending with gasoline fuel, such as E10. This can also bring us some benefits, such as higher volumetric efficiency, enhanced anti-knock effect, and greater thermal efficiency [6, 152]. All these benefits can be fully or partially attributed to the cooling effect of ethanol content, as the enthalpy of vaporisation of ethanol is about three times of gasoline's [6, 128, 154]. This means that the same mass of ethanol fuel can cool the intake air more than gasoline, thus resulting in a higher volumetric efficiency, increased power output, lower temperature during combustion, decreased knock propensity and higher compression ratio. Therefore, investigating the physical properties and cooling effect of ethanol-gasoline blends is of great importance.

Although the volatility of neat ethanol fuel is not as good as that of gasoline fuel, blending ethanol with gasoline can improve the fuel's volatility. Experiments showed that the vapour pressure of ethanol-gasoline blend was higher than that of either ethanol or gasoline. With the increase of ethanol percentage, the vapour pressure of the mixture reached the peak at 20% and then fell eventually to the level of neat ethanol [101, 115]. On the other hand, the more fuel injected into the cylinder, the larger amount of heat energy is required for the evaporation of ethanol fuel. The decrease of vapour pressure and the increase of latent heat required for a complete evaporation are two competing factors. Therefore, it was recommended that blends of 30-50% ethanol would achieve the maximum cooling effect [101]. Apart from vapour pressure, other physical properties of ethanol-gasoline blend, such as density, viscosity and surface tension, would have profound influence on the fuel spray characteristics [115]. The fuel spray process involves flow motion, evaporation, breakup, spray-wall interaction, and coalescence/collision sub-processes. They may significantly affect the actual cooling effect to be exploited out of the maximum charge cooling in theory (assuming that all of the latent heat of vaporisation is taken from the intake air).

The higher octane number of ethanol fuel (~106) over gasoline (~91-98) is another attractive merit. Higher octane number enables greater thermal efficiency through higher compression ratio and more aggressive turbocharging, downsizing and spark timing [155]. In order to distinguish the benefits of octane number and enthalpy of vaporisation of ethanol, a few investigations were carried out. It was concluded that both octane number and enthalpy of vaporisation were significant for anti-knock ability of ethanol direct injection, and they were of the same order of importance [146-148]. Therefore, when

selecting a fuel to improve the knock suppression ability, it necessary to consider not only octane number but also the charge cooling effect.

It is widely reported that ethanol fuel can lead to a higher engine thermal efficiency [6, 8, 20, 156]. This is not only because of ethanol's higher enthalpy of vaporisation and octane number, but also due to its faster combustion speed. Higher flame propagation speed is important to improve the combustion efficiency, mitigate the engine knock and increase the combustion stability. Vehicle tests showed that the alcohol-gasoline blends provided slightly higher combustion efficiency compared to gasoline and the effect increased with the increase of vehicle speed [20]. Experiments also showed increased efficiency and reduced engine-out emissions with ethanol/gasoline blends due to the faster flame speed and higher vapour pressure [6]. Ethanol fuel can make engines more tolerant to fuel spray, ignition timing and knock. Optical experiments showed that gasoline spray was more sensible to air motion and in-cylinder pressure than ethanol fuel was in a GDI engine [157]. It was found that ethanol showed a wider spark timing window than gasoline did due to improved anti-knock ability and increased charge cooling effect [158]. Experiments also observed that ethanol reduced the engine's knock propensity in terms of spark timing advance [159].

Apart from the enthalpy of vaporisation and octane number, the laminar flame speed of ethanol is faster than that of gasoline. Laminar flame speed is a key parameter in the turbulent combustion flames. Many experimental investigations have been carried out to measure the laminar flame speeds for gasoline and ethanol fuels under various initial conditions [102, 104-106]. They all measured a higher laminar flame speed of ethanol over gasoline fuel. Higher flame speed is helpful to reduce cycle-to-cycle variations, flame extinction and knock propensity [160]. To measure the laminar flame speed, the fuel is full vaporised and premixed with the air homogenously in quiescent conditions to eliminate the effect of other factors. However, the spray combustion phenomena inside the engine cylinder are much more complicated. As a result, different trends may be observed.

Optical engine experiments could provide information on the complex in-cylinder combustion process in real engine conditions and pioneering work was conducted by Keck et al. to measure the turbulent flame propagation speed in a transparent SI engine fuelled by iso-octane [161]. The experimental results showed that the initial flame front

propagation speed was very close to that of a laminar flame for the same charge. However the flame speed increased rapidly to a quasi-steady value of 10 times the laminar value as the flame expanded. The final burnout of the charge may be approximated by an exponentially decreasing burning rate with a time constant of 1 ms. Jiang et al. [45] visualized the in-cylinder combustion process of a dual-injection system with DMF or Ethanol DI plus gasoline PI. They found that ethanol-gasoline dual-injection strategy showed higher flame propagation speed than gasoline PI did. Aleiferis et al. [117] investigated the combustion characteristics of E85 and gasoline in an optical DI SI engine. They observed a slower combustion speed of E85, especially in low coolant temperature condition. This was explained by the potential effect of increased charge cooling. Table 2.3 compares the experimental conditions investigated in [45] and [117]. As shown in Table 2.3, the engine conditions in the two studies were very similar. However, they observed opposite trends regarding the combustion speed. The main difference may be the fuel injection system where one adopted only DI and the other combined the DI and PI. The results demonstrated the advantages of dual-injection over single injection.

Table 2.3: Experimental conditions in [45] and [117]

	Conditions in [45]	Conditions in [117]
Engine type	Single cylinder, four-stroke, four-valve, water cooled, SI, optical engine	
Injection system	ethanol or DMF DI + gasoline PI	E85 or gasoline DI
Bore × Stroke	89×90 mm	89.0×90.3 mm
Compression ratio	11.3	11.15
Load	Load 1: IMEP 3 bar Load 2: IMEP 5 bar	Part load: 0.5 bar intake pressure Full load: 1.0 bar intake pressure
Speed	1200 rpm	1500 rpm
Coolant temperature	80 °C	20 and 90 °C
Injection timing	280 CAD BTDC	280 CAD BTDC
Injection pressure	DI: 15 MPa PI: 0.3 MPa	DI: 15 MPa
Spark timing	Load 1: 25 CAD BTDC Load 2: 33 CAD BTDC	35 CAD BTDC

A main drawback of ethanol fuel frequently discussed is the lower heating value which (26.9 MJ/kg) is only two thirds of gasoline's (42.9 MJ/kg). However, as an oxygenated fuel, the stoichiometric air/fuel ratio of ethanol (9.0) is much lower than gasoline's (14.8). Therefore the energy densities of stoichiometric mixtures of ethanol and gasoline are comparable, with 2.69 and 2.72 MJ per kg mixture for ethanol and gasoline respectively. This means that the output power of an ethanol-fuelled engine would not suffer any decrease for a given engine displacement. On the contrary, the engine power may increase due to the improved combustion process. However, more mass of ethanol fuel should be injected in order to maintain the same equivalence ratio and power output. More injected fuel requires longer injection duration and more thermal heat for evaporation. This will lead to longer spray tip penetration, and consequently result in fuel wall-wetting and increased HC and CO emissions.

Regarding the engine emissions, most publications reported that ethanol addition would lead to a decrease in NO emission [6, 8, 156, 158]. They would attribute this decrease either to the lower combustion temperature due to the charge cooling effect or shorter residence time in high temperature conditions due to the faster flame speed. For CO and HC emissions, some researchers [156, 158] reported a decrease with ethanol addition, whilst others [8, 20] observed the opposite tendency. These differences would be caused by the differences in the fuelling system (DI or PI), injection and ignition timing, ethanol ratios, intake air temperatures and pressures (turbocharged or naturally aspirated), etc.

2.3.5 Fuel heating to generate fine and fast evaporating sprays

The mixing and evaporating processes of a liquid fuel spray can be affected by a number of factors. To achieve fast evaporation and mixing in direct injection SI engines, the most widely adopted strategy is high pressure injection which generates very fine droplets and thus makes it possible for the liquid fuel to evaporate in tens of crank angle degrees. However, high pressure injection system not only requires high cost, but also has other drawbacks. Firstly, high injection pressure enhances the spray tip penetration. This may increase the fuel impingement on the cylinder and piston walls, especially in downsized engines. Secondly, the droplet size can be effectively reduced by increasing injection pressure in a medium range. However further increasing the pressure to very high level does not reduce the droplet size much but increases the cost greatly [162]. Apart from the

injection pressure, the fuel temperature is another important factor that determines the droplet size and evaporation rate of a liquid fuel. Increasing the fuel temperature is an effective way to reduce the viscosity and increase the vapour pressure of the fuel, and consequently increase the break-up and evaporation rates. Since ethanol fuel has larger viscosity and surface tension than gasoline, E85 shows larger Sauter Mean Diameter (SMD) than gasoline does. With the increase of fuel temperature, the SMD reduces and the difference in E85 and gasoline's SMDs becomes small when the temperature is sufficiently high [117]. Particularly, when the fuel temperature is higher than its boiling point, vapour bubbles may form inside a droplet and burst it to smaller ones [132]. It is reported that the SMD of the spray droplets showed a rapid reduction when flash-boiling occurred [110]. Moreover, the vapour pressure of ethanol fuel is smaller than that of gasoline fuel in low temperature environment but larger when the fuel temperature is higher than 375 K. As a result, ethanol evaporates more slowly than gasoline does in low temperature environment, but they reach the similar evaporation rates when the fuel temperature is higher than 375 K [163]. The evaporation rate of a spray can be significantly enhanced in flash-boiling conditions [162, 163]. Therefore, Xu. et al. [164] proposed using flash-boiling to generate fine droplets as an alternative and economic method for high pressure injection.

Nwafor [165, 166] investigated the combustion and emission performance of a diesel engine fuelled with elevated fuel temperature of neat vegetable oil. The effect of fuel temperature on the performance of a diesel engine with rapeseed methyl ester (RME) fuel was investigated [167]. Kabasin et al. [168, 169] investigated the cold start performance of ethanol-fuelled SI engines equipped with heated injectors. The engine cold start time was reduced and the HC and CO emissions were significantly decreased when fuel heating was employed. Sales and Sodré [17, 170] investigated the cold start combustion and emission characteristics of a flexible fuel engine with heated intake air and ethanol fuel. By heating the intake air and the ethanol fuel, the ethanol fuelled engine could be started at cold ambient temperature of 0 °C and their reports showed significant reduction in HC and CO emissions.

As reviewed above, increasing the fuel temperature could be an effective and economic way to generate fine and fast evaporation sprays and to improve the performance of ethanol fuelled engines in cold start conditions. However, so far, rare work has been

reported on investigating the engine performance with heated ethanol fuel at warmed up conditions. To address the emission issues in the current EDI+GPI engine, Chapter 7 is conducted to investigate the potential of heated ethanol fuel in direct injection (EDI heating) on improving the combustion and emission characteristics of an SI engine equipped with EDI+GPI system.

Chapter Three

3 Experimental Setup and CFD Model

3.1 Test rig for investigating EDI sprays

To investigate the EDI spray and evaporation characteristics and provide experimental data for engine modelling, spray experiments were conducted in a constant volume chamber using the high-speed shadowgraphy imaging technique. This section introduces the experimental setup, procedures, test conditions and the image processing method.

3.1.1 EDI injector

The EDI injector used in this study is a 6-hole nozzle which was used in the preliminary experimental investigation of the EDI+GPI engine reported in [8]. Figure 3.1 shows the distribution of the nozzle holes on the EDI injector tip and the magnified image of the nozzle exit using a microscope. As shown in Figure 3.1, there are six holes on the injector tip, with five located near the edge of the hemispheric boss in the centre of the injector tip and one closer to the boss centre. There is a small chamfer at each orifice exit. The measured nozzle diameter using a microscope is 110 μm .

Since the six nozzle holes have different machining angles in the injector, the emanated spray bends to the direction of the injector solenoid valve, as demonstrated in Figures 3.2 and 3.3. The six plumes are distributed in three groups. The first group contains only one plume whose axis is the same as that of the injector. The second group contains three plumes with a bend angle 17° to the injector axis. The third group contains two plumes with a bend angle of 34° . As a result, the second group has the darkest colour and the first group has the lightest colour in the spray image in Figure 3.2. When the fuel temperature is higher than the saturation temperature, the first and third plume groups collapse to the middle one.

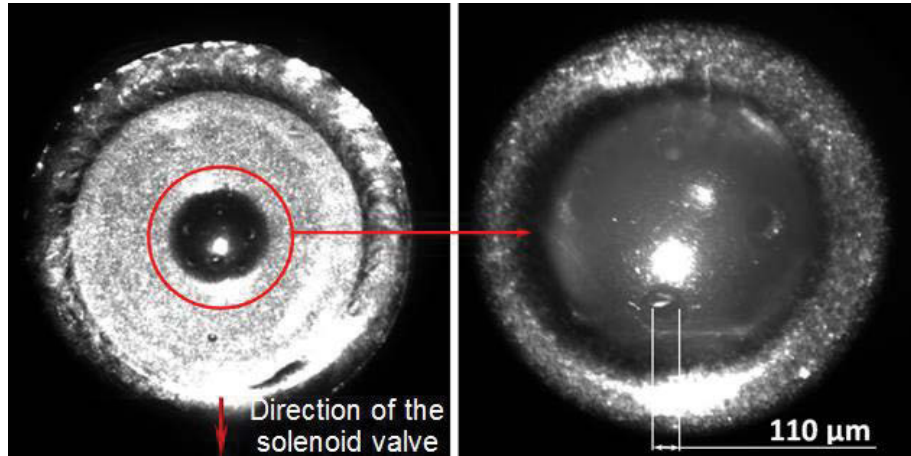


Figure 3.1: Overall view of the EDI injector tip (left) and the magnified image of the nozzle holes (right)

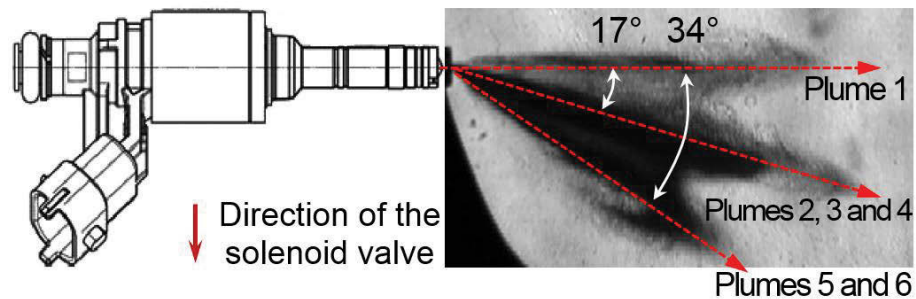


Figure 3.2: Lateral view of the spray plumes and their directions

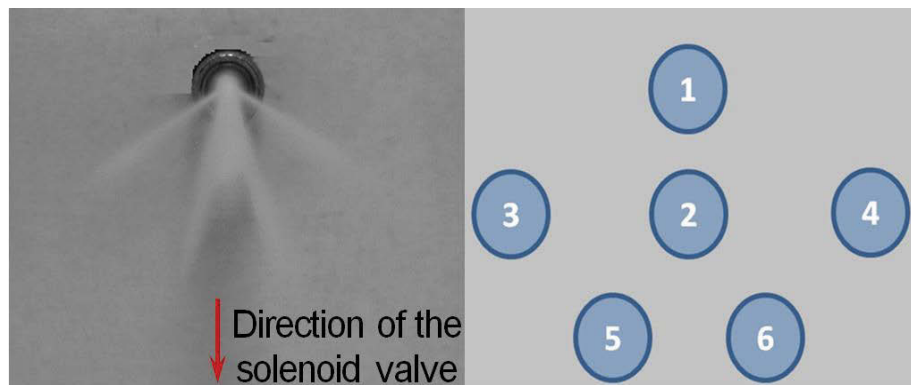
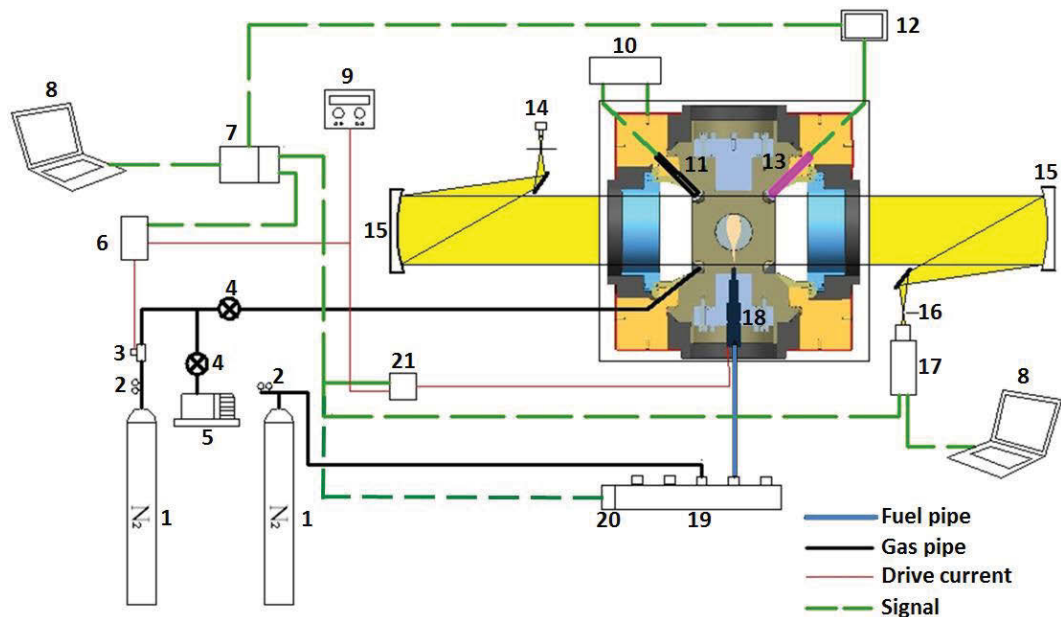


Figure 3.3: Front view of the spray plumes and their footprints

3.1.2 Constant volume chamber optical system

Figure 3.4 shows the schematic of the experimental apparatus including the constant volume chamber, the fuel injection system, the schlieren/shadowgraphy optical system and the vacuum system. The chamber is a cube with edge length of 136 mm. There are six main ports for optical access or injector installation and eight smaller ports located on the cube corners for installation of sensors or spark plug. The diameter of the quartz

window is 130 mm. Silicon heating sheets were adhered to the outside surfaces of the chamber body. The chamber was covered by insulation layer. A digital temperature controller (Type NO.: XMT604) was used to regulate the temperature with the feedback from a platinum resistance thermometer plugged into the chamber near the injector. Therefore, without heating by combustion, the fuel temperature (or injector temperature) and ambient gas temperature were the same as the chamber body temperature when the heating process reached a balance. The injector was mounted horizontally in one of the main ports. Its axis was perpendicular to the light pathway. The light source was the GB/T14094-1993 tungsten halogen lamp. The voltage for the lamp was kept at 100 V to supply the same light source for each measurement. Two nitrogen cylinders (maximum pressure was 13 MPa) were used to pressurize and control the injection pressure and ambient pressure respectively. The injection pulse with a width of 2.0 ms was generated by a single-chip computer. Meanwhile, the driving signal was used to trigger the MotionPro Y4S1 high speed CCD camera simultaneously. The fuel droplets injected from previous injections were removed by a vacuum pump (item 5 in Figure 3.4).



1. High pressure nitrogen cylinder 2. Pressure reducing valve 3. Solenoid valve 4. Hand valve 5. Vacuum pump 6. Solenoid valve control unit 7. NI USB-6251M data acquisition card 8. Computer 9. Power source 10. Temperature control unit 11. Pt100 temperature transducer 12. Kistler 5018 charge amplifier 13. Kistler 6052C pressure transducer 14. Tungsten halogen lamp 15. Reflective mirror 16. Knife edge 17. MotionPro Y4S1 CCD camera 18. Injector 19. High pressure fuel rail 20. Fuel rail pressure sensor 21. Fuel injection control unit

Figure 3.4: Schematic of the EDI spray experiment apparatus

Shadowgraphy and schlieren techniques are two of the most effective techniques used to visualize the time-resolved non-homogeneous transparent flow fields, such as the evaporating sprays and reacting spray flames. The only difference in these two methods is a knife edge (item 16 in Figure 3.4) is used in front of the camera in schlieren technique but not in shadowgraphy technique. Schlieren technique uses the knife edge to enhance the contrast but may lose some information [171, 172]. The knife edge was not used and only the shadowgraphy measurements were performed because the gas turbulence was weak and light attenuation through the air was low enough to highlight the spray area for the quiescent ambient conditions in the present study.

3.1.3 Test fuel

The ethanol fuel investigated in this study was the absolute ethyl alcohol with a purity of 99.9%. Some critical physical properties that would influence the spray behaviours were found from the Yaws' handbook [100]. As shown in Figure 3.5, with the increase of fuel temperature, the viscosity and surface tension decrease which would lead to a faster breakup rate, and the saturation vapour pressure and diffusion coefficient in air increase which would lead to a higher evaporation rate. Specifically, the saturation temperature (or boiling point) of ethanol fuel in atmospheric pressure is 351 K. This is the key point where ethanol spray may present different patterns.

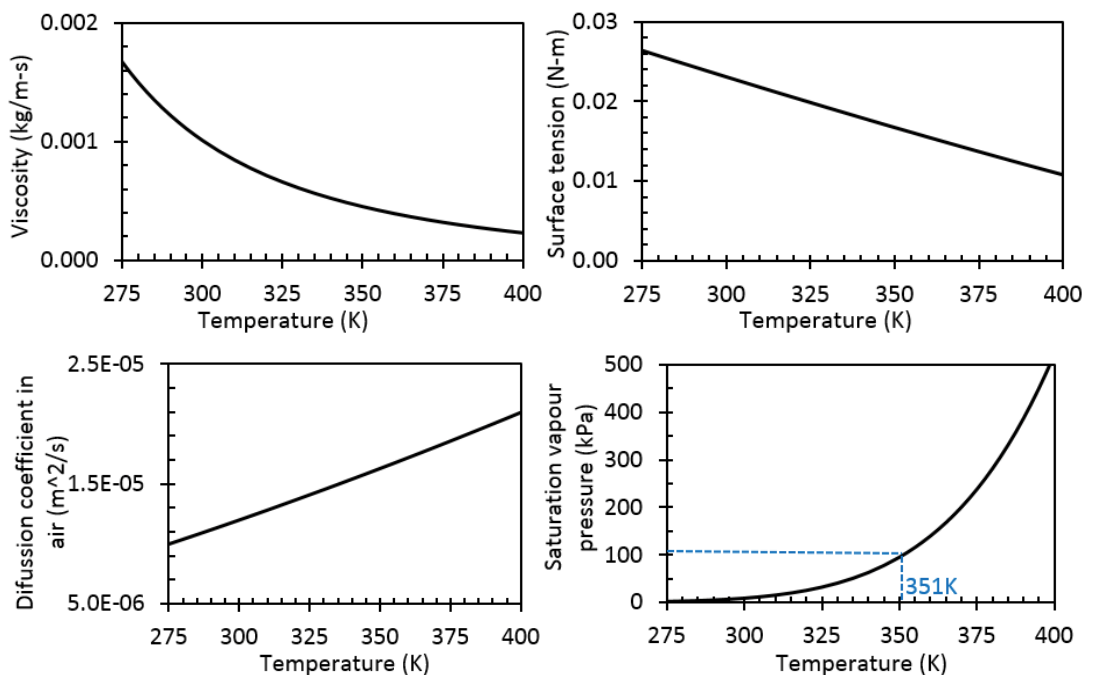


Figure 3.5: Ethanol fuel properties (data source: [100])

3.1.4 Experimental conditions

The fuel injection pressure of 6 MPa was adjusted using compressed nitrogen. 6 MPa was the direct injection pressure of the ethanol fuel applied in the experiments on the EDI+GPI research engine [8]. The ambient pressure was kept at 0.1 MPa which represented the in-cylinder pressure during early EDI injection with 36% throttle open. The tested fuel temperature varied from 275 K (non-evaporating spray) to 400 K (flash-boiling spray) with an increment of 25 K. However the temperature increment was reduced to 5 K during the transition process from normal-evaporating spray (350 K) to flash-boiling spray (375 K). The injection duration was held constant at 2 ms. To measure the fuel mass per injection pulse, the fuel injected of 300 consecutive sprays was collected and measured on a mass balance with an accuracy of 1 mg (1 mg over about 3000 mg). The measured fuel mass per injection was 10.844 mg @ 6 MPa \times 2 ms. The uncertainty of the fuel mass measurement was within 2% (standard deviation of five measurements). The speed of the imaging was 20000 fps @ 608 \times 288 pixels. The spatial resolution of the images was 0.203 mm/pixel. The liquid fuel spray was always firstly seen in the 19th or 20th spray image. Therefore the injection delay of the injector was about 1 ms. 198 spray images were obtained for each injection. The large quartz windows (with a diameter of 130 mm) made it possible to measure the spray characteristics until about 8 ms after the start of injection (ASOI). Each spray condition was repeated for five times.

3.1.5 Image Processing

The captured spray images were 8-bit grey scale images where 0 stands for black and 255 stands for white. The images were processed by a Matlab code. Figure 3.6 demonstrates the procedure of the spray image processing code. Firstly, the raw spray image Figure 3.6(b) was background corrected using a frame prior to the fuel injection Figure 3.6(a). This step eliminated the uncertainty of the back lighting and background noise caused by the gas flows in the chamber. Then, a threshold of 5% was used to convert the background corrected image Figure 3.6(c) to a binary image Figure 3.6(d). Finally the boundary of spray area Figure 3.6(e) can be determined based on the binary image Figure 3.6(d). The macroscopic spray characteristics were calculated based on the spray boundary. As shown in Figure 3.6(f), the spray tip penetration was defined as the longest distance that the spray travelled. The spray projected area was the area within the spray boundary. The spray

angle was defined according to the SAE J2715 Standard [173]. Four points have been located on the spray boundary: two near points have a horizontal distance of 5 mm to the injector tip, and the distance for the two further points is 15 mm. These four points were used to define two lines on each side of the spray boundary. The angle of the two lines was defined as the spray angle. The averaged image pixel intensity values were calculated based on the images without the background noise (background corrected image Figure 3.6(c)). The spray tip penetration, angle, projected area and averaged image pixel intensity reported in Chapter 4 were the averaged values of five repeated experiments. Error bars (± 1 standard deviation) were used to show the statistical uncertainty of each measurement, as shown in Figures 4.2-4.5 and 4.8-4.11.

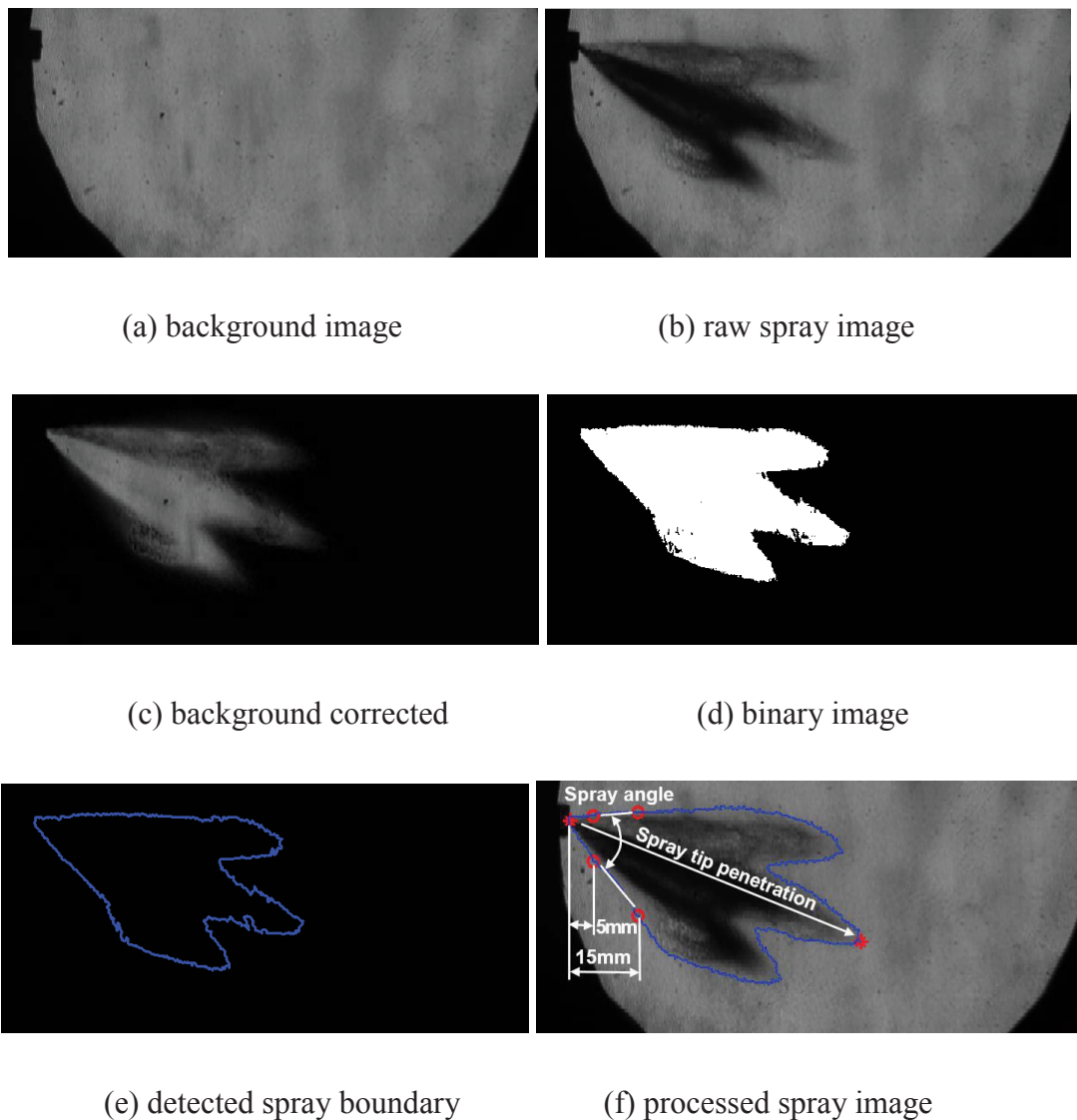
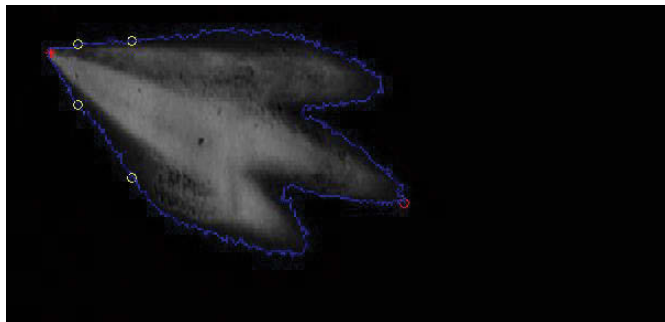
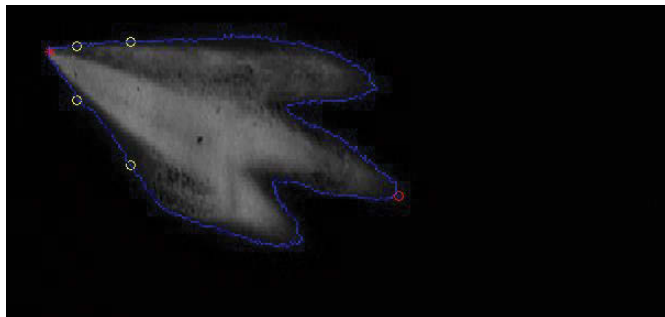


Figure 3.6: Shadowgraphy spray image processing method

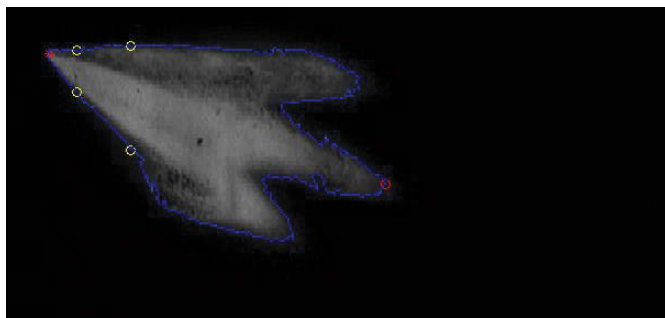
Obviously, the identification of the measured spray characteristics was strongly dependent to the threshold value, especially the spray projected area because smaller threshold value would include larger spray area. Figure 3.7 shows the sensitivity of the threshold values (2.5%, 5% and 10%). Figure 3.7(c) shows that the threshold 10% does not include some spray area at the spray tip, whilst the threshold 2.5% covers some area that does not belong to the spray area as shown in Figure 3.7(a). Therefore, the threshold 5% was selected for spray image processing in the present study. The same threshold value was also used in reference [174].



(a) threshold = 2.5%



(b) threshold = 5%



(c) threshold = 10%

Figure 3.7: Effect of the threshold vaule on the detected spray boundary

3.2 CFD model of EDI+GPI engine

Simulation of DI engines involves many interacting phenomena that should be taken into account and still represents a very challenging task for CFD modelling [175]. To simulate the spray combustion process in an EDI+GPI engine, the model should include the dynamic mesh that represents the engine geometry details, a set of numerical models for the in-cylinder flows, fuel sprays and combustion, appropriate initial and boundary conditions, and model verification.

In this section, an engine model was developed using the CFD code ANSYS FLUENT. The in-cylinder flows were modelled using the RANS based realizable $k-\varepsilon$ turbulence model because it gave a more accurate prediction of the spreading rate of both planar and round jets than the standard $k-\varepsilon$ model [79]. Standard Wall Functions were used for the near-wall treatment. Mass, energy and momentum conservation equations and heat transfer equation between the wall and air flow were numerically solved in each time step which was 0.25 crank angle degree (CAD). The time step and under-relaxation factor (URF) were reduced during the periods of valve opening or closing and EDI spray to achieve a more stable and convergent calculation. The pressure-velocity coupling scheme was the PISO (Pressure-Implicit with Splitting of Operators) which was developed from the SIMPLE method (Semi-Implicit Method for Pressure Linked Equations) in order to improve the computational efficiency for compressible flows. The spatial discretization scheme for gradient was the Green-Gauss Node Based scheme which was recommended for tetrahedral meshes. The PRESTO scheme was used for the pressure discretization which was suggested for flows in strongly curved domains. The Second Order Upwind discretization scheme was chosen for the density, momentum, energy, turbulent kinetic energy, turbulence dissipation rate and species equations.

The sprays were simulated by the Discrete Droplet Model (DDM) based on the Eulerian-Lagrangian approach. The Convection/Diffusion Controlled Model was adopted to model the evaporation process of ethanol and gasoline sprays, which provided the combustion model with the amount of vapour fuel for each fuel. The combustion process was modelled using the ECFM combustion model with the partially premixed combustion concept. A presumed five-dimensional double-delta PDF look-up table was used to model the dual-fuel turbulence-chemistry interactions.

3.2.1 Computational mesh

The computational mesh was generated based on the engine equipped with EDI+GPI used in the experiments. The geometry of the cylinder head was scanned by a local company Qubic. The point spacing resolution of the scan was 0.2 to 0.4 mm. Computer aided design modifications were made to the scanned model before generating the computational grids. As shown in Figure 3.8, the geometry includes the intake manifold with the throttle plate, the Kistler 6115B pressure measuring spark plug, the piston and the intake and exhaust valves. The throttle plate has an angle of 32.40° to the vertical surface corresponding to 36% throttle open.

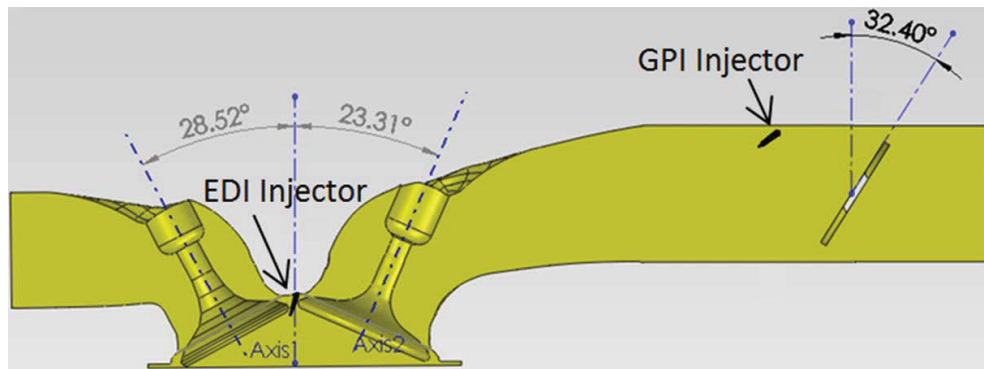


Figure 3.8: Cross-sectional view of the geometry of the cylinder head

The geometry was pre-processed by the ANSYS Design Modeler. As shown in Figure 3.9, the geometry was decomposed around the piston and valve volumes so that they could be meshed to different types of grids. The dynamic mesh was generated by the ANSYS Meshing. Three dynamic mesh schemes, namely smoothing, layering and remeshing, were used to tackle the challenge of moving boundaries of the piston and valves. As shown in Figure 3.10, the mesh mainly consists of tetrahedral grids. However the regions with moving boundaries were meshed to hexahedral grids for mesh deforming. The general cell size for the mesh was 4.00 mm, while the cell size near the valve seat regions was refined to be 0.4 mm. The position of the piston was calculated as a function of the crank angle degree, the engine stroke and the length of the connection rod. The moving boundaries of the intake and exhaust valves were meshed based on the measured cam lift curves which are shown in Figure 3.11. To avoid extremely small gaps between the valve and the valve seat, it was defined that the intake and exhaust valves were open/closed when the valve lift was larger/smaller than 0.50 mm. However, this may

over-predict the flow rate at the intake valve. To avoid this problem, the valve opening and closing angles were calculated using the trapezoidal method of numerical integration. The grids for the intake or exhaust manifolds were deactivated when the valve was closed in order to save the computation time.



Figure 3.9: Geometry decomposition

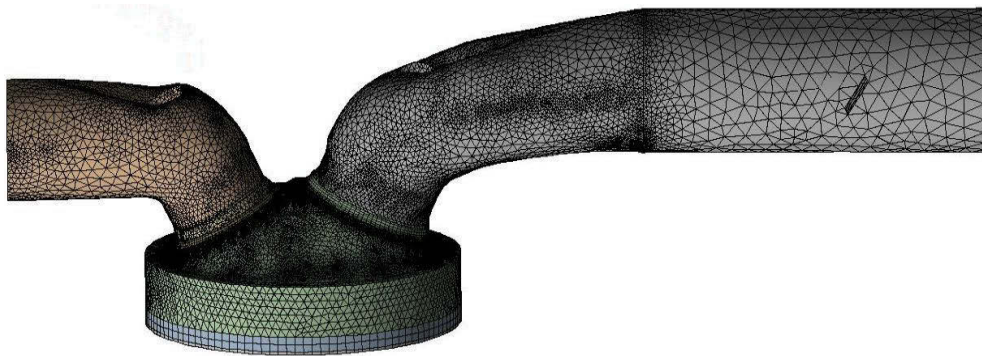


Figure 3.10: Computational mesh

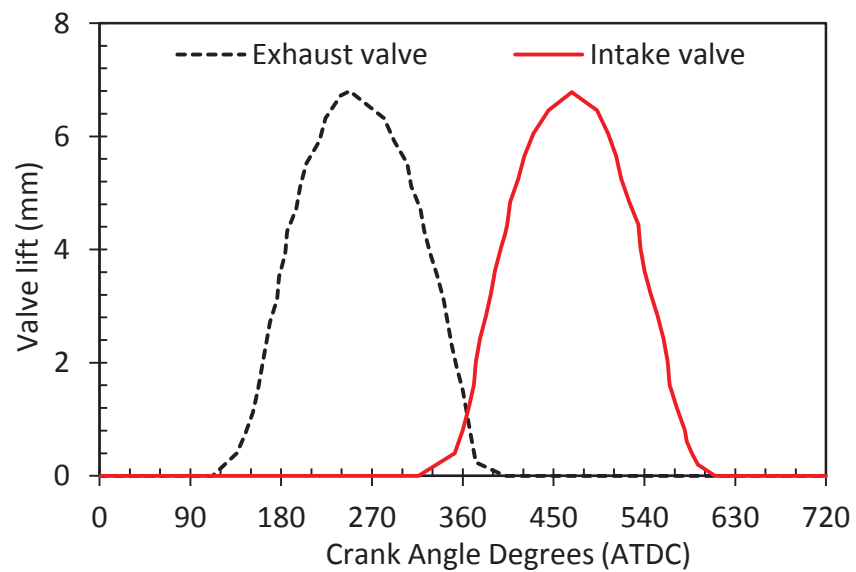


Figure 3.11: Measured valve lifts of the intake and exhaust valves

3.2.2 Spray sub-models

The liquid fuel spray process contains several sub-processes and they all have a significant influence on the mixture formation. These processes include primary and secondary break-up, turbulence dispersion, collision and coalescence, distortion and drag, evaporation and spray-wall interaction.

Droplet breakup is a key process in spray modelling. However, as reviewed in Section 2.2.2.2, modelling fuel atomisation (or primary breakup) is an extremely difficult task since the inner structure and fundamental mechanisms of liquid atomisation are still largely uncertain [63, 66]. An approximate method to represent the complexity of initial atomisation is the blob injection concept which has been adopted in the present modelling. The Rosin-Rammler Diameter Distribution Method was used to specify the initial droplet size at the nozzle exit. The Rosin-Rammler distribution function is based on the assumption that an exponential relationship exists between the droplet diameter (d) and the mass fraction (Y_d) of droplets with diameter greater than d ,

$$Y_d = e^{-(d/\bar{d})^n} \quad \text{Equation 3.1}$$

Where d is the droplet diameter, \bar{d} is the mean diameter, n is the spread number. The mean diameter was set as 300 μm for GPI spray droplets and 110 μm for EDI spray droplets. The spread number was 3.5 for the two sprays. To achieve an accurate statistical representation for the spray particles, a large number of parcels should be introduced into the domain [64]. Therefore 20 parcels per hole were released at the nozzle exit in each time step. For EDI+GPI E46 condition, the total number of parcels introduced into the computational domain was around 9000 for gasoline spray and 30000 for ethanol spray.

The consequent droplets breakup process was modelled by the WAVE model [176]. WAVE model is appropriate for high Weber number ($We > 100$) flows, which considers the breakup of the droplets to be induced by the relative velocity between the gas and liquid phases [79, 177]. In the present study, although the initial velocity of the gasoline droplet is relatively slow for low pressure (0.25 MPa) GPI spray, the air velocity in the intake manifold can be as high as 200 m/s. As a result, the We numbers for both the EDI and GPI droplets are greater than 100. Dynamic Drag model [80] was used to take into account the droplet distortion and drag. Since the simulated cases were completely

warmed up engine conditions, the cylinder wall temperature was hot and the Wall-jet model was adopted to model droplet-wall interactions. It provides a range of rebound directions and velocities when a liquid droplet collides with a wall [79].

It is critical to model the fuel evaporation process appropriately, which affects the consequent combustion and emission processes directly. This is because the droplets must vaporise before they can burn [75, 81]. The Convection/Diffusion Controlled Model was adopted to model the evaporation process of ethanol and gasoline droplets. It uses the vapour pressure as the driving force for droplets evaporation and incorporates the effect of the convective flow on the evaporating materials from the droplet surface to the bulk gas phase. The governing equation for the diffusion effect is described as [79],

$$N_i = k_c \left(\frac{P_{sat}}{RT_p} - X_i \frac{P}{RT_\infty} \right) \quad \text{Equation 3.2}$$

Where N_i is the molar flux of vapour (kmol/m²s). k_c is the mass transfer coefficient (m/s). P_{sat} is the saturated vapour pressure at the particle temperature T_p . X_i is the local bulk mole fraction of the species i . P is the absolute pressure, and T_∞ is the local bulk temperature in the gas. The vapour flux given by Equation 3.2 becomes a source of species i in the gas phase species transport equation. The evaporation rate of the droplet can be calculated by,

$$m_p(t + \Delta t) = m_p(t) - N_i A_p M_{w,i} \Delta t \quad \text{Equation 3.3}$$

Where $m_p(t + \Delta t)$ is the mass of the droplet (kg) at time $t + \Delta t$ and $m_p(t)$ is the droplet mass at t , A_p is the surface area of the droplet (m²), $M_{w,i}$ is the molecular weight of species i (kg/kmol), Δt is the time interval.

The effect of the convective flow on the evaporating material from the droplet surface to the bulk gas phase was also taken into account in the model by [79],

$$\frac{dm_p}{dt} = k_c A_p \rho_\infty \ln(1 + B_m) \quad \text{Equation 3.4}$$

Where ρ_∞ is the density of the bulk gas (kg/m³), B_m is the Spalding mass number and given by,

$$B_m = \frac{Y_{i,s} - Y_{i,\infty}}{1 - Y_{i,s}} \quad \text{Equation 3.5}$$

Where $Y_{i,s}$ is the vapour mass fraction at the droplet surface and $Y_{i,\infty}$ is the vapour mass fraction in the bulk gas.

The thermal heat for the phase change of fuel droplets comes from the ambient gas. The heat transfer between the droplets and gas is [79],

$$m_p c_p \frac{dT_p}{dt} = h A_p (T_\infty - T_p) - \frac{dm_p}{dt} h_{fg} \quad \text{Equation 3.6}$$

Where h is the convective heat transfer coefficient ($\text{W/m}^2\text{-K}$), h_{fg} is the enthalpy of vaporisation of the liquid fuel (J/kg), c_p is the heat capacity of the droplets (J/kg-K).

It can be seen from Equation 3.2 that the vapour pressure is the driving force for droplet evaporation in the model. Therefore it is critical to provide accurate vapour pressure values for gasoline and ethanol fuels over the entire range of possible droplet temperature in the modelling. In this study, iso-octane was used to represent gasoline fuel. Table 2.2 lists the physical and chemical properties of ethanol and gasoline fuels at the temperature of 300 K. All the physical and chemical properties of ethanol and gasoline fuels were taken from the Yaws' handbook [100] except for gasoline's vapour pressure. This is because the vapour pressure of gasoline is larger than iso-octane's because of the light components in gasoline fuel, as shown in Figure 2.10. Therefore the vapour pressure for gasoline used in the modelling was calculated using an empirical power law relationship of Equation 2.13 derived from the experimental data reported in [101]. More details about the calculation and verification of vapour pressure can be found in Section 2.3.1.

3.2.3 Combustion sub-models

Previous study showed that the gasoline and ethanol vapours distributed unevenly in the combustion chamber and the low evaporation rate of ethanol fuel in the low temperature condition before combustion led to many liquid ethanol droplets not evaporated by spark timing [121]. Therefore the combustion process in the EDI+GPI engine was identified to be a typical example of partially premixed combustion. In this study, the ECFM combustion model with the partially premixed combustion concept was adopted to simulate the dual-fuel combustion process, in which both the progress variable c and the

mixture fraction Z were solved. The ECFM model is based on the hypothesis that the smallest turbulence length scales (Kolmogorov eddies) are larger than the laminar flame thickness. So the effect of turbulence is to wrinkle the laminar flame sheet. However the internal laminar flame profile is not distorted. The increased surface area of the flame accelerates the net fuel consumption and flame speed. The ECFM model is applicable for IC engines typically operate in the wrinkled flamelet range. An expression for the transport of the net flame area per unit volume Σ (flame area density) can be derived based on these assumptions [91, 178]:

$$\frac{\partial \Sigma}{\partial t} + \nabla \cdot (\bar{u} \Sigma) = \nabla \cdot \left(\frac{\mu_t}{Sc_t} \nabla \left(\frac{\Sigma}{\rho} \right) \right) + (P_1 + P_2 + P_3) \Sigma + P_4 - D \quad \text{Equation 3.7}$$

Where P_1, P_2, P_3 and P_4 are the source terms due to turbulence interaction, dilatation in the flame, expansion of burned gas and normal propagation respectively. D is the dissipation of flame area. This equation requires closure terms for the production and destruction terms for flame area density. The Veynante scheme is used to close the equation which provides the best accuracy in most situations [55]:

$$P_1 = \alpha_1 K_t = \alpha_1 \frac{\varepsilon}{k} [(1 - \alpha_0) + \alpha_0 \Gamma_K] \quad \text{Equation 3.8}$$

$$P_2 = \alpha_2 \frac{2}{3} \nabla \cdot (\rho \bar{u}) \quad \text{Equation 3.9}$$

$$P_3 = \alpha_3 \beta_1 U_L \frac{\Sigma}{\bar{c}(1-\bar{c})} \quad \text{Equation 3.10}$$

$$P_4 = \alpha_4 U_L \nabla^2 \bar{c} \quad \text{Equation 3.11}$$

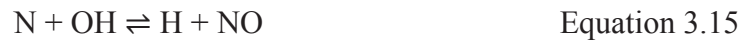
$$D = \beta_1 U_L \frac{\Sigma^2}{1-\bar{c}} \quad \text{Equation 3.12}$$

Where $\alpha_0, \alpha_1, \alpha_2, \alpha_3, \alpha_4, \beta_1$ are the model constants, Γ_K is the intermediate turbulent net flame stretch (ITNFS) term which can be calculated as a function of the two parameters $\frac{w}{U_L}$ and $\frac{l_t}{\delta_l^0}$, U_L is the laminar flame speed and δ_l^0 is the laminar flame thickness. It is clear from the closure terms that the ECFM combustion model is strongly depended on the accuracy of the expressions for the laminar flame speeds. For perfectly

premixed combustion, the unburnt mixture is treated as single composition and the laminar flame speed is constant. However, in partially premixed combustion, the laminar flame speed changes as the equivalence ratio of the mixture changes. Although the focus of theoretical studies of premixed turbulent combustion was on obtaining an analytical expression for the burning velocity of an unperturbed fully developed flame in the past decades, this problem has not been solved yet and new solutions are still being proposed in recent years [85]. Usually laminar flame speeds are measured from experiments or computed from 1-D simulations. In the present study, the laminar flame speeds of ethanol and gasoline fuels are taken from the experiments [102] in which the laminar flame speeds of gasoline and ethanol fuels were measured over the range of equivalence ratio from 0.6 to 2.0, as shown in Figure 2.12. Linear interpolation was used to calculate the flame speed in the mixture fraction range. The turbulent flame speed is calculated based on the laminar flame speed and the local turbulence intensity in the combustion model.

The combustion process was initiated by releasing a specific amount of energy to the cells at the spark plug gap using the Zimont spark model. The flame kernel increases from an initial radius 0.002 m to the final radius 0.005 m with a time exponent of 1/3. Whilst the spark model is active, the progress variable within the spark kernel is set to 1. The presumed PDF look-up tables were used to model the turbulence-chemistry interactions. The chemistry look-up tables were generated using complex reaction mechanisms which incorporated the latest insights on combustion chemical kinetics [96]. For single-fuel GPI or EDI only combustion modelling (single-mixture-fraction), a three-dimensional PDF table was generated to determine the instantaneous scalar values (species mass fractions, density and temperature) in the turbulent flame as a function of the fuel mixture fraction, the mixture fraction variance and the normalized heat loss/gain. For dual-fuel EDI+GPI combustion modelling (two-mixture-fraction), a five-dimensional PDF table was generated to take into account the secondary fuel. These information were calculated before combustion and stored in the PDF look-up tables. The mean values of mass fractions, density and temperature in each cell of the computational domain were obtained by interpolation during the calculation. The computational cost of implementing five-dimensional PDF table was much higher than the three-dimensional one. In this study, the computation time for EDI+GPI and GPI only simulations were about 73 and 19 hours respectively on a 16-core Intel(R) Xeon(R) E5-2687W @ 3.1 GHz workstation.

Generally the NO concentration in the combustion chamber is very low compared with other species. As a result, the effect of NO chemistry on the in-cylinder flow field, temperature distribution and major combustion product concentrations is negligible. Therefore, an efficient way to simulate the NO concentration is post-processing from the main combustion simulation results. Obviously, an accurate combustion solution is a prerequisite of NO prediction. Currently the quantity of NO cannot be pinpointed, but the variation trends can be accurately predicted. This can help reduce the laboratory tests and thus shorten the design cycle and reduce the cost. That is truly the power of the CFD in general [79]. In this modelling, only thermal NO formation mode is calculated since the other two NO formation modes, namely prompt and fuel NO formations, are not important in this study. Thermal NO formation is a set of highly temperature-dependent chemical reactions known as the extended Zeldovich mechanism. The principal reactions governing the formation of thermal NO are as follows [99, 179, 180],



The NO formation rate is significant only at high temperatures (greater than 1800 K) because the fixation of nitrogen requires the breaking of the strong N₂ triple bond [79]. The thermal NO formation rate is highly dependent on temperature, and also increases with the increase of oxygen concentration.

3.2.4 Boundary and initial conditions

The boundary and initialization conditions were set up based on the experimental conditions. Table A.1 in the Appendix provides the simulated engine conditions in this study and the related publications. In all the modelled cases, the engine speed was 4000 rpm, the throttle position was 36% and the spark timing was 15 CAD BTDC. The injection pressure was 0.25 MPa for GPI and 6.0 MPa for EDI. The GPI timing was kept at 410 CAD BTDC and the modelled EDI timings included early EDI timing during the intake stroke at 300 CAD BTDC (IT300), medium EDI timing at 180 CAD BTDC (IT180) and late EDI timing during the compression stroke at 100 CAD BTDC (IT100). The

ethanol ratio varied from 0% (GPI only) to 100% (EDI only), including E0, E25, E46, E58, E69, E76, E85 and E100 (E'X' means X% ethanol by volume. e.g. E46 is 46% ethanol via direct injection plus 54% gasoline via port injection). The injection durations for the two injectors were calculated from the injection pressure and mass of the fuel injected, using the calibration provided by Hents Technologies Inc. The equivalence ratio was kept around one. The surfaces of the piston, intake and exhaust valves were set as moving walls and others were set as fixed walls. The wall temperatures were set up based on the typical temperature distributions for SI engines operating at normal steady state conditions [81]. The wall temperatures were set to be 600 K for the cylinder head, 458 K for the cylinder linear, 573 K for the piston, 523 K for the intake valve, and 923 K for the exhaust valve. The wall temperatures of intake and exhaust ports were assumed to be 333 K and 723 K respectively. The inlet and outlet pressure values were constant as the atmospheric pressure. The intake air temperature was set to be the room temperature of the engine laboratory. Initial conditions for the combustion chamber, intake and exhaust manifolds were set up according to the measured in-cylinder pressure and exhaust gas temperature.

3.2.5 Model verification

Mesh density is an important concern in the use of CFD simulations. For the Eulerian-Lagrangian approach, a very fine mesh is not suitable because this would violate a basic requirement for the Lagrangian liquid phase description. This description is based on the assumption that the void fraction within a cell is close to one. Hence, the volume of liquid droplets inside a cell must be smaller than the cell volume [60]. To meet this requirement, the grid sizes near the nozzles are at least five times larger than the nozzle diameters [90, 181]. In this study, the initial maximum droplet sizes are 0.3 mm for ethanol and 0.6 mm for gasoline, and the grid sizes near the nozzles are 1.50 mm for the EDI injector and 4.00 mm for the GPI injector.

To test the mesh dependency, meshes with different grid sizes have been generated. Compared with Mesh 1, the grids for the combustion chamber were refined in Mesh 2 and Mesh 3, as shown in Figure 3.12. The in-cylinder pressure traces with different meshes were compared. The comparison of in-cylinder pressure as results of three of the tested grid sizes is shown in Figure 3.13. As shown in Figure 3.13, strong grid

dependencies have not been observed. However, the computation time for Mesh 2 and Mesh 3 increased by 23% and 82% respectively compared with that of Mesh 1. Fewer nodes will result in poor quality mesh. The Mesh 1 with 178887 nodes, therefore, is considered being sufficient to perform the computations with a reasonable accuracy and low computational cost.

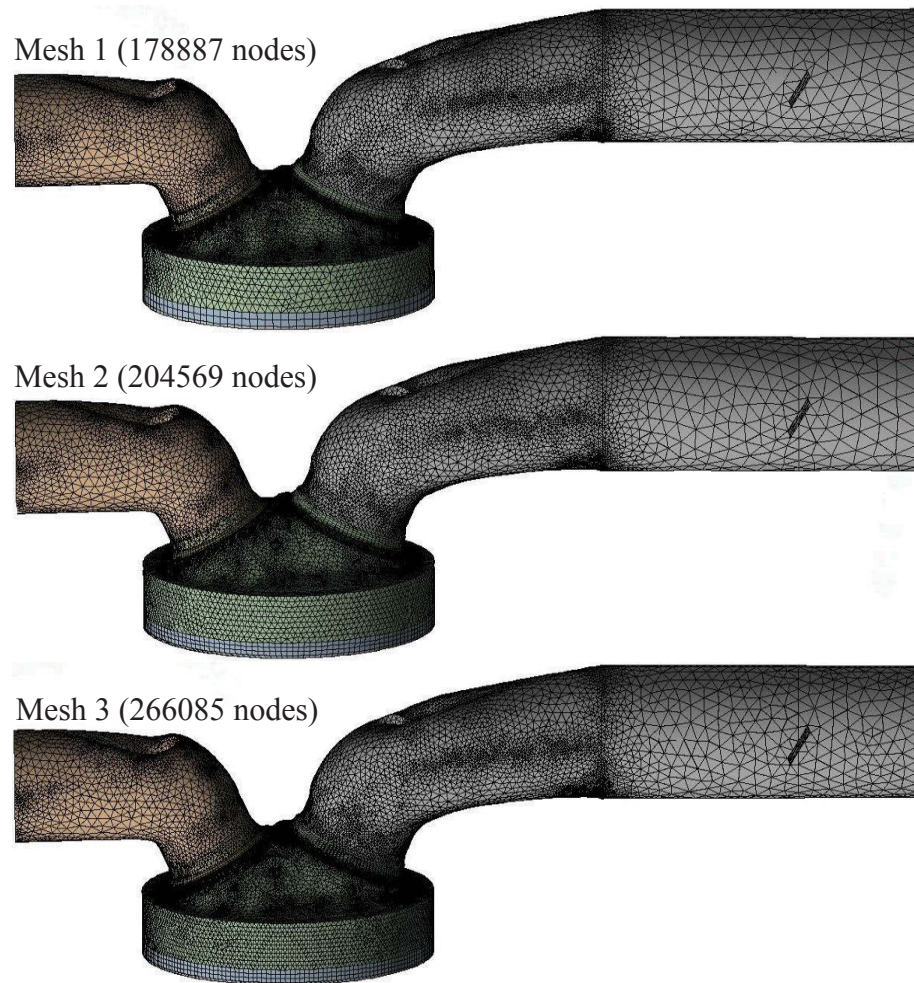


Figure 3.12: Computational meshes with different grid densities

The engine model includes the sub-models for fuel spray and combustion processes. Both are verified against the experimental data. To verify the spray model, the spray model was used to simulate the EDI spray process in the constant volume chamber. The EDI spray experiment was conducted in a condition with 350 K ambient temperature and 0.1 MPa ambient pressure to reproduce the in-cylinder conditions for an early EDI injection of 300 CAD BTDC. The injection pressure was 6 MPa which was applied in the engine test [8]. The time step for the spray verification modeling was 0.01 ms which was the same as that of the engine simulations (0.25 CAD @ 4000 rpm). The numerical results of

the spray pattern and spray tip penetration were compared with the experimental ones. As shown in Figure 3.14, the spray structure including its evolution is well simulated by the spray model. Figure 3.15 reports the comparison of measured and simulated spray tip penetrations varied with time. The simulated spray penetrates slightly faster than the experimental one in the earlier stage and reaches the similar length later. However, in general, the spray evolution is well modeled.

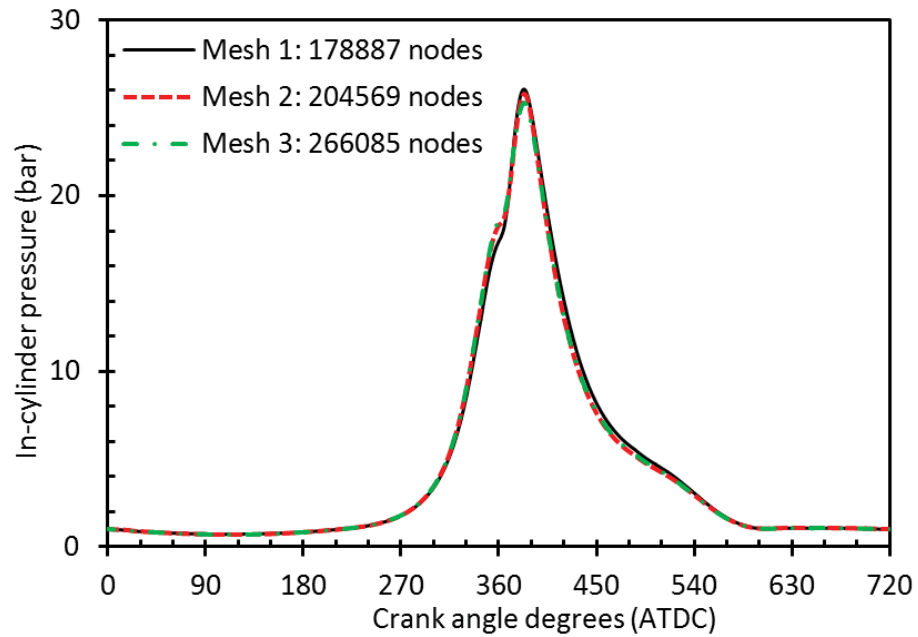


Figure 3.13: Grid size sensitivity

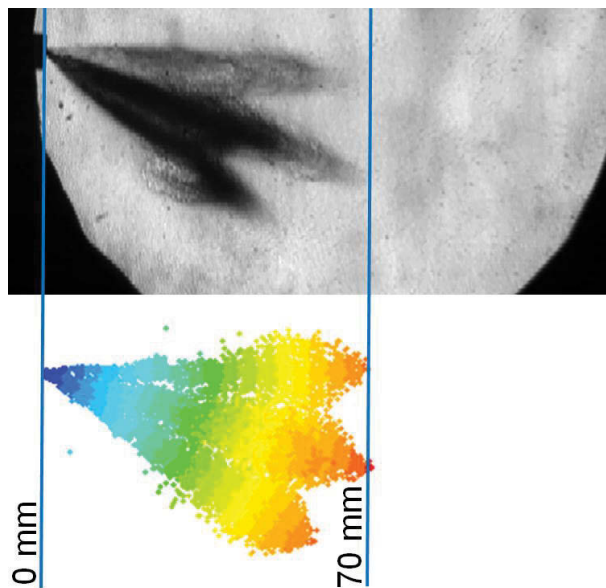


Figure 3.14: Comparison of the experimental and numerical results of EDI spray pattern at 1.5 ms ASOI in a constant volume chamber @ 6.0 MPa injection pressure, 0.1 MPa ambient pressure and 350 K ambient temperature

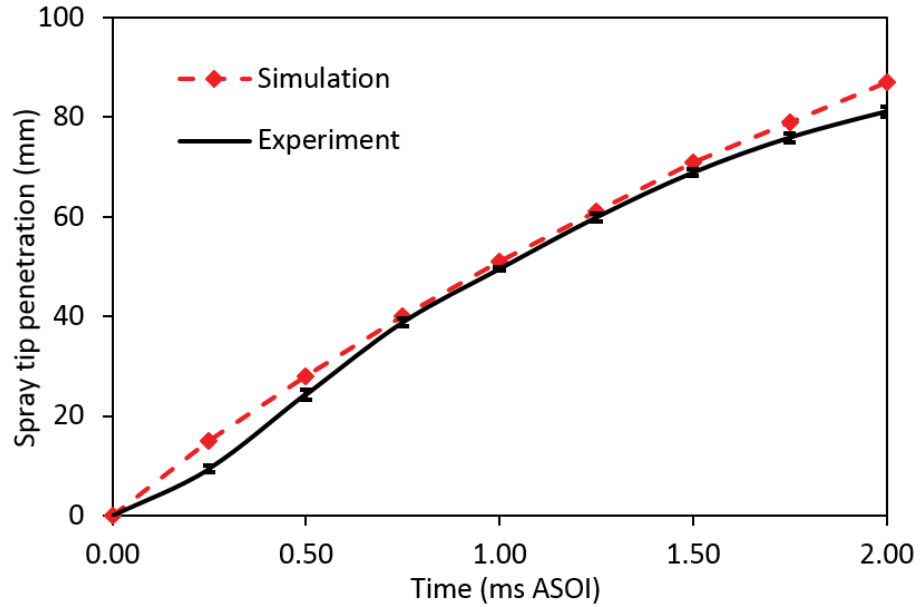


Figure 3.15: Comparison of the experimental and numerical results of EDI spray tip penetration in a constant volume chamber @ 6.0 MPa injection pressure, 0.1 MPa ambient pressure and 350 K ambient temperature

The verified spray model was then incorporated into the engine model for simulating the spray combustion process of the EDI+GPI engine. It simulated the process starting from GPI injection (410 CAD BTDC) and ending at the exhaust top dead centre (360 CAD ATDC). The ECFM combustion model was properly tuned by acting on the ITNFS term so that the simulated in-cylinder pressure would match the experimental data. To verify the engine combustion model, comparison was made between the numerical and experimental values of the in-cylinder pressure and heat release rate. As shown in Figure 3.16, the simulated cylinder pressure and heat release rate, including their magnitudes and phases, agree well with the measured data from the engine experiments. As the ethanol ratio increases to E76, the simulated in-cylinder pressure increases slightly more quickly than the measured one does after the spark timing. However, the starting phase and the magnitude of the heat release rate of the simulated curve still match with the measured one at E76. The errors of the simulated peak heat release rate value and its phase are within 0.5% and 2.0% respectively at E76. Therefore, the accuracy of the simulation is considered within the acceptable limit considering the current development of dual-fuel combustion modelling.

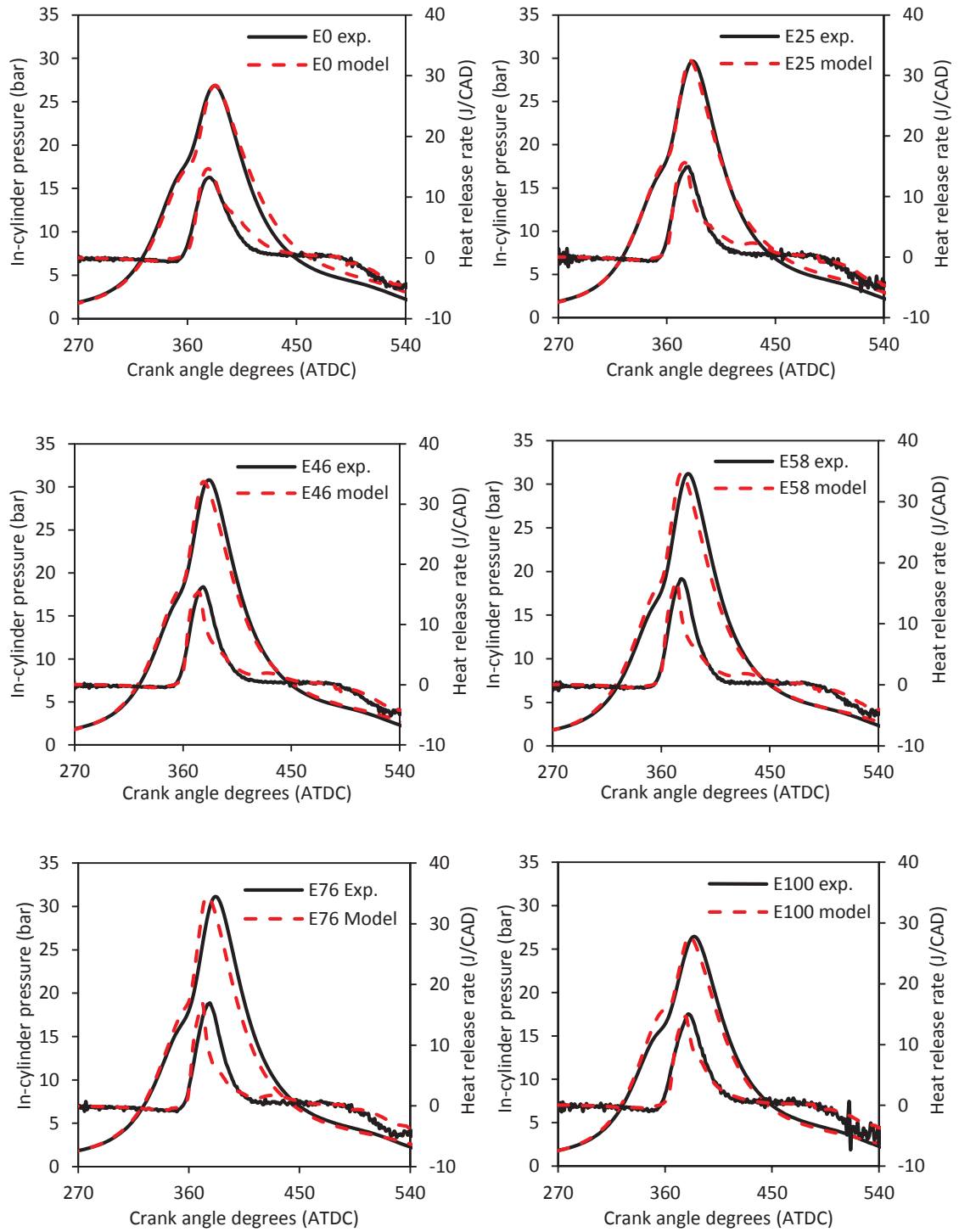


Figure 3.16: Comparison between the measured and simulated values of in-cylinder pressure and heat release rate at different ethanol ratios

3.3 Test rig for investigating EDI heating

3.3.1 Engine setup and ethanol heating

The experiments were conducted on a single-cylinder four-stroke air-cooled SI engine equipped with an EDI+GPI fuel system. Figure 3.17 shows the schematic of the engine test bench and Table 3.1 gives the specifications of the engine. The original engine was a port fuel injection engine which was used on the Yamaha YBR250 motorcycle. It was modified to EDI+GPI engine by adding an EDI fuel system to the engine. The EDI injector was a six-hole injector with a nozzle diameter of 110 μm . The spray cone angle is 34° and the bent angle is 17° . The EDI injector was mounted with spray plumes bent towards the spark plug to create an ignitable mixture around the spark plug. The tip of the injector was placed 15 mm to the spark plug on the intake valve side. The GPI injector was the original port fuel injector used in the Yamaha YBR250 motorcycle. Both the GPI injector and EDI injector were controlled by an electronic control unit. The EDI+GPI fuel system offers the flexibility to operate the engine over a full range of ethanol ratio from 0% (GPI only) to 100% (EDI only).

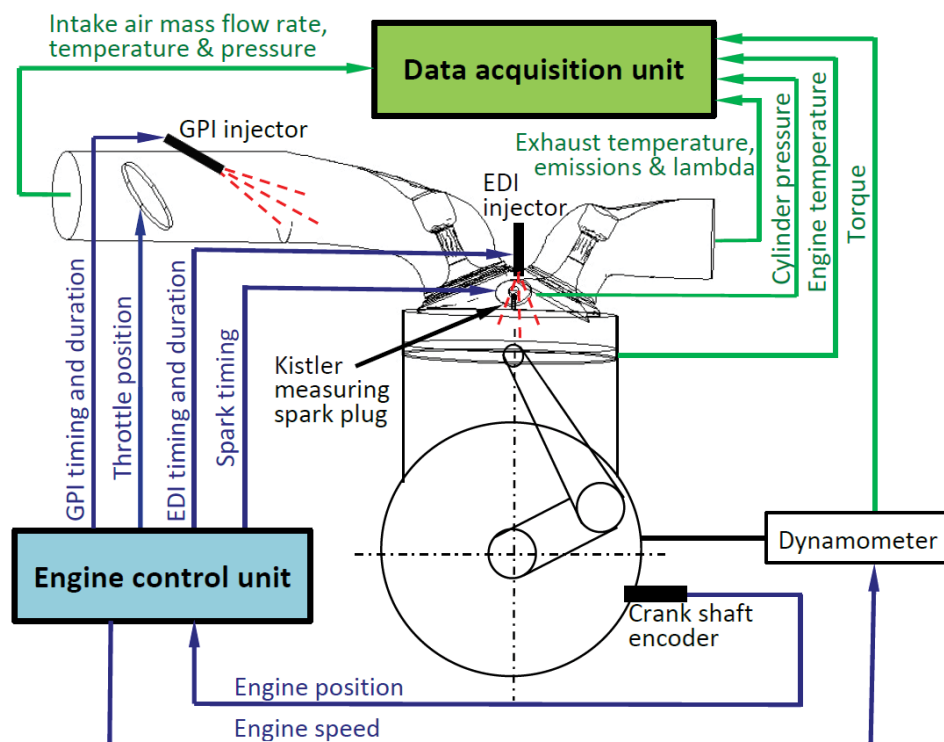


Figure 3.17: Schematic of the EDI+GPI engine

Table 3.1: Specifications of the EDI+GPI engine

Engine type	Single cylinder, air cooled, four-stroke
Displacement	249.0 cc
Stroke	58.0 mm
Bore	74.0 mm
Connecting rod	102.0 mm
Compression ratio	9.8:1
Intake valve open	22.20 CAD BTDC
Intake valve close	53.80 CAD ABDC
Exhaust valve open	54.60 CAD BBDC
Exhaust valve close	19.30 CAD ATDC
Ethanol delivery system	Direct injection
Gasoline delivery system	Port injection

Figure 3.18 shows the schematic of the fuel heating system. An electronic resistance heater made of Kanthal A1 heating resistance wire was used to heat the ethanol fuel in the high pressure rail. The heater was wrapped on the fuel rail upstream the injector. A T-type thermocouple was attached on the surface of the fuel rail at the entrance of the EDI injector to measure the ethanol fuel temperature. The temperature was fed back to a 2132 Eurotherm PID temperature controller, which controlled the relay of the heating system, so that the heating process stopped when the fuel temperature reached the required value. Therefore, the fuel rail temperature at the injector entrance was regarded as the fuel temperature in the present study. The accuracy of the temperature control was within ± 3 °C.

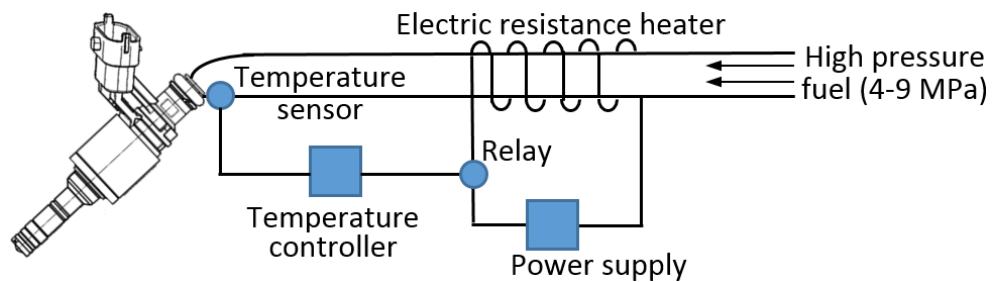


Figure 3.18: Schematic of EDI fuel heating system

3.3.2 Instruments and measurements

The mass flow rate of the intake air was measured with a ToCeil-20N hot-wire thermal flow meter. The engine speed was controlled by an eddy current DC dynamometer. The in-cylinder pressure was measured by a Kistler 6115B measuring spark plug pressure transducer at a resolution of 0.5 crank angle degree. A hundred consecutive cycles of pressure were recorded. The exhaust gas emissions were measured using a Horiba MEXA-584L gas analyzer. It measured the emissions in volume based units (% for CO and ppm for HC and NO). The volume based units were converted to g/kw-h according to the European emission standards [182]. Firstly, the measured dry based emissions were corrected to wet based values. Then the wet based emissions were converted to g/h with the fuel mass flow rate and the gas molecular weights. The emissions in g/h were divided by the engine power to get the specific emissions in g/kw-h.

The gasoline and ethanol fuel mass flow rates were determined by the injection pulse width of the injectors in the engine control unit. The calibration of the injector was carried out by the Hents Technologies Inc. The injected fuel mass was measured at pressure of 4-12 MPa with an interval of 2 MPa and pulse width of 800-4000 us with an interval of 800 us. A fuel injection MAP was generated based on the measurements and was included into the engine control unit. A linear function between the injector's pulse width and fuel mass was derived from the calibration results. The calibration of fuel mass and pulse width showed good and stable linearity at different injection pressures. The EDI injection pressure was controlled by the electronic control unit and the solenoid valve in the high pressure pump.

Measuring the lambda (excess air ratio) of a fuel using an appropriate lambda meter or oxygen sensor requires the information of the fuel chemical composition such as the hydrogen to carbon (H/C) and oxygen to carbon (O/C) atomic ratios. In the present study, the lambda was monitored and kept around one by adjusting the mass flow rates of the gasoline and ethanol fuels at a designated fuel ratio and a fixed throttle position. The Horiba MEXA-584L gas analyzer can measure the lambda of multiple fuels with H/C and O/C ratios of the fuel input by the user. The lambda of the gas analyzer is calculated upon the measurements of CO, CO₂, HC and O₂ using the Equation 3.16 [183].

$$\lambda = \frac{[CO_2] + \frac{[CO]}{2} + [O_2] + \left\{ \left(\frac{H/C}{4} \times \frac{3.5}{3.5 + \frac{[CO]}{[CO_2]}} - \frac{O/C}{2} \right) \times ([CO_2] + [CO]) \right\}}{\left(1 + \frac{H/C}{4} - \frac{O/C}{2} \right) \times \{ ([CO_2] + [CO]) + (K_1 \times [HC]) \}}$$

Equation 3.16

Where [] is the volume based concentration in % for CO₂, CO and O₂ and ppm for HC. K₁ is the conversion factor for HC if expressed in n-hexane (C₆H₁₄) equivalent, which is 0.0006 in this equation. To ensure the accuracy and correction of the lambda value, the lambda measured by the Horiba gas analyzer was also compared with the one calculated using the mass flow rates of the intake air, the ethanol and gasoline fuels.

3.3.3 Test fuels

Table 2.2 lists the main properties of the gasoline and ethanol fuels used in the present study. The gasoline fuel was the Unleaded Petrol (ULP) from the Caltex Australia with an octane number of 91. The ethanol fuel was provided by the Manildra Group, which was mixed with 0.1% of gasoline fuel.

3.3.4 Engine experiment conditions

The engine was started and warmed up by gasoline port injection only. The experiments were conducted when the engine body temperature became stable at around 200 °C. Then the amount of gasoline was reduced and the ethanol fuel was directly injected into the cylinder to substitute gasoline. Table 3.2 lists the engine conditions investigated in the present study. The experiments were conducted at medium load (IMEP 0.60~0.65 MPa). The tested engine speeds were 3500 and 4000 rpm. In all the tests, the lambda was kept around one. The GPI pressure was 0.25 MPa and the EDI pressure was 4 MPa. The GPI timing was 410 CAD BTDC and EDI timing was 300 CAD BTDC. The ethanol ratio started at E0 and then varied from E25 to E100 with an increment of 15% (E'X' means X% ethanol by volume. e.g. E40 is 40% ethanol by direct injection plus 60% gasoline by port injection). Firstly the experiments were conducted at spark timing of 15 CAD BTDC which was the spark timing in the original engine control system. One of the main advantages of EDI is that it allows more aggressive downsizing technologies without the knock issue, such as higher compression ratio and more advanced spark timing. Therefore,

the effect of EDI heating on engine combustion and emission characteristics was also investigated at the minimum spark advance for best torque (MBT) timing of 19 CAD BTDC.

Table 3.2: EDI heating experiment conditions

Engine speed	3500, 4000 rpm
Ethanol ratio by volume	0%, 25%, 40%, 55%, 70%, 85%, 100%
Spark timing	15 (original), 19 (MBT) CAD BTDC
GPI pressure	0.25 MPa
GPI timing	410 CAD BTDC
EDI pressure	4.0 MPa
EDI timing	300 CAD BTDC
EDI heating temperature	50 (baseline), 70 and 90°C

The experiments were firstly performed without the EDI heating system. The measured ethanol temperature was around 50 °C (± 2 °C). Then the EDI heating system was applied to heat the ethanol fuel to 70 °C and 90 °C. The power required for EDI heating was dependent on the fuel flow rate and the heating temperature. The maximum heating power was about 150 W at E100, 90 °C and 4000 rpm condition, which was about 3% of the engine output power. However, the heater only worked intermittently at this power and the power required was much smaller in lower ethanol ratio conditions. In production engines, the heating energy can be taken from the high-temperature exhaust gas (~400 °C in the present study) and thus eliminate the parasitic load of the heating element in the present experiments.

Since the experiments were conducted at steady conditions (constant engine speed and throttle opening), the variations of the measured data were relatively small. To ensure the accuracy of the results, five samples were recorded at each tested engine condition. The maximum standard deviation of the measurements were 5% for ISCO, 3% for ISNO, 5% for ISHC and 1% for lambda, which indicated acceptable quality of the experimental data and justified the use of averaged sample data for the presented results.

3.3.5 In-cylinder pressure data processing

A number of parameters were calculated from the measured in-cylinder, including the IMEP, heat release rate (HRR), mass fraction burnt (MFB), combustion initiation duration (CA0-10%) and major combustion duration (CA10-90%).

The IMEP is defined by Equation 3.17. It is calculated by integrating the curve to obtain the area enclosed in the P-V diagram.

$$IMEP = \frac{W_i}{V_d} = \frac{1}{V_d} \oint P dV \quad \text{Equation 3.17}$$

Where W_i is the indicated work per cycle, V_d is the displacement of the engine, P is the measured in-cylinder pressure, V is the volume of the cylinder.

The HRR is defined by Equation 3.18. It is calculated without considering the heat loss through the cylinder walls.

$$HRR = \frac{\gamma}{\gamma-1} P \frac{dV}{d\theta} + \frac{1}{\gamma-1} V \frac{dP}{d\theta} \quad \text{Equation 3.18}$$

Where θ is the crank angle degrees, γ is the specific heat ratio of the in-cylinder gas. γ is chosen as 1.37 for the compression process and 1.30 for the expansion process [89].

MFB is used to indicate the combustion speed and identify the combustion phases. It is calculated based on the logarithmic pressure-volume diagram showing in Figure 3.19 [184]. As shown in Figure 3.19, P_1 is the intersection of the extended compression line and the minimum volume line and P_3 is the intersection of the extended expansion line and the minimum volume line. P_2 is the projection of P_θ on the minimum volume line,

$$P_2 = P_\theta \left(\frac{V}{V_C} \right)^\gamma \quad \text{Equation 3.19}$$

Where V_C is the clearance volume of the combustion chamber. The MFB is then defined as,

$$MFB = \frac{P_2 - P_1}{P_3 - P_1} \quad \text{Equation 3.20}$$

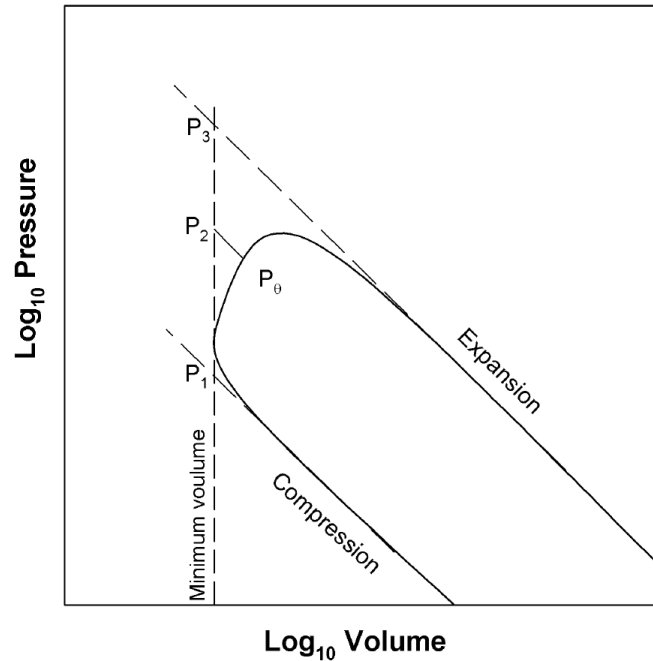


Figure 3.19: logarithmic pressure-volume diagram [184]

The combustion initiation duration, denoted by CA0-10%, is defined as the crank angle degrees from the spark timing to the timing of 10% of MFB. CA0-10% is directly related to the combustion stability and only after CA0-10% does flame velocity reach higher values with the corresponding fast rise in cylinder pressure and flame propagation [81]. The major combustion duration, denoted by CA10-90%, is defined as the crank angle degrees from 10% to 90% of MFB. The shorter is the CA10-90%, the closer the combustion process is to the constant volume and consequently the higher the thermal efficiency will be [81].

Chapter Four

4 EDI Spray Characteristics

This chapter presents and discusses the experimental results of the EDI spray and evaporation characteristics in a constant volume chamber in four sections. Section 4.1 and 4.2 investigate the characteristics of non-evaporating, evaporating and flash-boiling ethanol sprays. The spray images, spray tip penetrations, spray angles, spray projected areas and the evaporation rate represented by the averaged pixel intensity are discussed. In the third section, the transition process from the normal-evaporating to the flash-boiling sprays is investigated. Section 4.4 discusses the implications for engine emissions based on the evaporation characteristics of ethanol fuel.

4.1 Characteristics of non-evaporating and evaporating sprays

Figure 4.1 shows the ethanol spray behaviours in the fuel temperature range from 275 K to 350 K with an increment of 25 K. The saturation vapour pressure of ethanol at 275 K is 1.828 kPa which is relatively low compared with 8.773 kPa at 300 K, 32.092 kPa at 325 K and 95.074 kPa at 350 K. Therefore the spray can be considered as non-evaporating in the temperature of 275 K. As shown in Figure 4.1, the three plume groups are clearly identified when the fuel temperature is 275 K. The plumes are narrow and plume boundary is smooth. The interactions between plume and plume, plume and air are very weak. When the temperature is increased from 275 K to 325 K, the plumes become wider and some swirls start to form at the spray tip. This indicates a stronger interaction between the droplets and ambient gas. However, in general, the spray patterns of 275 K, 300 K and 325 K are rather similar. Spray plumes are narrow and can be clearly identified. Significant changes occur when the fuel temperature is further increased from 325 K to

350 K which is close to ethanol's boiling point 351 K. The plumes become wider and it is difficult to distinguish one plume from the other within 0.5 ms ASOI. The plume-plume and plume-air interactions are more significant. The first and third plume groups move towards the middle one. At the same time, a big swirl is formed at the tip of the third plume. The spray droplets lose their momentum faster, resulting in a shorter penetration. After 4.0 ms ASOI, the spray droplets lose almost all of their momentum floating at the same position in the chamber.

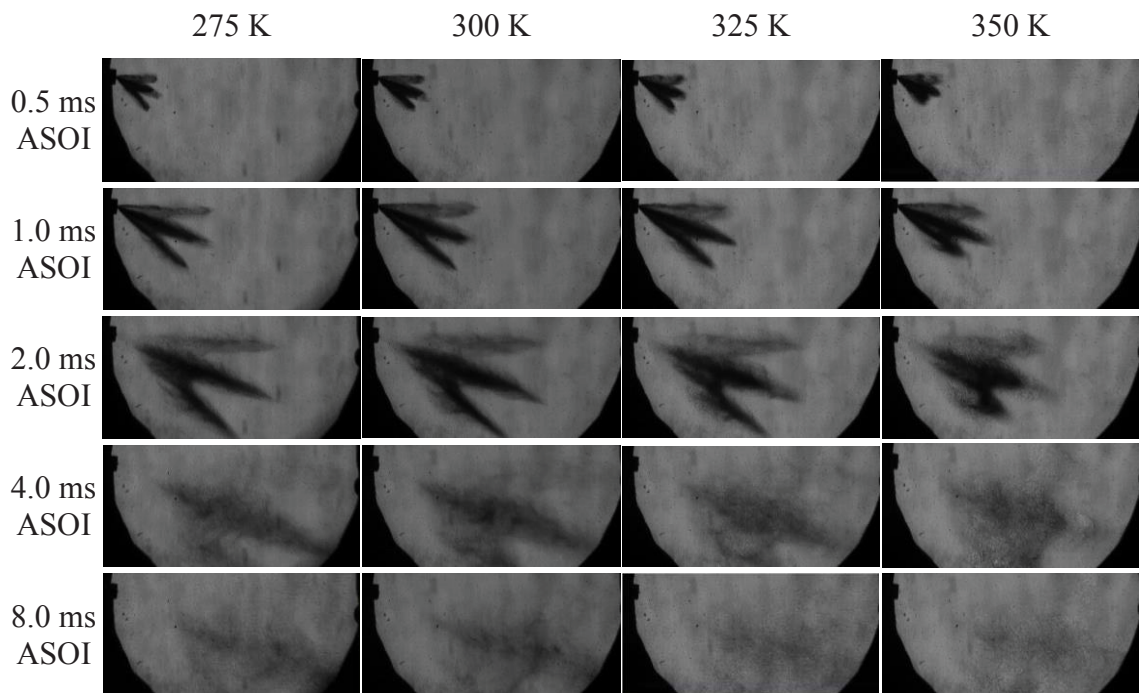


Figure 4.1: Spray images in non-evaporating and evaporating conditions

The effect of the fuel temperature on the spray evaporation process is shown in the images at 8.0 ms ASOI in Figure 4.1. The duration 8 ms is similar to the evaporation time (9.5 ms) allowed for early EDI spray in the engine experiments at EDI timing of 300 CAD BTDC, ignition timing of 15 CAD BTDC, and engine speed of 5000 rpm [8]. Figure 4.1 shows that the colour of the spray area becomes lighter with the increase of the fuel temperature. To make it easier for comparison, the averaged pixel intensity value of the spray area is shown in the Figure 4.2. The averaged intensity values are calculated based on the images without the background noises. The spray area is white with a value ranging from 0 (black) to 255 (white). A larger value means a higher concentration of the spray droplets and thus a lower evaporation rate. The averaged spray area pixel intensity values in Figure 4.2 illustrate the same trend as discussed above for the results in Figure 4.1

(spray patterns are similar for 275 K, 300 K and 325 K sprays, and significant changes occur at 350 K spray). The averaged image pixel intensity of 275 K spray at 8.0 ms ASOI is 10.605. It only reduces slightly to 10.562 and 10.207 when the fuel temperature is increased to 300 K and 325 K respectively. A significant decrease of the pixel intensity to 8.508 is observed when the temperature is further increased to 350 K. Therefore, the evaporation rate of ethanol fuel only increases slightly when the temperature is increased from 275 K to 325 K, but significantly when the temperature is further increased from 325 K to 350 K.

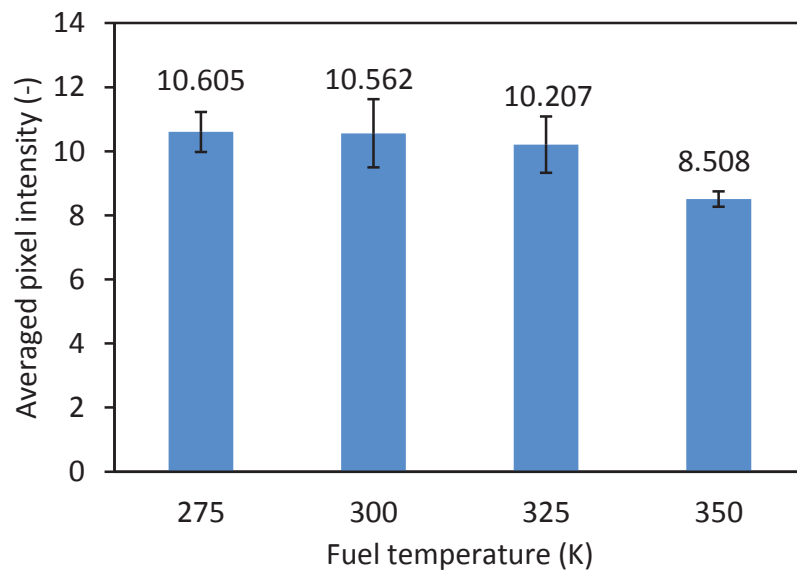


Figure 4.2: Averaged pixel intensity of the spray area at 8 ms ASOI for sprays in non-evaporating and evaporating conditions

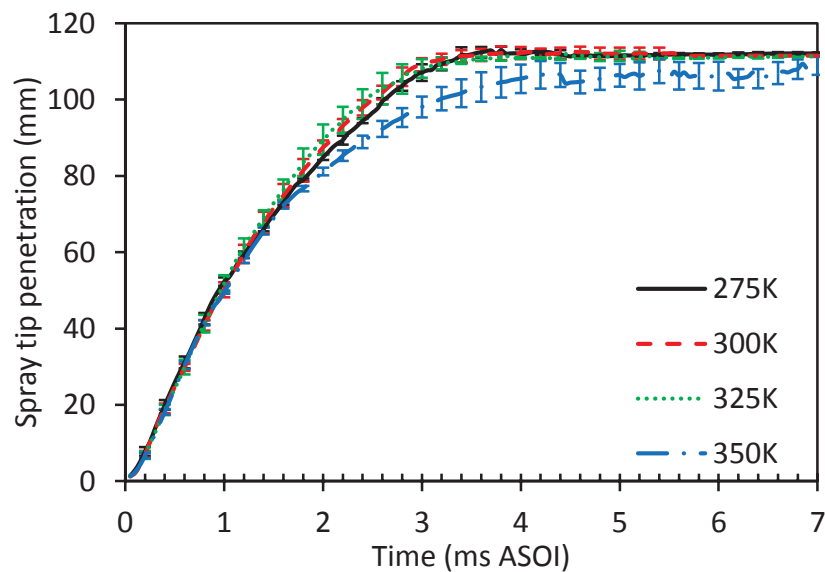


Figure 4.3: Spray tip penetrations in non-evaporating and evaporating conditions

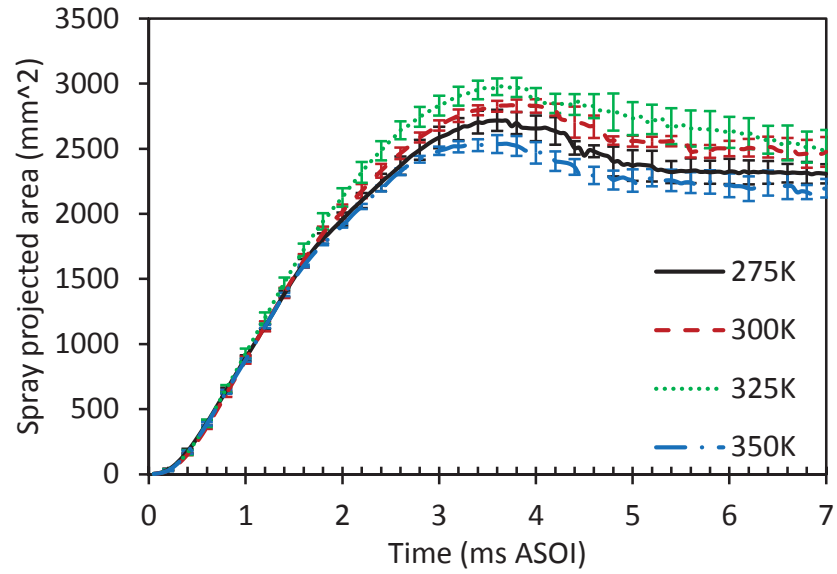


Figure 4.4: Spray projected areas in non-evaporating and evaporating conditions

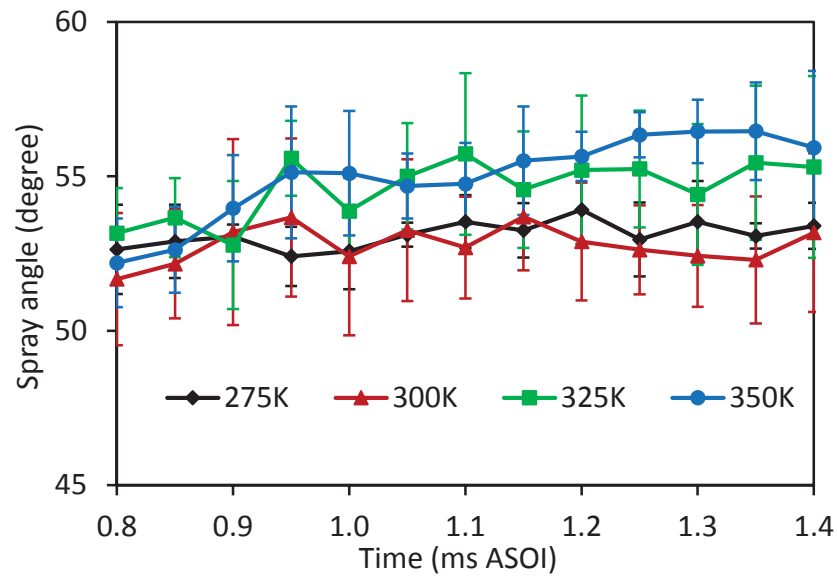


Figure 4.5: Spray angles in non-evaporating and evaporating conditions

Figures 4.3, 4.4 and 4.5 show the macroscopic characteristics of spray tip penetration, spray projected area and spray angle respectively. As shown in Figure 4.3, before 1.0 ms ASOI, the effect of fuel temperature on the spray penetration length is negligible. Then during 1.0-3.0 ms ASOI, the spray tip penetration increases a bit when the fuel temperature is increased from 275 K to 325 K. After 3.0 ms ASOI, they reach the similar penetration length. However the penetration length of 350 K spray is shorter than that of 275 K, 300 K and 325 K sprays. The shorter penetration length of spray at 350 K is due to the higher evaporation rate and stronger air-plume interaction than that at lower

temperatures. The influence of temperature on the fuel sprays can also be shown by the spray projected area. As shown in Figure 4.4, the spray area increases slightly when the fuel temperature is risen from 275 K to 325 K. However when the temperature is further increased from 325 K to 350 K, the spray area decreases noticeably to be smaller than that at 275 K. Regarding the spray angle, the effect of fuel temperature is not very clear. Figure 4.5 shows that the spray angles at 275 K are very similar to that at 300 K. The spray angles increase slightly when the temperature is increased from 300 K to 325 K and 350 K. This is because the stronger plume-air interaction makes the spray plumes wider, which consequently results in bigger spray angles. Nevertheless, the increase of spray angle with temperature is insignificant, which is less than 2° for each 25 K increment.

4.2 Characteristics of flash-boiling sprays

Significant changes occur to the spray patterns when the fuel temperature is higher than the ethanol's boiling point (351 K). Figure 4.6 shows the ethanol spray patterns in flash-boiling conditions. The droplet explosion process can be seen at the injector tip when the first droplets are emanated into the ambient gas at 0.1 ms ASOI, as indicated by the red circles. A small dark spray area is surrounded by a light area. The lighter area is again surrounded by a dark spray area. The droplet explosion process is caused by the fact that the spray droplets are superheated. Figure 4.7 is a schematic diagram demonstrating the explosion process of a droplet in superheated conditions. The heated ethanol droplet will be superheated once it is injected into the low pressure ambient gas. Vapour bubbles may form inside the droplet and burst it into smaller droplets, resulting in the dark and light areas observed.

Compared with 350 K spray in the early spray stages (within 0.5 ms ASOI), the three plume groups of flash-boiling sprays become totally unrecognizable and integrate into a single one. The explosion process makes the air-plume interaction much stronger and the spray boundary becomes more turbulent. The plume-plume interaction is stronger in flash-boiling sprays in late spray development stages. The first and third plume groups collapse towards the middle one. With flash-boiling, the evaporation process is greatly enhanced. As illustrated in Figure 4.8, the averaged spray image pixel intensity value at 8.0 ms ASOI decreases from 8.508 in 350 K to 4.989 in 375 K and 2.149 in 400 K.

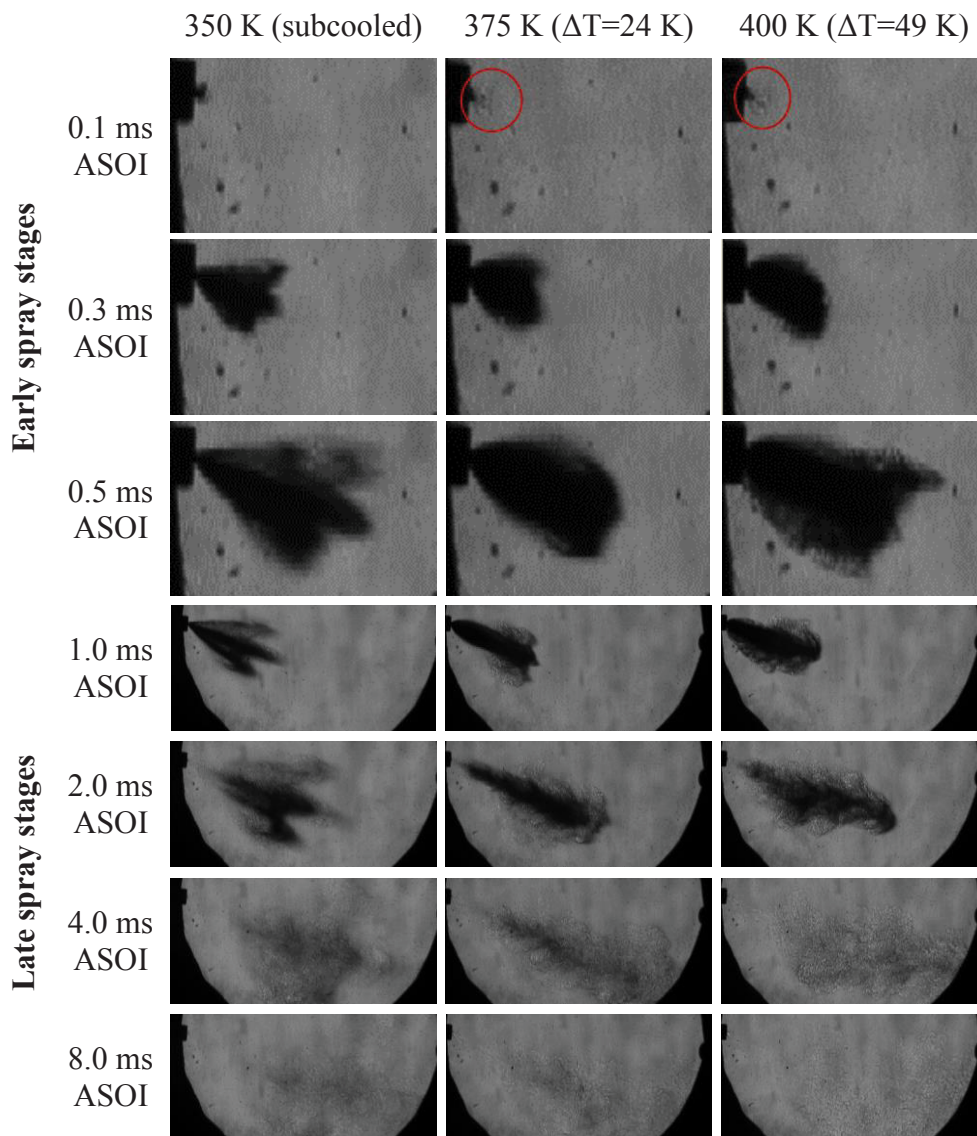


Figure 4.6: Spray images in flash-boiling conditions (Please refer to the electronic version of this figure for a clearer interpretation of the droplet explosion)

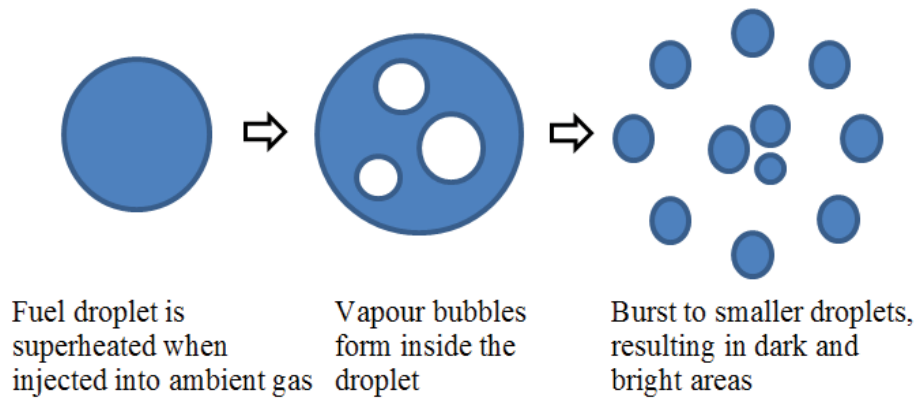


Figure 4.7: Schematic of the droplet flash-boiling process

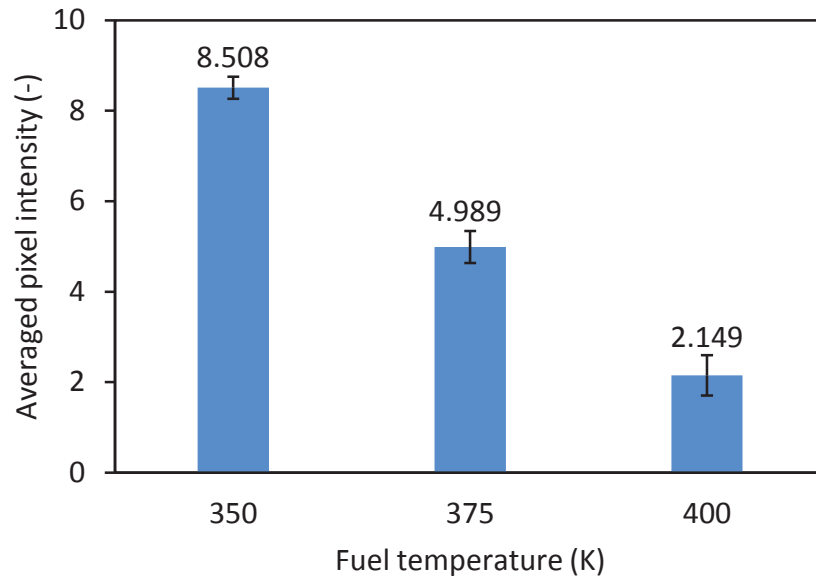


Figure 4.8: Averaged pixel intensity of the spray area at 8.0 ms ASOI for sprays in flash-boiling conditions

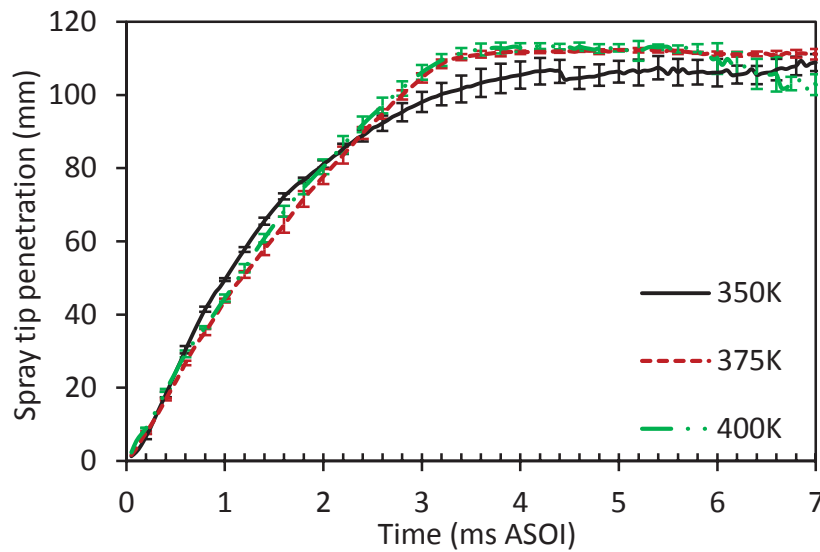


Figure 4.9: Spray tip penetrations in flash-boiling conditions

Regarding the macroscopic characteristics of flash-boiling sprays, as shown in Figure 4.9, the penetration length is shorter than the normal-evaporating spray's before 2.0 ms ASOI, but longer after that because the collapsed spray plumes focus all their momentum into a single direction. The significant faster evaporation rate of flash-boiling spray results in a smaller projected area than normal-evaporating spray's, as shown in Figure 4.10. Particularly, the projected area of 400 K spray at 7.0 ms ASOI reduces to a value of almost zero which means the liquid fuel is fully evaporated. Figure 4.11 shows that the spray

angles of flash-boiling sprays are much smaller than the normal-evaporating spray's because of the spray collapse.

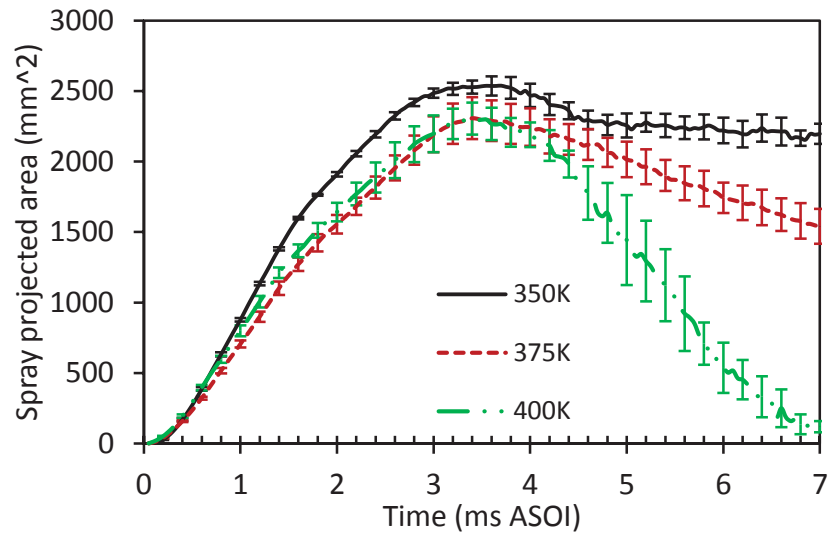


Figure 4.10: Spray projected areas in flash-boiling conditions

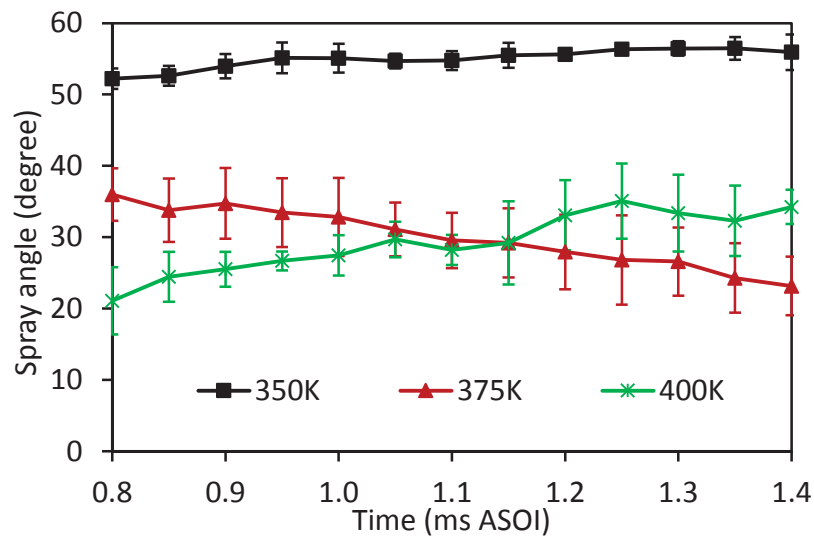


Figure 4.11: Spray angles in flash-boiling conditions

4.3 Spray transition process

Flash-boiling will occur in the condition of ambient gas pressure lower than the fuel saturation vapour pressure when the spray is emanated from the injector to the ambient gas. This phenomenon usually occurs in nozzles working in either high temperature or large pressure drop conditions. In a flash-boiling spray, the evaporating and break-up

rates are greatly increased. As a result, the spray patterns and mixture formation processes are very different to that of normal-evaporating sprays.

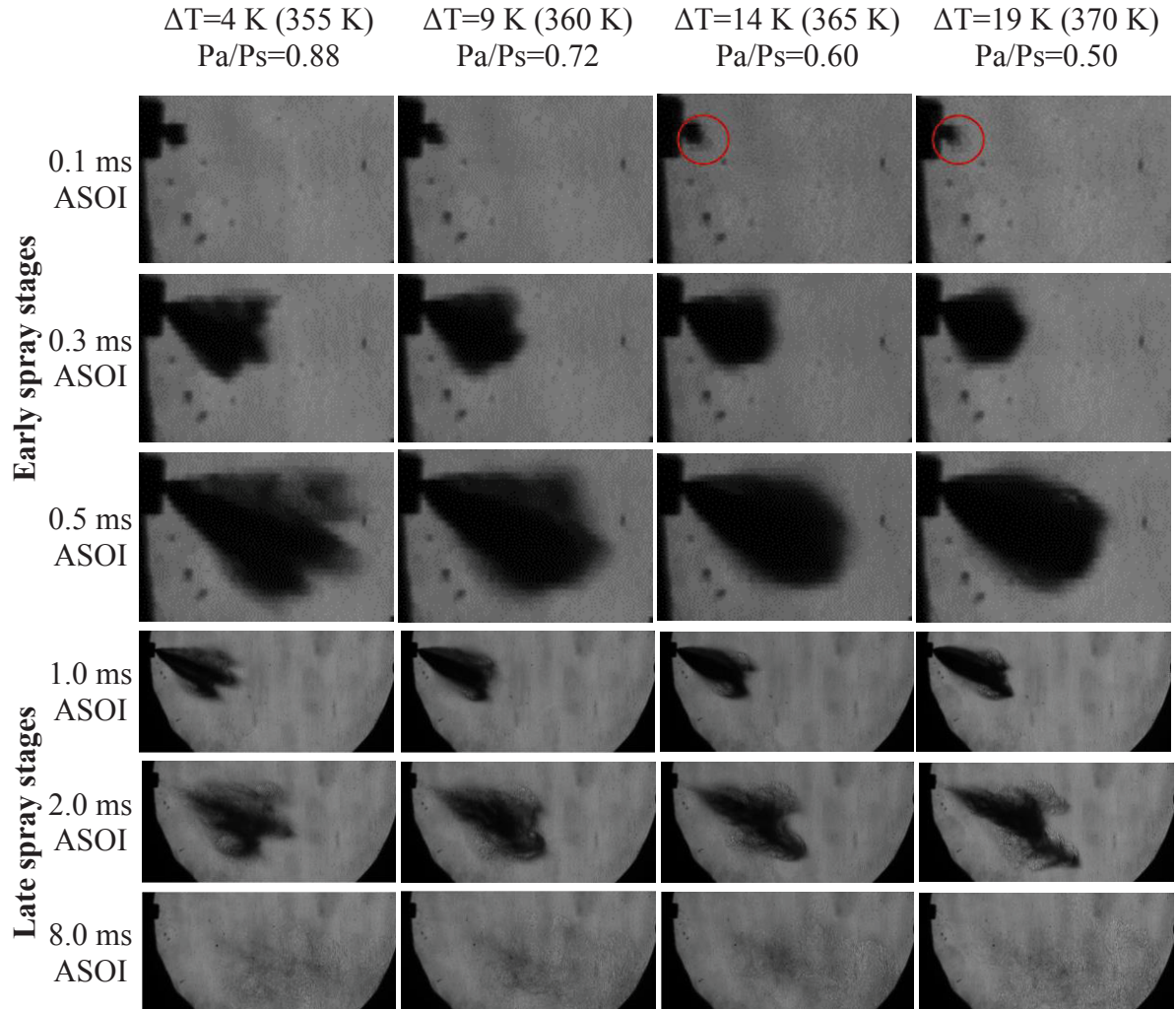


Figure 4.12: Spray images in the transition process (Please refer to the electronic version of this figure for a clearer interpretation of the spray cloud)

Figure 4.12 shows the transition process from a normal-evaporating spray to a flash-boiling spray. The spray excess temperature ΔT is used to quantify the superheat degrees. ΔT is defined as the fuel temperature minus the saturation temperature (351 K in the experimental conditions). Figure 4.12 shows that flash-boiling does not occur as soon as the fuel temperature is higher than the boiling temperature. There is no significant difference in the spray patterns between the sprays of $\Delta T=4\text{ K}$ and 350 K (subcooled). Compared with 350 K spray, the swirl at the tip of the $\Delta T=4\text{ K}$ spray becomes bigger because of the increased plume-air interaction, and the first and third plume groups move more closely to the middle one because of the stronger plume-plume interaction. However

the three plumes can still be recognised at 1.0 ms ASOI for the $\Delta T=4$ K spray. When the ΔT reaches 9 K, the spray collapses completely. The three plumes join together and become unidentifiable. Therefore, the transition temperature of spray collapse at atmospheric pressure is 360 K for ethanol fuel. The spray droplet explosion does not occur until the ΔT reaches 14 K, as indicated by the red circles at 0.1 ms ASOI. When ΔT s are 14 K and 19 K, some spray cloud with a much lighter colour starts to appear at the spray tip. This is because the spray droplets start to evaporate and boil internally. The explosion effect accelerates the breakup and evaporation rates greatly.

The results shown in Figure 4.12 are consistent with that of experiments for superheated water droplets [185]. As reported in [185], when ΔT was below 5 K, the evaporation was on the surface. The droplets started to boil internally when the ΔT was between 5 K and 18 K, but they did not flash and disintegrate until ΔT was above 18 K. Zeng et al. investigated the spray transformation process of n-hexane, methanol and ethanol fuels [109]. They used the ambient-to-saturation pressure ratio (P_a/P_s) to quantify the spray superheat degrees and concluded that flash-boiling occurred at $P_a/P_s=1.0$ and plume collapse occurred at $P_a/P_s=0.3$. However, experiments in this study found that neither flash-boiling nor plume collapse occurred as soon as the fuel temperature was higher than the boiling point ($P_a/P_s=1$). Instead, the spray maintained its structure when the spray was slightly superheated ($\Delta T < 4$ K) and flash boiled when the spray was further superheated ($\Delta T > 14$ K). Recent study in an optical engine showed that spray did not collapse when the P_a/P_s was 0.85, but collapsed when P_a/P_s reached 0.63 [186]. The spray flash boiled before it collapsed in Zeng's experiments was mainly because the injector had a relatively big angle of 60° between the plume axes, while the spray angle of the injector used in the present study was only 17° . This implies that the temperature of spray collapse is dependent on the spray angle of the injector, so that injectors with larger spray angles have higher spray collapse temperatures.

4.4 Implications for engine emissions

Figures 4.2 and 4.8 show that the evaporation of ethanol fuel only increases slightly when the fuel temperature is increased from 275 K to 325 K, but significantly from 325 K to 400 K. As the evaporation process affects the consequent combustion and emission generation significantly, the slow evaporation rate of ethanol fuel in low temperature

environment must be taken into account in developing the EDI+GPI engine. Experimental results on an EDI+GPI engine showed that the CO and HC emissions increased when EDI was applied [8]. The low compression ratio 9.8 and high engine speed 3500-5000 rpm indicated low temperature environment and short time for fuel evaporation. However experiments on a same dual-injection fuel system reported the decrease in CO and HC emissions with EDI, in which the engine had a higher compression ratio of 11.5 and lower engine speed of 1500 rpm [9, 43]. The injection timing was 300 CAD BTDC in [8] and 280 CAD BTDC in [9, 43]. The unfavourable conditions (short time and low temperature) for EDI evaporation in [8] would have caused the increased CO and HC emissions. Numerical studies showed that the evaporation rate of EDI was lower than that of gasoline in naturally aspirated spark ignition engines [121, 122]. However the simulated evaporation rate of ethanol was as high as that of gasoline in a turbocharged engine [123]. These results suggest that EDI should only be applied in high temperature engine environments, such as high compression ratio, full-load or turbocharged engines, to improve the fuel evaporation and mixture preparation processes and consequently avoid the increased CO and HC emissions.

4.5 Summary

The high speed shadowgraphy imaging technique was used to investigate the effect of fuel temperature on the EDI spray characteristics in a constant volume chamber. The experiments covered a wide range of fuel temperature from 275 K (non-evaporating) to 400 K (flash-boiling). Particularly the transition process of the ethanol spray from normal-evaporating to flash-boiling was investigated. The major results of this chapter can be concluded as follows.

- 1) The interactions between the plumes and between the plume and air were enhanced by the increased fuel temperature. With the increase of fuel temperature, the plumes became wider, the spray boundary became more turbulent, and the first and third plume groups collapsed towards the middle one.
- 2) The evaporation rate did not improve much when the fuel temperature was increased from 275 K to 325 K. Significant increase of evaporation rate occurred when the fuel temperature was higher than 350 K. The evaporation process was finished within 8.0 ms ASOI when the temperature reached 400 K. The low

evaporation rate of ethanol fuel in low temperature environment implied that EDI should only be applied in high temperature engine environment.

- 3) The macroscopic characteristics of non-evaporating sprays were similar to that of normal-evaporating sprays at temperatures lower than ethanol fuel's boiling temperature. Significant changes occurred with flash-boiling sprays. The spray tip penetration became slightly longer, while the spray angle and projected area became much smaller.
- 4) The flash-boiling (droplet explosion) did not occur when the fuel temperature was higher than the boiling point until the excess temperature reached 14 K. When excess temperature was smaller than 4 K, the spray behaved the same as subcooled spray did. The spray collapsed at excess temperature of 9 K. The spray collapse temperature was dependent on the spray angle of the injector, where injectors with larger spray angles had higher transition temperatures.

Chapter Five

5 Mixture Formation and Cooling Effect of EDI+GPI

This chapter presents and discusses the simulation results of the mixture formation and cooling effect of EDI+GPI in three sections. The first section demonstrates the fuel sprays of both EDI and GPI at the ethanol ratio of 46%. Spatial and temporal distributions of the fuel in vapour and liquid phases are visualized and analysed. In the second section, the cooling effect of EDI is analysed by comparing the numerical results of three operation modes, GPI only E0, EDI+GPI E46 and EDI only E100. The charge cooling effect is evaluated by the mean and spatial distribution of the in-cylinder temperature, the temporal variation of the evaporated fuel mass, and the latent heat required for the fuel evaporation. Finally, the effect of ethanol ratio on the charge cooling effect is discussed. The ethanol ratio is volume based and indicated by E'X'. For example, E46 means 46% ethanol via direct injection plus 54% gasoline via port injection.

5.1 EDI+GPI sprays

Figure 5.1 shows the spatial distributions of the spray droplets and the air flow velocity vectors of EDI+GPI E46 condition on the engine symmetry plane at the intake TDC (a), the end of GPI injection (b), 15 CAD after the start of EDI (c), and the spark timing (d). The red dots stand for the ethanol droplets and blue dots represent the gasoline droplets. It shows clearly that two horizontal swirls form near the cylinder wall during the intake stroke. The swirls keep moving towards each other and integrate into a larger one in the late compression stroke. The swirls have significant effects on the evolution of EDI and GPI sprays. Optical experiments proved that the PI spray particles followed the gas flow once the velocity was greater than 40 m/s [73]. In the present study, the air flow rate in the intake manifold is relatively small until the intake valve opens (IVO). Therefore the

GPI spray injected at 410 CAD BTDC (42 CAD before IVO) can maintain its plume shape during the early GPI injection process (Figure 5.1(a)).

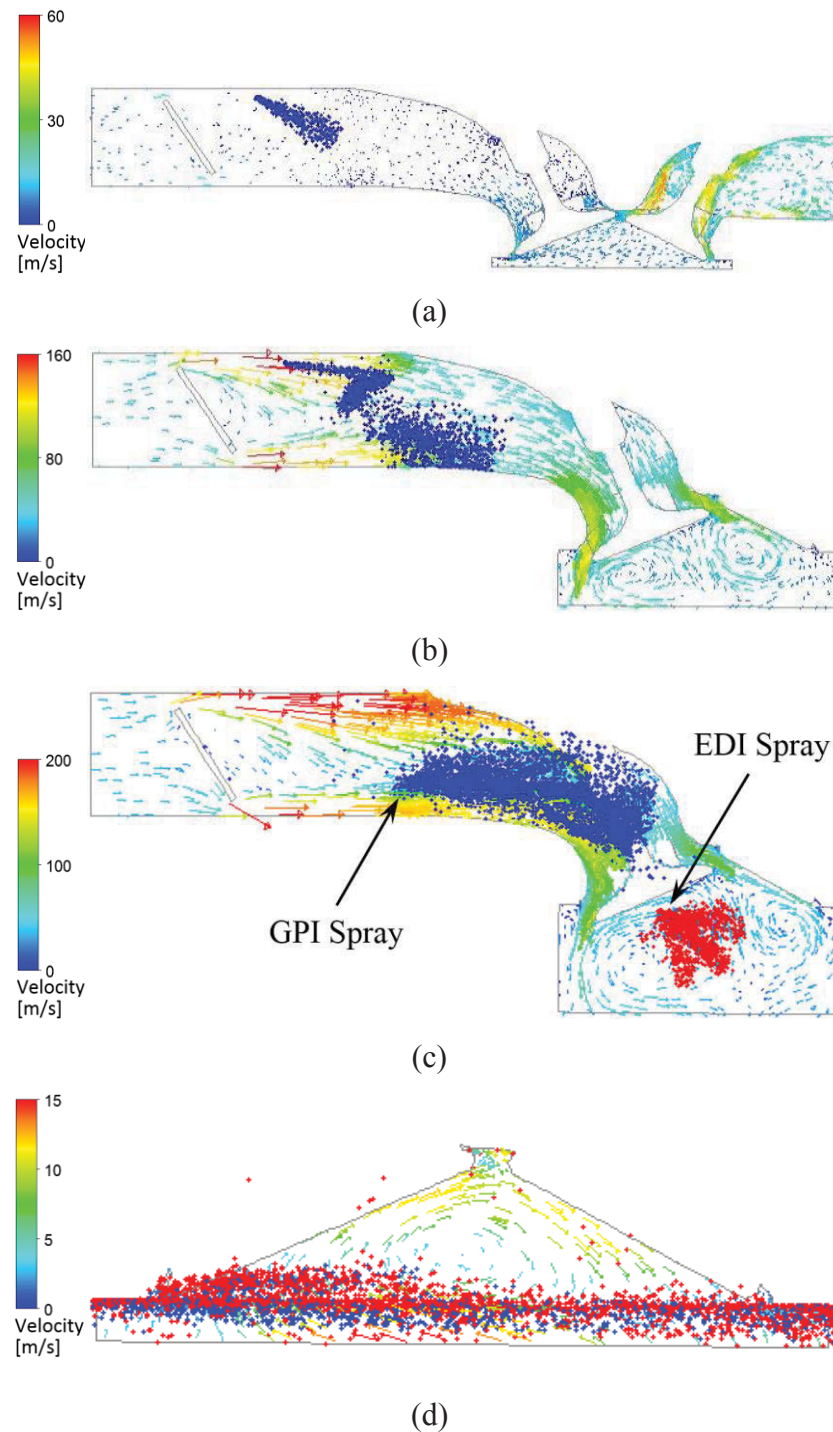
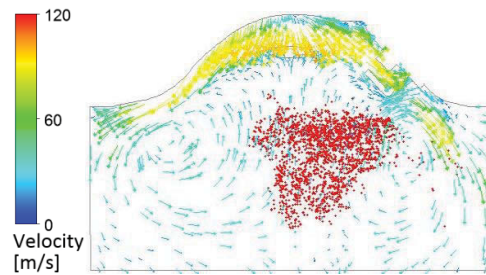


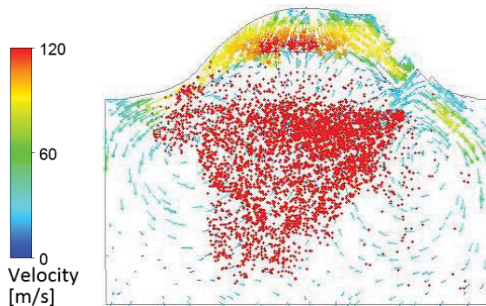
Figure 5.1: Spatial distributions of spray droplets and air flow velocity vectors on the engine symmetry plane of EDI+GPI E46 at: (a) the intake TDC, (b) the end of GPI injection, (c) 15 CAD after the start of EDI, and (d) at the spark timing

In the late GPI injection process, the intake air flow rate increases to as high as 200 m/s when the intake valve is fully open. This consequently leads to the deformation of the

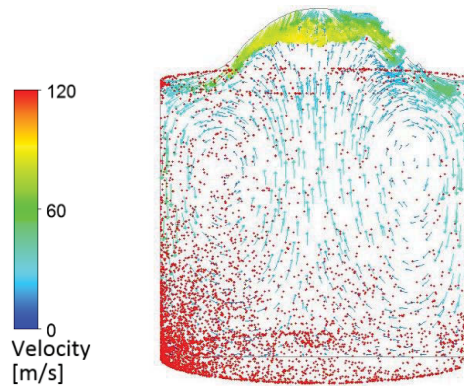
GPI spray shape (Figure 5.1(b)). The spray plume hits the lower wall of the manifold and then bounces back into the intake air flow. While mixing with the air, the gasoline droplets flow into the cylinder. It can also be seen from Figure 5.1(c) that more gasoline droplets are entering into the cylinder through the space between the exhaust and intake valves (right side of the intake valve in the figure).



(a)



(b)



(c)

Figure 5.2: Structure of the EDI spray at: (a) 15 CAD after the start of EDI injection, (b) the end of EDI injection and (c) the BDC

Unlike the GPI spray which can maintain its plume shape in the early injection stage, the EDI spray interacts with the ambient gas more significantly. As shown in Figure 5.2, the EDI spray plumes deform as soon as the ethanol fuel is injected into the cylinder. The two intake air swirls entrain the ethanol fuel droplets everywhere inside the cylinder. This

should increase the heat and mass transfer between the liquid fuel droplets and the ambient gas, thus accelerate the fuel evaporation and enhance the mixing. Compared with gasoline droplets, ethanol droplets are more concentrated at the lower left corner in the cylinder because of their larger initial momentum and injection direction. Following that until spark timing, most of the gasoline droplets have evaporated but some ethanol droplets were remained in the left bottom concern inside the cylinder (Figure 5.1(d)). This is because the saturation pressure of gasoline is higher than that of ethanol in low temperature conditions and will be discussed in more details in the next section.

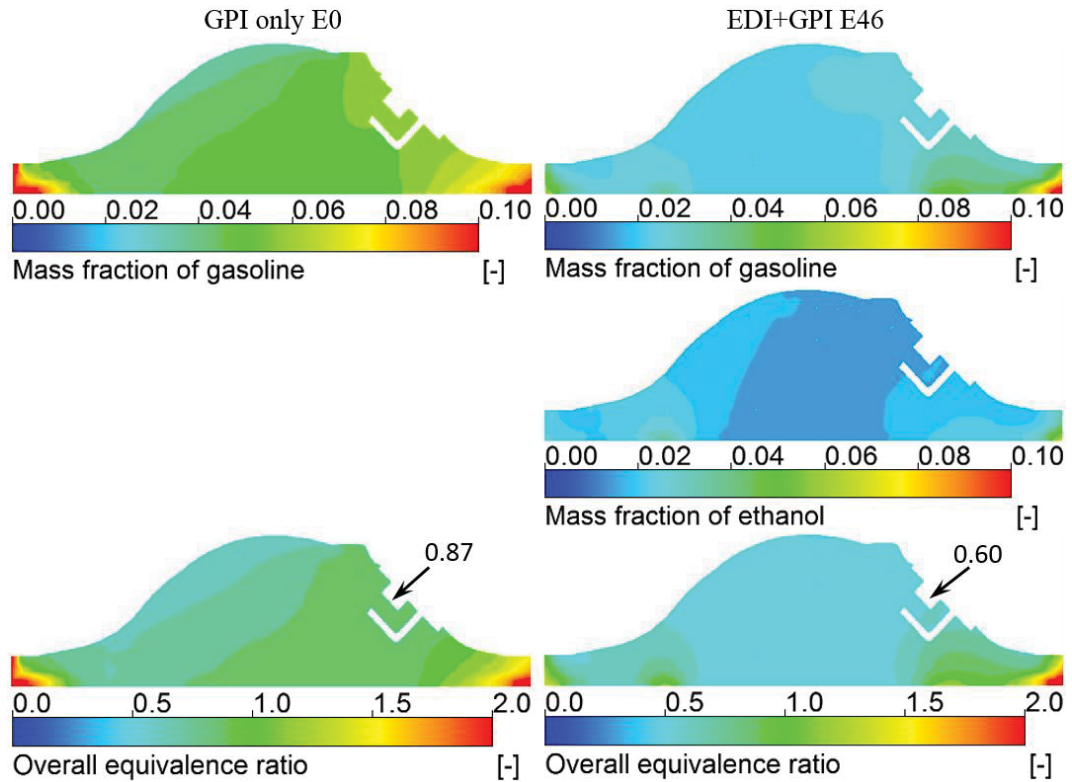


Figure 5.3: Distributions of gasoline and ethanol fuel mass fractions and overall equivalence ratio by spark timing

Ignitability of the mixture around the spark plug at the spark timing is critical for SI engines. It is defined by a fuel/air equivalence ratio of $0.5 < \Phi < 1.5$ [140]. Figure 5.3 shows the distributions of the mass fractions of gasoline and ethanol fuels and the overall equivalence ratio on a vertical plane passing through the spark plug by spark timing. The overall fuel/air equivalence ratio is defined as follows,

$$\Phi = \frac{Y_{C_2H_6O} \cdot (O/F)_{C_2H_6O} + Y_{C_8H_{18}} \cdot (O/F)_{C_8H_{18}}}{Y_{O_2}} \quad \text{Equation 5.1}$$

Where $Y_{C_2H_6O}$, $Y_{C_8H_{18}}$ and Y_{O_2} are the local mass fractions of ethanol, gasoline and oxygen in each cell, $(O/F)_{C_2H_6O}$ and $(O/F)_{C_8H_{18}}$ are the stoichiometric oxygen/fuel ratios of ethanol and gasoline fuels. As shown in Figure 5.3, the equivalence ratio is 0.87 at the plug position in GPI only condition. This ratio is close to the stoichiometric ratio of one and favorable for ignition and flame propagation. However the equivalence ratio is only 0.60 which is very lean in EDI+GPI condition, but still in the range of defined ignitability. This is caused by the low evaporation rate of ethanol fuel in low temperature environment before combustion. The numerical results in Figure 5.5(a) show that, by the time of spark, 94.3% (12.630/13.400 mg) of the gasoline fuel has evaporated in the GPI only condition, while the evaporation rates are 90.1% (7.655/8.500 mg) and 61.8% (4.947/8.000 mg) for gasoline and ethanol fuels respectively in the EDI+GPI E46 condition.

5.2 Cooling effect of EDI

The enthalpy of vaporisation of ethanol fuel is triple gasoline's. Therefore EDI+GPI has more charge cooling potential than GPI only does. The cooling effect is evaluated by comparing the mass averaged in-cylinder temperature values between the cases of GPI only E0, EDI+GPI E46 and EDI only E100 where E0 is used as the baseline for comparison. Variation of the evaporated fuel mass with time will be analyzed to understand the difference in cooling effect of the three operation modes.

Figure 5.4 compares the cooling effect enhanced by EDI. Figure 5.4(a) shows the mass averaged in-cylinder temperature in the three cases in one engine revolution ended at spark timing. Figure 5.4(b) shows the corresponding temperature difference which is the temperature of E0 minus that of E46 or E100. As shown in Figure 5.4(a), the temperature difference between the three conditions is negligible before the EDI injection starts, showing that the quantity of gasoline injected has little effect on the in-cylinder temperature during this time period. This is because the gasoline fuel droplets have not entered the cylinder yet until 70 CAD ATDC which is after the EDI starts. The cooling effect enhanced by EDI is evidenced by the rapid temperature drop after EDI starts at 300 CAD BTDC. For E46 condition, the temperature drop reaches four degrees at the time of about 30 CAD after the start of EDI. Then the temperature drop slows down before it rises rapidly again at the end of the compression stroke. While for E100 condition, the temperature drop increases a bit once the ethanol is injected into the cylinder, and then it

decreases to 0 K at about 40 CAD after the start of EDI. This is because more gasoline fuel is injected in GPI only mode than that injected in EDI+GPI mode to keep the stoichiometric equivalence ratio. However most of the gasoline droplets do not evaporate in the intake manifold because of the relatively low temperature and large droplet size. Instead they evaporate inside the cylinder and absorb the thermal heat from the cylinder gas, thus lead to the decrease of the temperature drop. At the end of compression stroke, the increased cylinder temperature accelerates the ethanol evaporation and enhances the temperature drop again.

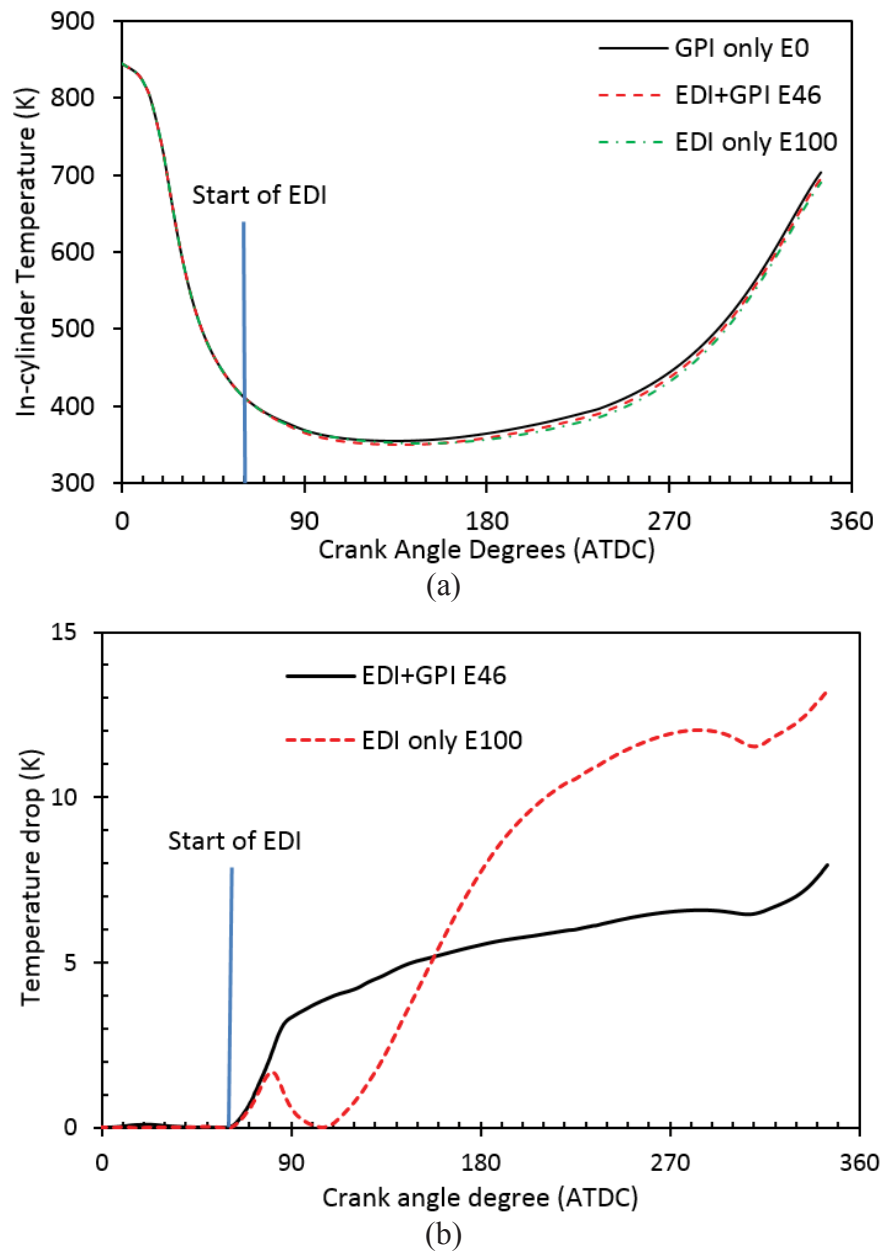
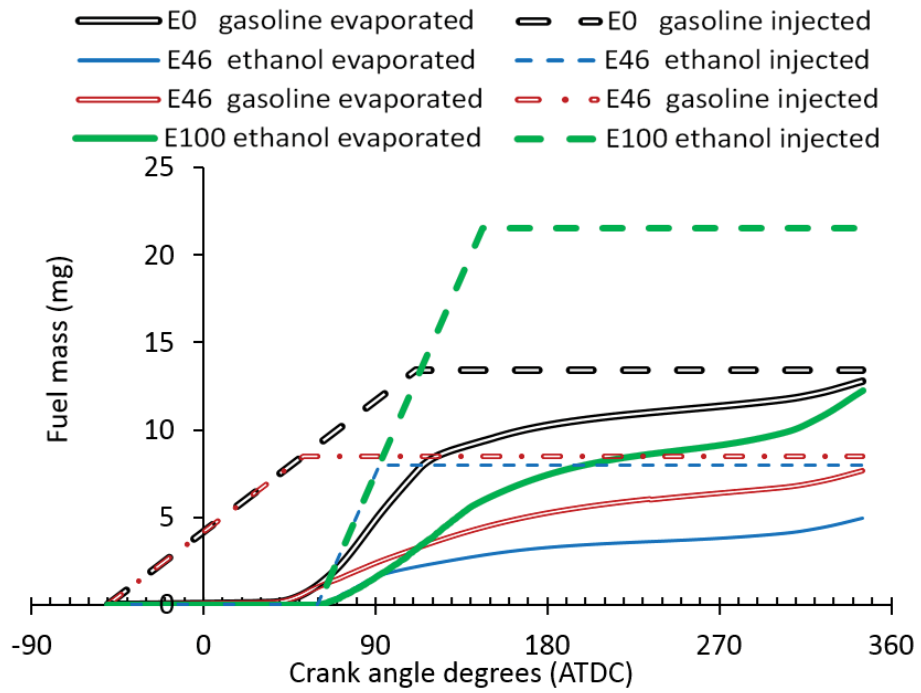


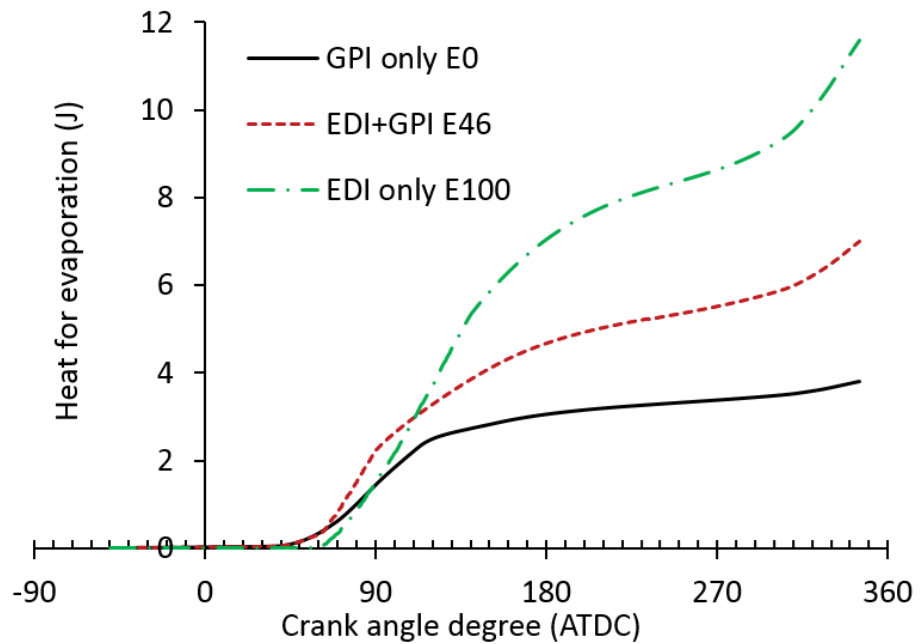
Figure 5.4: Cooling effect enhancement of EDI: (a) comparison of in-cylinder mean temperature in E0, E46 and E100 conditions, (b) the temperature reduced by EDI

Figure 5.5 shows the mass of injected and evaporated fuels (a) and the latent heat for their evaporation (b) varied with time in E0, E46 and E100 conditions. As shown in Figure 5.5(a), for the port injected gasoline fuel in both GPI only and EDI+GPI E46 conditions, most of the gasoline droplets have evaporated during the intake stroke and only a small percentage of liquid fuel (~30%) is left to evaporate in the compression stroke. The simulated results in the present study agrees well with the conclusion in the experiments reported in [101], which found that the temperature rise of port injection of gasoline-ethanol blends was only 1–6% lower than that of the no-fuelling condition. It was concluded that only a small amount of liquid fuel was evaporated in the compression stroke. The ethanol fuel's enthalpy of vaporisation (948 kJ/kg) is 218% greater than gasoline's (298 kJ/kg). It leads to the decrease of in-cylinder temperature at the beginning of EDI. From 100 to 300 CAD ATDC, the cylinder temperature is about 350 K. The evaporation rate of ethanol droplets is slow in this low temperature environment. In comparison, the gasoline fuel injected by GPI evaporates more quickly. Consistently shown in Figure 5.4(b), the difference in cylinder temperature between the three modes rises slowly during the same time period. However, this temperature difference increases quickly again after 300 CAD ATDC. This is because that the cylinder temperature raises rapidly to be above 500 K and the evaporation rate of ethanol fuel rises with the increased temperature. By the time of spark, 94.3% of the injected gasoline has evaporated in E0, while the evaporation rates are 90.1% and 61.8% for gasoline and ethanol fuels respectively in the E46 condition and 56.8% for the ethanol fuel in the E100 condition.

The temperature drop in Figure 5.4(b) is consistent with the variation of the latent heat of the evaporated fuels as shown in Figure 5.5(b). The absorbed heat is equal to the enthalpy change during vaporisation. Figure 5.5(b) shows that the heat absorbed in E46 exceeds that in E0 once the ethanol fuel is injected into the cylinder. While in E100 condition, the absorbed heat by the fuel is less than that in GPI only before 90 CAD ATDC. This explains the small peak with temperature drop increased until 80 CAD ATDC and then fell down to 0 K at 100 CAD ATDC in Figure 5.4(b). At the end of the compression process, the thermal energy absorbed by evaporating ethanol increases rapidly, leading to the faster temperature drop shown in Figure 5.4(b).



(a)



(b)

Figure 5.5: Mass of the injected and evaporated fuels (a) and the enthalpy for their evaporation (b) in E0, E46 and E100 conditions

The results in Figures 5.4 and 5.5 can be explained by Figure 5.6 which shows the saturation vapour pressures of gasoline and ethanol fuels. Saturation vapour pressure is

an important factor indicating the liquid's volatility and it is the driving force for the droplet evaporation process incorporated in the Convection/Diffusion Controlled Evaporation Model. As gasoline fuel is comprised mostly of organic compounds ranging from C2 to C14, its vapour pressure is higher than that of ethanol fuel in lower temperature (< 375 K) conditions because of the low boiling components [114, 119]. However, the vapour pressure of ethanol fuel becomes higher than that of gasoline when the temperature is greater than 375 K. Therefore, ethanol vaporises more quickly than gasoline does in higher temperature conditions [120, 187]. The poor evaporation and mixing of ethanol droplets in ethanol fuelled engines was also reported in [122]. It might be caused by ethanol's low evaporation rate when the temperature was low.

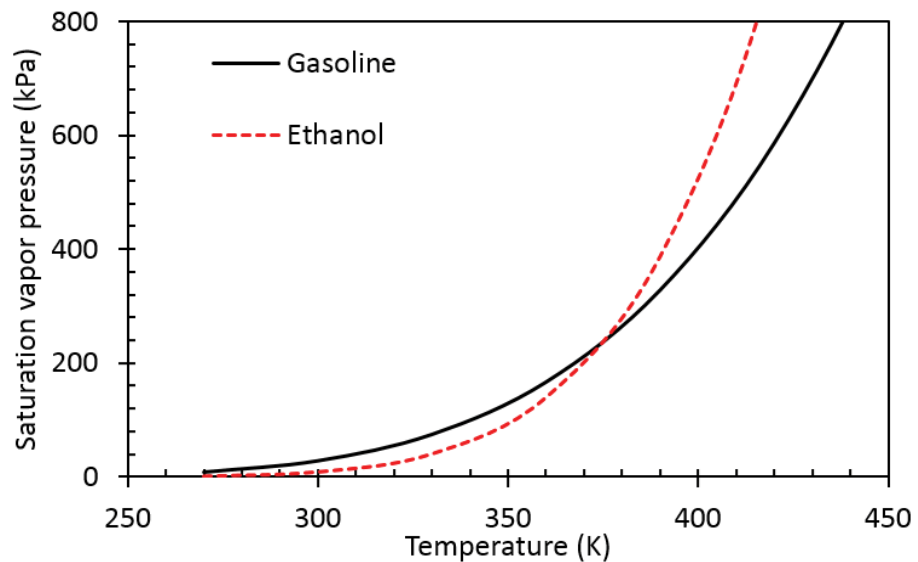


Figure 5.6: Saturation vapour pressures of gasoline [101] and ethanol [100] fuels

Figure 5.7 shows the temperature distribution of E0, E46 and E100 conditions on a vertical plane passing through the centreline of the spark plug at spark timing. Compared with E0, the lighter colour in E46 and E100 conditions indicates the lower temperature due to the cooling effect enhanced by EDI. Particularly, the temperature in the right side of the combustion chamber is noticeably lower than that in the rest region in EDI+GPI, as shown in Figures 5.7(b) and 5.7(c). The results in Figure 5.2 may explain it. As shown in Figure 5.2, the ethanol fuel is directly injected toward this corner and results in richer mixture and more fuel evaporation in this region. With EDI injection, the lower cylinder temperature should reduce the NO emission. As reported in the EDI+GPI engine experiments [8], the NO emission decreased from 1.90 to 1.49 g/kW·h when the ethanol

content was increased from 0% to 60% at 4000 rpm and medium load (36% throttle). In the present study, the cylinder temperature is 8 K lower in E46 and 13 K lower in E100 than that in E0 by the time of spark. This explains why the NO emission was reduced in the experiments.

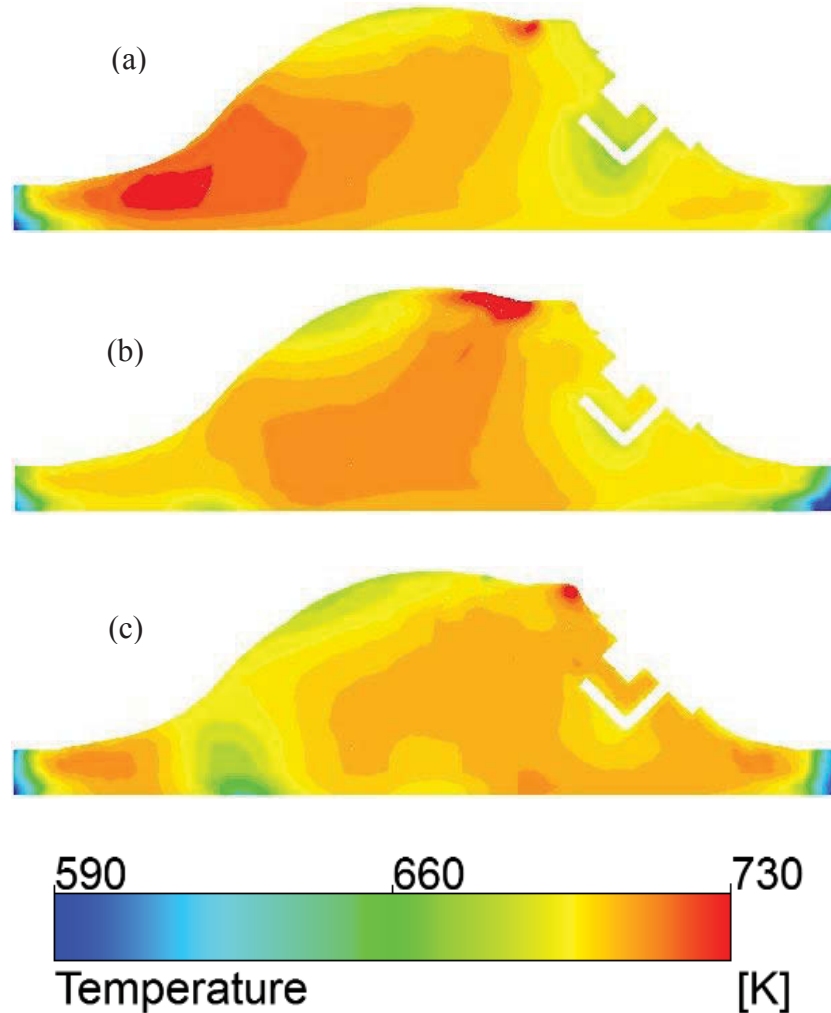


Figure 5.7: In-cylinder temperature distribution on a vertical plane passing through the spark plug predicted for GPI only E0 (a), EDI+GPI E46 (b) and EDI only E100 (c) conditions at the spark timing

Figure 5.8 illustrates the temperature distributions on a horizontal plan cut below the spark plug at spark timing in E0, E46 and E100 conditions. Consistently the lighter colour in Figures 5.8(b) and 5.8(c) shows that the temperature is lower in EDI+GPI mode than that in GPI only mode (Figure 5.8(a)). Particularly the temperature in the region next to the cylinder wall is cooled more significantly by EDI. The near-wall region under the exhaust valve (right side in Figure 5.8) is over cooled to a very low temperature (~ 500 K) by the spark timing. The lower temperature region is where the ethanol droplets are

concentrated in. The ethanol droplets evaporate and absorb the thermal heat from this region. As a result, this region has lower temperature (Figure 5.8) and richer mixture (Figure 5.3) than other regions.

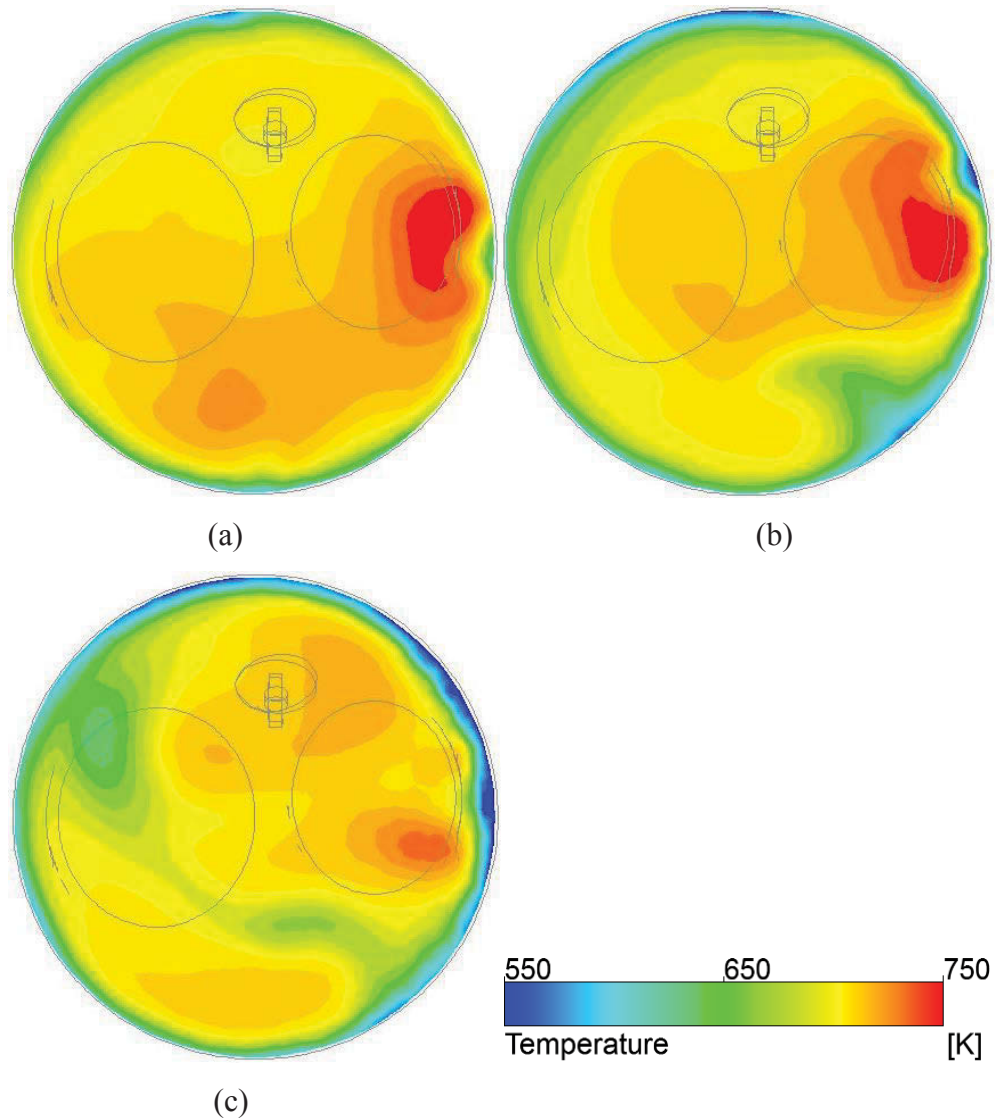


Figure 5.8: In-cylinder temperature distribution on a horizontal plane predicted for GPI only E0 (a), EDI+GPI E46 (b) and EDI only E100 (c) conditions at the spark timing

5.3 Effect of ethanol ratio on charge cooling

In direct injection engines, the heat and mass transfer processes limit the completeness of cooling effect that can be extracted from the enthalpy of vaporisation of the fuel. Experiments showed that the load and intake air temperature influenced the charge

cooling effect [146]. The cooling effect in an EDI+GPI engine enhanced by EDI is also dependent on the ethanol/gasoline ratio.

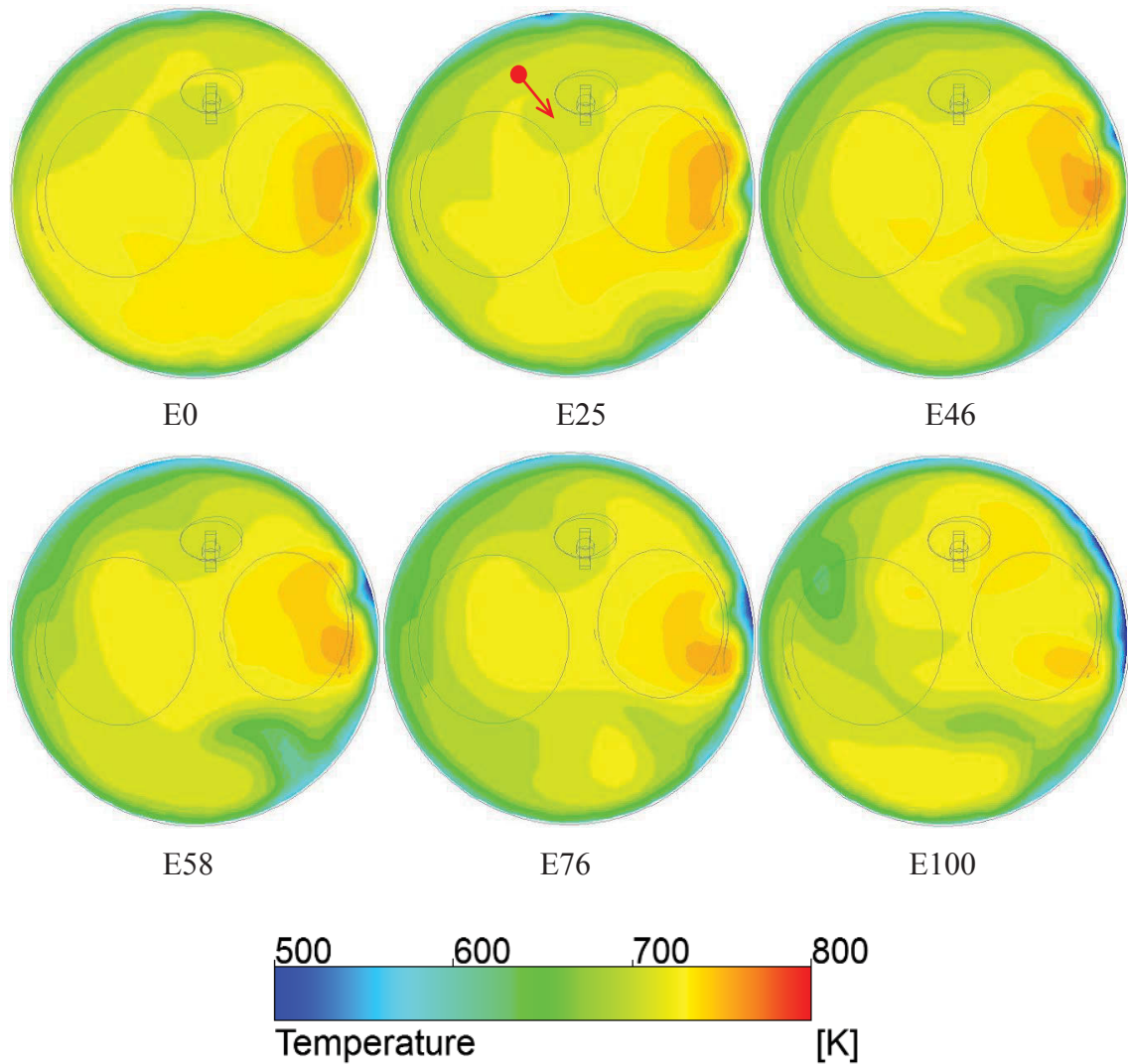


Figure 5.9: In-cylinder temperature distributions by spark timing

Figure 5.9 shows the spatial distributions of in-cylinder temperature at different ethanol ratios on a plane cut below the spark plug at spark timing from simulation. The red dot and arrow indicate the position and direction of the EDI injector. As shown in Figure 5.9, the charge cooling in the area under the exhaust valve (right hand side in the figure) is more effective than that in other areas. This cooling effect becomes stronger with the increase of the ethanol ratio. When the ethanol ratio is greater than or equal to 58%, the near-wall area close to the exhaust valve is over cooled because the temperature is reduced to be lower than 500 K while the mean cylinder temperature is around 690 K. The local over-cooling is due to the most concentration of ethanol droplets in this area.

Figure 5.10 shows the distributions of ethanol droplets of EDI+GPI E46 at the end of EDI (left) and the spark timing (right). As shown in Figure 5.10, by the spark timing, the ethanol droplets are more concentrated in the area near the cylinder wall. In the late compression stroke, the gas velocity becomes low and the ethanol droplets move slowly, causing low heat transfer rate and thus local over-cooling. As the ethanol droplets evaporate and absorb the thermal heat from this area, this area has a lower temperature and richer mixture. Such an over-cooled and rich mixture area causes incomplete combustion, and consequently increases the HC and CO emissions.

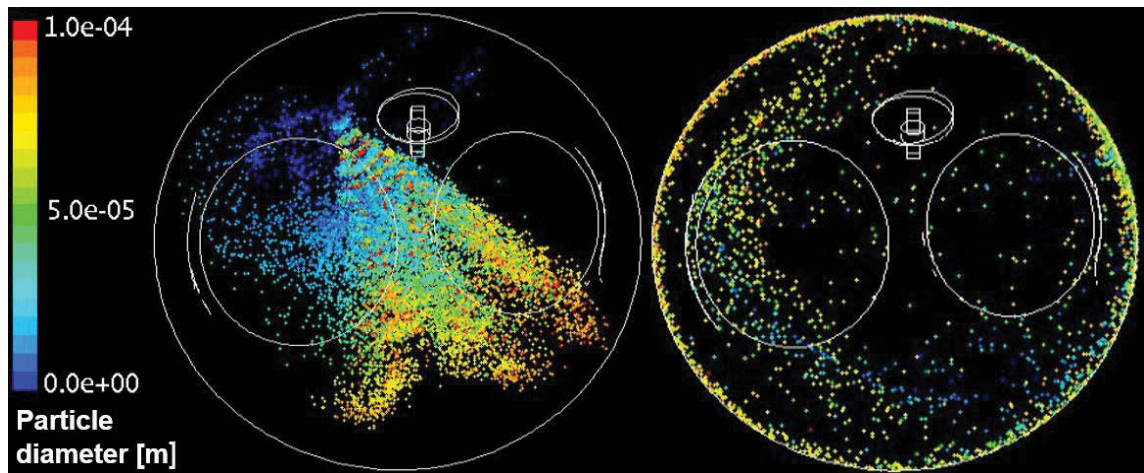


Figure 5.10: Ethanol droplet distributions of EDI+GPI E46 at the end of EDI (left) and spark timing (right)

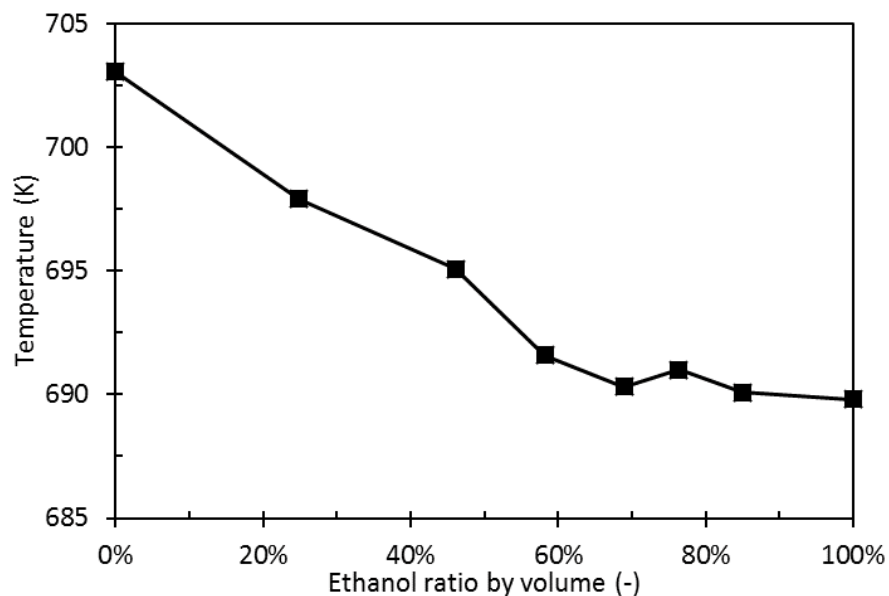


Figure 5.11: Variation of mean in-cylinder temperature by spark timing with the ethanol ratio

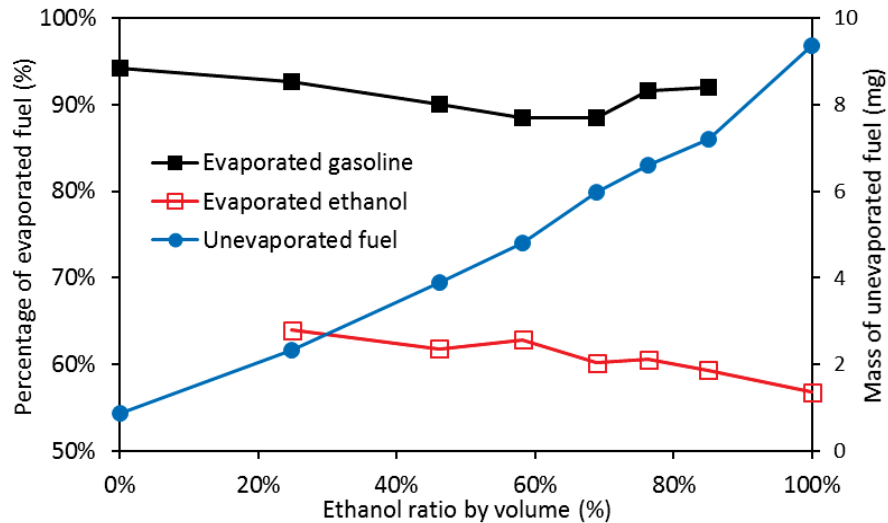


Figure 5.12: Completeness of the ethanol and gasoline evaporation by spark timing

Although over-cooling occurs locally in some regions in cylinder, the overall cooling effect does not increase with ethanol ratio when the ethanol ratio is greater than 58%. As shown in Figure 5.11, the predicted mean in-cylinder temperature at spark timing decreases quickly with the increase of ethanol content until the ethanol ratio reaches 58%. However, when the ethanol ratio is greater than 58%, the overall cooling effect of EDI does not increase much. This is because the EDI cooling effect is limited by the low evaporation rate of the ethanol fuel due to its low saturation vapour pressure. Figure 5.12 shows the simulated results of the variation of the evaporated/unevaporated ethanol and gasoline fuels with the ethanol ratio by spark timing. It is clear that gasoline fuel has a higher completeness of evaporation than ethanol does because gasoline's vapour pressure is bigger than ethanol's. With the increase of ethanol ratio, the mean cylinder temperature decreases, leading to reduced evaporation rates for both ethanol and gasoline fuels. The evaporation rate of gasoline drops from 94.3% to 92.0% when the ethanol ratio increases from 0% to 85%. The evaporation rate of ethanol drops from 64.0% to 56.8% when the ethanol ratio increases from 25% to 100%. As a result, the total mass of un-evaporated gasoline and ethanol droplets increases rapidly from 0.873 mg to 9.367 mg when the ethanol ratio increases from 0% to 100%. Higher ethanol ratio has greater cooling potential, but may leave a large number of liquid droplets in the combustion chamber by spark timing. These liquid droplets will keep evaporating during the combustion process and the droplet combustion may occur. This is unfavourable for combustion and leads to high HC and CO emissions.

Figure 5.13 shows the ideal cooling potential and actual charge cooling realized at different ethanol ratios. The GPI only E0 condition is chosen as the baseline for comparison. The ideal cooling potential ΔT_{ideal} of EDI+GPI E'X' condition is defined as,

$$\Delta T_{ideal} = \frac{Q_{EDI+GPI EX} - Q_{GPI only E0}}{c_{p,mixture} \cdot m_{mixture}} \quad \text{Equation 5.2}$$

Where $Q_{EDI+GPI EX}$ and $Q_{GPI only E0}$ are the latent heat needed for the complete evaporation of the injected fuels of EDI+GPI E'X' and GPI only E0 respectively. $c_{p,mixture}$ is the specific heat of the mixture. $m_{mixture}$ is the mass of the mixture inside the combustion chamber. The actual temperature drop ΔT_{actual} is calculated as the temperature of E0 by spark timing minus that of E'X'. The percentage of charge cooling realized is calculated as,

$$\phi_{realized} = \frac{\Delta T_{actual}}{\Delta T_{ideal}} \times 100\% \quad \text{Equation 5.3}$$

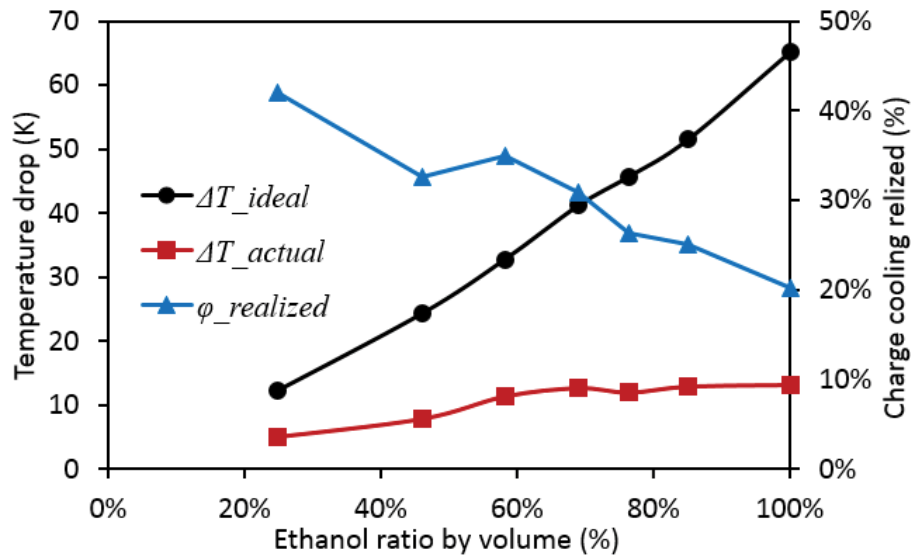


Figure 5.13: Ideal cooling potential and charge cooling realized

As shown in Figure 5.13, since the enthalpy of vaporisation of ethanol fuel is two times larger than gasoline's, the ideal cooling potential of EDI+GPI operation mode increases rapidly from 12.25 K in E25 to 65.23 K in E100. However the actual temperature drop only increases from 4.94 K to 13.03 K when the ethanol content increases from 25% to 100%. As a result, the actual percentage of the charge cooling realized decreases from 40.4% in E25 to 20.0% in E100. Higher ethanol ratio means greater cooling potential.

However, this cooling potential is also dependent on the evaporation temperature and limited by the completeness of evaporation. As discussed above, ethanol's vapour pressure in low temperature conditions is smaller than gasoline's, thus leads to ethanol's low evaporation rate. More ethanol content needs more energy and time to evaporate, which will lead to a lower completeness of evaporation in the same engine condition.

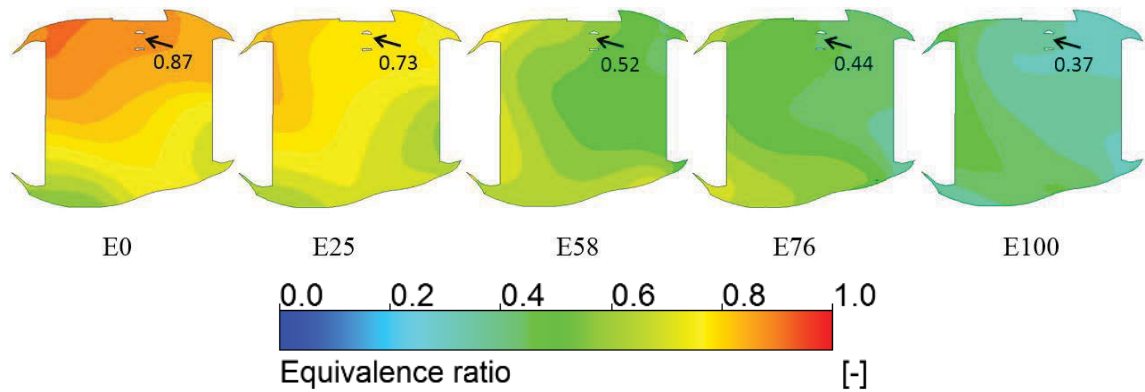


Figure 5.14: Distribution of equivalence ratio around the spark plug by spark timing

Since ethanol fuel evaporates slowly in the low temperature environment before the combustion takes place, high ethanol ratio also leads to lean mixture in the combustion chamber. Figure 5.14 shows the distributions of the equivalence ratio (Φ) around the spark plug by spark timing. As clearly shown in Figure 5.14, the equivalence ratio at the plug position decreases with the increase of ethanol ratio. High ethanol ratio ($> 58\%$) does not enhance the overall cooling effect of EDI. On the contrary, it deteriorates the consequent combustion and emission processes. When the ethanol ratio is higher than 58% , the equivalence ratio around the spark plug decreases to be less than 0.5 (0.44 in E76 and 0.37 in E100). Such a lean mixture is out of the ignitable equivalence ratio range of $0.5 < \Phi < 1.5$ [140]. The lean mixture around the spark plug is difficult to be ignited and consequently leads to incomplete combustion and high HC and CO emissions, whose results will be further discussed in Chapter 6.

Moreover, greater ethanol ratio requires longer injection duration of EDI. Longer injection duration enhances the spray penetration and may lead to fuel impingement on the piston and cylinder walls, resulting in increased HC and soot emissions during engine operation [119]. Figure 3.14 shows the comparison of the measured and simulated EDI spray patterns at 1.5 ms ASOI in a constant volume chamber. The injection pressure was 6 MPa, the ambient temperature was 350 K and the ambient pressure was 0.1 MPa. These

conditions reproduced the in-cylinder conditions for an early EDI injection of 300 CAD BTDC in the engine experiments. As shown in Figure 3.14, the ethanol spray tip penetration reaches 70 mm at 1.5 ms ASOI. The penetration length 70 mm is about the bore diameter (74 mm) and the duration 1.5 ms (equal to 36 CAD at engine speed of 4000 rpm) is close to the EDI injection duration (32 CAD) at ethanol ratio of 46%. Figure 3.14 implies that the ethanol fuel impingement may have occurred in engine conditions when ethanol ratio is greater than 46%. Figure 5.15 shows the distributions of the ethanol spray droplets in the engine cylinder at the end of EDI injection with different ethanol ratios. As shown in Figure 5.15, by the end of EDI injection, the ethanol spray tip does not reach the cylinder wall when ethanol ratio is lower than 58%. With the increase of ethanol ratio, the spray penetration length increases and more ethanol droplets reach the cylinder wall, resulting in more wall impingement. This is another factor contributing to the increased HC and CO emissions in the engine experiments.

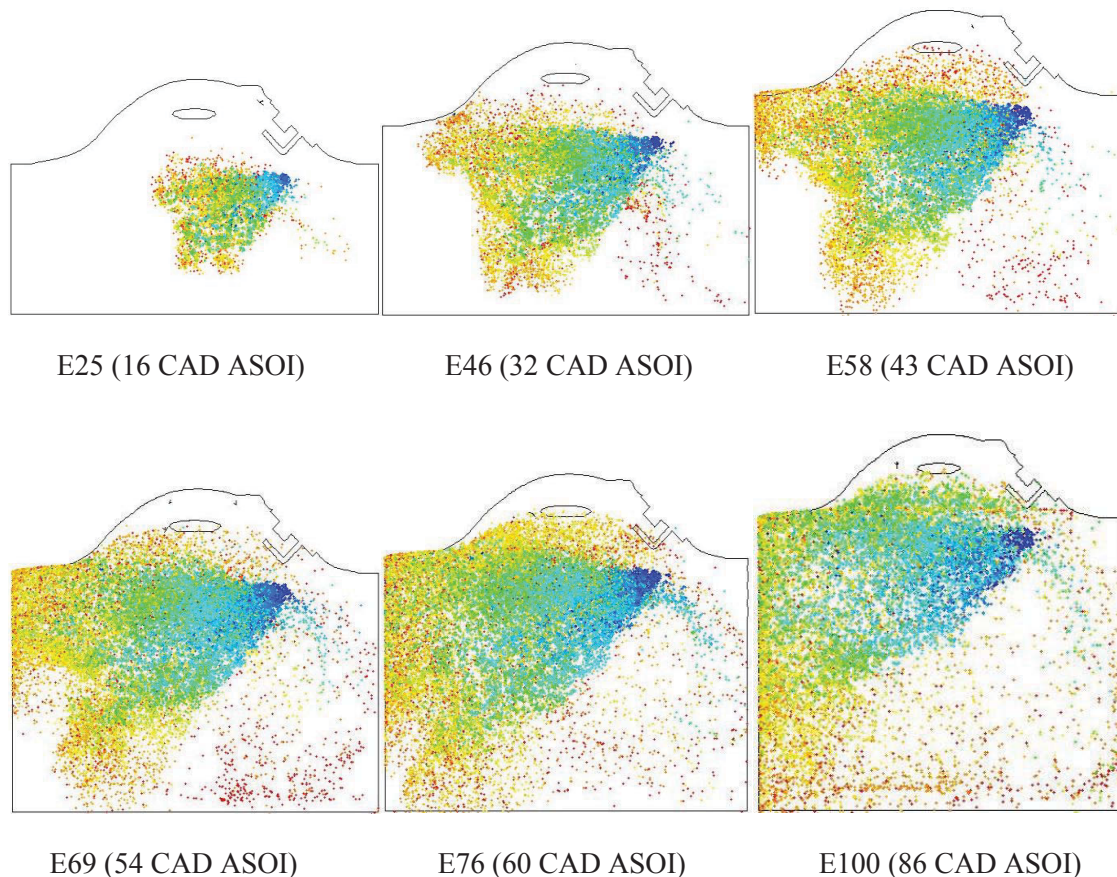


Figure 5.15: Distributions of the ethanol spray droplets at the end of EDI injection

Higher ethanol ratio requires greater latent heat for fuel evaporation. However, the amount of this cooling potential realised is limited by ethanol's low evaporation rate.

More ethanol content needs more energy and time to evaporate, which may lead to incomplete evaporation in the same engine condition. The ethanol ratio and its evaporation are two competing factors that determine the final level of cooling effect and combustion performance: lower ethanol ratio (< 58%) leads to a higher completeness of cooling effect, but limited by its cooling potential; higher ethanol ratio (> 58%) contains more cooling potential, but only a small percentage of it may be realised. Moreover, when the ethanol ratio is higher than 58%, the near-wall area next to the exhaust valve is over-cooled (shown in Figure 5.9), the mixture at the spark plug gap is over-lean (shown in Figure 5.14) and the fuel impingement on the cylinder wall becomes severer (shown in Figure 5.15). All these factors cause incomplete combustion and increased CO and HC emissions. When taking the quality of the mixture into consideration, the competing of cooling potential and its evaporation suggests that 40-60% of ethanol ratio can realise the maximum overall cooling effect while avoiding the local over-cooling, the too lean mixture at the spark gap and the fuel impingement on the cylinder wall. A similar ratio of 30-50% has been recommended for ethanol/gasoline blends for the conventional single injection engines [101].

5.4 Summary

This chapter presented and discussed the numerical results of mixture formation and cooling effect processes in the EDI+GPI engine, including the evolution of the in-cylinder flows and sprays of dual-injection, charge cooling effect and fuel impingement of EDI, and the effect of ethanol ratio on charge cooling. The major results of this chapter can be concluded as follows.

- 1) The intake swirls affected the evolution of both GPI and EDI sprays. They enhanced the heat and mass transfer between the fuel and the gas. The ethanol fuel evaporated more slowly than the gasoline fuel did due to its lower vapour pressure than gasoline's in low temperature conditions. The evaporation rate of ethanol fuel became greater in the late compression stroke due to the increased in-cylinder temperature.
- 2) As the gasoline fuel was injected just before IVO, its majority was evaporated inside the cylinder. The cooling effect of EDI+GPI was stronger than that of GPI only due

to ethanol's greater latent heat than gasoline's, although the ethanol fuel's evaporation was slower than gasoline's.

- 3) The cooling effect was examined with the evaporation rates and the latent heat of the ethanol and gasoline fuels. Compared with GPI only, EDI+GPI demonstrates stronger effect on charge cooling by decreased in-cylinder temperature. The cooling effect is limited by the low evaporation rate of the ethanol fuel.
- 4) The overall cooling effect of EDI increased with the increase of ethanol ratio until it reached 58%. Further increase of ethanol ratio did not increase the overall cooling effect, but left a large number of liquid ethanol droplets in the combustion chamber by the time of spark. Moreover, the local over-cooling occurred in the near-wall region, the fuel impingement on the cylinder wall became severe and the mixture became too lean when the ethanol ratio was higher than 58%. This would lead to incomplete combustion and explained the increased CO and HC emissions with the increased ethanol ratio as reported in the experimental investigations.
- 5) The cooling potential and the completeness of ethanol evaporation were two competing factors that determined the final cooling effect of EDI. This implied that 40-60% of ethanol ratio could realise the maximum overall cooling effect while avoiding the local over-cooling, the too lean mixture at the spark gap and the fuel impingement on the cylinder wall.

Chapter Six

6 Combustion and Emission characteristics of EDI+GPI

This chapter presents and discusses the simulation results of the combustion and emission formation processes of EDI+GPI in four sections. Section 6.1 reports the combustion and emission characteristics of EDI+GPI E46 based on comparison with GPI only E0. Spatial and temporal distributions of the flame front, combustion temperature and emissions are visualized and analysed. Sections 6.2 reports the effect of ethanol ratio on the combustion characteristics of EDI+GPI, including the IMEP, emissions, combustion phases, combustion temperature and intermediate radicals. Section 6.3 reports the effect of EDI timing on fuel evaporation, mixing, wall-wetting, combustion and emission processes of EDI+GPI E46. The potential of direct injection of small amount of ethanol fuel that cannot be realised on the current research engine on reducing the wall-wetting and incomplete combustion caused by late EDI timing has also been examined numerically in Section 6.4.

6.1 Combustion and emissions of EDI+GPI

In premixed combustion modelling, the progress variable c is introduced to indicate the state of the reactants, where $c = 0$ stands for fresh mixture and $c = 1$ for burnt mixture. A value between 0 and 1 indicates the flame-brush. Figure 6.1 shows the flame propagation visualized on a vertical plane crossing the spark plug at five time points. As shown in Figure 6.1, the flame propagation speed is slow before 355 CAD in both GPI only and EDI+GPI conditions. However, the flame speed increases significantly after 355 CAD. This agrees well with the experimental results in an optical SI engine reported by Keck

et al. [161], who found that the initial expansion speed of the flame front was close to that of a laminar flame but it accelerated rapidly later.

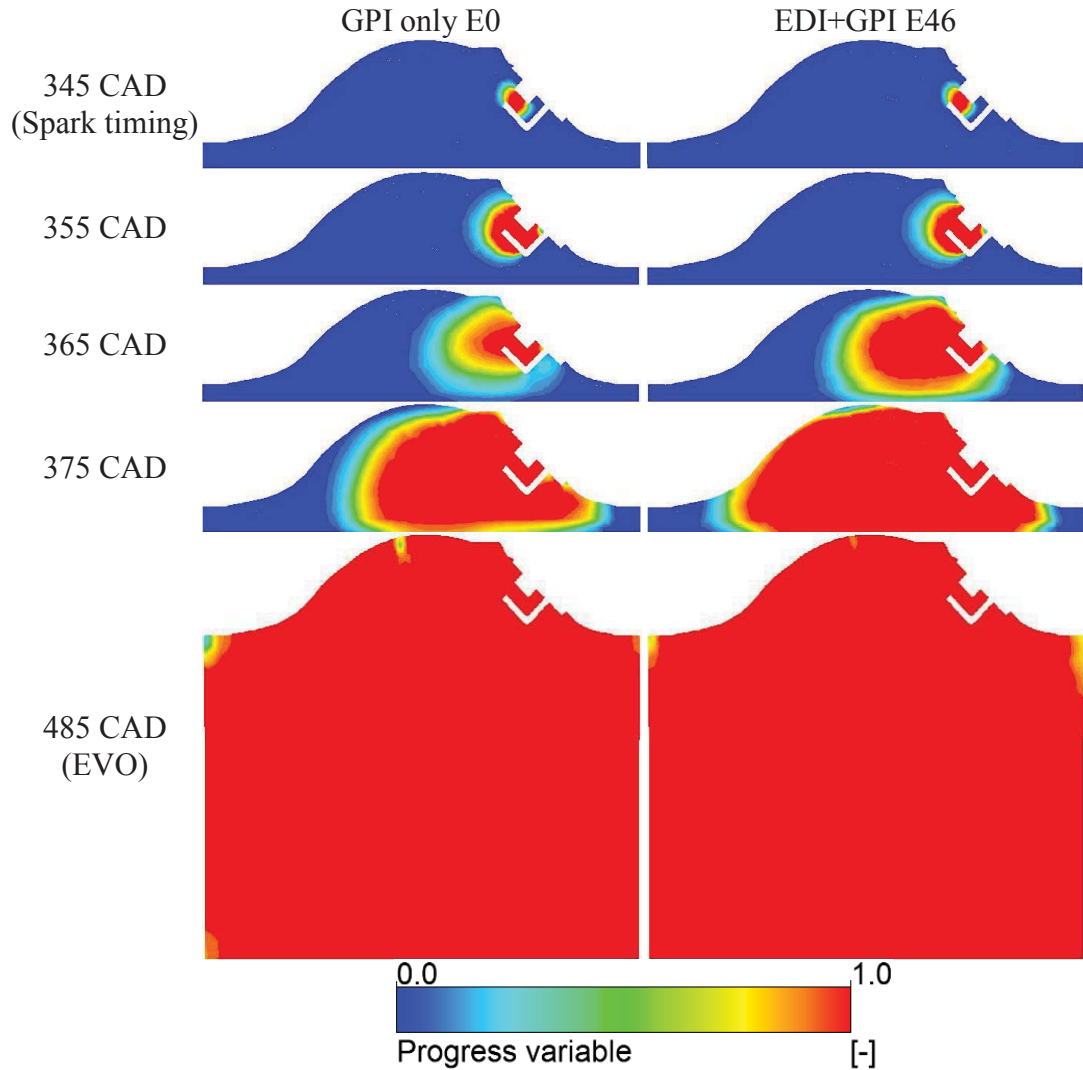


Figure 6.1: Flame propagation in GPI only E0 and EDI+GPI E46

Figure 6.1 shows that the mixture burns faster in EDI+GPI condition than that in GPI only condition. This is because the ethanol fuel has a higher laminar flame speed than gasoline does in a wide range of equivalence ratio which is shown in Figure 2.12. This consequently leads to the higher heat release rate in EDI+GPI than that in GPI only. By the time of exhaust valve open (EVO), the flame has reached the cylinder wall. In EDI+GPI, although ethanol has higher flame speed, there is still some unburnt mixture in the right near-wall region. The unburnt mixture will be exhausted to the air as unburnt HC emission. This is caused by two factors. Firstly, the mixture is very rich in the right-near wall region which can be seen from Figure 5.3. Rich mixture means lack of oxygen for chemical reaction and the flame speed is very slow when the equivalence ratio reaches

2.0 (Figure 2.12). Secondly, the liquid ethanol droplets concentrated in the near wall region (Figure 5.1) worsen the situation. The concentrated ethanol droplets over-cool the mixture (Figure 5.9), which makes it easier for the flame to extinguish in the near wall region.

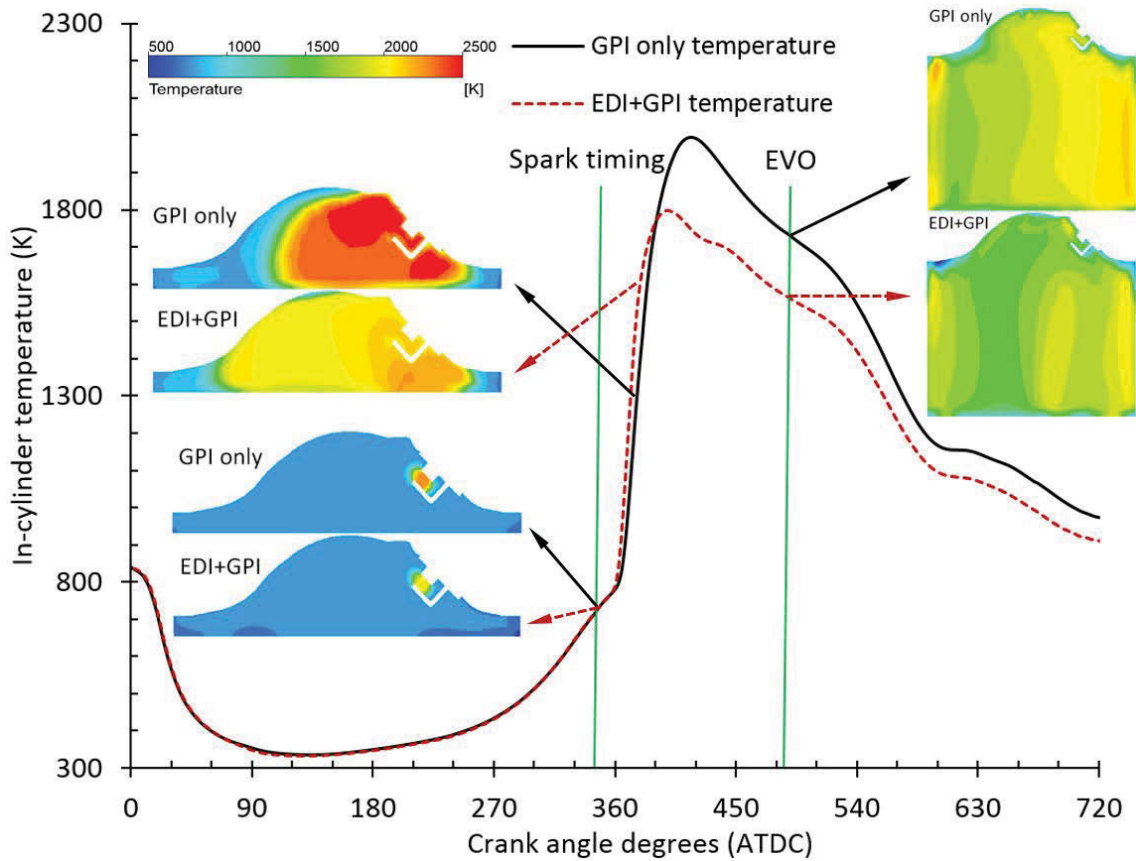


Figure 6.2: In-cylinder temperature in GPI only E0 and EDI+GPI E46 conditions

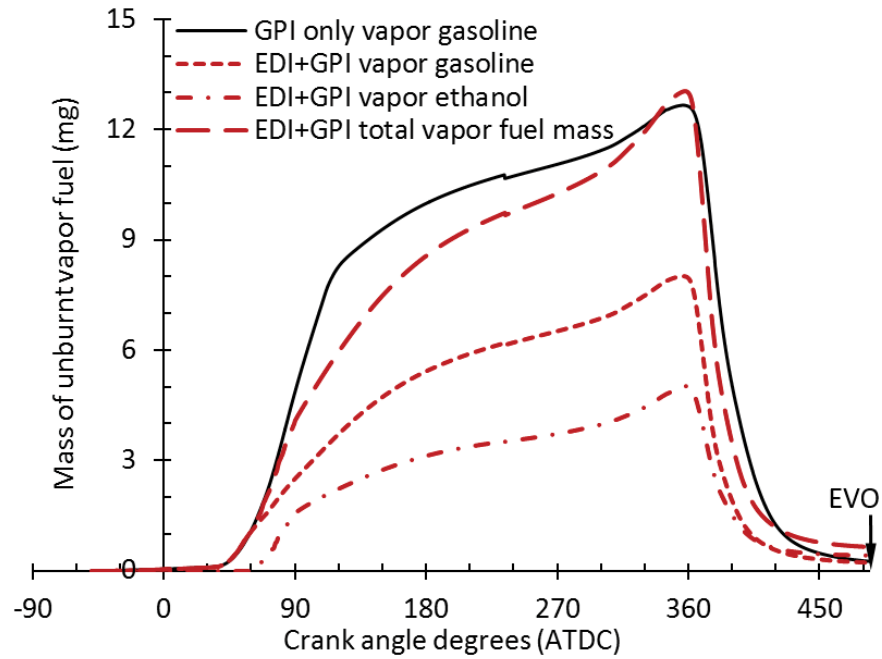
Figure 6.2 shows the temporal mean cylinder temperature in GPI only and EDI+GPI conditions. It can be seen that the mean cylinder temperature rises faster and is higher in EDI+GPI than that in GPI only during the early combustion period from 360 to 390 CAD. This is due to the higher flame propagation speed of ethanol fuel. After that, the cylinder mean temperature is much lower in EDI+GPI than that in GPI only. Two main factors contribute to this result. Firstly, the adiabatic flame temperature of ethanol (2144 K) is lower than that of gasoline (2300 K) [188]. The temperature difference is 156 K. The second factor is the low equivalence ratio in EDI+GPI due to the partially premixed combustion mode. The flame temperature reaches the peak at the stoichiometric ratio. Either rich or lean mixture will decrease the flame temperature. For example, with the initial mixture condition of 10 atm and 700 K, the constant volume adiabatic flame

temperature values are about 2900 K, 2300 K and 2700 K at the equivalence ratios of 1.0, 0.6 and 1.4 respectively [189]. The temperature drop can be more than 600 K. In GPI only condition, most of the port injected gasoline fuel has evaporated by spark timing. The mixture is close to the stoichiometric ratio. This leads to the higher combustion temperature in GPI only. On the other hand, the mixture is relatively lean in EDI+GPI due to ethanol's low evaporation rate in the low temperature environment before combustion. The lean mixture is the main cause for the low combustion temperature in EDI+GPI compared based on the temperature decreases.

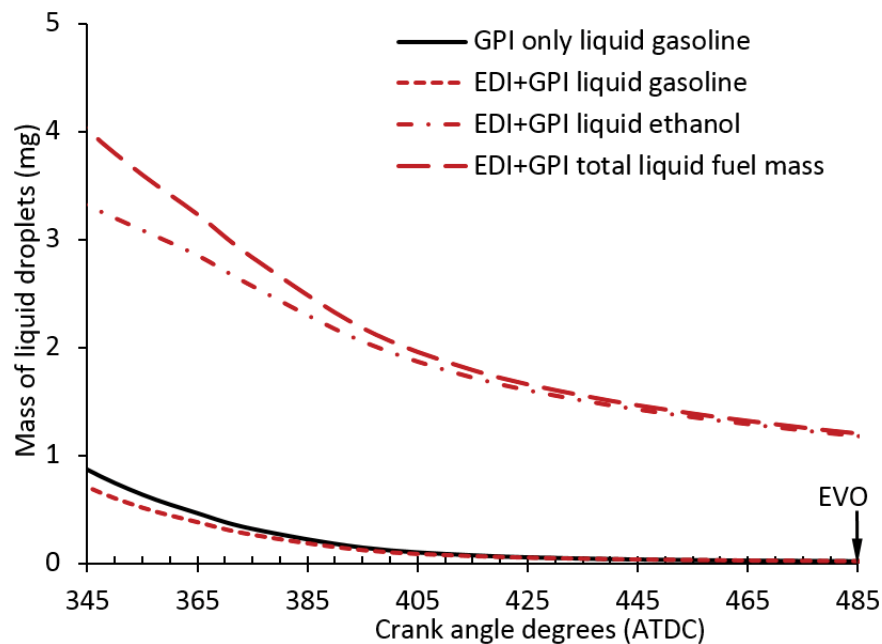
In the two modelled cases, the latent heat is only 3.99 J per cycle for 13.40 mg gasoline to evaporate in GPI only condition and 10.12 J for 8.50 mg gasoline plus 8.00 mg ethanol to evaporate in EDI+GPI condition. The latent heat in EDI+GPI is 6.13 J higher than that in GPI only. Assuming all this cooling potential could be realized, where the thermal heat for the fuel evaporation is completely from the gas in the cylinder, the cylinder temperature of EDI+GPI would be 24 K lower than that of GPI only. However, the actual cooling of EDI realized in engine condition is only 7 K which was much smaller than 24 K. This is because that not all the ethanol fuel was evaporated including the fuel impinged to the cylinder wall. Reconsidering the two factors leading to the EDI+GPI's lower combustion temperature, each factor can result in more than a hundred degrees of temperature drop. Therefore, the two factors, adiabatic flame temperature and equivalence ratio, are more effective than the charge cooling enhanced by EDI on reducing the cylinder temperature during the combustion process.

Figure 6.3 shows the variation of the mass of unburnt gasoline and ethanol vapour fuels (a) and of the mass of gasoline and ethanol liquid droplets (b) with CAD during the combustion process by the time of EVO. As shown in Figure 6.3(a), gasoline fuel evaporates more quickly than the ethanol fuel does because the gasoline fuel's vapour pressure is higher than the ethanol fuel's when the fuel temperature is lower than 375 K. For the port injected gasoline fuel in both GPI only and EDI+GPI conditions, most of the gasoline droplets (94.3% for GPI only and 90.1% for EDI+GPI) have evaporated by the spark timing. However, only 61.8% of the ethanol fuel has evaporated and 38.2% is still in the phase of liquid droplets before the combustion takes place. After the spark timing, the vapour fuels are burnt fast in the flame brush during the time period within 360-400

CAD. For GPI only, most of the gasoline fuel is burnt by the time of EVO. For EDI+GPI, however, there are still some unburnt vapour and liquid ethanol fuel by the time of EVO.



(a)

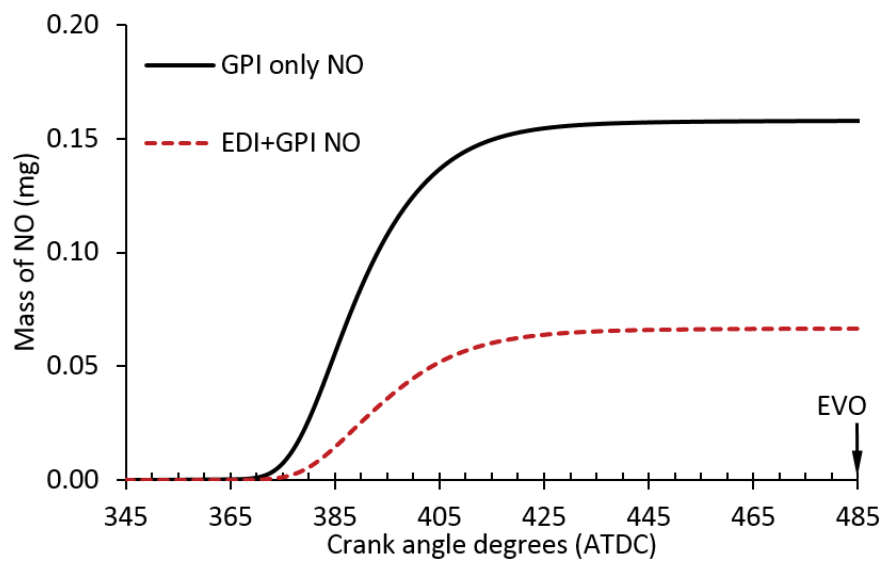


(b)

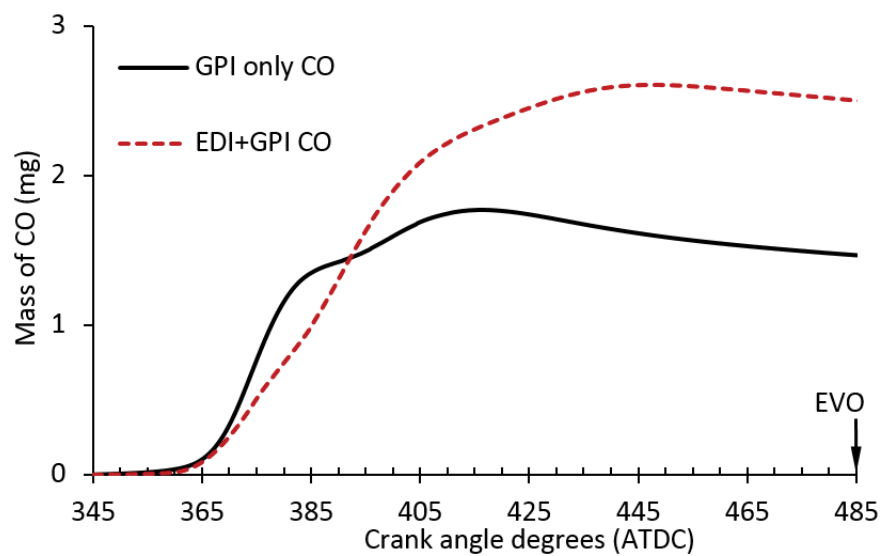
Figure 6.3: The mass of unburnt vapour (a) and liquid (b) fuels

As shown in Figure 6.3(b), about 2.5 mg (31.3%) ethanol fuel has not evaporated but the flame has reached most of the space in the combustion chamber at 375 CAD. The ethanol fuel evaporated after this time may occur at the back of the flame-brush. However ethanol

droplets evaporated in this region cannot be completely burnt because the flame has passed them and consumed the oxygen. In EDI+GPI condition, by the time of EVO, there are 1.8524 mg unburnt fuel including 0.2302 mg vapour and 0.0222 mg liquid gasoline fuel and 0.4228 mg vapour and 1.1772 mg liquid ethanol fuel. In GPI only condition, 0.2674 mg gasoline fuel is unburnt by the time of EVO, including 0.2543 mg vapour and 0.0131 mg liquid gasoline fuel. These unburnt fuels are exhausted as HC emission. The mass of unburnt fuels in EDI+GPI is much higher than that in GPI only. This explains why the HC emission in EDI+GPI condition is greater than that in GPI only condition in the experimental investigations [8].



(a)



(b)

Figure 6.4: Formation of NO (a) and CO (b) emissions during the combustion

Figure 6.4 shows the variation of the mass of the NO (a) and CO (b) emissions in the combustion chamber from the spark timing to the time of EVO. As shown in Figure 6.4(a), the predicted mass of the NO in GPI only is greater than that in EDI+GPI because of the higher combustion temperature in GPI only than that in EDI+GPI. The NO emission forms quickly during the period from 370 CAD to 410 CAD when the cylinder temperature increases very quickly. During the combustion, the cylinder mean temperature in GPI only condition reaches as high as 1995 K, while it is only 1797 K in EDI+GPI condition. As introduced in Section 3.2.3, the formation of NO emission is only significant when the temperature is higher than 1800 K. As a result, the NO concentration in GPI only is much higher than that in EDI+GPI. By the time of EVO, the mass of NO emission reaches a stable level of 0.1581 mg in GPI only condition and 0.0666 mg in EDI+GPI condition. After EVO, the cylinder mean temperature drops quickly to be below 1800 K and the NO formation stops. For CO emission, the simulated CO emission in EDI+GPI is higher than that in GPI only. This is consistent with the experimental results of CO emission. As shown in Figure 6.4(b), by the time of EVO, the mass of CO emission is 1.4647 mg in GPI only and 2.5006 mg in EDI+GPI.

The NO formation is a result of high temperature and rich oxygen. Figure 6.5 shows the spatial distributions of temperature, O, OH and NO mass concentrations at 405 CAD. The NO has a relatively high concentration in the region around the spark plug in GPI only condition. The mixture around the spark plug is close to the stoichiometric ratio, which leads to a very high combustion temperature (~2500 K, as shown in Figures 6.2 and 6.5). The high temperature and concentrations of O and OH in this region lead to extensive NO formation in GPI only. On the other hand, the partially premixed combustion mode in EDI+GPI reduces the combustion temperature significantly. Consequently much less NO is formed in EDI+GPI than that in GPI only condition.

CO is an intermediate combustion product and a result of incomplete combustion. The contours in Figure 6.6 show the distributions of O₂ and CO concentrations at 405 CAD. Obviously the near wall regions have the highest CO concentration for both operation conditions. This is because the mixture in these regions is much richer than the stoichiometric equivalence ratio (as shown in Figure 5.3) and there is not enough oxygen for complete burning.

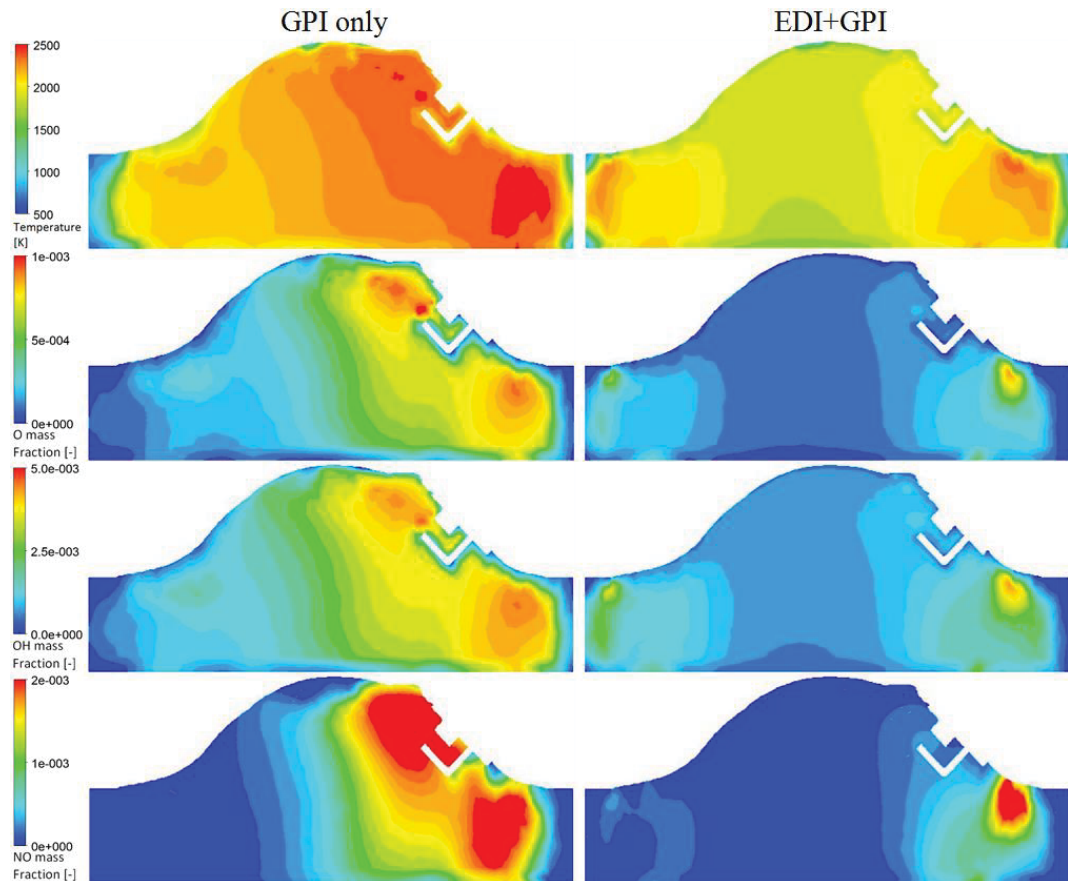


Figure 6.5: Spatial distributions of temperature, O, OH, and NO at 405 CAD

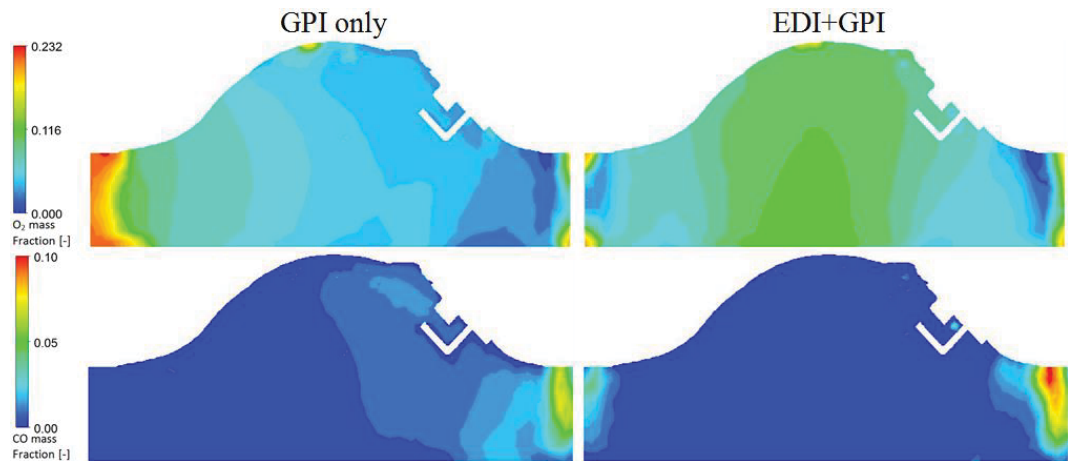


Figure 6.6: Distributions of O₂ and CO at 405 CAD

6.2 Effect of ethanol ratio on combustion

To evaluate the effect of ethanol ratio on combustion characteristics of the EDI+GPI, the in-cylinder pressure, IMEP, combustion initiation duration and major combustion duration are discussed. Figure 6.7 shows the variation of experimentally measured in-

cylinder pressure with the crank angle degree at ethanol ratios from 0% to 100%. As shown in Figure 6.7, the peak cylinder pressure increases quickly with the increase of ethanol ratio from 0% to 58% and decreases when the ethanol ratio is further increased from 58% to 100%. The in-cylinder pressure with EDI is lower than that of GPI only during the compression stroke (<360 CAD) due to the cooling effect of EDI, indicating less negative work on the piston. During the expansion stroke (>400 CAD), the pressure with EDI is larger than that of GPI only, indicating more positive work on the piston. Consistently shown in Figure 6.8, the IMEP increases quickly when ethanol ratio is in 0-46% and slowly in 46-76%, and decreases in 76-100%.

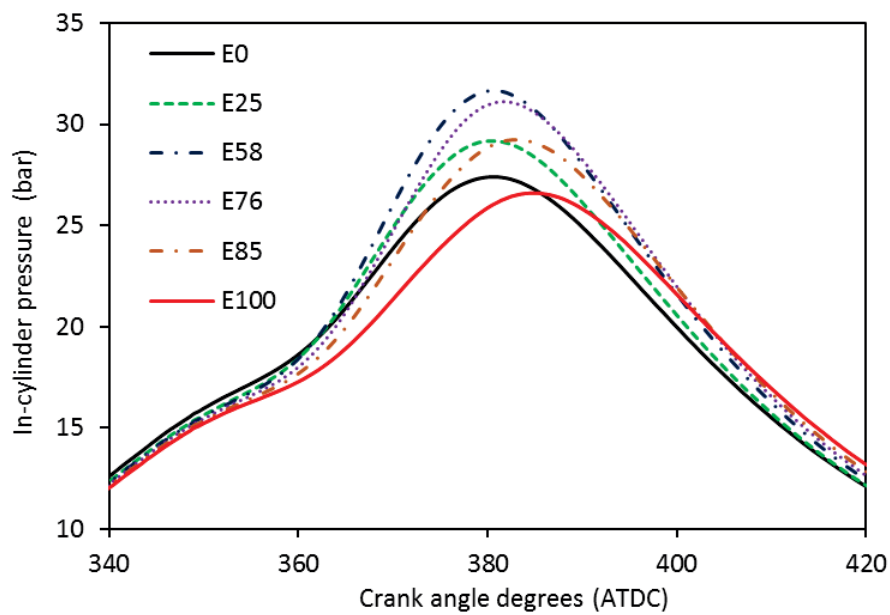


Figure 6.7: In-cylinder pressure varying with the ethanol ratio

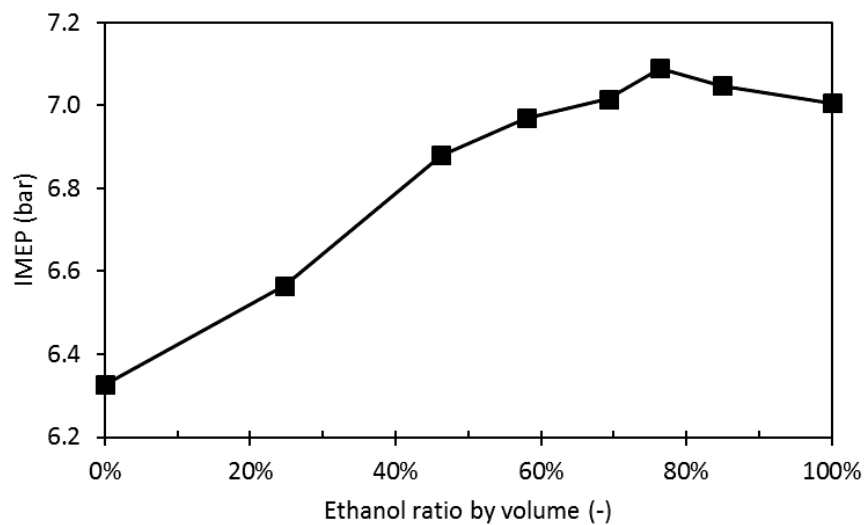


Figure 6.8: IMEP varying with the ethanol ratio

Figure 6.9 shows the combustion initiation duration (CA0-10%) and the major combustion duration (CA10-90%) at different ethanol ratios from 0% to 100% derived from the cylinder pressure shown in Figure 6.7. As shown in Figure 6.9, the combustion initiation duration decreases with the increase of ethanol ratio from 0% to 58%, indicating an improved combustion stability. However, the CA0-10% starts to increase quickly when the ethanol ratio is higher than 58%. This can be explained by the numerical results shown in Figure 5.14. As shown in Figure 5.14, the equivalence ratio decreases with the increase of the ethanol ratio. Within 0-58%, the equivalence ratio is in the ignitable equivalence ratio range of $0.5 < \Phi < 1.5$. The faster flame speed of ethanol fuel contributes to the shorter combustion initiation duration and thus higher combustion stability. However when the ethanol ratio is higher than 58%, the mixture is too lean and out of the ignitable range which causes the increased CA0-10%. As shown in Figure 6.9, the major combustion duration CA10-90% decreases quickly with the increase of ethanol ratio from 0% to 58% and slowly from 58% to 76%. However, CA10-90% increases when the ethanol ratio is increased from 76% to 100%. The decreased CA10-90% indicates an improved combustion efficiency in the range of ethanol ratio from 0% to 76%.

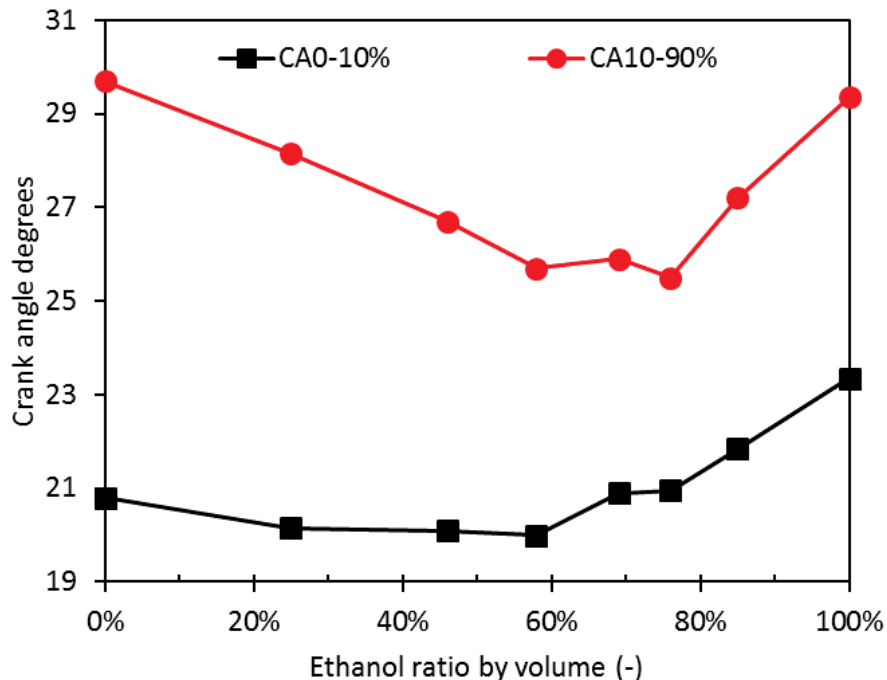


Figure 6.9: CA0-10% and CA10-90% varying with the ethanol ratio

Figure 6.10 shows the flame propagation and distributions of OH mass fraction at different ethanol ratios at 375 CAD and 395 CAD, which correspond to the crank angle

degrees of CA50% and CA90% respectively. As shown by the images at 375 CAD in Figure 6.10, the mixture burns more quickly in EDI+GPI condition than that in GPI only when ethanol ratio is less than 76%. However, the flame speed at the ethanol ratio of 100% becomes lower than that at the ethanol ratio of 76%. By the time of 395 CAD, the flame has reached most volume of the combustion chamber. The presence of OH radical is an indicator of the main heat release event [28]. Figure 6.10 shows that the generation of OH radical is weak at 375 CAD but becomes intensive at 395 CAD. This is consistent with the experimental results shown in Figure 6.7, where the cylinder pressure at E100 is smaller than that at low ethanol ratios in 360-390 CAD but becomes greater after 400 CAD. Although EDI+GPI conditions have higher combustion speed than that in GPI only condition, there is still some unburnt mixture in the near wall region, as shown in Figure 6.10. This is because the ethanol droplets concentrate and evaporate in the near wall region, which will be discussed in Figure 6.11.

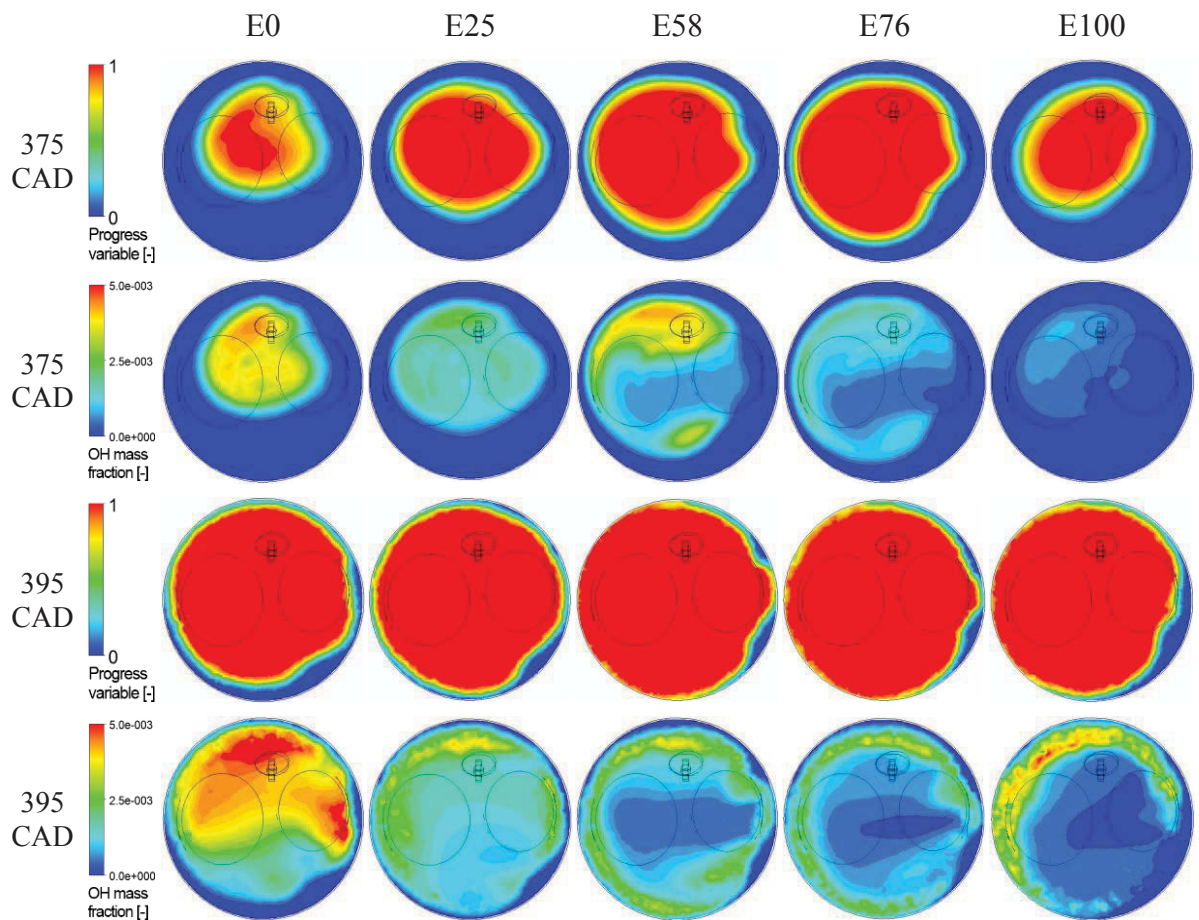


Figure 6.10: Flame propagation and distributions of OH mass fraction at 375 CAD and 395 CAD varying with the ethanol ratio

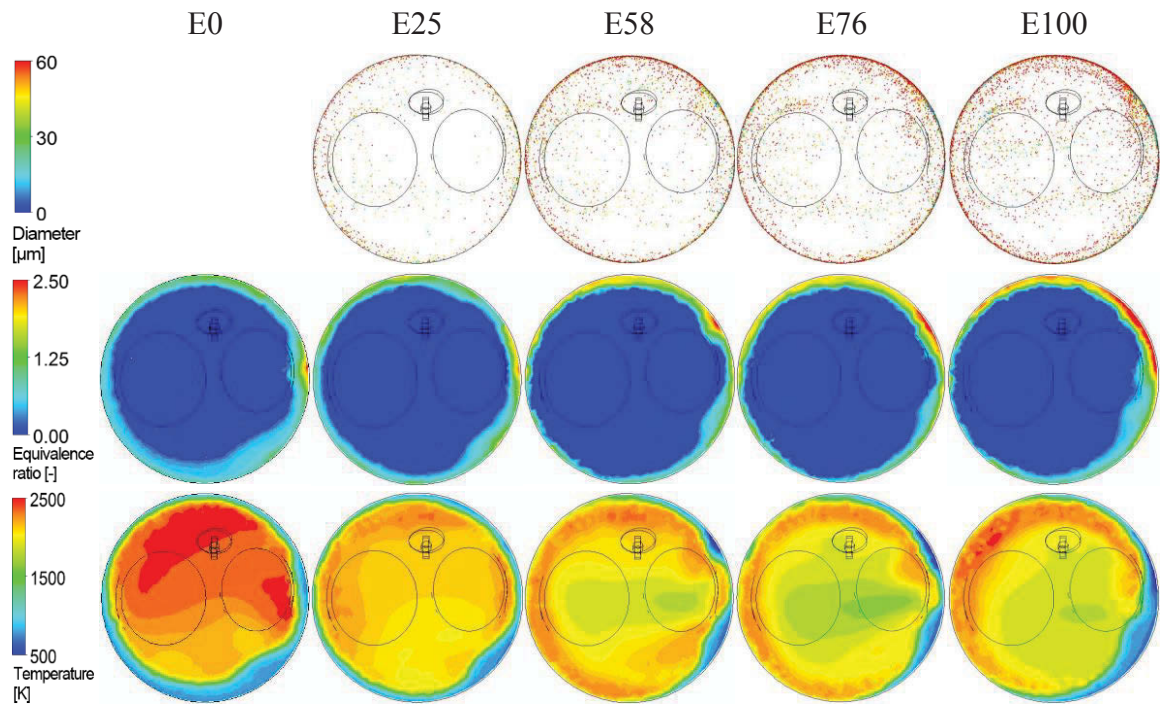


Figure 6.11: The distributions of ethanol liquid droplets, equivalence ratio and cylinder temperature at 395 CAD varying with the ethanol ratio

Figure 6.11 shows the distributions of ethanol liquid droplets, equivalence ratio and cylinder temperature at 395 CAD. The ethanol droplets evaporate and absorb thermal heat from the mixture in the near wall region. As a result, this region has a very rich mixture ($\Phi > 2.0$) and is over-cooled (< 500 K). The over-cooling and over-rich mixture in the near wall region make it hard for the flame to propagate to this region. Consequently, most of the CO and HC emissions should be formed in this region as a result of incomplete combustion. On the other hand, the cylinder temperature is much lower in EDI+GPI condition than that in GPI only condition due to the enhanced cooling effect and lean mixture in EDI+GPI. Particularly, the extremely high temperature region (~ 2500 K) observed in GPI only is disappeared when EDI is applied, as shown in Figure 6.11. Following the thermal NO mechanism of Zeldovich, the NO reduces with the increased ethanol ratio. These explain the experimentally measured emissions shown in Figure 6.12. The measured CO and HC emissions increase, and NO emission decreases with the increase of ethanol ratio from 0% to 100%. Moreover the CO and HC emissions become significantly higher when the ethanol ratio is greater than 58%.

The combustion performance of EDI+GPI engine is improved when implementing EDI within ethanol ratio of 0-58%. The cylinder pressure and IMEP are increased and the

combustion initiation and major combustion durations are decreased when ethanol ratio is increased from 0% to 58%. When further increasing the ethanol ratio from 58% to 100%, the combustion initiation duration and major combustion duration start to increase, while the cylinder pressure decreases, and IMEP increases slightly from 58% to 76% and decreases from 76% to 100%. Regarding the engine emissions, the NO emission decreases when EDI is applied due to the lower combustion temperature and stronger cooling effect. Meanwhile, the HC and CO emissions are increased, and are extremely high at high ethanol ratios (>58%) due to local over-cooling and incomplete combustion. Although the engine shows the maximum IMEP at 76%, the exhaust-out CO and HC emissions are very high when ethanol ratio is higher than 58%. The overall cooling effect does not increase with ethanol ratio greater than 58% but leaves a large number of ethanol droplets unevaporated during combustion. Furthermore, over-lean and local over-cooling occur, fuel impingement becomes severe on cylinder wall, and combustion initiation and major combustion durations increase when ethanol ratio is high. Based on comparison of results in all the aspects, the best engine performance may exist in the range of ethanol ratio of 40-60% in terms of IMEP, combustion efficiency, cooling effect and emissions.

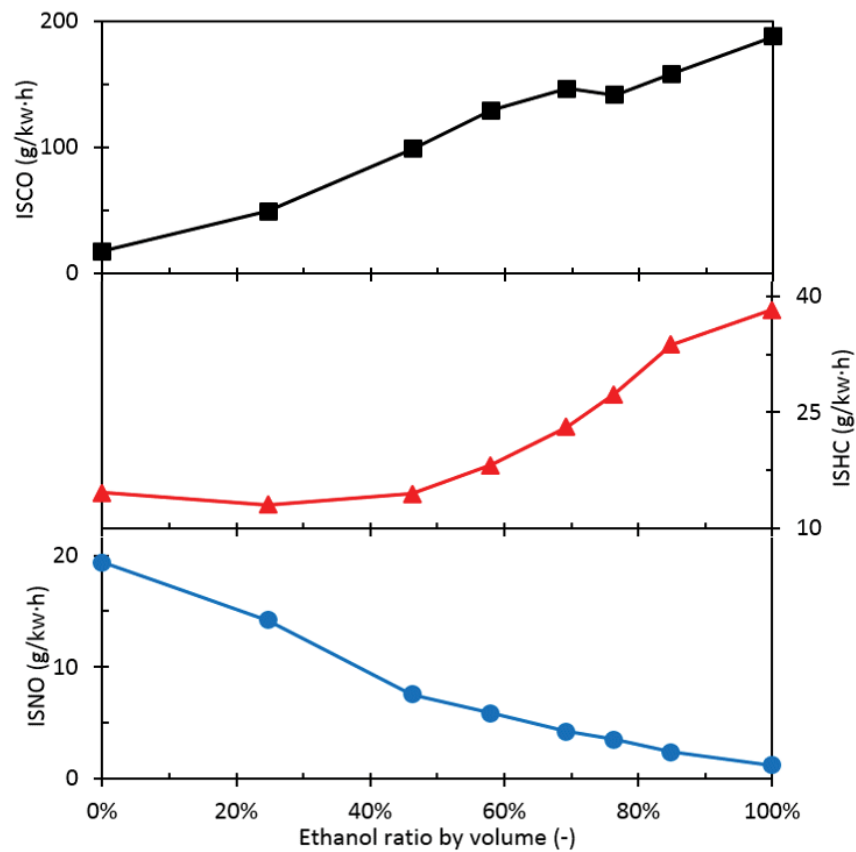


Figure 6.12: Measured engine emissions varying with the ethanol ratio

6.3 Effect of EDI timing on fuel evaporation, mixing and combustion

In the initial idea of EDI+GPI, late EDI timing was desired because it was thought to be more effective than early EDI timing on knock mitigation. Experimental results showed that late EDI timing allowed more advanced spark timing without knock issue than early EDI timing did, but also deteriorated the combustion and emission performance of the engine [12]. As shown in Figure 6.13, the measured CO and HC emissions increase and IMEP and NO emission decrease when EDI timing is retarded in the EDI+GPI E46 condition. In order to understand the experimental results and the mechanisms behind, including the fuel impingement, the droplet-wall interaction model of Wall-jet used in simulations reported in previous chapters has been changed to a wall film model based on the work of Stanton [190] and O'Rourke [191]. This section will present and discuss the effect of injection timing on the mixture formation, wall-film, combustion and emission processes of the EDI+GPI engine in the experimentally tested conditions.

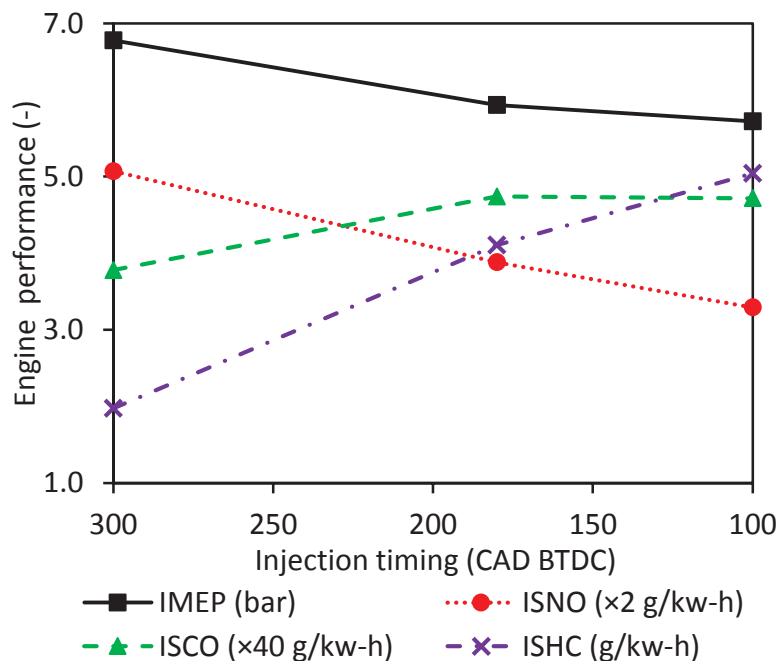


Figure 6.13: Experimental results of IMEP, ISNO, ISCO and ISHC varying with EDI timing

Figure 6.14 shows the variations of the mass of evaporated ethanol fuel with crank angle degree from intake top dead centre to EVO. As shown in Figure 6.14, the mass percentage of evaporated ethanol fuel at spark timing decreases from 93.4% (7.47mg/8.00mg) at

IT300 condition to 89.4% (7.16mg/8.00mg) in IT180 condition and 44.8% (3.583mg/8.00mg) at IT100 condition. This is because the flow field is less intensive in the compression stroke and the time is shorter for the fuel to evaporate and to mix with air with retarded EDI timing. As introduced in Section 3.2.2, the Convection/Diffusion Controlled model [83] is used to simulate the evaporation processes of gasoline and ethanol droplets in the present study. The gradient diffusion effect is governed by the fuel saturation vapour pressure and the convection effect is governed by the flow velocity. In high velocity flows, the effect of convective flow on taking the evaporating material from the droplet surface to the bulk gas phase becomes significant.

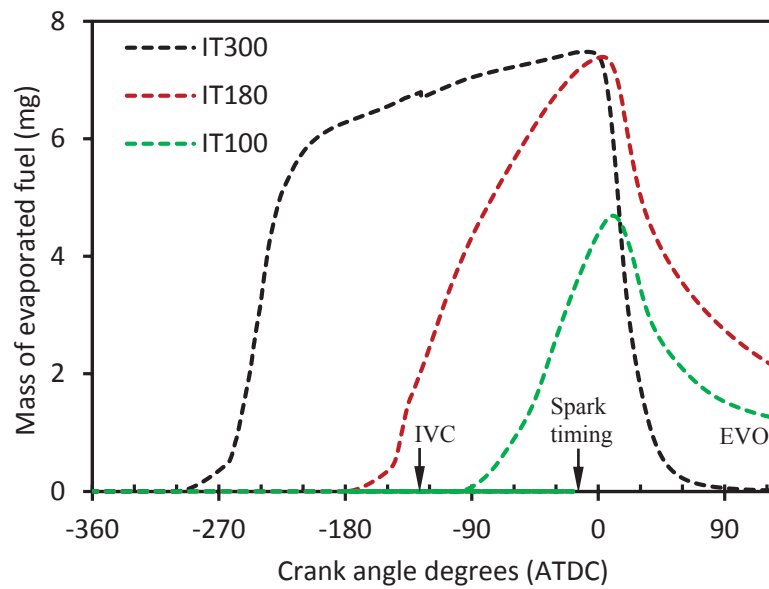


Figure 6.14: Variations of mass of the vapour ethanol fuel with crank angle degrees at three injection timings

Figure 6.15 shows the in-cylinder flow velocity vectors at the start and the end of the EDI injection with different injection timings. As shown in Figure 6.15, for IT300 condition, the intake valve is fully open and the intake flow rate is as high as 200 m/s. This high flow rate increases the heat and mass transfer between the fuel droplets and the ambient gas, thus accelerates the fuel evaporation and enhances the mixing. The in-cylinder flows become much slower in the compression stroke. This leads to the low evaporation rate of ethanol fuel at retarded EDI timings of IT180 and IT100. Particularly, the intake gas flow rate reduces significantly from 150 m/s at the start of EDI injection to 90 m/s at the end of EDI injection for IT180 due to the intake valve closing, as shown in Figure 6.15. This significant change in air velocity may lead to the fluctuation of IMEP when EDI timing is between 120 and 250 CAD BTDC in the engine experiments, as reported in [12]. The

lower evaporation rate of late EDI injection has significant effect on the following combustion process. As the EDI timing retards, the combustion speed becomes slower to propagate to the regions with too-rich and over-cooled mixture (which will be discussed in Figure 6.20). As a result, after the combustion takes place, both the gasoline and ethanol vapour fuels are burnt/consumed more slowly in IT180 and IT100 than that in IT300, as shown in Figure 6.14. By the time of EVO, there are 0.018 mg (0.21%) unburnt gasoline and 0.041 mg (0.51%) unburnt ethanol in the IT300 condition. The unburnt gasoline and ethanol fuels increase to 0.504 mg (5.93%) and 2.196 mg (27.45%) respectively in IT180 condition and 0.340 mg (4.00%) and 2.081 mg (26.01%) in IT100 condition. These unburnt fuels contribute to the increased HC emission in the engine experiments.

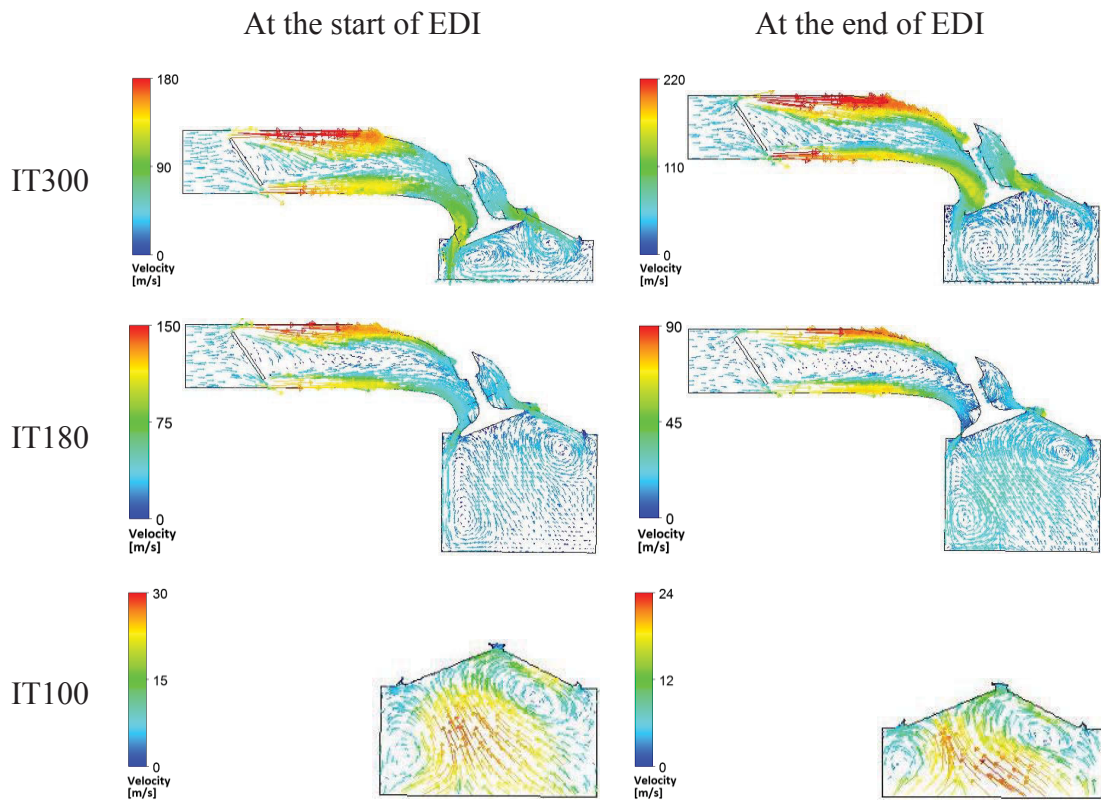


Figure 6.15: Air flow velocity vectors on the engine symmetry plane at the start and end of EDI injection with different EDI timings

Figure 6.16 shows the spatial mass distributions of gasoline and ethanol vapours and the equivalence ratio on a vertical plane passing through the spark plug by spark timing. With retarded EDI timing, the gasoline fuel becomes leaner in the left side of the combustion chamber because more ethanol fuel is vaporised in this region, which consequently cools this region and slows down the gasoline evaporation. As the EDI timing retards, the ethanol droplets have less time to interact with the intake swirls which would entrain the

ethanol fuel to the right region of the combustion chamber. As a result, the ethanol mass fraction becomes leaner in the right side, but richer in the left side. With the retarded EDI timing, the mixture around the spark plug becomes leaner from 0.83 equivalence ratio in IT300 condition to 0.67 in IT180 condition and 0.68 in IT100 condition. This leads to longer combustion initiation duration, lower flame propagation speed and difficulty for the flame to reach the near wall regions. Consequently it reduces the peak cylinder pressure and combustion temperature and increases the HC and CO emissions. This will be further discussed later.

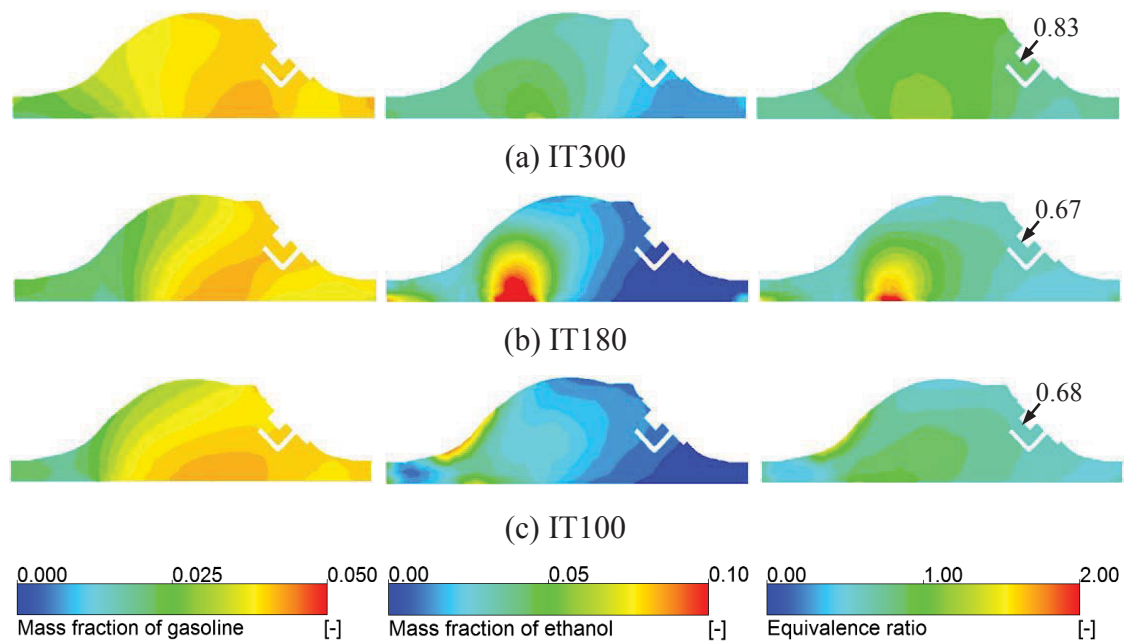


Figure 6.16: Distributions of the vapour mass fractions of gasoline and ethanol fuels and the equivalence ratio on a vertical plane passing through the spark plug by spark timing

Figure 6.17 shows the variation of wall film mass with crank angle degrees at the EDI timings of 300, 180 and 100 CAD BTDC. As shown in Figure 6.17, the fuel impingement on the cylinder and piston walls becomes severer when EDI timing is retarded from 300 to 180 and then to 100 CAD BTDC. At the EDI timing of 300 CAD BTDC (during the intake stroke), the intake air flow rate is high and the piston is moving downward, as shown in Figure 6.15. The ethanol droplets are being entrained into the intake air swirls. This avoids the ethanol spray collision on the cylinder and piston walls. When EDI timing is retarded to be in the compression stroke (IT180 and IT100), the volume of the combustion chamber becomes smaller and the in-cylinder flow rate reduces. However, the in-cylinder pressure during the IT180 and IT100 spray injections does not increase

significantly when EDI timing is retarded from 300 to 100 CAD BTDC. As a result, the ethanol droplets reach the cylinder and piston walls more easily at late EDI timings, causing severer fuel impingement. Moreover, at early EDI timing of 300 CAD ATDC, the wall film has more time to absorb the heat from the hot cylinder walls and evaporate before the combustion takes place. While the wall film formed in IT180 and IT100 conditions does not have enough time to evaporate by the time of spark timing, as shown in Figure 6.17. The increased wall film becomes another import source for the formation of HC emission of late EDI timing conditions.

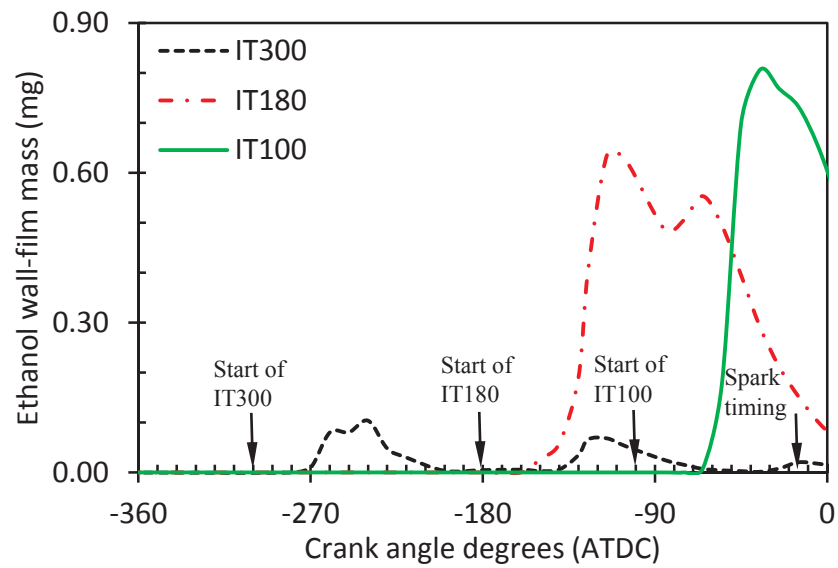


Figure 6.17: Variation of wall film mass with crank angle degrees

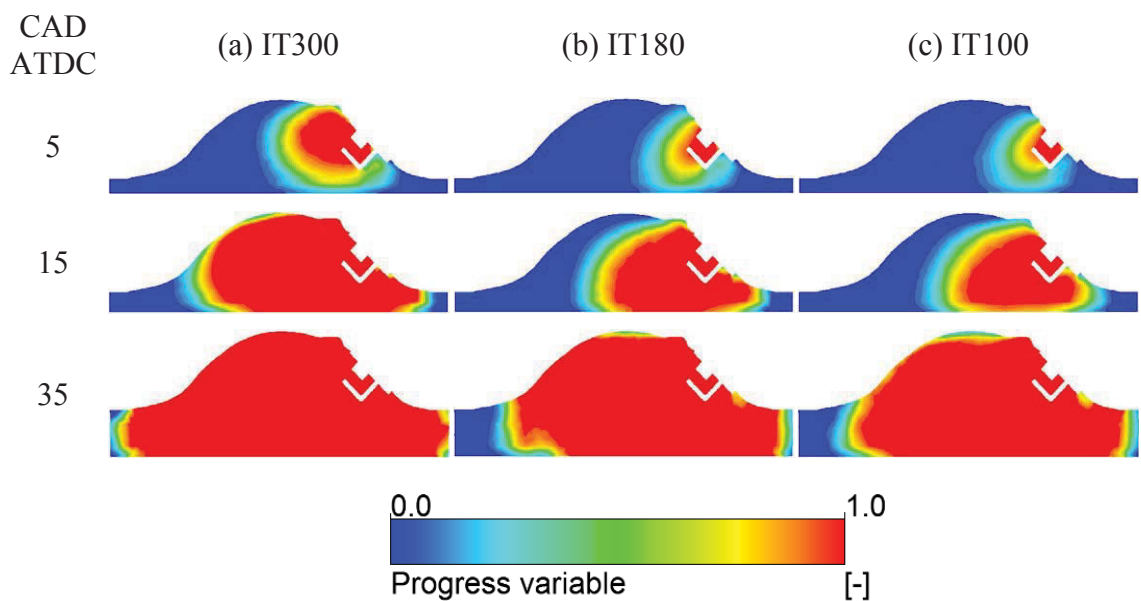


Figure 6.18: Evolution of flame-brush with different EDI timings

Figure 6.18 shows the distributions of flame-brush on a plane cutting through the spark plug varying with the crank angle degree at different EDI timings and Figure 6.19 shows the corresponding distributions of combustion temperature. Figure 6.18 shows that the ignition flame kernel is well formed at 5 CAD ATDC in IT300 condition but still very small in IT180 and IT100 conditions, demonstrating a shorter combustion initiation duration of IT300 than that of IT180 and IT100. The calculated combustion initiation duration (CA0-10%) from the measured cylinder pressure increased from 20.7 CAD in IT300 to 24.3 CAD in IT180 and 24.8 CAD in IT100. Consistently the flame propagates much faster in IT300 than that in IT180 and IT100. This is because the mixtures are leaner in IT180 and IT100 due to the less intensive in-cylinder flows and less time for ethanol to evaporate and to mix with the air, as shown in Figures 6.14 and 6.15. The flame speed and combustion temperature reach their peaks at the stoichiometric equivalence ratio. Either lean or rich mixture results in much lower combustion speed and temperature [102, 189]. Consequently, as shown in Figure 6.19, the combustion temperature is much lower in IT180 and IT100 conditions than that in IT300 condition. Particularly, the temperature in the region next to the spark plug is relatively high (~ 2500 K) in IT300 condition. This is because this region has equivalence ratio closer to 1, as shown in Figure 6.16. This higher temperature region is also the main place for the NO formation, as shown in Figure 6.21 which will be discussed later.

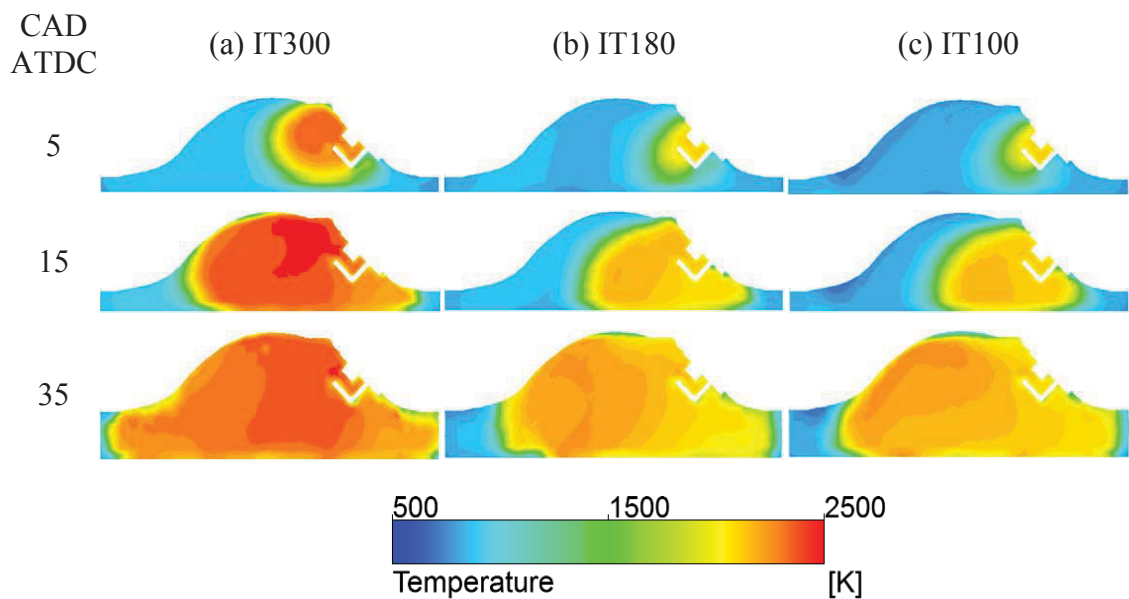


Figure 6.19: Spatial distributions of combustion temperature with different EDI timings

Figure 6.20 shows the distributions of flame brush, ethanol droplets, equivalence ratio and combustion temperature on a horizontal plane under the spark plug at EVO. Compared with IT300 condition, there are larger unburnt regions in IT180 and IT100 conditions. This is caused by the fuel not evaporated yet and poor quality of mixture at late EDI injection, resulting in a large proportion of unevaporated ethanol droplets during the combustion and uneven distribution of equivalence ratio.

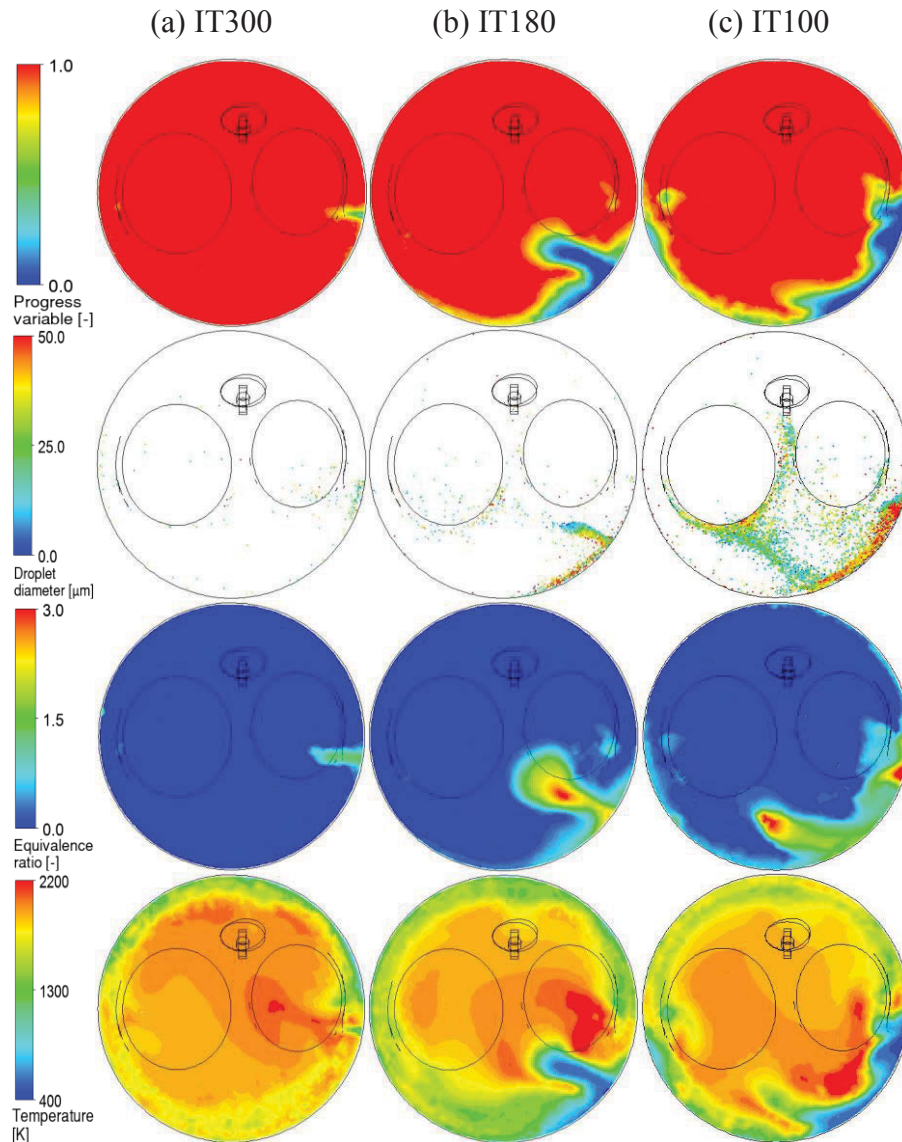


Figure 6.20: Distributions of flame brush, ethanol droplets, equivalence ratio and combustion temperature at EVO with different EDI timings

Figure 6.20 shows clearly that the regions in which the flame cannot propagate to are the regions where the ethanol droplets concentrate in. By the time of spark, 6.6% of ethanol fuel remains unevaporated in IT300 condition, 10.6% in IT180 and 55.2% in IT100 (Figure 6.14). As the flame propagating, most of the ethanol droplets have evaporated

and been burnt by the time of EVO at IT300. However, as shown in Figure 6.20, there are still some ethanol droplets remaining in the near wall regions with late EDI injections of IT180 and IT100. The high ethanol droplet concentration deteriorates the combustion process in two ways. Firstly, as shown in Figure 6.20, the ethanol droplets evaporate and lead to very rich mixture in the high concentration regions. When the equivalence ratio is higher than 2.0, the flame speed becomes very slow [102]. Secondly, the over-cooling effect becomes significant with late EDI injections. When ethanol droplets evaporate in the high concentration regions, they need a large amount of thermal energy for the phase change. This results in over-cooling effect in the corresponding regions. As shown in Figure 6.20, larger regions in IT180 and IT100 conditions have been cooled to as low as 400 K. Such a low temperature makes it more difficult for the flame to reach these regions.

Figure 6.21 shows the spatial distribution of the NO concentration at EVO. The formation of thermal NO is a result of high temperature ($>1800\text{K}$) and rich oxygen concentration. As shown in Figure 6.21, the high temperature regions shown in Figure 6.19 have the highest NO concentrations. The formation of NO emission becomes less intensive with the retarding of the EDI timing because of the reduced cylinder temperature. As shown in Figure 6.13, the measured indicated specific NO emission decreased from 10.14 g/kw-h in IT300 condition to 7.76 g/kw-h in IT180 condition and 6.58 g/kw-h in IT100 condition.

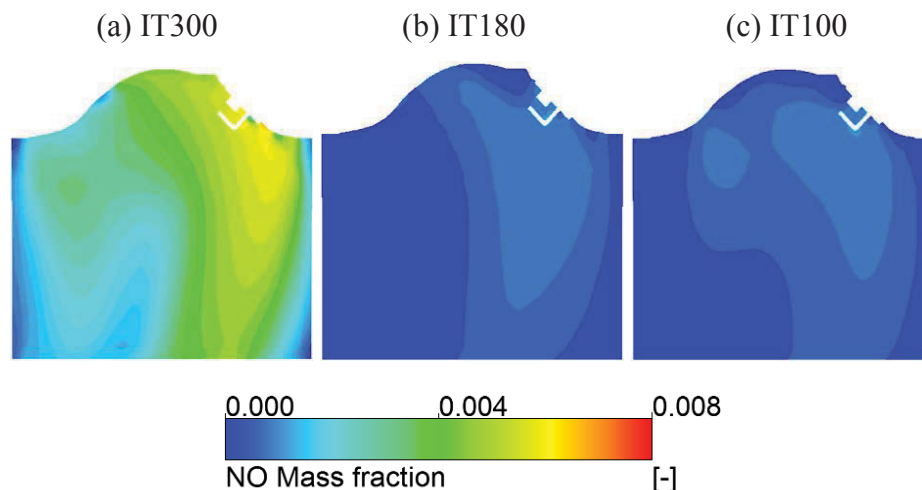


Figure 6.21: Distribution of NO mass fraction at EVO

CO is generated in rich mixture and high temperature conditions. Experimental results showed that the indicated specific CO and HC emissions increased from 151.13 and 1.98

g/kw-h to 188.67 and 5.04 g/kW-h respectively when injection timing was retarded from 300 to 100 CAD BTDC, as shown in Figure 6.13. This is mainly caused by the poor mixing (Figure 6.16) and wall-wetting (Figure 6.17) of late EDI injection. Figure 6.22 shows the distribution of CO concentration at EVO from simulation. It can be seen that the left region in the combustion chamber has the highest CO formation rate. This is because the mixture in these regions is richer than the stoichiometric equivalence ratio and there is not enough oxygen for a complete burning (Figure 6.16). Consequently CO is generated in incomplete combustion. The CO concentration is higher in late EDI injections (IT180 and IT100) than that in early EDI injection (IT300) due to the uneven mixture (Figures 6.16 and 6.20). Moreover, there are more liquid fuel droplets (Figure 6.20) and wall-film (Figure 6.17) in IT180 and IT100 conditions than that in IT300 condition. These will also contribute to the increased CO and HC emissions of late EDI timing conditions.

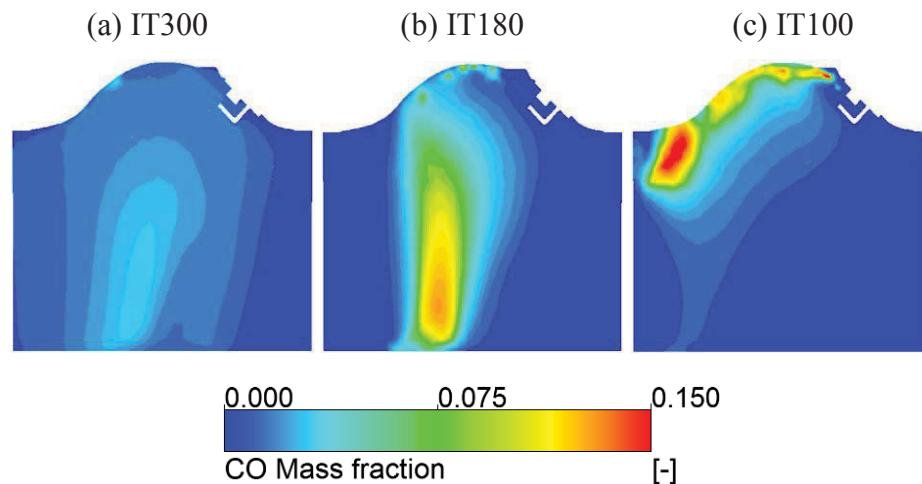


Figure 6.22: Distribution of CO mass fraction at EVO

6.4 Effect of small ethanol ratio on reducing fuel impingement

In the original proposal of EDI [11], only a small proportion of ethanol fuel was used to significantly reduce the consumption of gasoline fuel in SI engines by implementing engine downsizing technologies. Simulations are conducted to investigate the potential of direct injection of small amount of ethanol fuel on reducing the wall-wetting and incomplete combustion of late EDI timing at 100 CAD BTDC.

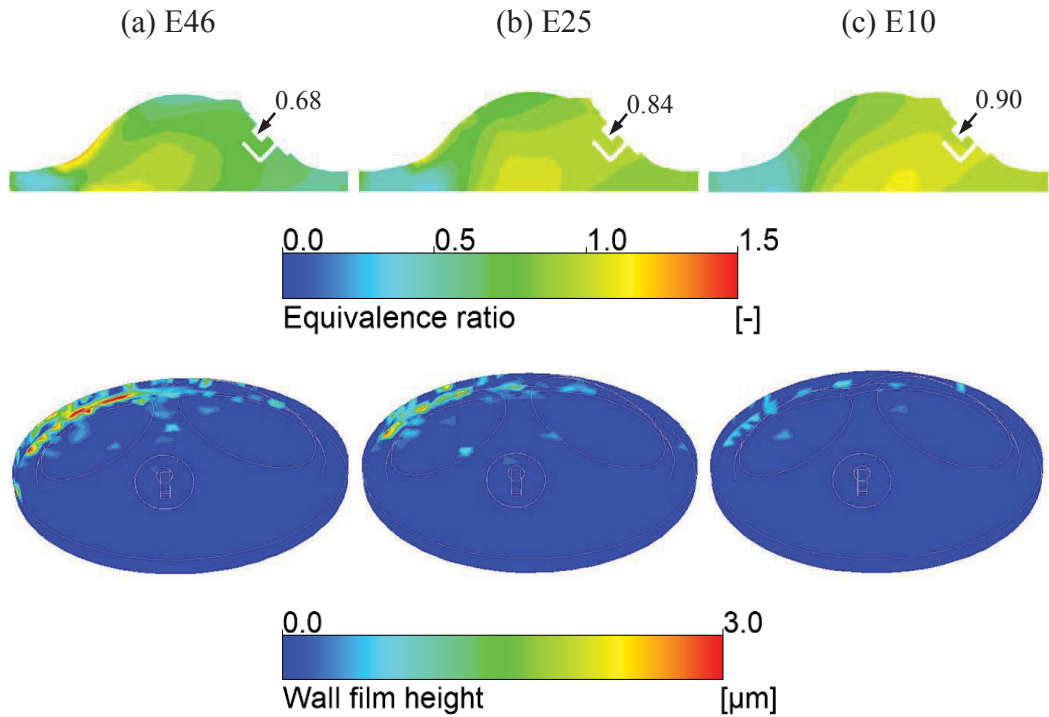


Figure 6.23: Distributions of the equivalence ratio and wall film of smaller amount of ethanol fuel at IT100 by spark timing

Figure 6.23 shows the distributions of equivalence ratio and wall film height of E46, E25 and E10 at the spark timing. As shown in Figure 6.23, the equivalence ratio around the spark plug increases due to the increase of gasoline vapour with the decrease of ethanol ratio. This should lead to readier ignition and consequently faster combustion. Meanwhile, the fuel impingement on the piston and cylinder walls becomes much less with smaller amount of EDI. The calculated wall-film mass reduces significantly from 0.733 mg in E46 to 0.330 mg in E25 and 0.071 mg in E10. This is because smaller amount of EDI requires shorter injection time, which reduces the spray penetration length and leads to less fuel impingement, resulting in reduced HC and soot emissions [119].

Figure 6.24 shows the spatial distributions of unburnt mixture, ethanol droplets and in-cylinder temperature at the time of EVO. When the ethanol ratio is reduced from E46 to E25 and then E10, the area of unburnt mixture ($c=0$) at EVO reduces significantly and the unevaporated ethanol droplets are greatly reduced. These should reduce the over-rich mixture and over-cooling regions as identified and discussed in Figure 6.20, and consequently reduce the HC and CO emissions. As shown in Figure 6.24, the local over-cooling regions with temperature lower than 400 K are reduced from E46 to E25 and eliminated at E10. Figures 6.23 and 6.24 suggest that the fuel impingement and

incomplete combustion caused by the local over-rich and over-cooling of late EDI timing can be addressed by direct injection of smaller amount of ethanol fuel, such as E25 and E10.

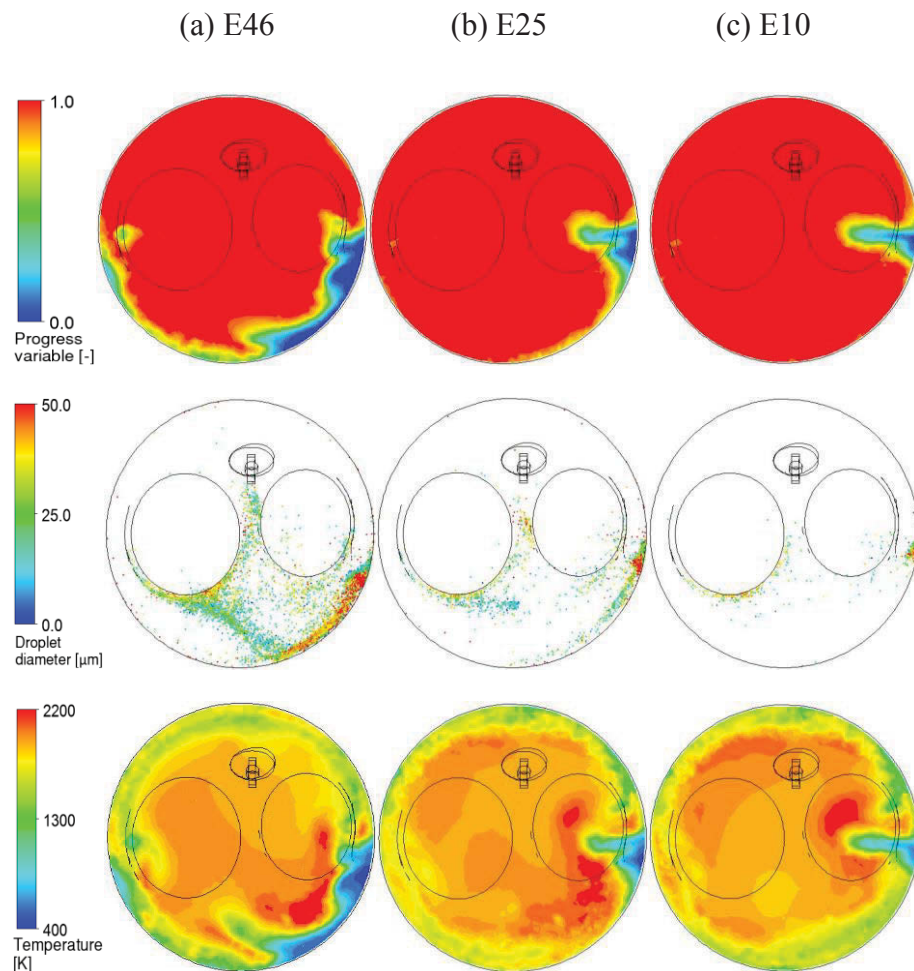


Figure 6.24: Distributions of flame brush, ethanol droplets and in-cylinder temperature of smaller amount of ethanol fuel at IT100 at the time of EVO

6.5 Summary

This chapter presented and discussed the numerical results of combustion and emission characteristics of the EDI+GPI engine, including the combustion process of dual-injection system, the effects of ethanol ratio and EDI timing on the combustion characteristics. The major results of this chapter can be concluded as follows.

- 1) The higher flame speed of ethanol fuel in the EDI+GPI condition contributed to the higher pressure rise rate and maximum cylinder pressure than that in GPI only condition, which consequently resulted in higher power output and thermal

efficiency. The IMEP was increased, and combustion initiation and major combustion durations were decreased when ethanol ratio was in the range of 0-58%. The combustion performance was deteriorated when the ethanol ratio was greater than 58%, indicated by decreased IMEP and increased combustion initiation and major combustion durations. This was caused by the over-lean mixture around the spark plug, local over-cooling and fuel impingement at high ethanol ratio conditions (>58%).

- 2) Compared with GPI only, the lower adiabatic flame temperature of ethanol, partially premixed combustion mode and stronger cooling effect of ethanol direct injection in EDI+GPI led to reduced combustion temperature which resulted in the decrease of NO emission. Among these three factors, the lower adiabatic flame temperature of ethanol and partially premixed combustion mode were the dominating factors that resulted in the low combustion temperature of EDI+GPI. The NO emission was decreased with the increase of ethanol ratio.
- 3) The CO and HC emissions were increased with the increase of ethanol ratio due to the incomplete combustion and increased fuel impingement on cylinder wall. The incomplete combustion was caused by the fact that ethanol fuel evaporated slowly in the low temperature environment before combustion, which consequently left a large number of liquid ethanol droplets concentrating in the near-wall region, resulting in locally over-cooled and over-rich mixture.
- 4) The experimental and numerical results showed that the IMEP, thermal efficiency and emission performance of this EDI+GPI engine could be the best in the range of ethanol ratio of 40-60%, resulted from the effective charge cooling and improved combustion efficiency while avoiding the wall wetting, over-lean and local over-cooling issues.
- 5) When EDI timing was retarded from 300 to 180 and 100 CAD BTDC, the mixture around the spark plug became leaner and the distribution of equivalence ratio became more uneven due to the slower in-cylinder flows and reduced time for ethanol fuel to evaporate and to mix with air. The combustion speed was decreased because of the leaner mixture around the spark plug when EDI timing was retarded. As a result, the IMEP and combustion temperature of IT180 and IT100 conditions were smaller than that of IT300 condition.

- 6) The fuel impingement on cylinder and piston walls became severe with the retarding of EDI timing because of the reduced combustion chamber volume and gas flow rate in the compression stroke. Moreover, late EDI timing caused over-cooling effect and over-rich mixture in the region opposite the spark plug, which consequently led to incomplete combustion. This explained why the HC emission increased at late EDI timing in the experimental investigation. The NO decreased with the retarding of EDI timing due to the reduced combustion temperature. The CO increased with the retarding of EDI timing due to the poor mixing process. The fuel impingement and incomplete combustion caused by the local over-rich and over-cooling of late EDI timing could be addressed by reducing the ratio of ethanol fuel to an appropriate point.

Chapter Seven

7 Effect of EDI Heating on Engine Performance

The above results of CFD modelling on the EDI+GPI engine and spray experiments in the constant volume chamber have illustrated that ethanol fuel evaporated slowly in low temperature environment, which resulted in the mixture unready for combustion by the time of spark and the consequent increase of CO and HC emissions. Moreover, the mixture becomes over-lean around the spark plug and local over-cooling and fuel impingement occur in high ethanol ratio conditions (>58%). As reviewed in Section 2.3.5, increasing the fuel temperature is an effective way to reduce the viscosity and surface tension and increase the vapour pressure of a liquid fuel, and consequently accelerate the spray break-up and evaporation rates. To address the emission issues in the current EDI+GPI engine, this work is carried out to investigate the potential of EDI heating on improving the combustion and emission characteristics of an SI engine equipped with the EDI+GPI system.

This chapter presents and discusses the experimental results in three sections. Section 7.1 reports the effect of EDI heating on the engine performance represented by IMEP and emissions of CO, HC and NO at the original engine spark timing of 15 CAD BTDC. In Section 7.2, the combustion characteristics are discussed to analyse the causes of the results at the original spark timing. Section 7.3 focuses on the effect of EDI heating enhanced by adjusting the spark timing to the MBT timing of 19 CAD BTDC.

7.1 Engine performance of EDI heating at original spark timing

Figure 7.1 shows the effect of ethanol fuel temperature on the IMEP of the EDI+GPI engine at different ethanol ratios and engine speeds. The spark timing was 15 CAD BTDC

which was the timing set for GPI only in the original engine control unit. As shown in Figure 7.1, the IMEP increases with the increase of ethanol ratio from 0% to 70% without EDI heating, resulting from the effective charge cooling effect and faster combustion speed of ethanol fuel. However, the IMEP decreases when the ethanol ratio is further increased from 70% to 100%. This is because the mixture becomes over-lean around the spark plug, and local over-cooling and severe fuel impingement occur at high ethanol ratios [108]. When the ethanol fuel temperature is increased from 50 °C to 70 °C, the IMEP decreases slightly at each ethanol ratio. It decreases noticeably at high ethanol ratios when the ethanol fuel temperature reaches 90 °C. The maximum reduction of IMEP at 3500 rpm is 2.2% at fuel temperature of 70 °C and 4.5% at 90 °C when the ethanol ratio is 70%. The maximum reduction of IMEP at 4000 rpm is 2.2% at 70 °C and 5.4% at 90 °C at the ethanol ratio of 70%. This is caused by the decrease of the combustion speed when the ethanol fuel is heated, which will be discussed referring to Figure 7.6.

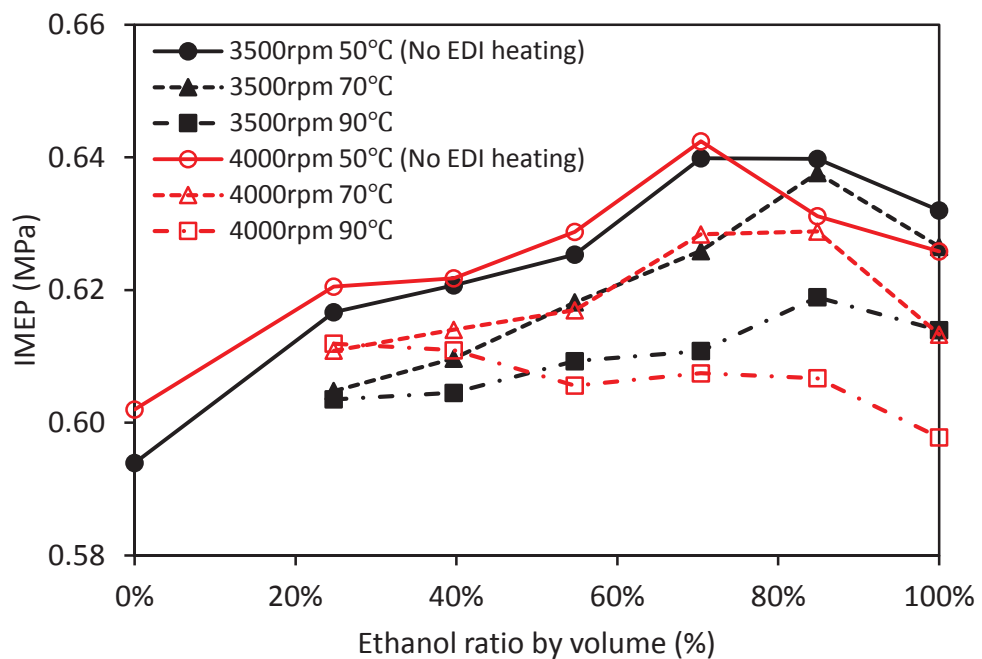


Figure 7.1: Effect of ethanol fuel temperature on the IMEP

Figure 7.2 shows the effect of ethanol fuel temperature on the indicated thermal efficiency. In the present study, the lambda was kept around one. As the air-fuel ratio of ethanol is 9.0 and that of gasoline is 14.8, 64% more mass of ethanol is injected to replace the reduced mass of gasoline fuel in order to keep the lambda at one. On the other hand, the heating value of gasoline fuel (42.9 MJ/kg) is 59% higher than that of ethanol fuel (26.9

MJ/kg). This indicates that the total energy input at each ethanol ratio condition is close to that of GPI only condition. Consequently, the effect of ethanol fuel temperature on the indicated thermal efficiency shows the same tendencies as that of IMEP in Figure 7.1. As shown in Figure 7.2, the thermal efficiency increases with the increase of ethanol ratio from 0% to 70% without EDI heating, but decreases when the ethanol ratio is further increased from 70% to 100%. When EDI heating is applied, the thermal efficiency decreases slightly at ethanol fuel temperature of 70 °C and decreases noticeably at 90 °C.

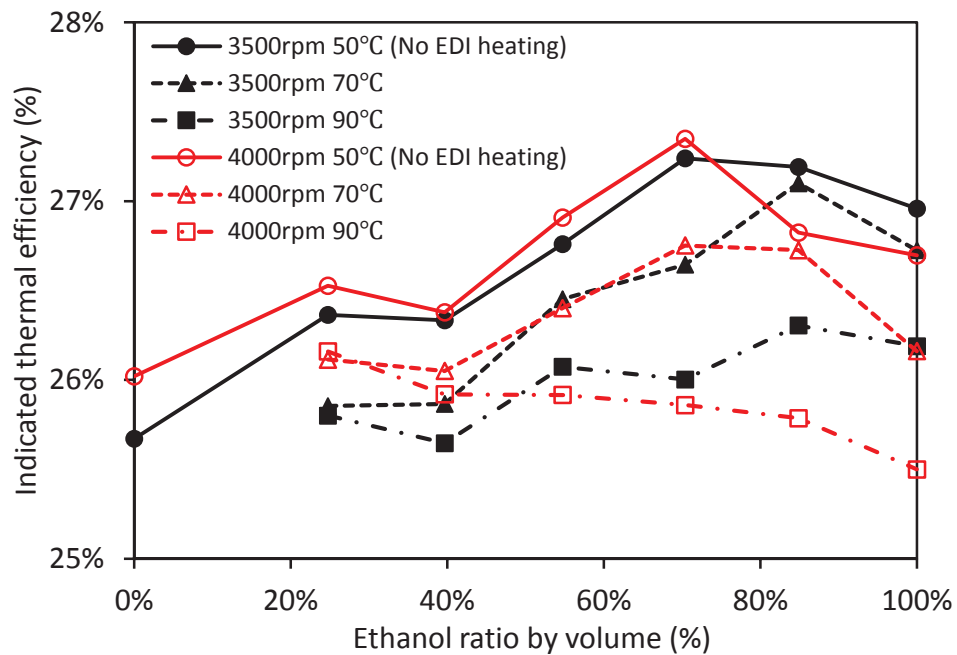


Figure 7.2: Effect of ethanol fuel temperature on the indicated thermal efficiency

Figures 7.3 and 7.4 show significant reduction of indicated specific carbon monoxide (ISCO) and hydrocarbon (ISHC) emissions with EDI heating. As shown in Figures 7.3 and 7.4, without EDI heating, both the ISCO and ISHC emissions increase with the increase of ethanol ratio due to the incomplete combustion caused by ethanol's poor evaporation, local over-cooling and fuel impingement of EDI [108]. When the ethanol fuel is heated, both ISCO and ISHC emissions are reduced significantly, and this reduction is enhanced with the increase of ethanol ratio. Compared with that without EDI heating, as shown in Figure 7.3, the ISCO emission is reduced by 21.8-43.2% at 3500 rpm and 11.1-30.6% at 4000 rpm when the ethanol fuel temperature is increased from 50 °C to 70 °C in the ethanol ratio range of 25-100%. The ISCO is reduced by 39.2-49.1% at 3500 rpm and 41.0-47.7% at 4000 rpm when the fuel temperature is increased from

50 °C to 90 °C. As shown in Figure 7.4, compared with that without EDI heating, the ISHC emission is reduced by 10.8-29.9% at 3500 rpm and 14.1-46.0% at 4000 rpm when the ethanol fuel temperature is increased from 50 °C to 70 °C. The ISHC is reduced by 15.7-38.1% at 3500 rpm and 20.6-61.2% at 4000 rpm when the fuel temperature is increased from 50 °C to 90 °C. Particularly, in low ethanol ratio conditions, EDI heating effectively reduces the CO (25-40% ethanol ratio) and HC (25-70% ethanol ratio) emissions to be lower than that in GPI only condition.

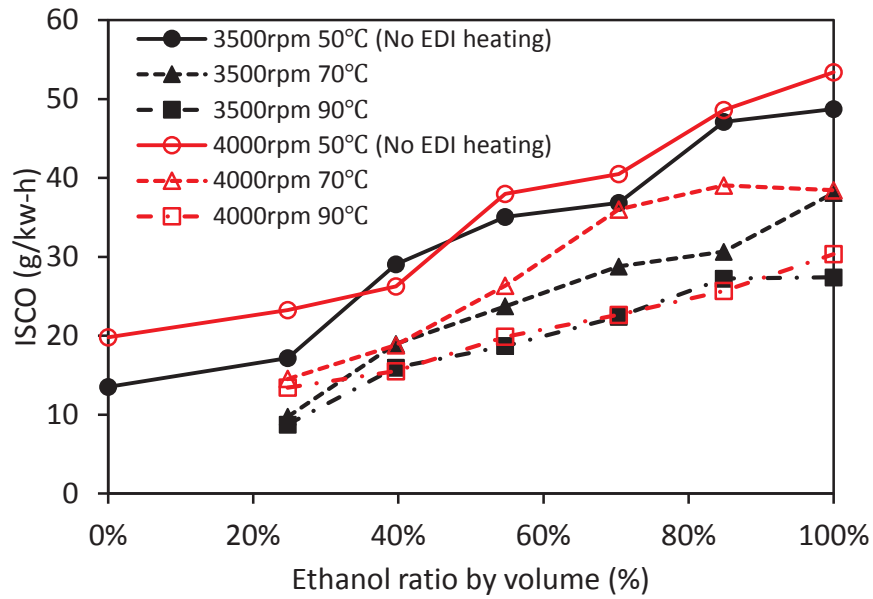


Figure 7.3: Variation of ISCO with ethanol fuel temperature

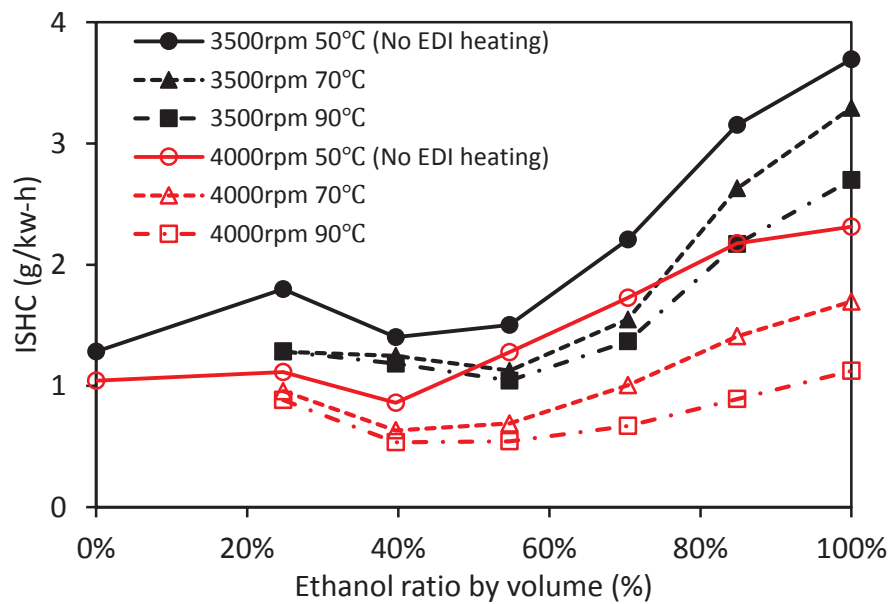


Figure 7.4: Variation of ISHC with ethanol fuel temperature

The reduction of ISCO and ISHC emissions can be attributed to the improved ethanol fuel's evaporation and mixing processes which are the original aims of EDI heating. As analysed in the numerical investigation of the same engine used in the present study [51, 108], the low evaporation rate of ethanol fuel resulted in a large number of ethanol droplets in the late compression and combustion strokes. The in-cylinder flows were slow and thus the heat and mass transfer between the liquid fuel and air were weak. This caused not only lean mixture around the spark plug, but over-rich mixture and over-cooling in the regions where the ethanol droplets were concentrated in. Moreover, the fuel impingement on the cylinder and piston walls became severe when the ethanol ratio was high, due to the longer spray penetration length of longer injection duration. The uneven distribution of mixture, local over-cooling effect, unburnt liquid ethanol droplets and fuel impingement caused the increase of ISCO and ISHC emissions with the increase of ethanol ratio in the engine conditions without EDI heating. However, when EDI heating is applied, the evaporation of ethanol fuel should be accelerated. As a result, the liquid ethanol droplets, local over-cooling and fuel impingement during combustion process should be reduced, resulting in the reduction of ISCO and ISHC emissions. Figure 7.8 shows the EDI spray images taken in a constant volume chamber. It shows that the EDI spray tip penetration is slightly decreased due to the enhanced evaporation and spray-air interaction when the ethanol fuel is heated from 52 °C to 92 °C. Moreover, more fuel in the spray will be in vapour phase when the fuel is heated than that without fuel heating. Fuel impingement will not occur when vapour fuel reaches the cylinder wall. Significant reduction of CO and HC emissions was also reported in the investigation of pre-heating the ethanol fuel in cold start conditions [168-170, 192].

Figure 7.5 shows the effect of EDI heating on indicated specific nitric oxide (ISNO) emission. As shown in Figure 7.5, the influence of EDI heating on ISNO is insignificant. With or without EDI heating, the ISNO emission reduces quickly with the increase of ethanol ratio due to the stronger cooling effect of EDI and lower combustion temperature of ethanol fuel [51, 188]. When EDI heating is applied, the ISNO emission increases slightly at each ethanol ratio condition. This may be caused by the increased combustion temperature resulted from the heated fuel. However, even with EDI heating, the ISNO emission is still much smaller than that of GPI only condition. The slight increase of NO emission by fuel heating was also observed for ethanol fuelled engines in cold start conditions [168, 169, 193].

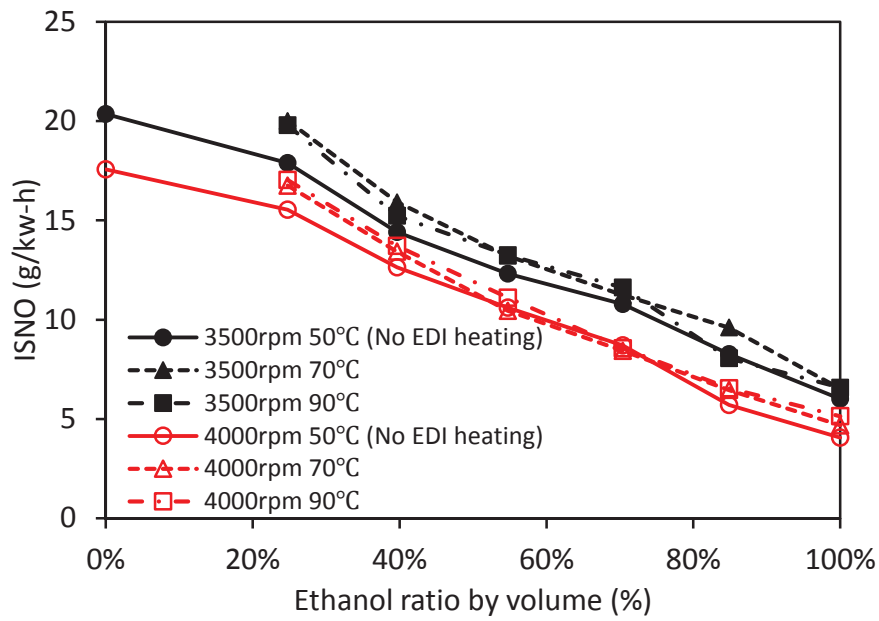


Figure 7.5: Variation of ISNO with ethanol fuel temperature

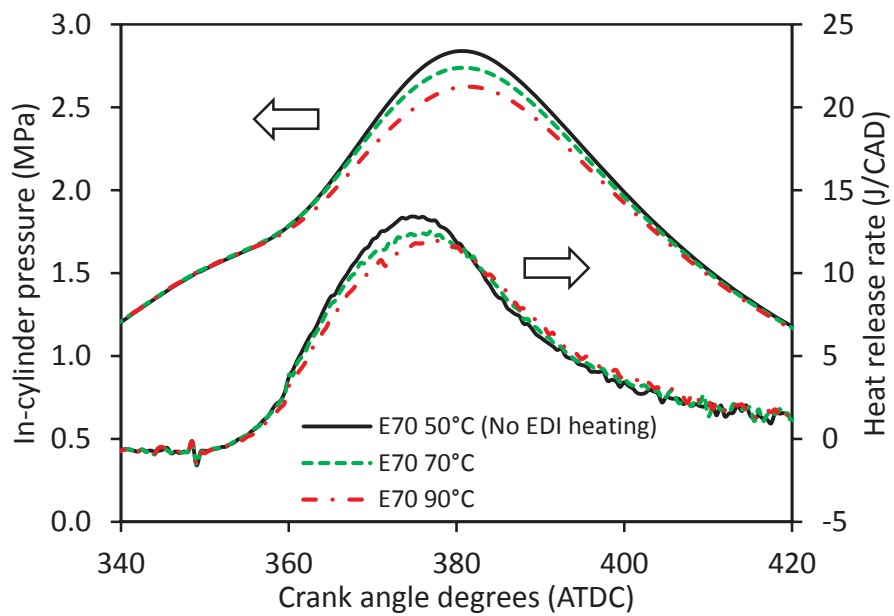


Figure 7.6: Effect of ethanol fuel temperature on the in-cylinder pressure and heat release rate

7.2 Combustion characteristics of EDI heating at original spark timing

Figure 7.6 shows the in-cylinder pressure and the corresponding heat release rate (HRR) at the ethanol fuel temperatures of 50 °C (no fuel heating), 70 °C and 90 °C. The engine

speed is 3500 rpm and the ethanol ratio is 70%. As shown in Figure 7.6, the starting phase of HRR is not affected by the ethanol fuel temperature. However, HRR reduces with the increased fuel temperature after that, indicating slower combustion speed. As a result, the peak in-cylinder pressure is reduced during the combustion process with the increase of ethanol fuel temperature. This reduced peak pressure was also observed in compression-ignition engines fuelled with heated rapeseed methyl ester (RME) [167], dimethyl ether (DME) [194], diesel and cetane [195].

The decrease of combustion speed with increased ethanol fuel temperature may be caused by the following two causes. Firstly, the fuel viscosity, surface tension and density decreasing with the increased fuel temperature should have affected the injection process. When the ethanol fuel temperature is increased from 50 °C to 90 °C, the density of the ethanol fuel decreases from 763 to 721 kg/m³, viscosity decreases from 0.676 to 0.374 mPa-s, and surface tension decreases from 0.0202 to 0.0152 N/m [100]. Experiments and simulations on the fuel injection process showed that, when the fuel temperature was increased, the actual injection timing was retarded, the peak rail pressure was decreased and the injection duration was prolonged [194, 196]. The fuel mass flow rate was decreased with the increase of fuel temperature because of the decreased fuel density [167, 197, 198]. Furthermore, the size of vapour bubbles at the injector's nozzle exit increased with the increase of the fuel temperature [199], which would decrease the nozzle discharge coefficient. All these factors reduced the mass of ethanol fuel directly injected into the combustion chamber when the ethanol was heated in the present study. This has been evidenced by the slight increase of lambda with the increase of fuel temperature in the experiments. Figure 7.7 shows the variation of measured lambda values with ethanol fuel temperature at different ethanol ratios. As described in Section 3.3.4, to compare the results with and without EDI heating, the throttle opening, injection pressure and pulse width were kept unchanged at each engine speed and ethanol ratio. So that the intake airflow rates were the same in both test conditions with and without EDI heating. As shown in Figure 7.7, the lambda increases slightly with the increase of fuel temperature at each ethanol ratio and the change becomes more significant at high ethanol ratios. At ethanol ratio of 100%, the lambda increases by about 2% for every 20 °C of fuel temperature increase at the two tested engine speeds. The reduction of ethanol fuel supply might lead to the decrease of IMEP by EDI heating. This suggests that the injection pulse

width should be increased to get the lambda back to one when implementing EDI heating in order to avoid the decrease of IMEP.

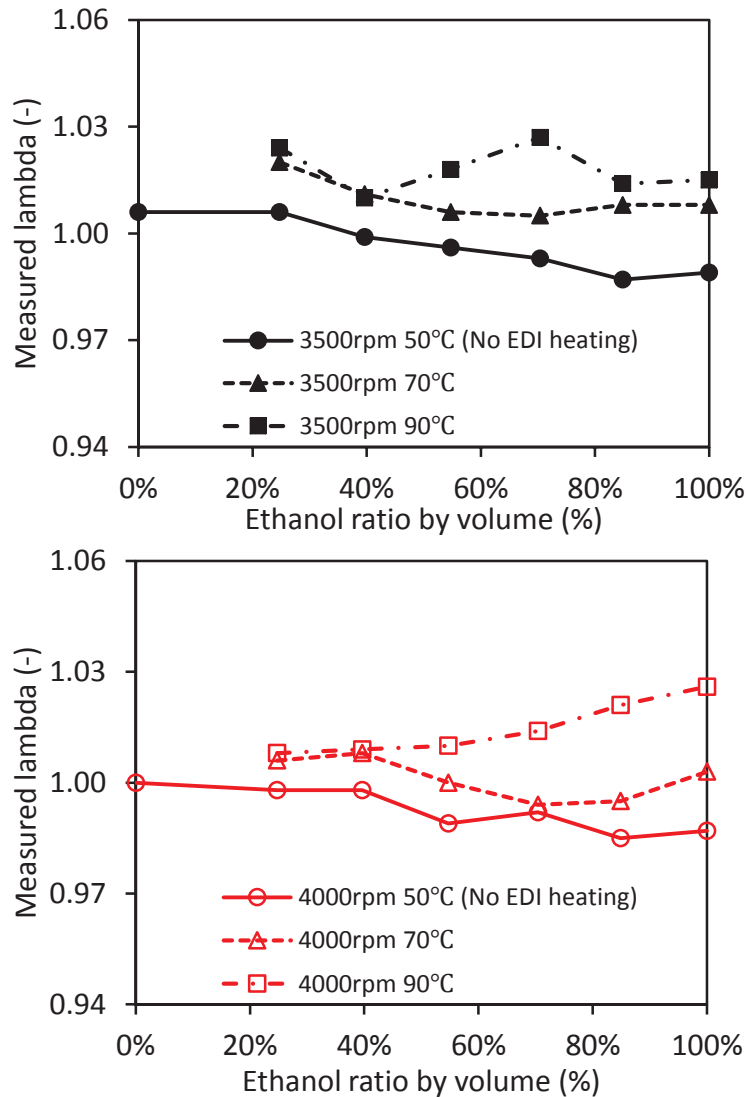


Figure 7.7: Variation of lambda with ethanol fuel temperature

The second cause to the reduced IMEP is that the fuel spray process might be changed by flash-boiling which is a phenomenon occurs when the fuel temperature is higher than the saturation temperature of the fuel at the ambient pressure. Experiments showed that the multi-jet spray might collapse to a single-jet spray when flash-boiling occurred by either increasing the fuel temperature or decreasing the ambient pressure [109, 110, 117]. The EDI injector used in the present study was a six-hole nozzle. Figure 7.8 shows the spray structures of the EDI injector at 2.0 ms after the start of injection in a constant volume chamber at three ethanol fuel temperatures of 52 °C, 77 °C and 92 °C [132]. The injection

pressure was 6 MPa and the ambient pressure was 0.1 MPa, which reproduced the in-cylinder conditions of early EDI injection in the present engine experiments. As shown in Figure 7.8, the two side plumes of the ethanol spray converge towards the middle one when the fuel temperature is increased from 52 °C to 77 °C. The three spray plumes collapse completely when the temperature reaches 92 °C. As described in Section 3.3.1, the EDI injector has a spray bent angle of 17° and was installed with the spray plumes bent towards the spark plug in the EDI+GPI engine to create an ignitable mixture around the plug gap by the time of ignition. However, the results in Figure 7.8 showed that the spray was not collapsed at 52 °C or 77 °C, but collapsed only at 92 °C. The collapsed spray might deform the designed fuel distribution in the combustion chamber, and consequently slow down the ignition and combustion processes, resulting in the reduced peak cylinder pressure and heat release rate as shown in Figure 7.6.

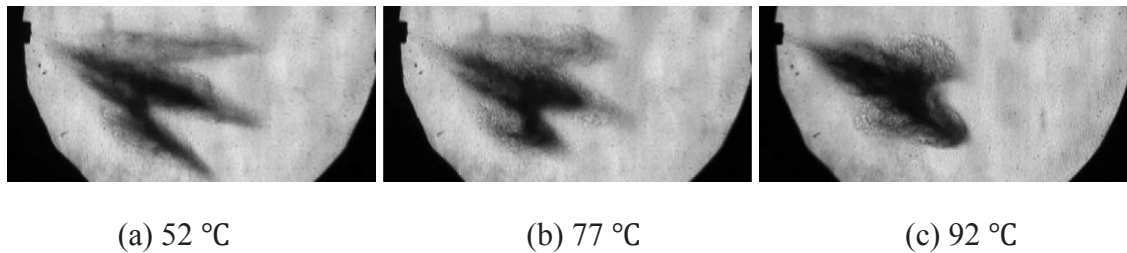


Figure 7.8: Effect fuel temperature on the EDI spray structure

Figure 7.9 shows the variation of combustion initiation duration (CA0-10%) with ethanol fuel temperature at different ethanol ratios at the original spark timing of 15 CAD BTDC. CA0-10% is directly related to the combustion stability. Shorter CA0-10% means more stable combustion [81]. As shown in Figure 7.9, without EDI heating, the CA0-10% at ethanol ratio in the range of 25-70% is shorter than that in GPI only condition. This indicates an improved combustion stability with ethanol ratio up to 70%. It can be attributed to the faster flame speed of ethanol fuel. However, the CA0-10% increases when the ethanol ratio is higher than 70%. This may be because the mixture was too lean due to the low evaporation rate of ethanol fuel and local over-cooling and fuel impingement occurred in high ethanol ratio conditions [108]. As shown in Figure 7.9, the ethanol ratio of 70% at which the CA0-10% starts to increase has been extended to 85% with EDI heating. With EDI heating, the CA0-10% is shorter than that without EDI heating when the ethanol ratio is greater than 70%. This may be because EDI heating supplies additional thermal energy required by the ethanol droplets to evaporate, which

reduces the over-cooling problem in higher ethanol ratio conditions. However, the CA0-10% with EDI heating is longer than that without EDI heating when the ethanol ratio is less than 70%. This may be due to the reduced mass of ethanol fuel injected and spray collapse, as discussed for the results in Figures 7.7 and 7.8.

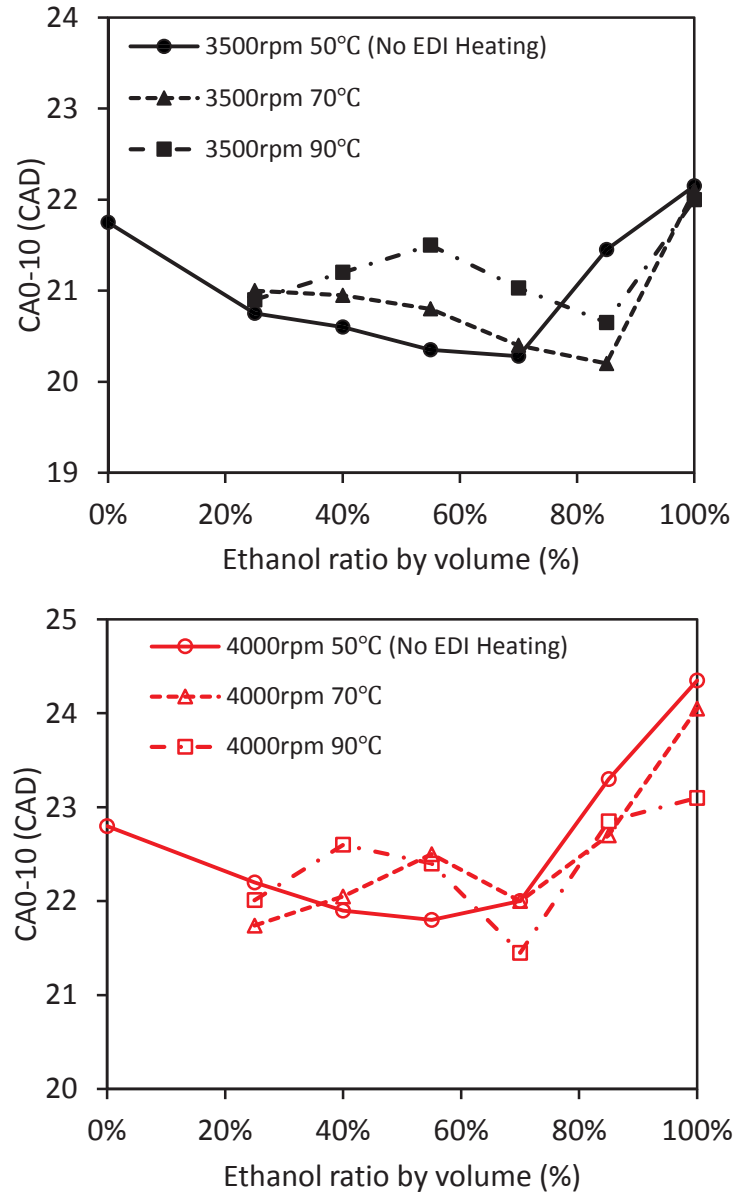


Figure 7.9: Variation of CA0-10% with ethanol fuel temperature

Figure 7.10 shows the effect of ethanol fuel temperature on the major combustion duration (CA10-90%) at different ethanol ratios at the original spark timing of 15 CAD BTDC. The shorter the CA10-90% is, the closer the combustion process is to the constant volume process which consequently results in higher thermal efficiency [81]. As shown in Figure 7.10, in general, the CA10-90% is longer with EDI heating than that without

EDI heating. Consistently with the causes to the longer initial combustion duration, the combustion speed is decreased by the the reduced mass of ethanol fuel and the deformation of ethanol spray structure when EDI heating is applied. Less mass of ethanol fuel injected makes the mixture leaner which slows down the combustion speed. Moreover the deformation of ethanol spray changes the designed in-cylinder mixture distribution and consequently results in longer combustion duration.

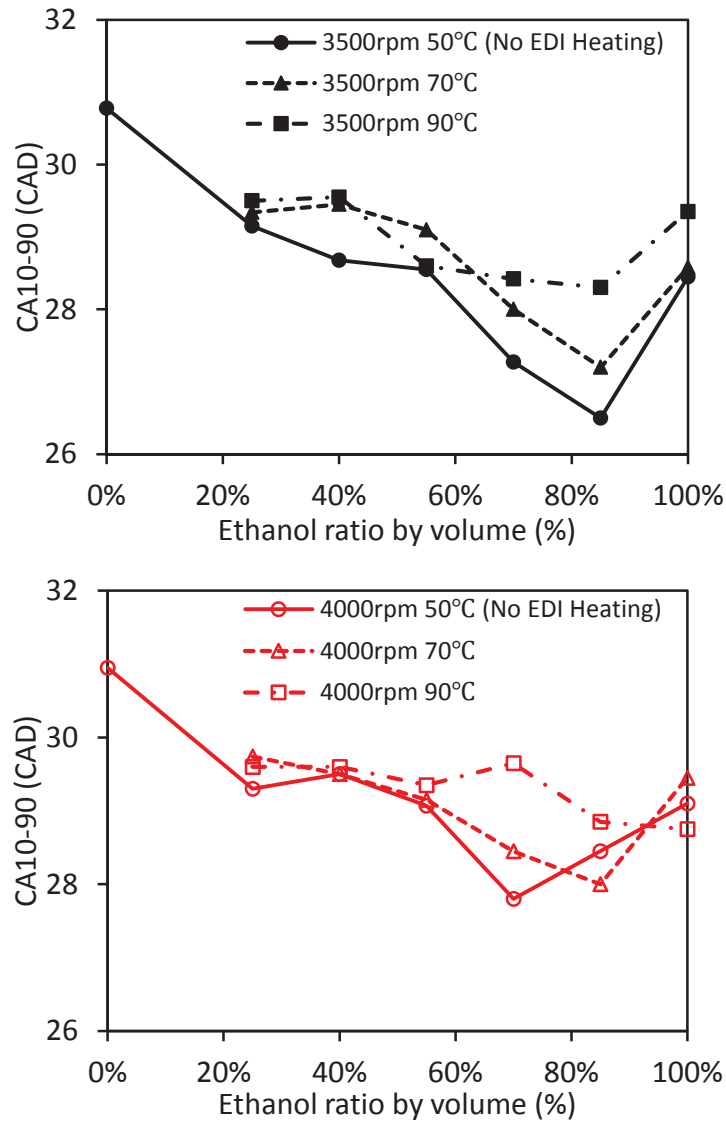
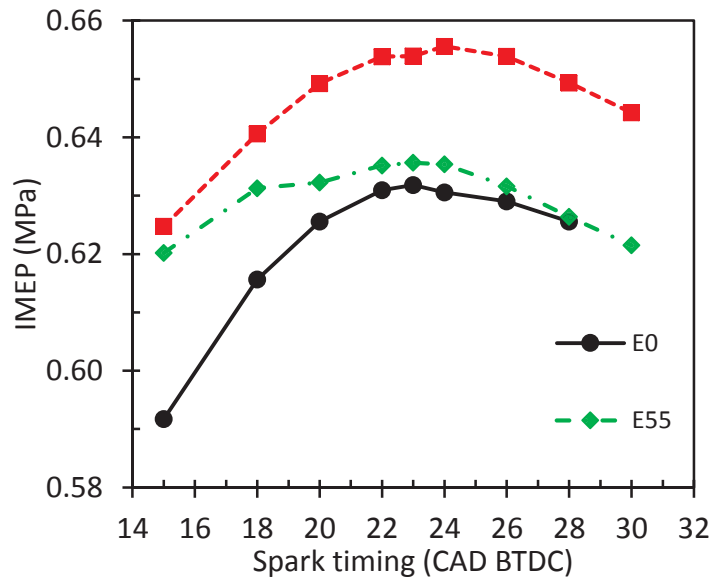


Figure 7.10: Variation of CA10-90% with ethanol fuel temperature

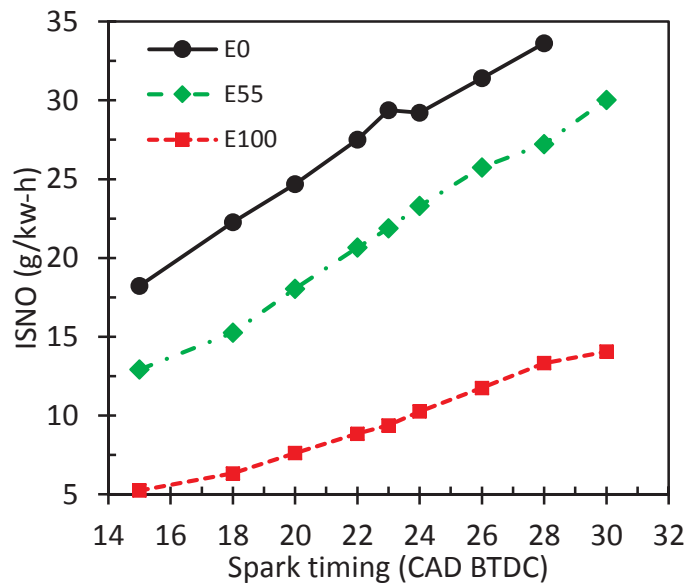
7.3 Engine performance of EDI heating at MBT timing

As shown in Figures 7.3 and 7.4, the CO and HC emissions were reduced effectively by EDI heating. However, the IMEP was reduced when EDI heating was applied. As

analysed in Section 7.2, the decrease of IMEP may be due to the change in combustion phase and the associated decrease of combustion speed. To recover the IMEP, experiments were conducted to find the ‘best’ spark timing when EDI heating was applied to the EDI+GPI engine. This section reports the effect of EDI heating on the engine performance at the minimum spark advance for best torque (MBT) timing.



(a)



(b)

Figure 7.11: Effect of spark timing on IMEP (a) and NO emission (b) at ethanol ratios of 0%, 55% and 100%

Figure 7.11 shows the variations of IMEP and NO emission with spark timing. The engine speed is 3500 rpm and the three ethanol ratios are 0% (GPI only), 55% (EDI+GPI) and 100% (EDI only). As shown in Fig 7.11(a), the IMEP increases quickly with the advance

of spark timing from 15 to 22 CAD BTDC. It becomes stable at the spark timing of 22 to 24 CAD BTDC and then decreases with further advance of spark timing. The maximum IMEP can be achieved at the spark timing around 23 CAD BTDC for the designated three ethanol ratios. As shown in Figure 7.11(b), the NO emission increases sharply with the advance of spark timing. This suggests that if the spark timing is slightly retarded from the maximum IMEP timing, the engine output power would hardly suffer but the NO emission would be significantly reduced. Moreover, slight knock occurs when the spark timing is earlier than 24 CAD BTDC in GPI only condition. Therefore, the MBT timing is defined as a spark retard of 4 degrees from the angle of maximum IMEP [200]. Based on this definition, the MBT timing is 19 CAD BTDC in the present study.

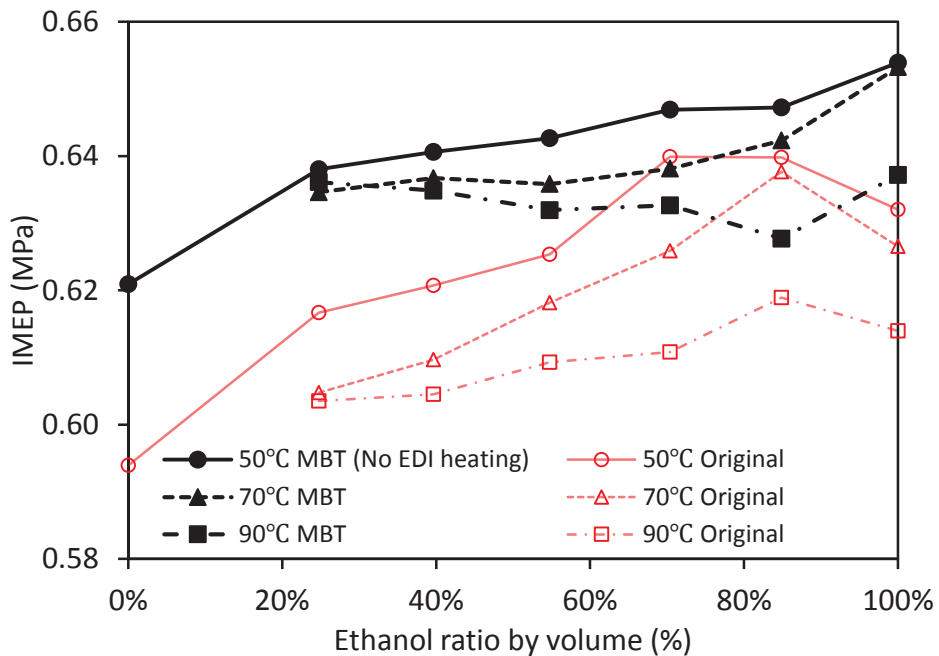


Figure 7.12: Effect of EDI heating on IMEP at the MBT timing

Figure 7.12 shows the variation of IMEP with ethanol fuel temperature. The spark timing is the MBT timing and the engine speed is 3500 rpm. As shown in Figure 7.12, the IMEP increases continuously with the increase of ethanol ratio in the entire range from 0% to 100%. This implies that the decrease of IMEP in high ethanol ratio conditions (as shown in Figure 7.1) can be avoided by adjusting the spark timing. When the ethanol fuel temperature is increased from 50 °C to 70 °C, the IMEP is lower than that without EDI heating but still increases with the increase of ethanol ratio. However, IMEP becomes to decrease with the ethanol ratio and noticeably lower than that at 50 °C and 70 °C in high ethanol ratio conditions when the fuel temperature is further increased to 90 °C. This may

be caused by the decrease of fuel supply and collapse of spray when the fuel temperature is too high like 90 °C, as discussed in Section 7.2. The maximum reduction in IMEP is 0.8% at ethanol fuel temperature of 70 °C and 3.0% at 90 °C at the ethanol ratio of 85% which is much smaller than that at the original spark timing of 15 CAD BTDC.

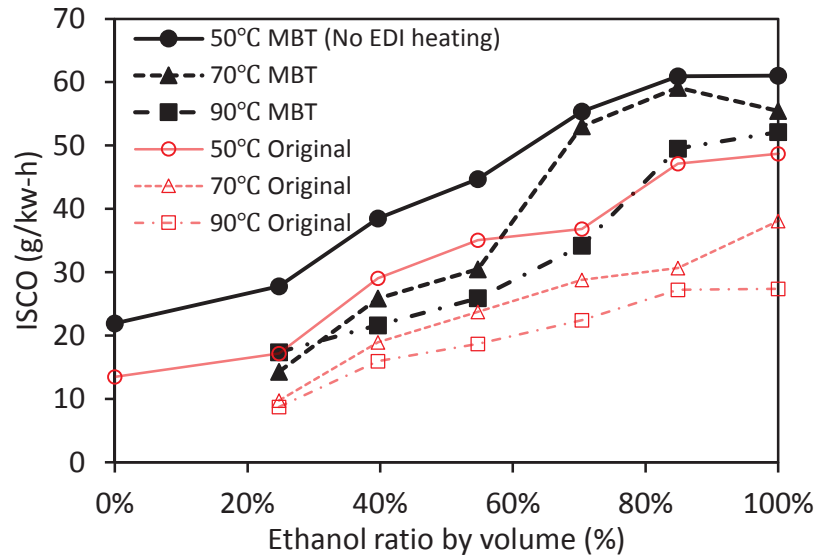


Figure 7.13: Effect of EDI heating on ISCO at the MBT timing

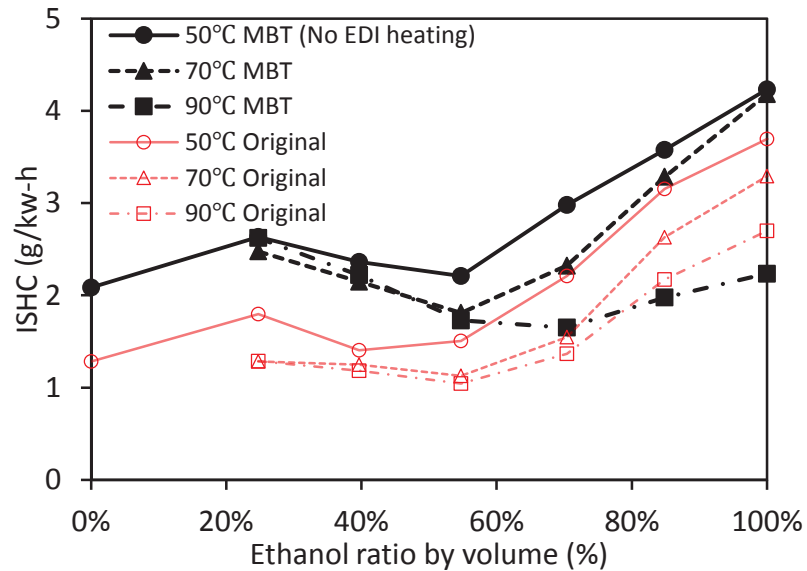


Figure 7.14: Effect of EDI heating on ISHC at the MBT timing

Figures 7.13, 7.14 and 7.15 shows the effect of EDI heating on the emissions of ISCO, ISHC and ISNO at the MBT spark timing. Comparison based on spark timing shows that the CO, HC and NO emissions at MBT timing are slightly higher than that at the original spark timing of 15 CAD BTDC. However, compared with that without EDI heating, both

ISCO and ISHC emissions at MBT timing are significantly reduced and this reduction is enhanced by the increase of ethanol fuel temperature. The maximum reduction is 15% for ISCO and 47% for ISHC at E100 when the ethanol fuel temperature is increased from 50 °C to 90 °C. Particularly, the ISHC emission reduces significantly in the ethanol ratio range of 70-100% at the ethanol fuel temperature of 90°C. Meanwhile, the ISNO emission is slightly increased by EDI heating, as shown in Figure 7.15. However this increase does not offset the ISNO reduction caused by the strong cooling effect and low combustion temperature of EDI.

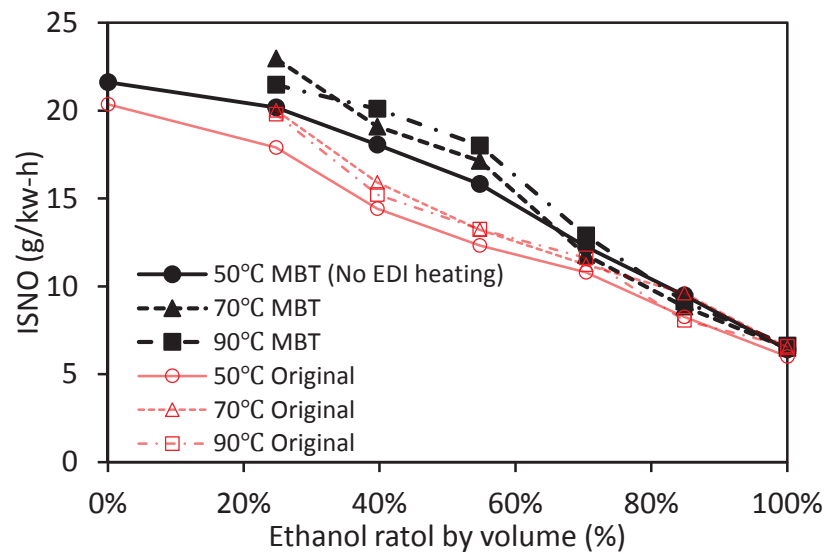


Figure 7.15: Effect of EDI heating on ISNO at the MBT timing

7.4 Summary

Based on the conclusions gained from the CFD simulation, heating the ethanol fuel to be injected directly was proposed to address the slow evaporation and poor mixing issues in the EDI+GPI engine. Experiments were conducted to investigate the effect of EDI heating on improving the combustion and emission performance of a single-cylinder SI engine equipped with EDI+GPI. The major results of this chapter can be concluded as follows.

- 1) At the original engine's spark timing of 15 CAD BTDC, EDI heating effectively reduced the ISCO and ISHC emissions due to increased ethanol's evaporation rate, and reduced fuel impingement and local over-cooling effect. The reduction of ISCO and ISHC was enhanced with the increase of ethanol ratio. When the ethanol fuel

was heated from 50 °C to 90 °C, the ISCO was reduced by 43% and the ISHC was reduced by 51% in EDI only condition. On the other hand, the ISNO emission was slightly increased, but still much smaller than that in GPI only condition due to EDI's strong cooling effect and low combustion temperature. However, the IMEP and combustion speed were slightly reduced by EDI heating. The largest decrease of IMEP was about 5% at the ethanol ratio of 70% when ethanol fuel temperature was increased from 50 °C to 90 °C.

- 2) At the MBT spark timing of 19 CAD BTDC, the IMEP increased with the increase of ethanol ratio in the entire range from 0% to 100%. This indicated that the decrease of IMEP in high ethanol ratio conditions at the original spark timing of 15 CAD BTDC was avoided by adjusting the spark timing. When the ethanol fuel temperature was increased from 50 °C to 90 °C, the ISCO was reduced by 15% and ISHC was reduced by 47% in EDI only condition. Meanwhile, the reduction of IMEP by EDI heating was less than 3% which was smaller than that at the original spark timing.
- 3) When the ethanol fuel temperature was increased to the flash-boiling region, the ethanol spray collapsed which deformed the designed fuel distribution in the combustion chamber and consequently deteriorated the combustion process. Meanwhile, the mass of fuel injected into the cylinder decreased when the ethanol fuel was heated, resulted from the decreased fuel density, viscosity, surface tension and injector discharge coefficient. As a result, the IMEP and combustion speed were slightly decreased by EDI heating.
- 4) Results indicate that EDI heating is effective to address the issues of ethanol's low evaporation rate in low temperature engine environment and over-cooling effect at high ethanol ratio condition in the development of EDI+GPI engines in terms of minimizing the engine emissions.

Chapter Eight

8 Conclusions and Future Work

8.1 Conclusions

To contribute to the development of EDI+GPI, CFD simulations and experiments have been conducted to investigate the mixture formation and combustion processes of an EDI+GPI engine. Numerical simulations were performed using the commercial CFD code ANSYS FLUENT as a platform. Experiments were performed in a constant volume chamber and on an EDI+GPI research engine.

The experiments conducted in a constant volume chamber were aimed to investigate the effect of fuel temperature on the EDI spray and evaporation characteristics in non-evaporating, transition and flash-boiling conditions and to verify the CFD model of the EDI+GPI engine. The major conclusions of the spray experiments can be drawn as follows.

- 1) The interactions between the plumes and between the plume and air were enhanced by increased fuel temperature. With the increase of fuel temperature, the plumes became wider, the spray boundary became more turbulent, and the first and third plume groups collapsed towards the middle one. The macroscopic characteristics of non-evaporating sprays were similar to that of normal-evaporating sprays at temperature lower than ethanol fuel's boiling temperature. Significant changes occurred with flash-boiling sprays. The spray tip penetration became slightly longer, while the spray angle and projected area became much smaller.
- 2) The evaporation rate did not improve much when the fuel temperature was increased from 275 K to 325 K. Significant increase of evaporation rate occurred when the fuel temperature was higher than 350 K. The low evaporation rate of

ethanol fuel in low fuel temperature implied that EDI should be only applied in high temperature engine environment.

- 3) The flash-boiling (droplet explosion) did not occur when the fuel temperature was higher than the boiling point until the excess temperature reached 14 K. When excess temperature was smaller than 4 K, the sprays behaved the same as subcooled sprays did. The sprays collapsed at excess temperature of 9 K. The spray collapse temperature was dependent on the spray angle of the injector, where injectors with larger spray angles had higher transition temperatures.

A full cycle CFD model including both PI and DI sprays was developed to investigate the in-cylinder flows, spray evaporation and mixing, charge cooling effect, fuel impingement, combustion and emission formation processes of the EDI+GPI engine. The major conclusions of the engine modelling can be drawn as follows.

- 1) Modelling the spray combustion of EDI+GPI is a difficult task because it is a typical example of partially premixed SI combustion and the distributions of the two fuels at each computational grid vary. To model the EDI+GPI engine, the combustion process was modelled with the ECFM partially premixed combustion concept in which both the mixture fraction and progress variable were solved. The turbulence-chemistry interaction of the two-fraction-mixture combustion was solved by a five-dimensional presumed double-delta PDF look-up table. By doing so, it overcame a major limitation in the current modelling of dual-injection system, which did not include the fuel port injection process but assumed that the port injected fuel was homogenous in the combustion chamber before combustion or IVC.
- 2) The simulation results showed that the combustion process of EDI+GPI was partially premixed combustion because of the low evaporation rate of ethanol spray in low temperature environment before combustion. Compared with GPI only, the higher flame speed of ethanol fuel contributed to the greater pressure rise rate and maximum in-cylinder pressure in EDI+GPI condition, which consequently resulted in higher thermal efficiency. The lower adiabatic flame temperature of ethanol, partially premixed combustion mode and stronger cooling effect of ethanol direct injection in EDI+GPI led to the reduced combustion temperature which contributed to the decrease of NO emission. Among these three factors, the lower adiabatic flame temperature and partially premixed combustion mode were the dominating

factors that resulted in the low combustion temperature of EDI+GPI. On the other hand, CO and HC emissions increased because of the ethanol's low evaporation rate, which caused incomplete combustion.

- 3) The IMEP was increased, combustion initiation duration and major combustion duration were decreased when ethanol ratio was in 0-58% due to the faster combustion speed of ethanol fuel and the charge cooling effect enhanced by EDI. When the ethanol ratio was greater than 58%, the combustion was deteriorated by over-cooling and fuel impingement and the CO and HC emissions were increased due to incomplete combustion. Experimental and numerical results showed that the thermal efficiency, charge cooling effect and emissions of this EDI+GPI engine could be the best in the range of ethanol ratio of 40-60%.
- 4) When the EDI timing was retarded from 300 to 180 and 100 CAD BTDC, the mixture around the spark plug became leaner and the distribution of equivalence ratio became more uneven. Moreover, late EDI timing resulted in severe fuel impingement and caused local over-cooling effect and over-rich mixture. Consequently, the combustion speed and temperature were decreased by retarded EDI timing, leading to the reduced NO emission and increased HC and CO emissions. The fuel impingement and incomplete combustion caused by the local over-rich and over-cooling of late EDI timing could be addressed by reducing the ethanol ratio.

Experiments on the EDI+GPI engine were conducted to verify the idea of EDI heating on improving the engine performance, which was developed based on the understanding gained from the numerical investigation. The ethanol fuel temperature was increased from 50 °C (no EDI heating) to 70 °C and 90 °C (flash-boiling spray). The effect of EDI heating on the engine performance was investigated at both the original spark timing of 15 CAD BTDC and the MBT timing of 19 CAD BTDC. The major conclusions of the EDI heating experiments can be drawn as follows.

- 1) EDI heating effectively reduced the CO and HC emissions of the engine due to the increase of evaporation rate and reduced fuel impingement and local over-cooling. The reduction of CO and HC became more significant with the increase of ethanol ratio. When the temperature of the ethanol fuel was increased from 50 °C to 90 °C, the CO and HC were reduced by as much as 43% and 51% respectively in EDI only

condition at the original spark timing, and 15% and 47% respectively at the MBT timing. On the other hand, the NO emission was slightly increased, but still much smaller than that in GPI only condition due to the strong cooling effect and low combustion temperature of EDI.

- 2) The IMEP and combustion speed were slightly reduced by EDI heating due to the decrease of injector fuel flow rate and spray collapse of flash-boiling. The largest decrease of IMEP was 5% at the original spark timing and 3% at the MBT timing. Moreover, at the MBT timing, the IMEP increased continuously with the increase of ethanol ratio in the entire range from 0% to 100%. This indicated that the decrease of IMEP in high ethanol ratio conditions at the original spark timing could be avoided by adjusting the spark timing.
- 3) The experimental results indicated that EDI heating was effective to address the issues of ethanol's low evaporation rate in low temperature environment and over-cooling effect at high ethanol ratio condition in the development of EDI+GPI engine in terms of minimizing the engine emissions.

8.2 Suggestions for future work

Based on the current research facilities and conclusions, a more detailed study may be needed in the following aspects.

Firstly, experiments in the constant volume chamber showed the correlations between the spray excess temperature and the spray transition process. When the excess temperature was smaller than 4 K, the spray behaved the same as subcooled spray did. The spray collapsed at excess temperature of 9 K and flashed boiled when excess temperature reached 14 K. However, more experimental works are needed to validate the applicability of these correlations. For example, it will be interesting to investigate the spray transition process with more liquid fuels in different injection pressures or ambient pressures. Besides, experimental results showed that although the physical properties of ethanol and gasoline fuels are very different, the macroscopic spray characteristics of the two fuels were quite similar in terms of spray tip penetration, spray projected area and spray angle. It was inferred that the real effect of fuel properties on sprays might be in the microscopic characteristics, such as the primary break-up and evaporation processes. Therefore, it will

be of great importance to investigate the near-nozzle fields of a liquid spray or a single droplet using a microscope. By doing so, it is possible to better understand the effect of fuel temperature on the spray evaporation and transition processes, and thus to better arrange the fuel injection in IC engines in the wide operation conditions.

Secondly, preliminary experimental study showed that EDI heating significantly reduced the HC and CO emissions of the EDI+GPI engine, but the IMEP of the engine decreased slightly as well. It was inferred that the decrease of engine power could be caused by the reduction of fuel injection rate with the elevated ethanol fuel temperature and the spray collapse of flash-boiling which deformed the designed fuel distribution in the combustion chamber. To understand the mechanisms associated with the experimental results, it is needed to investigate the effect of ethanol fuel temperature on the mixture formation and combustion processes of the EDI+GPI engine using CFD simulation. However, the current spray model does not have the ability to predict the transformation behaviours from non-collapsed to collapsed sprays at different fuel temperatures. Moreover, only a few numerical works have been done in this field. A recent study showed that the spray collapse behaviours could be modelled by adjusting the initial droplet size and plume cone angle [201]. Therefore, based on the current EDI+GPI engine CFD model, it will be interesting to improve the EDI spray model by introducing a correlation between the initial droplet size (plume cone angle) and fuel temperature so that the spray model will have the capability to predict the behaviours of both normal-evaporating and flash-boiling sprays. The correlation can be verified by the experimental spray data in Chapter 4. Then, the improved engine model will be applied to investigate the effect of ethanol fuel temperature on the spray and combustion processes of the EDI+GPI engine and numerically adjust the EDI injector arrangement to avoid the decrease of IMEP at elevated fuel temperature.

Finally, EDI heating has been proven effective on reducing the HC and CO emissions of the EDI+GPI engine. However this may offset some of the charge cooling effect and knock mitigation ability of EDI which are two of the most important advantages of the EDI+GPI engine. Therefore, more engine experiments are needed to address this concern. For example, the effect of ethanol fuel temperature on the angle of knock limited spark advance (KLSA) should be investigated.

References

- [1] S.M. Sarathy, P. Oßwald, N. Hansen, K. Kohse-Höinghaus. Alcohol combustion chemistry. *Progress in Energy and Combustion Science* 2014; 44: 40-102.
- [2] M. Guo, W. Song, J. Buhain. Bioenergy and biofuels: History, status, and perspective. *Renewable and Sustainable Energy Reviews* 2015; 42: 712-725.
- [3] N. Fraser, H. Blaxill, G. Lumsden, M. Bassett. Challenges for Increased Efficiency through Gasoline Engine Downsizing. *SAE Int. J. Engines* 2009; 2: 991-1008.
- [4] I. Schifter, L. Diaz, R. Rodriguez, J.P. Gómez, U. Gonzalez. Combustion and Emissions Behavior for Ethanol–gasoline Blends in a Single Cylinder Engine. *Fuel* 2011; 90: 3586-3592.
- [5] R. Delgado, S. Paz. Effect of Different Ethanol-Gasoline Blends on Exhaust Emissions and Fuel Consumption. SAE paper 2012-01-1273; 2012.
- [6] D. Turner, H. Xu, R.F. Cracknell, V. Natarajan, X. Chen. Combustion Performance of Bio-ethanol at Various Blend Ratios in a Gasoline Direct Injection Engine. *Fuel* 2011; 90: 1999-2006.
- [7] W.D. Hsieh, R.H. Chen, T.L. Wu, T.H. Lin. Engine Performance and Pollutant Emission of an SI Engine Using Ethanol–gasoline Blended Fuels. *Atmospheric Environment* 2002; 36: 403-410.
- [8] Y. Zhuang, G. Hong. Primary Investigation to Leveraging Effect of Using Ethanol Fuel on Reducing Gasoline Fuel Consumption. *Fuel* 2013; 105: 425-431.
- [9] X. Wu, R. Daniel, G. Tian, H. Xu, Z. Huang, D. Richardson. Dual-injection: The flexible, bi-fuel concept for spark-ignition engines fuelled with various gasoline and biofuel blends. *Applied Energy* 2011; 88: 2305-2314.
- [10] R.A. Stein, C.J. House, T.G. Leone. Optimal Use of E85 in a Turbocharged Direct Injection Engine. *SAE Int. J. Fuels Lubr.* 2009; 2: 670-682.
- [11] D.R. Cohn, L. Bromberg, J. Heywood. Fuel Management System for Variable Ethanol Octane Enhancement of Gasoline Engines. US Patent 2010175659; 15 July, 2010.
- [12] Y. Zhuang, G. Hong. Effects of direct injection timing of ethanol fuel on engine knock and lean burn in a port injection gasoline engine. *Fuel* 2014; 135: 27-37.

- [13] F. Catapano, S. Di Iorio, A. Magno, P. Sementa, B.M. Vaglieco. A comprehensive analysis of the effect of ethanol, methane and methane-hydrogen blend on the combustion process in a PFI (port fuel injection) engine. *Energy* 2015; 88: 101-110.
- [14] M.K. Balki, C. Sayin. The effect of compression ratio on the performance, emissions and combustion of an SI (spark ignition) engine fueled with pure ethanol, methanol and unleaded gasoline. *Energy* 2014; 71: 194-201.
- [15] F. Catapano, P. Sementa, B.M. Vaglieco. Optical characterization of bio-ethanol injection and combustion in a small DISI engine for two wheels vehicles. *Fuel* 2013; 106: 651-666.
- [16] P. Rodrigues de Almeida, A.L. Nakamura, J.R. Sodr . Evaluation of catalytic converter aging for vehicle operation with ethanol. *Applied Thermal Engineering* 2014; 71: 335-341.
- [17] L.C. Monteiro Sales, J.R. Sodr . Cold start characteristics of an ethanol-fuelled engine with heated intake air and fuel. *Applied Thermal Engineering* 2012; 40: 198-201.
- [18] C. Liang, C. Ji, B. Gao, X. Liu, Y. Zhu. Investigation on the performance of a spark-ignited ethanol engine with DME enrichment. *Energy Conversion and Management* 2012; 58: 19-25.
- [19] G. Karavalakis, D. Short, D. Vu, R.L. Russell, A. Asa-Awuku, H. Jung, K.C. Johnson, T.D. Durbin. The impact of ethanol and iso-butanol blends on gaseous and particulate emissions from two passenger cars equipped with spray-guided and wall-guided direct injection SI (spark ignition) engines. *Energy* 2015; 82: 168-179.
- [20] A.N. Ozsezen, M. Canakci. Performance and combustion characteristics of alcohol-gasoline blends at wide-open throttle. *Energy* 2011; 36: 2747-2752.
- [21] R. Suarez-Bertoa, A.A. Zardini, H. Keuken, C. Astorga. Impact of ethanol containing gasoline blends on emissions from a flex-fuel vehicle tested over the Worldwide Harmonized Light duty Test Cycle (WLTC). *Fuel* 2015; 143: 173-182.
- [22] B. Tesfa, R. Mishra, F. Gu, A.D. Ball. Water injection effects on the performance and emission characteristics of a CI engine operating with biodiesel. *Renewable Energy* 2012; 37: 333-344.
- [23] B. Kegl, S. Pehan. Reduction of Diesel Engine Emissions by Water Injection. *SAE International* 2001-01-3259; 2001.
- [24] Z. Şahin, M. Tuti, O. Durgun. Experimental investigation of the effects of water adding to the intake air on the engine performance and exhaust emissions in a DI automotive diesel engine. *Fuel* 2014; 115: 884-895.
- [25] K.A. Subramanian. A comparison of water-diesel emulsion and timed injection of water into the intake manifold of a diesel engine for simultaneous control of NO and smoke emissions. *Energy Conversion and Management* 2011; 52: 849-857.

- [26] X. Tauzia, A. Maiboom, S.R. Shah. Experimental study of inlet manifold water injection on combustion and emissions of an automotive direct injection Diesel engine. *Energy* 2010; 35: 3628-3639.
- [27] V. Chintala, K.A. Subramanian. Experimental investigation of hydrogen energy share improvement in a compression ignition engine using water injection and compression ratio reduction. *Energy Conversion and Management* 2016; 108: 106-119.
- [28] R.D. Reitz. Directions in internal combustion engine research. *Combustion and Flame* 2013; 160: 1-8.
- [29] J. Benajes, S. Molina, A. García, E. Belarte, M. Vanvolsem. An investigation on RCCI combustion in a heavy duty diesel engine using in-cylinder blending of diesel and gasoline fuels. *Applied Thermal Engineering* 2014; 63: 66-76.
- [30] J.M. Desantes, J. Benajes, A. García, J. Monsalve-Serrano. The role of the in-cylinder gas temperature and oxygen concentration over low load reactivity controlled compression ignition combustion efficiency. *Energy* 2014; 78: 854-868.
- [31] B. Yang, M. Yao, W.K. Cheng, Y. Li, Z. Zheng, S. Li. Experimental and numerical study on different dual-fuel combustion modes fuelled with gasoline and diesel. *Applied Energy* 2014; 113: 722-733.
- [32] J. Benajes, S. Molina, A. García, J. Monsalve-Serrano. Effects of direct injection timing and blending ratio on RCCI combustion with different low reactivity fuels. *Energy Conversion and Management* 2015; 99: 193-209.
- [33] A. Gharehghani, R. Hosseini, M. Mirsalim, S.A. Jazayeri, T. Yusaf. An experimental study on reactivity controlled compression ignition engine fueled with biodiesel/natural gas. *Energy* 2015; 89: 558-567.
- [34] J. Benajes, S. Molina, A. García, J. Monsalve-Serrano. Effects of low reactivity fuel characteristics and blending ratio on low load RCCI (reactivity controlled compression ignition) performance and emissions in a heavy-duty diesel engine. *Energy* 2015; 90, Part 2: 1261-1271.
- [35] L. Zhu, Y. Qian, X. Wang, X. Lu. Effects of direct injection timing and premixed ratio on combustion and emissions characteristics of RCCI (Reactivity Controlled Compression Ignition) with N-heptane/gasoline-like fuels. *Energy* 2015; 93, Part 1: 383-392.
- [36] D.R. Cohn, L. Bromberg, J.B. Heywood, Direct Injection Ethanol Boosted Gasoline Engines: Biofuel Leveraging for Cost Effective Reduction of Oil Dependence and CO₂ Emissions, in, Massachusetts Institute of Technology, Cambridge, MA 02139, 2005.
- [37] T. Ikoma, S. Abe, Y. Sonoda, H. Suzuki, Y. Suzuki, M. Basaki. Development of V-6 3.5-liter Engine Adopting New Direct Injection System. SAE paper 2006-01-1259; 2006.

- [38] Toyota Camry 2.0 D-4S 6AR-FSE engine specifications, <http://www.gac-toyota.com.cn/minisite/campaigns/2014/camry/p/config?index=0>.
- [39] Ford's Twin-Fuel 'Bobcat' Engine Could Replace Power Stroke Diesels, <http://www.autoguide.com/auto-news/2009/06/fords-twin-fuel-bobcat-engine-could-replace-power-stroke-diesels.html>.
- [40] Ford's direct ethanol injected Bobcat engine not based on new 5.0L V8, <http://www.autoblog.com/2010/01/14/fords-direct-ethanol-injected-bobcat-engine-not-based-on-new-5/>.
- [41] G. Zhu, D. Hung, H. Schock. Combustion characteristics of a single-cylinder spark ignition gasoline and ethanol dual-fuelled engine. Proc. IMechE Part D: Automobile Engineering 2010; 224: 387-403.
- [42] Z. Wang, H. Liu, Y. Long, J. Wang, X. He. Comparative study on alcohols–gasoline and gasoline–alcohols dual-fuel spark ignition (DFSI) combustion for high load extension and high fuel efficiency. Energy 2015; 82: 395-405.
- [43] R. Daniel, C. Wang, H. Xu, G. Tian, D. Richardson. Dual-Injection as a Knock Mitigation Strategy Using Pure Ethanol and Methanol. SAE Int. J. Fuels Lubr. 2012; 5: 772-784.
- [44] H. Liu, Z. Wang, J. Wang. Methanol-gasoline DFSI (dual-fuel spark ignition) combustion with dual-injection for engine knock suppression. Energy 2014; 73: 686-693.
- [45] C. Jiang, X. Ma, H. Xu, S. Richardson. An Optical Study of DMF and Ethanol Combustion Under Dual-Injection Strategy. SAE paper 2012-01-1237; 2012.
- [46] S. Wei, K. Ji, X. Leng, F. Wang, X. Liu. Numerical simulation on effects of spray angle in a swirl chamber combustion system of DI (direct injection) diesel engines. Energy 2014; 75: 289-294.
- [47] S.L. Kokjohn, R.M. Hanson, D.A. Splitter, R.D. Reitz. Experiments and Modeling of Dual-Fuel HCCI and PCCI Combustion Using In-Cylinder Fuel Blending. SAE Int. J. Engines 2009; 2: 24-39.
- [48] J. Li, W.M. Yang, H. An, D.Z. Zhou, W.B. Yu, J.X. Wang, L. Li. Numerical investigation on the effect of reactivity gradient in an RCCI engine fueled with gasoline and diesel. Energy Conversion and Management 2015; 92: 342-352.
- [49] X. Lu, X. Zhou, L. Ji, Z. Yang, D. Han, C. Huang, Z. Huang. Experimental studies on the dual-fuel sequential combustion and emission simulation. Energy 2013; 51: 358-373.
- [50] N. Ishikawa, A. Hiraide, T. Takabayashi. Air/Fuel Distribution Simulation in a Port Injected Gasoline Lean-burn Engine. SAE paper 2001-01-1230; 2001.

- [51] Y. Huang, G. Hong, R. Huang. Numerical investigation to the dual-fuel spray combustion process in an ethanol direct injection plus gasoline port injection (EDI+GPI) engine. *Energy Conversion and Management* 2015; 92: 275-286.
- [52] M. Yumoto, K. Goto, S. Kato, M. Iida. The Investigation of Mixture Formation and Combustion with Port Injection System by Visualization of Flame and Wall Film. SAE paper 2011-01-1887; 2011.
- [53] D.F. Elger, B. C. Williams, C.T. Crowe, J.A. Roberson. *Engineering fluid mechanics* (10th edition). Wiley; 2012.
- [54] S.A. Basha, K. Raja Gopal. In-cylinder fluid flow, turbulence and spray models—A review. *Renewable and Sustainable Energy Reviews* 2009; 13: 1620-1627.
- [55] D. Veynante, L. Vervisch. Turbulent combustion modeling. *Progress in Energy and Combustion Science* 2002; 28: 193-266.
- [56] S. Richard, O. Colin, O. Vermorel, A. Benkenida, C. Angelberger, D. Veynante. Towards large eddy simulation of combustion in spark ignition engines. *Proceedings of the Combustion Institute* 2007; 31: 3059-3066.
- [57] P.R. Spalart. Strategies for turbulence modelling and simulations. *International Journal of Heat and Fluid Flow* 2000; 21: 252-263.
- [58] C.J. Rutland. Large-eddy simulations for internal combustion engines - a review. *International Journal of Engine Research* 2011; 12: 421-451.
- [59] S.B. Pope. Ten questions concerning the large-eddy simulation of turbulent flows. *New Journal of Physics* 2004; 6: 1-24.
- [60] C. Baumgarten. *Mixture Formation in Internal Combustion Engines*. Berlin : Springer, c2006; 2006.
- [61] K.N.C. Bray. The challenge of turbulent combustion. *Symposium (International) on Combustion* 1996; 26: 1-26.
- [62] D.C. Haworth. A Review of Turbulent Combustion Modeling for Multidimensional In-Cylinder CFD. SAE paper 2005-01-0993; 2005.
- [63] X. Jiang, G.A. Siamas, K. Jagus, T.G. Karayiannis. Physical Modelling and Advanced Simulations of Gas-liquid Two-phase Jet Flows in Atomization and Sprays. *Progress in Energy and Combustion Science* 2010; 36: 131-167.
- [64] L. Postrioti, F. Mariani, M. Battistoni. Experimental and numerical momentum flux evaluation of high pressure Diesel spray. *Fuel* 2012; 98: 149-163.
- [65] S.P. Lin, R.D. Reitz. Drop and Spray Formation From A Liquid Jet. *Annual Review of Fluid Mechanics* 1998; 30: 85-105.
- [66] F.V. Bracco. *Modeling of Engine Sprays*. SAE paper 850394; 1985.

- [67] M. Gorokhovski, M. Herrmann. Modeling Primary Atomization. *Annual Review of Fluid Mechanics* 2008; 40: 343-366.
- [68] M. Xie. *Computational Combustion Theory of IC Engines (in Chinese)*. 2nd ed., Dalian, China: Dalian University of Technology Press; 2005.
- [69] M. Battistoni, C. Grimaldi, F. Mariani. Coupled Simulation of Nozzle Flow and Spray Formation Using Diesel and Biodiesel for CI Engine Applications. SAE paper 2012-01-1267; 2012.
- [70] M. Battistoni, C.N. Grimaldi. Numerical analysis of injector flow and spray characteristics from diesel injectors using fossil and biodiesel fuels. *Applied Energy* 2012; 97: 656-666.
- [71] J. Ishimoto, F. Sato, G. Sato. Computational Prediction of the Effect of Microcavitation on an Atomization Mechanism in a Gasoline Injector Nozzle. *J Eng Gas Turb Power* 2010; 132: 082801.
- [72] S. Henriot, D. Bouyssounouse, T. Baritaud. Port Fuel Injection and Combustion Simulation of a Racing Engine. SAE paper 2003-01-1845; 2003.
- [73] T. Kiura, T.A. Shedd, B.C. Blaser. Investigation of Spray Evaporation and Numerical Model Applied for Fuel-injection Small Engines. *SAE Int. J. Engines* 2008; 1: 1402-1409.
- [74] S. Jafarmadar. Three-dimensional modeling and exergy analysis in Combustion Chambers of an indirect injection diesel engine. *Fuel* 2013; 107: 439-447.
- [75] P. Jenny, D. Roekaerts, N. Beishuizen. Modeling of turbulent dilute spray combustion. *Progress in Energy and Combustion Science* 2012; 38: 846-887.
- [76] N. Zeoli, S. Gu. Numerical modelling of droplet break-up for gas atomisation. *Computational Materials Science* 2006; 38: 282-292.
- [77] D. Jajcevic, R. Almbauer, S. Schmidt, K. Glinsner, M. Fitl. CFD Study of Spray Design for a GDI High Performance 2-Stroke Engine. SAE paper 2010-32-0014; 2010.
- [78] P.J. O'Rourke, A.A. Amsden. The TAB Method for Numerical Calculation of Spray Droplet Breakup. SAE Paper 872089; 1987.
- [79] ANSYS FLUENT Theory Guide. 2012.
- [80] A.B. Liu, D. Mather, R.D. Reitz. Modeling the Effects of Drop Drag and Breakup on Fuel Sprays. SAE paper 930072; 1993.
- [81] W.W. Pulkrabek. *Engineering Fundamentals of the Internal Combustion Engine*. Prentice-Hall, Inc.; 1997.
- [82] W.A. Sirignano. *Fluid dynamics and transport of droplets and sprays*. Cambridge, U.K. : Cambridge University Press; 1999.

- [83] S.S. Sazhin. Advanced models of fuel droplet heating and evaporation. *Progress in Energy and Combustion Science* 2006; 32: 162-214.
- [84] AVL FIRE Lagrangian multiphase. 2009.
- [85] A. Lipatnikov. *Fundamentals of Premixed Turbulent Combustion*. CRC Press; 2012.
- [86] N. Swaminathan, K.N.C. Bray. *Turbulent Premixed Flames*. Cambridge University Press; 2011.
- [87] M. Mikami, K. Yamamoto, O. Moriue, N. Kojima. Combustion of partially premixed spray jets. *Proceedings of the Combustion Institute* 2005; 30: 2021-2028.
- [88] T. Echekki, E. Mastorakos. *Turbulent Combustion Modeling*. Springer Netherlands; 2011.
- [89] H. An, W. Yang, J. Li, A. Maghbouli, K.J. Chua, S.K. Chou. A numerical modeling on the emission characteristics of a diesel engine fueled by diesel and biodiesel blend fuels. *Applied Energy* 2014; 130: 458-465.
- [90] A. Maghbouli, W. Yang, H. An, J. Li, S.K. Chou, K.J. Chua. An advanced combustion model coupled with detailed chemical reaction mechanism for D.I diesel engine simulation. *Applied Energy* 2013; 111: 758-770.
- [91] V. Knop, A. Benkenida, S. Jay, O. Colin. Modelling of combustion and nitrogen oxide formation in hydrogen-fuelled internal combustion engines within a 3D CFD code. *International Journal of Hydrogen Energy* 2008; 33: 5083-5097.
- [92] B. Franzelli, B. Fiorina, N. Darabiha. A tabulated chemistry method for spray combustion. *Proceedings of the Combustion Institute* 2013; 34: 1659-1666.
- [93] C. Ji, X. Liu, B. Gao, S. Wang, J. Yang. Numerical investigation on the combustion process in a spark-ignited engine fueled with hydrogen-gasoline blends. *International Journal of Hydrogen Energy* 2013; 38: 11149-11155.
- [94] Y. Bai, J. Wang, Z. Wang, S. Shuai. Knocking Suppression by Stratified Stoichiometric Mixture With Two-Zone Homogeneity in a DISI Engine. *Journal of Engineering for Gas Turbines and Power* 2013; 135: 012803-012801-012803-012809.
- [95] D.C. Haworthy, A probability density function/flamelet method for partially premixed turbulent combustion, in: *Proceedings of the Summer Program, Center for Turbulence Research, The Pennsylvania State University*, 2000.
- [96] F. Tap, P. Schapotschnikow. *Efficient Combustion Modeling Based on Tabkin® CFD Look-up Tables: A Case Study of a Lifted Diesel Spray Flame*. SAE paper 2012-01-0152; 2012.
- [97] G. Subramanian, L. Vervisch, F. Ravet. *New Developments in Turbulent Combustion Modeling for Engine Design: ECFM-CLEH Combustion Submodel*. SAE paper 2007-01-0154; 2007.

- [98] J.W. Campbell, A.D. Gosman, G. Hardy. Analysis of Premix Flame and Lift-Off in Diesel Spray Combustion using Multi-Dimensional CFD. *SAE Int. J. Engines* 2008; 1: 571-590.
- [99] F. Bazdidi-Tehrani, H. Zeinivand. Presumed PDF modeling of reactive two-phase flow in a three dimensional jet-stabilized model combustor. *Energy Conversion and Management* 2010; 51: 225-234.
- [100] C.L. Yaws. *Yaws' Handbook of Thermodynamic and Physical Properties of Chemical Compounds*. Knovel; 2003.
- [101] K. Kar, T. Last, C. Haywood, R. Raine. Measurement of Vapor Pressures and Enthalpies of Vaporization of Gasoline and Ethanol Blends and Their Effects on Mixture Preparation in an SI Engine. *SAE Int. J. Fuels Lubr.* 2008; 1: 132-144.
- [102] G. Tian, R. Daniel, H. Li, H. Xu, S. Shuai, P. Richards. Laminar Burning Velocities of 2,5-Dimethylfuran Compared with Ethanol and Gasoline. *Energy & Fuels* 2010; 24: 3898-3905.
- [103] B.E. Poling, J.M. Prausnitz, J.P. O'Connell. *The Properties of Gases and Liquids (Fifth Edition)*. McGRAW-HILL; 2001.
- [104] S. Jerzembeck, N. Peters, P. Pepiot-Desjardins, H. Pitsch. Laminar burning velocities at high pressure for primary reference fuels and gasoline: Experimental and numerical investigation. *Combustion and Flame* 2009; 156: 292-301.
- [105] P. Dirrenberger, P.A. Glaude, R. Bounaceur, H. Le Gall, A.P. da Cruz, A.A. Konnov, F. Battin-Leclerc. Laminar burning velocity of gasolines with addition of ethanol. *Fuel* 2014; 115: 162-169.
- [106] J.P.J. van Lipzig, E.J.K. Nilsson, L.P.H. de Goey, A.A. Konnov. Laminar burning velocities of n-heptane, iso-octane, ethanol and their binary and tertiary mixtures. *Fuel* 2011; 90: 2773-2781.
- [107] F. Zhao, M.C. Lai, D.L. Harrington. Automotive spark-ignited direct-injection gasoline engines. *Progress in Energy and Combustion Science* 1999; 25: 437-562.
- [108] Y. Huang, G. Hong, R. Huang. Investigation to charge cooling effect and combustion characteristics of ethanol direct injection in a gasoline port injection engine. *Applied Energy* 2015; 160: 244-254.
- [109] W. Zeng, M. Xu, G. Zhang, Y. Zhang, D.J. Cleary. Atomization and vaporization for flash-boiling multi-hole sprays with alcohol fuels. *Fuel* 2012; 95: 287-297.
- [110] P.G. Aleiferis, Z.R. van Romunde. An analysis of spray development with iso-octane, n-pentane, gasoline, ethanol and n-butanol from a multi-hole injector under hot fuel conditions. *Fuel* 2013; 105: 143-168.
- [111] T.N.C. Anand, A. Madan Mohan, R.V. Ravikrishna. Spray characterization of gasoline-ethanol blends from a multi-hole port fuel injector. *Fuel* 2012; 102: 613-623.

- [112] S.H. Park, H.J. Kim, H.K. Suh, C.S. Lee. Atomization and spray characteristics of bioethanol and bioethanol blended gasoline fuel injected through a direct injection gasoline injector. *International Journal of Heat and Fluid Flow* 2009; 30: 1183-1192.
- [113] X. Wang, J. Gao, D. Jiang, Z. Huang, W. Chen. Spray Characteristics of High-Pressure Swirl Injector Fueled with Methanol and Ethanol. *Energy & Fuels* 2005; 19: 2394-2401.
- [114] J. Gao, D. Jiang, Z. Huang. Spray Properties of Alternative Fuels: A Comparative Analysis of Ethanol-Gasoline Blends and Gasoline. *Fuel* 2007; 86: 1645-1650.
- [115] B. Zhu, M. Xu, Y. Zhang, G. Zhang. Physical Properties of Gasoline-Alcohol Blends and Their Influences on Spray Characteristics from a Low Pressure DI Injector. *Proceedings of the 14th Asia Annual Conference on Liquid Atomization and Spray Systems (ILASS-Asia)*; 2010.
- [116] Y. Bao, S. Padala, Q.N. Chan, S. Kook, E.R. Hawkes. Influence of injection pressure on ethanol and gasoline spray penetrations in a spark-ignition fuelling system. *18th Australasian Fluid Mechanics Conference* 2012.
- [117] P.G. Aleiferis, J. Serras-Pereira, Z. van Romunde, J. Caine, M. Wirth. Mechanisms of spray formation and combustion from a multi-hole injector with E85 and gasoline. *Combustion and Flame* 2010; 157: 735-756.
- [118] W. Zeng, M. Xu, M. Zhang, Y. Zhang, D.J. Cleary. Macroscopic characteristics for direct-injection multi-hole sprays using dimensionless analysis. *Experimental Thermal and Fluid Science* 2012; 40: 81-92.
- [119] A. Matsumoto, W.R. Moore, M.-C. Lai, Y. Zheng, M. Foster, X.-B. Xie, D. Yen, K. Confer, E. Hopkins. Spray Characterization of Ethanol Gasoline Blends and Comparison to a CFD Model for a Gasoline Direct Injector. *SAE Int. J. Engines* 2010; 3: 402-425.
- [120] H. Oh, C. Bae, K. Min. Spray and Combustion Characteristics of Ethanol Blended Gasoline in a Spray Guided DISI Engine under Lean Stratified Operation. *SAE Int. J. Engines* 2010; 3: 213-222.
- [121] Y. Huang, G. Hong, X. Cheng, R. Huang. Investigation to Charge Cooling Effect of Evaporation of Ethanol Fuel Directly Injected in a Gasoline Port Injection Engine. *SAE paper 2013-01-2610*; 2013.
- [122] S. Srivastava, H. Schock, F. Jaber, D.L.S. Hung. Numerical Simulation of a Direct-Injection Spark-Ignition Engine with Different Fuels. *SAE paper 2009-01-0325*; 2009.
- [123] P.K. Kasseris, Knock Limits in Spark Ignited Direct Injected Engines Using Gasoline/Ethanol Blends, in: Department of Mechanical Engineering, Massachusetts Institute of Technology, PhD Thesis, Cambridge, 2011.
- [124] L. Araneo, A. Coghe, G. Brunello, R. Dondé. Effects of Fuel Temperature and Ambient Pressure on a GDI Swirled Injector Spray. *SAE paper 2000-01-1901*; 2000.

- [125] K. Nakama, E. Murase, M. Imada, J. Kusaka, Y. Daisho. Effects of High Temperature Fuel on In-Cylinder Fuel Mixture Formation Process for Direct Injection Engine. SAE paper 2003-32-0003; 2003.
- [126] E. Murase, K. Nakama, S. Toyoda, J. Kusaka, Y. Daisho. The Effects of Fuel Temperature on a Direct Injection Gasoline Spray in a Constant Volume Chamber. SAE paper 2003-01-1810; 2003.
- [127] K. Kannaiyan, R. Sadr. Experimental investigation of spray characteristics of alternative aviation fuels. *Energy Conversion and Management* 2014; 88: 1060-1069.
- [128] A. Matsumoto, Y. Zheng, X.-B. Xie, M.-C. Lai, W. Moore. Characterization of Multi-hole Spray and Mixing of Ethanol and Gasoline Fuels under DI Engine Conditions. SAE paper 2010-01-2151; 2010.
- [129] J. Serras-Pereira, P.G. Aleiferis, D. Richardson, S. Wallace. Characteristics of Ethanol, Butanol, Iso-Octane and Gasoline Sprays and Combustion from a Multi-Hole Injector in a DISI Engine. *SAE Int. J. Fuels Lubr.* 2008; 1: 893-909.
- [130] Z. van Romunde, P.G. Aleiferis, R.F. Cracknell, H.L. Walmsley. Effect of Fuel Properties on Spray Development from a Multi-Hole DISI Engine Injector. SAE Paper 2007-01-4032; 2007.
- [131] P.G. Aleiferis, J. Serras-Pereira, A. Augoye, T.J. Davies, R.F. Cracknell, D. Richardson. Effect of fuel temperature on in-nozzle cavitation and spray formation of liquid hydrocarbons and alcohols from a real-size optical injector for direct-injection spark-ignition engines. *International Journal of Heat and Mass Transfer* 2010; 53: 4588-4606.
- [132] Y. Huang, S. Huang, P. Deng, R. Huang, G. Hong. The Effect of Fuel Temperature on the Ethanol Direct Injection Spray Characteristics of a Multi-hole Injector. *SAE Int. J. Fuels Lubr.* 2014; 7: 792-802.
- [133] S. Zanforlin, E. Musu, S. Frigo, R. Gentili. Direct Injection and Charge Stratification in a 50 cc Two-Stroke Engine: CFD Studies and Test Bench Results. *ASME Conference Proceedings*; 2006.
- [134] A.M. Lippert, S.H. El Tahry, M.S. Huebler, S.E. Parrish, H. Inoue, T. Noyori. Development and Optimization of a Small-Displacement Spark-Ignition Direct-Injection Engine - Full-Load Operation. SAE paper 2004-01-0034; 2004.
- [135] D. Jajcevic, R.A. Almbauer, S.P. Schmidt, K. Glinsner. Simulation of Scavenging Process, Internal Mixture Preparation, and Combustion of a Gasoline Direct Injection Two-Cylinder Two-Stroke Engine. SAE paper 2009-32-0046; 2009.
- [136] J.J. López, R. Novella, A. García, J.F. Winklinger. Investigation of the ignition and combustion processes of a dual-fuel spray under diesel-like conditions using computational fluid dynamics (CFD) modeling. *Mathematical and Computer Modelling* 2013; 57: 1897-1906.

- [137] M. Costa, U. Sorge, L. Allocca. Numerical study of the mixture formation process in a four-stroke GDI engine for two-wheel applications. *Simulation Modelling Practice and Theory* 2011; 19: 1212-1226.
- [138] M. Costa, B. Iorio, U. Sorge, S. Alfuso. Assessment of a Numerical Model for Multi-Hole Gasoline Sprays to be Employed in the Simulation of Spark Ignition GDI Engines with a Jet-Guided Combustion Mode. SAE paper 2009-01-1915; 2009.
- [139] W. Waidmann, A. Boemer, M. Braun. Adjustment and Verification of Model Parameters for Diesel Injection CFD Simulation. SAE paper 2006-01-0241; 2006.
- [140] H. Li, C. li, X. Ma, P. Tu, H. Xu, S.-J. Shuai, A. Ghafourian. Numerical Study of DMF and Gasoline Spray and Mixture Preparation in a GDI Engine. SAE paper 2013-01-1592; 2013.
- [141] W. Anderson, J. Yang, D.D. Brehob, J.K. Vallance, R.M. Whiteaker. Understanding the Thermodynamics of Direct Injection Spark Ignition (DISI) Combustion Systems: An Analytical and Experimental Investigation. SAE paper 962018 1996.
- [142] P. Price, B. Twiney, R. Stone, K. Kar, H. Walmsley. Particulate and Hydrocarbon Emissions from a Spray Guided Direct Injection Spark Ignition Engine with Oxygenate Fuel Blends. SAE paper 2007-01-0472; 2007.
- [143] M. Anbari Attar, M.R. Herfatmanesh, H. Zhao, A. Cairns. Experimental investigation of direct injection charge cooling in optical GDI engine using tracer-based PLIF technique. *Experimental Thermal and Fluid Science* 2014; 59: 96-108.
- [144] K.-h. Ahn, H. Yilmaz, A. Stefanopoulou, L. Jiang. Ethanol Content Estimation in Flex Fuel Direct Injection Engines Using In-Cylinder Pressure Measurements. SAE paper 2010-01-0166; 2010.
- [145] L.P. Wyszynski, C.R. Stone, G.T. Kalghatgi. The Volumetric Efficiency of Direct and Port Injection Gasoline Engines with Different Fuels. SAE paper 2002-01-0839; 2002.
- [146] E. Kasseris, J. Heywood. Charge Cooling Effects on Knock Limits in SI DI Engines Using Gasoline/Ethanol Blends: Part 1-Quantifying Charge Cooling. SAE paper 2012-01-1275; 2012.
- [147] E. Kasseris, J. Heywood. Charge Cooling Effects on Knock Limits in SI DI Engines Using Gasoline/Ethanol Blends: Part 2-Effective Octane Numbers. *SAE Int. J. Fuels Lubr.* 2012; 5: 844-854.
- [148] R.A. Stein, D. Polovina, K. Roth, M. Foster, M. Lynskey, T. Whiting, J.E. Anderson, M.H. Shelby, T.G. Leone, S. VanderGriend. Effect of Heat of Vaporization, Chemical Octane, and Sensitivity on Knock Limit for Ethanol - Gasoline Blends. *SAE Int. J. Fuels Lubr.* 2012; 5: 823-843.
- [149] J. Milpied, N. Jeuland, G. Plassat, S. Guichaous, N. Dioc, A. Marchal, P. Schmelzle. Impact of Fuel Properties on the Performances and Knock Behaviour of a Downsized

Turbocharged DI SI Engine - Focus on Octane Numbers and Latent Heat of Vaporization. *SAE Int. J. Fuels Lubr.* 2009; 2: 118-126.

- [150] S.M. Shahed, K.-H. Bauer. Parametric Studies of the Impact of Turbocharging on Gasoline Engine Downsizing. *SAE Int. J. Engines* 2009; 2: 1347-1358.
- [151] R.A. Stein, J.E. Anderson, T.J. Wallington. An Overview of the Effects of Ethanol-Gasoline Blends on SI Engine Performance, Fuel Efficiency, and Emissions. *SAE Int. J. Engines* 2013; 6: 470-487.
- [152] C.D. Marriott, M.A. Wiles, J.M. Gwidt, S.E. Parrish. Development of a Naturally Aspirated Spark Ignition Direct-Injection Flex-Fuel Engine. *SAE Int. J. Engines* 2008; 1: 267-295.
- [153] R.P. Selvam, M. Sarkar, R. Ponnappan. Effect of Thermal Conductivity and Latent Heat of Vaporization of Liquid on Heat Transfer in Spray Cooling. *SAE paper* 2006-01-3068; 2006.
- [154] C. Wang, R. Daniel, X. Ma. Comparison of Gasoline (ULG), 2,5-Dimethylfuran (DMF) and Bio-Ethanol in a DISI Miller Cycle with Late Inlet Valve Closing Time. *SAE paper* 2012-01-1147; 2012.
- [155] J.E. Anderson, D.M. DiCicco, J.M. Ginder, U. Kramer, T.G. Leone, H.E. Raney-Pablo, T.J. Wallington. High octane number ethanol-gasoline blends: Quantifying the potential benefits in the United States. *Fuel* 2012; 97: 585-594.
- [156] M.K. Balki, C. Sayin, M. Canakci. The effect of different alcohol fuels on the performance, emission and combustion characteristics of a gasoline engine. *Fuel* 2014; 115: 901-906.
- [157] P. Sementa, B. Maria Vaglieco, F. Catapano. Thermodynamic and optical characterizations of a high performance GDI engine operating in homogeneous and stratified charge mixture conditions fueled with gasoline and bio-ethanol. *Fuel* 2012; 96: 204-219.
- [158] R. Daniel, G. Tian, H. Xu, S. Shuai. Ignition timing sensitivities of oxygenated biofuels compared to gasoline in a direct-injection SI engine. *Fuel* 2012; 99: 72-82.
- [159] D.A. Rothamer, J.H. Jennings. Study of the knocking propensity of 2,5-dimethylfuran-gasoline and ethanol-gasoline blends. *Fuel* 2012; 98: 203-212.
- [160] J. Wang, Z. Huang, H. Miao, X. Wang, D. Jiang. Characteristics of direct injection combustion fuelled by natural gas-hydrogen mixtures using a constant volume vessel. *International Journal of Hydrogen Energy* 2008; 33: 1947-1956.
- [161] G.P. Beretta, M. Rashidi, J.C. Keck. Turbulent flame propagation and combustion in spark ignition engines. *Combustion and Flame* 1983; 52: 217-245.
- [162] G. Zhang, D.L.S. Hung, M. Xu. Experimental study of flash boiling spray vaporization through quantitative vapor concentration and liquid temperature measurements. *Experiments in Fluids* 2014; 55: 1-12.

- [163] Y. Huang, S. Huang, R. Huang, G. Hong. Spray and evaporation characteristics of ethanol and gasoline direct injection in non-evaporating, transition and flash-boiling conditions. *Energy Conversion and Management* 2016; 108: 68-77.
- [164] M. Xu, Y. Zhang, W. Zeng, G. Zhang, M. Zhang. Flash Boiling: Easy and Better Way to Generate Ideal Sprays than the High Injection Pressure. *SAE Int. J. Fuels Lubr.* 2013; 6: 137-148.
- [165] O.M.I. Nwafor. The effect of elevated fuel inlet temperature on performance of diesel engine running on neat vegetable oil at constant speed conditions. *Renewable Energy* 2003; 28: 171-181.
- [166] O.M.I. Nwafor. Emission characteristics of diesel engine running on vegetable oil with elevated fuel inlet temperature. *Biomass and Bioenergy* 2004; 27: 507-511.
- [167] R. Mamat, N.R. Abdullah, H. Xu, M.L. Wyszynski, A. Tsolakis. Effect of Fuel Temperature on Performance and Emissions of a Common Rail Diesel Engine Operating with Rapeseed Methyl Ester (RME). SAE paper 2009-01-1896; 2009.
- [168] D. Kabasin, K. Hoyer, J. Kazour, R. Lamers, T. Hurter. Heated Injectors for Ethanol Cold Starts. *SAE Int. J. Fuels Lubr.* 2009; 2: 172-179.
- [169] D.F. Kabasin, Y. Joseph, W. Fedor, S. Geiger, T. Hurter. Emission Reduction with Heated Injectors. *SAE Int. J. Engines* 2010; 3: 982-995.
- [170] L.C.M. Sales, J.R. Sodré. Cold start emissions of an ethanol-fuelled engine with heated intake air and fuel. *Fuel* 2012; 95: 122-125.
- [171] J.V. Pastor, J.M. García, J.M. Pastor, L.D. Zapata. Evaporating Diesel Spray Visualization using a Double-pass Shadowgraphy/Schlieren imaging. SAE paper 2007-24-0026; 2007.
- [172] J.V. Pastor, R. Payri, J.M. Garcia-Oliver, F.J. Briceño. Schlieren Methodology for the Analysis of Transient Diesel Flame Evolution. *SAE Int. J. Engines* 2013; 6: 1661-1676.
- [173] Gasoline Fuel Injector Spray Measurement and Characterization. SAE standard J2715; 2007.
- [174] K. Kim, D. Kim, Y. Jung, C. Bae. Spray and combustion characteristics of gasoline and diesel in a direct injection compression ignition engine. *Fuel* 2013; 109: 616-626.
- [175] T. Lucchini, G. D'Errico, A. Onorati, G. Bonandrini, L. Venturoli, R. Di Gioia. Development of a CFD Approach to Model Fuel-Air Mixing in Gasoline Direct-Injection Engines. SAE paper 2012-01-0146; 2012.
- [176] R.D. Reitz. Mechanisms of Atomization Processes in High-Pressure Vaporizing Sprays. *Atomization and Spray Technology* 1988; 3: 309-337.
- [177] R. Scarcelli, T. Wallner, N. Matthias, V. Salazar, S. Kaiser. Mixture Formation in Direct Injection Hydrogen Engines: CFD and Optical Analysis of Single- and Multi-Hole Nozzles. *SAE Int. J. Engines* 2011; 4: 2361-2375.

- [178] J.M. Duclos, D. Veynante, T. Poinso. A comparison of flamelet models for premixed turbulent combustion. *Combustion and Flame* 1993; 95: 101-117.
- [179] F. Haglind. A review on the use of gas and steam turbine combined cycles as prime movers for large ships. Part III: Fuels and emissions. *Energy Conversion and Management* 2008; 49: 3476-3482.
- [180] V. Chintala, K.A. Subramanian. Hydrogen energy share improvement along with NO_x (oxides of nitrogen) emission reduction in a hydrogen dual-fuel compression ignition engine using water injection. *Energy Conversion and Management* 2014; 83: 249-259.
- [181] G. Stiesch. *Modeling engine spray and combustion processes*. Springer; 2003.
- [182] Directive 2002/88/EC of the European Parliament and of the Council. <http://eur-lex.europa.eu/LexUriServ/LexUriServ.do?uri=OJ:L:2003:035:0028:0081:en:PDF>.
- [183] *Automotive Emission Analyzer MEXA-584L Instruction Manual*. 2007.
- [184] J.S. Wijesinghe, Investigation of auto-ignition combustion in a small two-stroke engine, in: *School of Electrical, Mechanical and Mechatronic Systems, University of Technology Sydney, PhD Thesis, Sydney, 2009*.
- [185] *Handbook of Atomization and Sprays: Theory and Applications*. Springer; 2011.
- [186] Q.N. Chan, Y. Bao, S. Kook. Effects of injection pressure on the structural transformation of flash-boiling sprays of gasoline and ethanol in a spark-ignition direct-injection (SIDI) engine. *Fuel* 2014; 130: 228-240.
- [187] M. Chato, S. Fukuda, K. Sato, T. Fujikawa, R. Chen, Z. Li, J. Tian, K. Nishida. Fuel Spray Evaporation and Mixture Formation Processes of Ethanol/Gasoline Blend Injected by Hole-Type Nozzle for DISI Engine. *SAE Int. J. Engines* 2012; 5: 1836-1846.
- [188] S. Mcallister. *Fundamentals of Combustion Processes*. New York: Springer; 2011.
- [189] J.B. Heywood. *Internal Combustion Engine Fundamentals*. McGraw-Hill Book Company; 1988.
- [190] D.W. Stanton, C.J. Rutland. Modeling Fuel Film Formation and Wall Interaction in Diesel Engines. SAE paper 960628; 1996.
- [191] P.J. O'Rourke, A.A. Amsden. A Spray/Wall Interaction Submodel for the KIVA-3 Wall Film Model. SAE paper 2000-01-0271; 2000.
- [192] M.F. Brunocilla, F. Lepsch. Influence of hot fuel injection on air/fuel mixture preparation and effects on Flex Fuel Engines. SAE paper 2006-01-2619; 2006.
- [193] R. Krenus, M.R.V. Passos, T. Ortega, K. Mowery, Y.J. Kim, L.G. Lavan, K. Lee, C.J. Park, K. Han. Ethanol Flex Fuel system with Delphi Heated injector application. SAE paper 2014-01-1369; 2014.

- [194] G. Guangxin, Y. Zhulin, Z. Apeng, L. Shenghua, W. Yanju. Effects of Fuel Temperature on Injection Process and Combustion of Dimethyl Ether Engine. *Journal of Energy Resources Technology* 2013; 135: 042202-042202.
- [195] M. Kubota, K. Yoshida, H. Shoji, H. Tanaka. 8 A Study of the Influence of Fuel Temperature on Emission Characteristics and Engine Performance of Compression Ignition Engine. SAE paper 2002-32-1777; 2002.
- [196] G. Chen. Study of Fuel Temperature Effects on Fuel Injection, Combustion, and Emissions of Direct-Injection Diesel Engines. *Journal of Engineering for Gas Turbines and Power* 2008; 131: 022802-022802.
- [197] F.J. Salvador, J. Gimeno, M. Carreres, M. Crialesi-Esposito. Fuel temperature influence on the performance of a last generation common-rail diesel ballistic injector. Part I: Experimental mass flow rate measurements and discussion. *Energy Conversion and Management* 2016; 114: 364-375.
- [198] R. Payri, F.J. Salvador, M. Carreres, J. De la Morena. Fuel temperature influence on the performance of a last generation common-rail diesel ballistic injector. Part II: 1D model development, validation and analysis. *Energy Conversion and Management* 2016; 114: 376-391.
- [199] S. Wu, M. Xu, D.L.S. Hung, H. Pan, S. Tong. Characterization of Superheated Internal Flow in a Two-Dimensional Transparent Nozzle. *ILASS-Asia* 2014.
- [200] C.R. Ferguson. *Internal Combustion Engines: Applied Thermosciences*. John Willey & Sons; 1986.
- [201] C. Price, A. Hamzehloo, P. Aleiferis, D. Richardson. Aspects of Numerical Modelling of Flash-Boiling Fuel Sprays. SAE International 2015-24-2463; 2015.

Appendix

Table A.1: List of engine simulation conditions and related publications

Case name	EDI timing	GPI mass	EDI mass	Ethanol ratio	Spray verification	Combustion model	Wall-film model	Related papers*
-	CAD BTDC	mg	mg	vol%	-	-	-	-
GPI only	300	13.4	-	0%	No	No	Wall-jet	[1]
EDI+GPI	300	8.5	8.00	46%	No	No	Wall-jet	[1]
GPI only	300	13.4	-	0%	Yes	Yes	Wall-jet	[2], [3]
EDI+GPI	300	8.5	8.0	46%	Yes	Yes	Wall-jet	[2], [3]
E0	300	13.4	-	0%	Yes	No	Wall-jet	[4]
E25	300	11.1	4.0	25%	Yes	No	Wall-jet	[4]
E46	300	8.5	8.0	46%	Yes	No	Wall-jet	[4]
E58	300	7.1	10.7	58%	Yes	No	Wall-jet	[4]
E69	300	5.4	13.4	69%	Yes	No	Wall-jet	[4]
E76	300	4.2	15.0	76%	Yes	No	Wall-jet	[4]
E85	300	2.8	17.3	85%	Yes	No	Wall-jet	[4]
E100	300	-	21.7	100%	Yes	No	Wall-jet	[4]
E0	300	13.4	-	0%	Yes	Yes	Wall-jet	[5]
E25	300	11.1	4.0	25%	Yes	Yes	Wall-jet	[5]
E46	300	8.5	8.0	46%	Yes	Yes	Wall-jet	[5]
E58	300	7.1	10.7	58%	Yes	Yes	Wall-jet	[5]
E69	300	5.4	13.4	69%	Yes	Yes	Wall-jet	[5]
E76	300	4.2	15.0	76%	Yes	Yes	Wall-jet	[5]
E85	300	2.8	17.3	85%	Yes	Yes	Wall-jet	[5]
E100	300	-	21.7	100%	Yes	Yes	Wall-jet	[5]
IT300	300	8.5	8.0	46%	Yes	Yes	Stanton&O'Rourke	[6]
IT180	180	8.5	8.0	46%	Yes	Yes	Stanton&O'Rourke	[6]
IT100	100	8.5	8.0	46%	Yes	Yes	Stanton&O'Rourke	[6]

* List of related publications (Chapters 5 & 6)

- [1] Y. Huang, G. Hong, X. Cheng, R. Huang. Investigation to Charge Cooling Effect of Evaporation of Ethanol Fuel Directly Injected in a Gasoline Port Injection Engine. *SAE paper 2013-01-2610*; 2013.
- [2] Y. Huang, G. Hong. Development of a Numerical Model for Investigating the EDI+GPI Engine. *19th Australasian Fluid Mechanics Conference*, Melbourne Australia; 2014.
- [3] Y. Huang, G. Hong, R. Huang. Numerical investigation to the dual-fuel spray combustion process in an ethanol direct injection plus gasoline port injection (EDI+GPI) engine. *Energy Conversion and Management* 2015; 92: 275-286.
- [4] Y. Huang, G. Hong, R. Huang. Numerical Investigation to the Effect of Ethanol/Gasoline Ratio on Charge Cooling in an EDI+GPI Engine. *SAE paper 2014-01-2612*; 2014.
- [5] Y. Huang, G. Hong, R. Huang. Investigation to charge cooling effect and combustion characteristics of ethanol direct injection in a gasoline port injection engine. *Applied Energy* 2015; 160: 244-254.
- [6] Y. Huang, G. Hong, R. Huang. Effect of injection timing on mixture formation and combustion in an ethanol direct injection plus gasoline port injection (EDI+GPI) research engine. *Energy* 2016; 111: 92-103.

Table A.2: List of spray experiment conditions and related publications

Task NO.	Test fuel	Injection pressure	Ambient pressure	Fuel temperature	Notes	Related papers *
-	-	Mpa	Bar	K	-	
1	Ethanol	6	1	275	Non-evaporating, transition and flash-boiling	[8], [9]
2	Ethanol	6	1	300		[7], [8], [9]
3	Ethanol	6	1	325		[8], [9]
4	Ethanol	6	1	350		[8], [9]
5	Ethanol	6	1	355		[8], [9]
6	Ethanol	6	1	360		[8], [9]
7	Ethanol	6	1	365		[8], [9]
8	Ethanol	6	1	370		[8], [9]
9	Ethanol	6	1	375		[8], [9]
10	Ethanol	6	1	400		[8], [9]
11	Ethanol	6	1	300	Micro-view	[7]
12	Gasoline	6	1	275	Non-evaporating, transition and flash-boiling	[9]
13	Gasoline	6	1	300		[7], [9]
14	Gasoline	6	1	325		[9]
15	Gasoline	6	1	340		[9]
16	Gasoline	6	1	345		[9]
17	Gasoline	6	1	350		[9]
18	Gasoline	6	1	355		[9]
19	Gasoline	6	1	360		[9]
20	Gasoline	6	1	375		[9]
21	Gasoline	6	1	400		[9]
22	Gasoline	6	1	300	Micro-view	[7]

* List of related publications (Chapter 4)

- [7] Y. Huang, S. Huang, R. Huang, G. Hong. Macroscopic and Microscopic Characteristics of Ethanol and Gasoline Sprays. *19th Australasian Fluid Mechanics Conference*, Melbourne Australia; 2014.
- [8] Y. Huang, S. Huang, P. Deng, R. Huang, G. Hong. The Effect of Fuel Temperature on the Ethanol Direct Injection Spray Characteristics of a Multi-hole Injector. *SAE Int. J. Fuels Lubr.* 2014; 7: 792-802.
- [9] Y. Huang, S. Huang, R. Huang, G. Hong. Spray and evaporation characteristics of ethanol and gasoline direct injection in non-evaporating, transition and flash-boiling conditions. *Energy Conversion and Management* 2016; 108: 68-77.

Table A.3: List of engine experiment conditions and related publications

Task NO.	Speed	EDI timing	Throttle	GPI mass	EDI mass	Ethanol ratio	EDI heating	Notes	Related papers *
-	rpm	CAD BTDC	%	mg	mg	Vol%	°C	-	
1	3500	300	33%	13.4	-	0%	No	Effect of ethanol ratio	[10]
2	3500	300	33%	8.5	8.0	46%	No		[10]
3	3500	300	33%	7.1	10.7	58%	No		[10]
4	3500	300	33%	5.4	13.4	69%	No		[10]
5	3500	300	33%	4.2	15.0	76%	No		[10]
6	3500	300	33%	2.8	17.3	85%	No		[10]
7	3500	300	33%	-	21.7	100%	No		[10]
8	4000	300	36%	13.4	-	0%	No		[5], [10]
9	4000	300	36%	8.5	8.0	46%	No		[5], [10]
10	4000	300	36%	7.1	10.7	58%	No		[5], [10]
11	4000	300	36%	5.4	13.4	69%	No		[5], [10]
12	4000	300	36%	4.2	15.0	76%	No		[5], [10]
13	4000	300	36%	2.8	17.3	85%	No		[5], [10]
14	4000	300	36%	-	21.7	100%	No		[5], [10]
15	3500	300	33%	8.0	8.8	50%	45, 60, 75, 90, 105	Effect of ethanol temperature	[11]
16	4000	300	36%	8.0	8.8	50%	45, 60, 75, 90, 105		[11]
17	3500	300	33%	13.4	-	0%	50, 70, 90	Effect of EDI heating	[12]
18	3500	300	33%	11.1	4.0	25%	50, 70, 90		[12]
19	3500	300	33%	9.4	6.8	40%	50, 70, 90		[12]
20	3500	300	33%	7.5	10.0	55%	50, 70, 90		[12]
21	3500	300	33%	5.2	13.5	70%	50, 70, 90		[12]
22	3500	300	33%	2.8	17.3	85%	50, 70, 90		[12]
23	3500	300	33%	-	21.7	100%	50, 70, 90		[12]
24	4000	300	36%	13.4	-	0%	50, 70, 90		[12]
25	4000	300	36%	11.1	4.0	25%	50, 70, 90		[12]
26	4000	300	36%	9.4	6.8	40%	50, 70, 90		[12]
27	4000	300	36%	7.5	10.0	55%	50, 70, 90		[12]
28	4000	300	36%	5.2	13.5	70%	50, 70, 90		[12]
29	4000	300	36%	2.8	17.3	85%	50, 70, 90		[12]
30	4000	300	36%	-	21.7	100%	50, 70, 90		[12]

* Notes: List of related publications (Chapter 7)

[10] Y. Huang, G. Hong, R. Huang. The Effect of Volume Ratio of Ethanol Directly Injected in a Gasoline Port Injection Spark Ignition Engine. *10th Asia-Pacific Conference on Combustion*, the Combustion Institute, Beijing China; 2015.

[11] Y. Huang, G. Hong. An Investigation of the Performance of a Gasoline Spark Ignition Engine Fuelled with Hot Ethanol Direct Injection. *Australian Combustion Symposium*, the Combustion Institute, Melbourne Australia; 2015.

[12] Y. Huang, G. Hong. Investigation of the effect of heated ethanol fuel on combustion and emissions of an ethanol direct injection plus gasoline port injection (EDI + GPI) engine. *Energy Conversion and Management* 2016; 123: 338-347.